

Dynamic Imperfections in the Compact Linear Collider



Chetan Gohil
Wadham College, Oxford

*Thesis submitted in fulfilment of the requirements for the degree of
Doctor of Philosophy at the University of Oxford*

Hilary Term, 2020



Abstract

The Compact Linear Collider (CLIC) is a proposed TeV-scale electron-positron collider under development at the European Organization for Nuclear Research (CERN). CLIC adopts a staged approach with three centre-of-mass energies: 380 GeV, 1.5 TeV and 3 TeV. This work focuses on the first stage, which has been optimised for studies of the Higgs boson and top-quark physics.

A high luminosity is achieved by targeting ultra-small beam sizes at the collision point. Realising these beam sizes relies on the production and transport of ultra-low emittance beams. The preservation of emittance is important in three sections: the Ring to Main Linac (RML), the Main Linac (ML) and the Beam Delivery System (BDS). Typically, each section is studied individually. In this work, they are integrated into a single simulation, referred to as an ‘integrated simulation’. In an integrated simulation, particles are tracked through the RML, ML and BDS to reach the collision point. The luminosity is calculated with a full simulation of the collision including beam-beam effects.

Imperfections lead to emittance growth and degrade luminosity. Integrated simulations are performed to evaluate the impact of static and dynamic imperfections. The impact of static imperfections is mitigated with well known beam-based tuning procedures. This work focuses on the impact of dynamic imperfections and their mitigation.

A well studied dynamic imperfection is ground motion. Integrated simulations in this work show ground motion can be mitigated with a feedback system that corrects the beam trajectory and a stabilisation system for quadrupole magnets.

Much of this work is devoted to a newly considered dynamic imperfection, that is stray magnetic fields (SMFs). CLIC is sensitive to sub-nT SMFs. The typical amplitude of SMFs found in an accelerator environment is several orders of magnitude larger than this. Therefore, SMFs are a serious consideration in the design and operation of CLIC.

A dedicated mitigation system is needed to ensure SMFs do not significantly impact luminosity. A passive shielding technique is investigated. Measurements of the shielding provided by mu-metal for small-amplitude external magnetic fields are performed. With these measurements, a magnetic shielding model is validated. The proposed mitigation strategy for CLIC is to surround sensitive regions of the beamline with a 1 mm mu-metal layer.

SMFs at two accelerator facilities at CERN are surveyed. With these measurements, a model for SMFs is developed. Integrated simulations including SMFs are performed and show luminosity loss is effectively mitigated with a beam trajectory feedback system and mu-metal shield.

Acknowledgements

I would like to thank my supervisors Philip Burrows and Daniel Schulte for the opportunity to work on this project and for their support and guidance, which has shaped this work.

I would also like to thank my colleagues at CERN and other institutions, which contributed to this work. In particular, I would like to thank Neven Blaskovic Kraljevic and Balazs Heilig who provided many useful discussions and participated in measurements. I would also like to thank Edu Marin and Marco Buzio for their contribution at the start of this project and Andrea Latina for his help with simulations.

I would like to thank the past and present members of the FONT group and the CLIC Beam Physics group for providing a welcoming and supportive environment to work in.

Contents

1	Introduction	1
1.1	The Standard Model of Particle Physics	1
1.2	Particle Accelerators and Colliders	3
1.2.1	Particle Accelerators	4
1.2.2	Colliders	6
1.3	Thesis Outline	9
2	Linear Colliders	10
2.1	Physics Potential	10
2.2	Projects	13
2.2.1	The ILC	15
2.2.2	CLIC	15
2.3	Beam Dynamics	17
2.4	Luminosity	23
2.5	Imperfections	27
2.5.1	Static Imperfections	28
2.5.2	Dynamic Imperfections	30
3	Integrated Simulations	32
3.1	Simulation Codes	32
3.2	Machine Description	34
3.3	Perfect Machine Performance	37
3.4	Nominal Performance	38
3.5	Static Imperfections	39
3.6	Dynamic Imperfections	43
3.6.1	Beam-Beam Offset and Jitter	44
3.6.2	Phase Errors	46
4	Ground Motion	49
4.1	Models	49
4.1.1	Power Spectral Densities	51

4.1.2	Generators	53
4.1.3	Impact on Luminosity	54
4.2	Mitigation Methods	54
4.2.1	Beam Trajectory Feedback System	54
4.2.2	Quadrupole Stabilisation System	57
4.3	Integrated Simulations	59
4.3.1	Specific Sections	59
4.3.2	Models	60
4.4	IP Feedback Systems	61
5	Stray Magnetic Field Sensitivity and Tolerances	66
5.1	Stray Magnetic Fields	66
5.1.1	Temporal and Spatial Variation	67
5.1.2	Impact on Luminosity	68
5.2	Spatial Profiles	74
5.2.1	Point-Like SFs	74
5.2.2	Sinusoidal SFs	77
5.2.3	Homogeneous SFs	83
5.3	Summary	84
6	Magnetic Field Sensors	85
6.1	Measurements	85
6.1.1	Magnetometers	85
6.1.2	Magnetic Field Calculations	87
6.1.3	Requirements	88
6.2	Mag-13	89
6.2.1	Sensitivity	92
6.2.2	Linearity	94
6.2.3	Noise	96
7	Passive Shielding	98
7.1	Magnetic Shielding Theory	98
7.1.1	Magnetic Materials	98
7.1.2	Shielding Mechanisms	101
7.1.3	Shielding Factor and Transfer Function	102
7.2	Applications in Accelerators	106
7.3	The LHC Beam Screen	108
7.4	Soft Magnetic Materials	110
7.4.1	Soft Iron	111
7.4.2	Supra 36	113

7.4.3	Mu-Metal	114
7.5	Mitigation of Stray Magnetic Fields	118
7.5.1	Strategy	118
7.5.2	Transfer Functions	119
8	Natural Stray Magnetic Fields	123
8.1	The Geomagnetic Field	123
8.2	Geomagnetic Storms	125
8.3	Sources Above 1 Hz	127
8.3.1	Lightning	128
9	Environmental Stray Magnetic Fields	131
9.1	Ambient Magnetic Field at CERN	131
9.1.1	The PS	134
9.2	The Electrical Grid	136
9.2.1	Power Lines	137
9.2.2	Sub-Power Stations	139
9.2.3	Integrated Simulations	144
9.3	Transport Infrastructure	149
10	Technical Stray Magnetic Fields	152
10.1	Magnets	152
10.2	Power Cables	156
10.3	Radio-Frequency Systems	159
10.4	Ventilation Systems	162
10.5	Lights	165
10.6	Other Elements	166
11	Stray Magnetic Fields in Accelerator Environments	167
11.1	The CLEAR Facility	168
11.2	The LHC	172
11.3	Modelling	183
11.4	Integrated Simulations	188
12	Design Choices	189
12.1	Mitigation Options	189
12.2	High-Luminosity CLIC	194
12.3	Final Stage	196
13	Conclusions	200

A	Signal Processing	205
A.1	Discrete-Time Signals	205
A.2	Spectral Estimation	206
A.3	Linear Time-Invariant Filters	208
A.4	Measurement Errors	210
	Bibliography	215

Glossary

AC Alternating Current

BDS Beam Delivery System

BPM Beam Position Monitor

BSM Beyond Standard Model

CA Central Arc

CERN European Organisation for Nuclear Research

CLEAR CERN Linear Electron Accelerator for Research

CLIC The Compact Linear Collider

CMS Compact Muon Solenoid

CSD Cross Spectral Density

DAQ Data Acquisition System

DC Direct Current

DR Damping Ring

DFT Discrete Fourier Transform

ECS Energy Collimation Section

EM Electromagnetic

FD Final Doublet

FFS Final Focus System

FFT Fast Fourier Transform

FONT Feedback on Nanosecond Timescales

GM Ground Motion

GUINEA-PIG Generator of Unwanted Interactions for Numerical Experiment Analysis -
Program Interfaced to GEANT

HERA Hadron-Electron Ring Accelerator

HL-LHC High-Luminosity Large Hadron Collider
ILC International Linear Collider
IP Interaction Point
LEP Large Electron-Positron
LH Left Hand
LHC Large Hadron Collider
LTI Linear Time-Invariant
LTL Long Transfer Line
ML Main Linac
NI National Instruments
NTE Nominal Target Emittance
PLACET Programme for Linear Accelerator Correction Efficiency Tests
PS Proton Synchrotron
PSD Power Spectral Density
PSU Power Supply Unit
RF Radio Frequency
RH Right Hand
RMS Root Mean Square
RTML Ring to Main Linac
SF Stray Field
SLAC Stanford Linear Accelerator Laboratory
SM Standard Model
SPS Super Proton Synchrotron
SR Synchrotron Radiation
STE Static Target Emittance
TAL Turn-Around Loop
VT Vertical Transfer
XBOX High-Gradient X-Band Test Facility

Chapter 1

Introduction

1.1 The Standard Model of Particle Physics

There are four known fundamental forces in the universe: the *weak* force; the *strong* force; the *electromagnetic* (EM) force and the *gravitational* force. Modern particle physics describes three of these forces (the weak, strong and EM) with a theory known as the *Standard Model* (SM) [1]. The SM describes the interaction between particles of two distinct types: ‘matter’ particles known as *fermions* and ‘force-carrying’ particles known as *bosons*. These two groups of particles differ in their intrinsic angular momentum, referred to as *spin*, where fermions are particles with half-integer spin and bosons are particles with integer spin. Fermions and bosons of the SM are listed in Table 1.1. Every particle in the SM also has an associated anti-particle, with the same mass but opposite electric charge.

Fermions are grouped into three generations of increasing mass, with all stable matter being comprised of first-generation fermions. The interactions between fermions (forces) are mediated by the exchange of gauge bosons. All fermions experience weak interactions, but only electrically charged fermions experience EM interactions. There are two types of fermions: *quarks*, which possess a property known as *colour*, and *leptons*, which do not possess colour. Only particles that possess colour may experience strong interactions. Therefore, leptons do not experience the strong interaction.

Leptons (Spin-1/2)				
Particle	Symbol	Generation	Q [e]	m [MeV/ c^2]
Electron	e^-	1	-1	0.511
Muon	μ^-	2	-1	105.7
Tau	τ^-	3	-1	1,777
Electron Neutrino	ν_e	1	0	$< 3 \times 10^{-6}$
Muon Neutrino	ν_μ	2	0	-
Tau Neutrino	ν_τ	3	0	-
Quarks (Spin-1/2)				
Particle	Symbol	Generation	Q [e]	m [GeV/ c^2]
Up	u	1	2/3	0.0015–0.004
Charm	c	2	2/3	1.15–1.35
Top	t	3	2/3	169–174
Down	d	1	-1/3	0.004–0.008
Strange	s	2	-1/3	0.08–0.13
Bottom	b	3	-1/3	4.1–4.4
Gauge Bosons (Spin-1)				
Particle	Symbol	Force	Q [e]	m [GeV/ c^2]
Photon	γ	EM	0	0
W, Z-Boson	W^\pm, Z	Weak	$\pm 1, 0$	80.4, 91.2
Gluon	g	Strong	0	0
Scalar Bosons (Spin-0)				
Particle	Symbol	Force	Q [e]	m [GeV/ c^2]
Higgs Boson	H	-	0	125.1

Table 1.1: Elementary particles of the SM [1, 2]. Q is the electric charge of the particle given in units of electron charge $e = 1.6 \times 10^{-19}$ C and m is the rest mass of the particle as stated in [1, 2].

The strong force binds combinations of quarks together to form composite particles known as *hadrons*, of which there are two types: *mesons* and *baryons*. Mesons consist of quark–anti-quark pairs, whereas baryons are bound states of an odd number of quarks, typically three. The proton p is a baryon consisting of uud and the neutron n consists of udd . Exotic baryons consisting of four quarks and one anti-quark are known as *pentaquarks*.

The final particle described by the SM is a scalar boson known as the *Higgs boson*. Its existence was postulated to explain the masses of the other particles in the SM, which arise from a process of symmetry breaking known as the *Higgs mechanism* [3]. A particle

consistent with the Higgs boson was discovered in 2012 at the *Large Hadron Collider* (LHC) at the *European Organization for Nuclear Research* (CERN) in Geneva, Switzerland [4, 5].

Despite the success of the SM, there are several known phenomena it neither includes nor explains. For example: gravity [6]; dark matter [7]; neutrino oscillations [8].

1.2 Particle Accelerators and Colliders

Particle accelerators have been an important tool used to study the SM. The approach is to impact high-energy particles onto other particles. The higher the collision energy, the smaller the spatial scale that is probed. For sufficiently high energies, an interaction occurs which results in the production of new particles. The rate at which an interaction X occurs is given by

$$R_X = \sigma_X(E_{\text{CM}}) \mathcal{L}, \quad (1.1)$$

where \mathcal{L} is the *luminosity*, which is a property of the setup of the experiment, and $\sigma_X(E_{\text{CM}})$ is the *cross-section* of the interaction, which depends on the centre-of-mass energy E_{CM} of the colliding particles.

The experimental setup can either be:

- A *fixed-target* experiment, where a beam interacts with a stationary target.
- A *collider*, where two beams interact.

Fixed-target experiments tend to have large luminosities due to a large number of target particles. However, momentum must be conserved in any interaction. As a result, the final-state particles of a fixed-target experiment must carry the momentum of the incoming beam. A collider with beams of equal and opposite momenta is a more appealing setup in the search for new particles because all of the initial energy is available for particle production.

1.2.1 Particle Accelerators

In modern particle accelerators, cavities filled with EM waves referred to as *accelerating cavities* (or *radio-frequency* (RF) *cavities*) are used to increase the energy of charged particles. This process is known as *acceleration*. The energy gain per unit length and charge is known as the *accelerating gradient*. The nature of EM waves leads to the accelerated particles being pushed longitudinally into groups called *bunches*. A series of bunches is referred to as a *train* (or *pulse*).

The penetration of EM waves into a cavity's wall is determined by the *skin depth* [9]

$$\delta = \frac{1}{\sqrt{\pi f \mu \sigma}}, \quad (1.2)$$

where f is the EM wave frequency, which is known as the *RF frequency*, μ is the magnetic permeability and σ is the electrical conductivity of the material forming the cavity. The penetration of the EM waves into the cavity walls leads to the flow of current and losses on the surface. These losses are minimised by using a material with a high electrical conductivity, which leads to a small skin depth. *Superconducting RF cavities* are formed from a superconducting material, such as niobium [10]. Alternatively, *normal conducting RF cavities* are formed from copper.

The trajectory of the particles in an accelerator is controlled with magnets. Modern accelerators use a series of *quadrupole* magnets to transversely focus a beam and *dipole* (or *bending*) magnets to bend a beam. Quadrupoles and dipoles are said to be linear elements because the force they exert is a linear function of the beam offset in the magnet. Higher-order magnets, such as *sextupoles* and *octupoles*, are non-linear and are typically used in colliders to manipulate a beam just before collision.

Linear and Circular Accelerators

Particle accelerators guide beams on straight or circular trajectories. In the case of a straight trajectory, the accelerator is referred to as a *linear accelerator* (*linac*). Here, particles are injected at their initial energy at one end and extracted at their final energy at the other end. Conversely, in the case of a circular accelerator, particles are kept on a curved path with bending magnets and circulate the machine many times, gaining a fraction of their final energy each time. Circular accelerators can maintain a beam at a constant radius by increasing the bending magnet strength synchronously with the beam energy; such accelerators are referred to as *synchrotrons*. Circular machines that maintain a beam at a fixed energy are referred to as *storage rings*.

When a charged particle follows a curved trajectory, it radiates photons tangential to the direction of travel. This is known as *synchrotron radiation* (SR). The power P emitted by a particle as SR is proportional to [11]

$$P \propto \frac{1}{\rho^2} \frac{E^4}{m^4}, \quad (1.3)$$

where ρ is the bending radius of the particle, E is the energy of the particle and m is the rest mass of the particle. In a synchrotron or storage ring, SR losses are replenished by accelerating cavities.

The final energy of an accelerator is determined by its size, the technology used and the amount of SR emitted. Assuming the particle mass or bending radius is sufficiently large for SR not to be a concern, the final energy of an accelerator is proportional to

$$E \propto \begin{cases} RB & \text{for circular accelerators,} \\ LG & \text{for linear accelerators,} \end{cases} \quad (1.4)$$

where for a circular accelerator R is the radius and B is the bending magnet strength and for a linear accelerator L is the length and G is the effective accelerating gradient. The radius of a circular accelerator and length of a linear accelerator are determined by

financial considerations, but the bending magnet strength and effective accelerating gradient are determined by the available technology. The bending magnet strength of the LHC, which is the world's highest energy collider, is 8.3 T [12]. Bending magnets which could reach a field of 20 T are being developed [13]. The maximum accelerating gradient that is achievable depends on the technology being considered. Current superconducting cavities are limited to gradients of up to 55 MV/m [10], whereas normal conducting cavities can reach gradients above 100 MV/m [14].

1.2.2 Colliders

Linear and Circular Colliders

A *linear collider* is essentially a pair of independent linacs pointed towards each other. The collision occurs at a single location, referred to as the *interaction point* (IP), which is surrounded by a *particle detector* to measure the resultant final-state particles of an interaction. A *circular collider* is a pair of circular accelerators with oppositely directed adjacent beams. Circular colliders can have several collision points. The geometry of linear and circular colliders is illustrated in Figure 1.1.

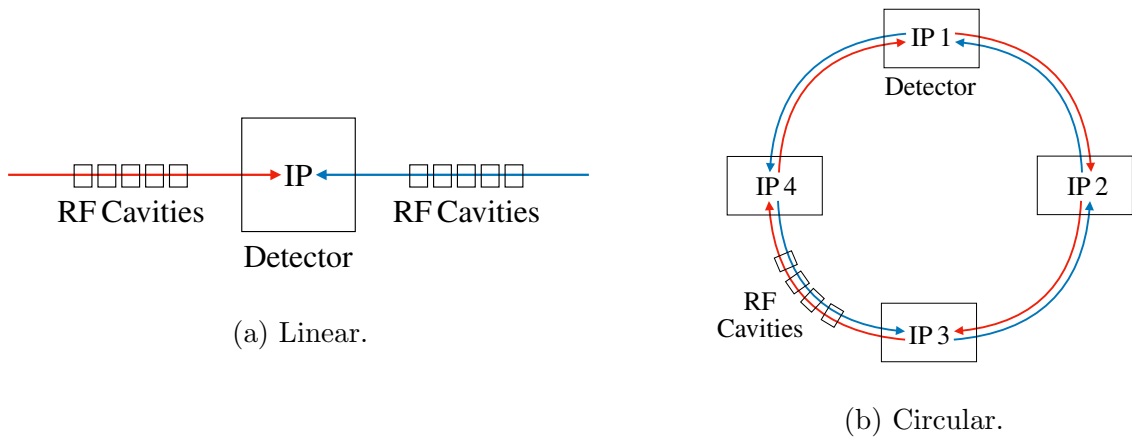


Figure 1.1: Geometry of linear and circular colliders. The colliding beams are shown in blue and red.

The luminosity of a collider is proportional to [11]

$$\mathcal{L} \propto \frac{f}{\sigma_x^* \sigma_y^*}, \quad (1.5)$$

where in a circular collider f is the revolution frequency, or in a linear collider f is the train repetition frequency, and σ_x^* (σ_y^*) is the horizontal (vertical) beam size at the IP. Typically, the train repetition frequency in a linear collider is much lower than the revolution frequency in a circular collider. Therefore, to obtain competitive luminosities linear colliders target extremely small beam sizes at the IP.

Hadron and Lepton Colliders

Hadron colliders, particularly the LHC, have been used to comprehensively probe the strong interaction at the TeV scale. However, hadron colliders present several challenges for particle detectors and data analysis. Hadrons are not elementary particles, but rather composed of quarks bound by gluons. In a head-on collision of two hadrons, it is the constituent quarks and gluons that collide. These quarks and gluons can carry any fraction of the hadron's total energy, which leads to an uncertainty in the centre-of-mass energy of the collision. Additionally, strong interactions between quarks and gluons contribute to a large background, which makes particle identification and tracking in the detector difficult.

Because leptons do not partake in the strong interaction, they provide a clean environment to perform measurements. Leptons are also elementary, therefore the centre-of-mass energy of a lepton collision is precisely known and can be tuned to maximise the production cross-section of a particular process.

Future Colliders

A particle must be stable for long enough to be accelerated for it to be used in a collider. Muons and taus have very short lifetimes, $2.2\,\mu\text{s}$ and $0.29\,\text{ps}$ respectively, which makes acceleration extremely difficult. Therefore, the choice of particle species in a lepton collider is

limited to electrons and positrons. Electrons and positrons are very light. Consequently, as described in Equation (1.3), they emit a large amount of SR in circular accelerators. The SR losses must be replenished by accelerating cavities to maintain a constant energy and radius.

One approach to overcome SR is to increase the radius of the accelerator. This is the basis of one branch of the *Future Circular Collider* (FCC) project, known as the FCC-ee [15]. This project envisages a 80 to 100 km ring, which can host an e^+e^- collider of $E_{\text{CM}} = 350 \text{ GeV}$. The ring could later host a hadron collider, referred to as FCC-hh, which could reach $E_{\text{CM}} = 100 \text{ TeV}$ [16]. The same strategy has been adopted by the CEPC-SppC project, which is a 54 km ring that would initially host an e^+e^- collider (CEPC) with $E_{\text{CM}} = 240 \text{ GeV}$, followed by a pp collider (SppC) with $E_{\text{CM}} = 70 \text{ TeV}$ [17].

The feasibility of a circular e^+e^- collider depends on the desired centre-of-mass energy. To study the Higgs boson requires a minimum $E_{\text{CM}} \approx 216 \text{ GeV}$, which is achievable with a circular collider. However, reaching the TeV scale demands a linear collider as a circular collider would either require a very large ring or have a very high power consumption to replenish SR losses.

There are currently two TeV-scale linear e^+e^- colliders under development: the *International Linear Collider* (ILC) and the *Compact Linear Collider* (CLIC). These projects are discussed further in Sections 2.2.1 and 2.2.2. They both plan for an initial stage operating at a comparable centre-of-mass energy to FCC-ee and CEPC followed by upgrades to reach the TeV scale.

1.3 Thesis Outline

The next chapter presents the physics of linear colliders and the two current projects in more detail. Chapter 2 also describes the factors that affect the luminosity of a linear e^+e^- collider and the codes used in this work to simulate linear colliders.

This work primarily focuses on the first stage of CLIC at $E_{\text{CM}} = 380 \text{ GeV}$. Chapter 3 benchmarks the luminosity performance of this collider including static imperfections. Following this, the impact of the most important dynamic imperfections is considered, these are ground motion and external magnetic fields, referred to as *stray magnetic fields*. Chapter 4 evaluates the impact of ground motion, including the effect of mitigation techniques.

Chapters 5 to 11 are devoted to stray magnetic fields. Sensitivities and tolerances for stray magnetic fields in CLIC are presented in Chapter 5. Chapter 6 describes the magnetic field sensors used in this work to survey stray magnetic fields at CERN. Chapter 7 describes a magnetic shielding technique to mitigate stray magnetic fields. Chapters 8, 9 and 10 look at specific stray magnetic field sources and their impact on CLIC. Stray magnetic fields in realistic accelerator environments are characterised in Chapter 11 and their impact on CLIC is simulated with different mitigation techniques.

Design choices in CLIC relating to dynamic imperfections are discussed in Chapter 12 and a conclusion is presented in Chapter 13.

In the rest of this work, basic concepts and common terms used to describe and analyse signals are assumed. The reader should refer to Appendix A for a summary.

Chapter 2

Linear Colliders

A brief description of the physics of linear colliders is presented in this chapter. Two TeV-scale e^+e^- colliders: the ILC and CLIC are described.

2.1 Physics Potential

This section briefly describes some of the particle physics studies that can be performed with linear e^+e^- colliders. For a more comprehensive overview, the reader should refer to [18, 19].

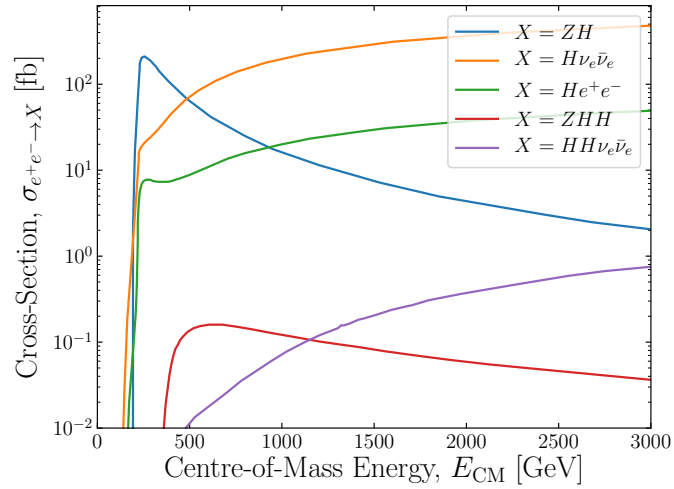


Figure 2.1: Higgs boson production cross-sections vs centre-of-mass energy for unpolarised e^+e^- interactions [20].

Higgs Physics

The cross-section for an interaction depends on the centre-of-mass energy of the colliding particles. The cross-section for different Higgs production mechanisms from e^+e^- interactions is shown in Figure 2.1 and respective tree-level Feynman diagrams are shown in Figure 2.2.

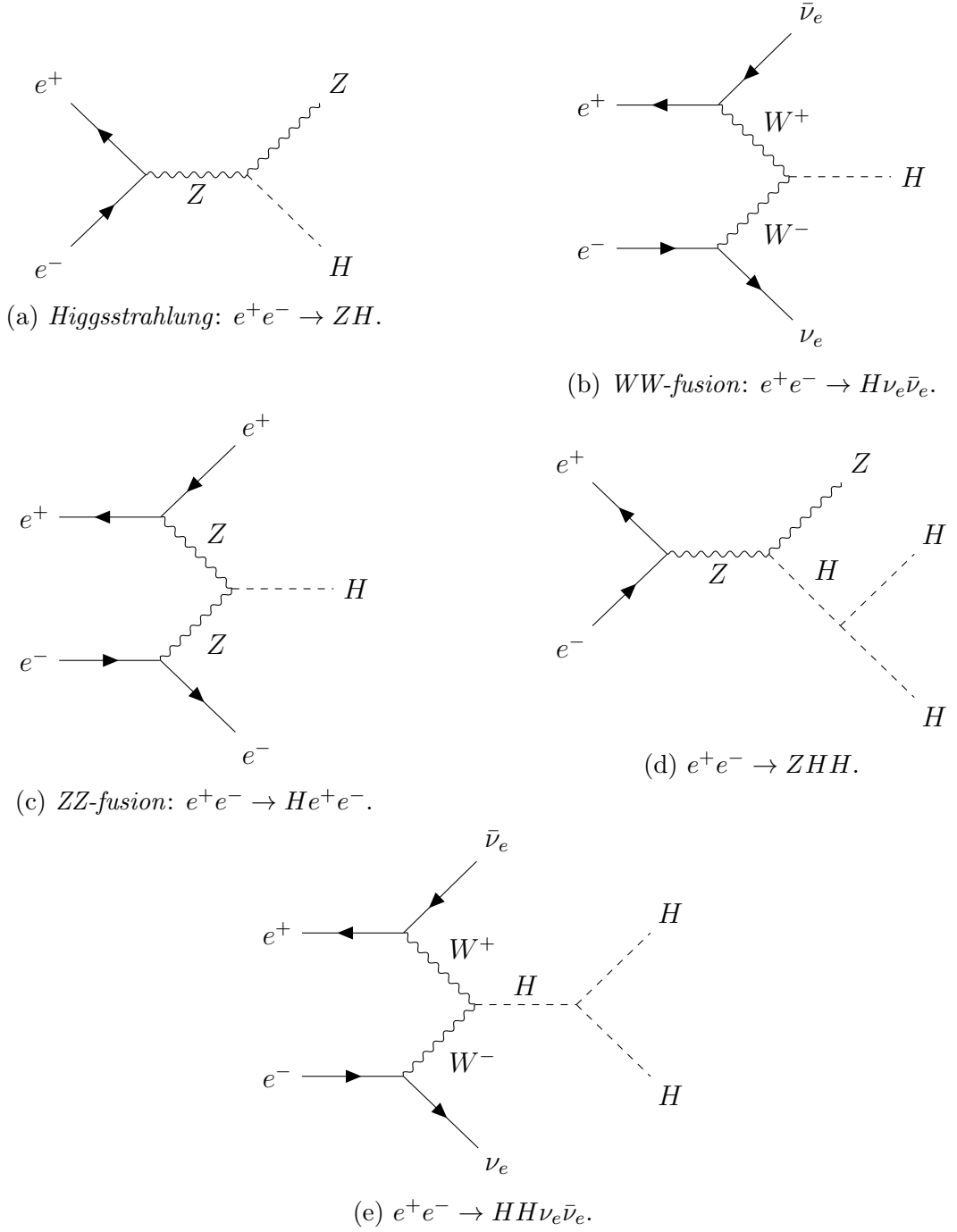


Figure 2.2: Feynman diagrams for Higgs boson production mechanisms in linear e^+e^- colliders.

The strength of an interaction between two particles is referred to as the *coupling*. In the SM, the coupling of the Higgs boson to a fermion is directly proportional to the fermion's mass. Any deviation from this would indicate *beyond SM* (BSM) physics. To probe different theories, the couplings should be known to a precision of 1% or better, which can be provided by e^+e^- colliders through combined studies of Higgsstrahlung and WW-fusion [20].

Higgsstrahlung can also provide a precise measurement of the Higgs boson mass using the *recoil mass technique* [20]. The advantage of this technique is that the measurement is independent of the Higgs decay mechanism.

Another important measurement is of the Higgs' coupling to itself, the *Higgs self-coupling*. Its value is sensitive to different BSM theories [20]. The Higgs self-coupling can be measured through studies of $e^+e^- \rightarrow HH\nu_e\bar{\nu}_e$ and $e^+e^- \rightarrow ZHH$ [20]. These processes occur at the TeV scale, and therefore require a linear e^+e^- collider.

Top-Quark Physics

The cross-section for different top-quark production mechanisms from e^+e^- interactions is shown in Figure 2.3 and respective tree-level Feynman diagrams are shown in Figure 2.4.

The cross-section for top-quark pair production is sensitive to the mass of the top quark. This can be exploited to measure the top-quark mass with a *threshold scan* [21]. The coupling of the Higgs boson to the top quark can be measured from studies of $e^+e^- \rightarrow t\bar{t}H$ [21].

Historically, the top quark has been produced in hadron colliders. e^+e^- colliders provide the opportunity to directly study the coupling of the top quark to the neutral electroweak bosons (Z and γ), which is sensitive to different BSM theories [18].

In the SM, flavour changing top-quark decays ($t \rightarrow qX$, where $q = u, c$ and $X = \gamma, g, Z, H$) are very strongly suppressed. There are many extensions to the SM that enhance these decays [18]. A linear e^+e^- collider can study these processes to greater precision than current colliders.

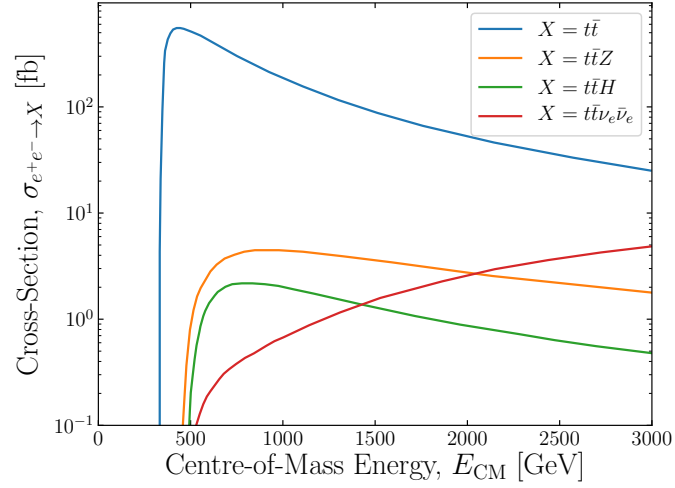


Figure 2.3: Top-quark production cross-sections vs centre-of-mass energy for unpolarised e^+e^- interactions [21].

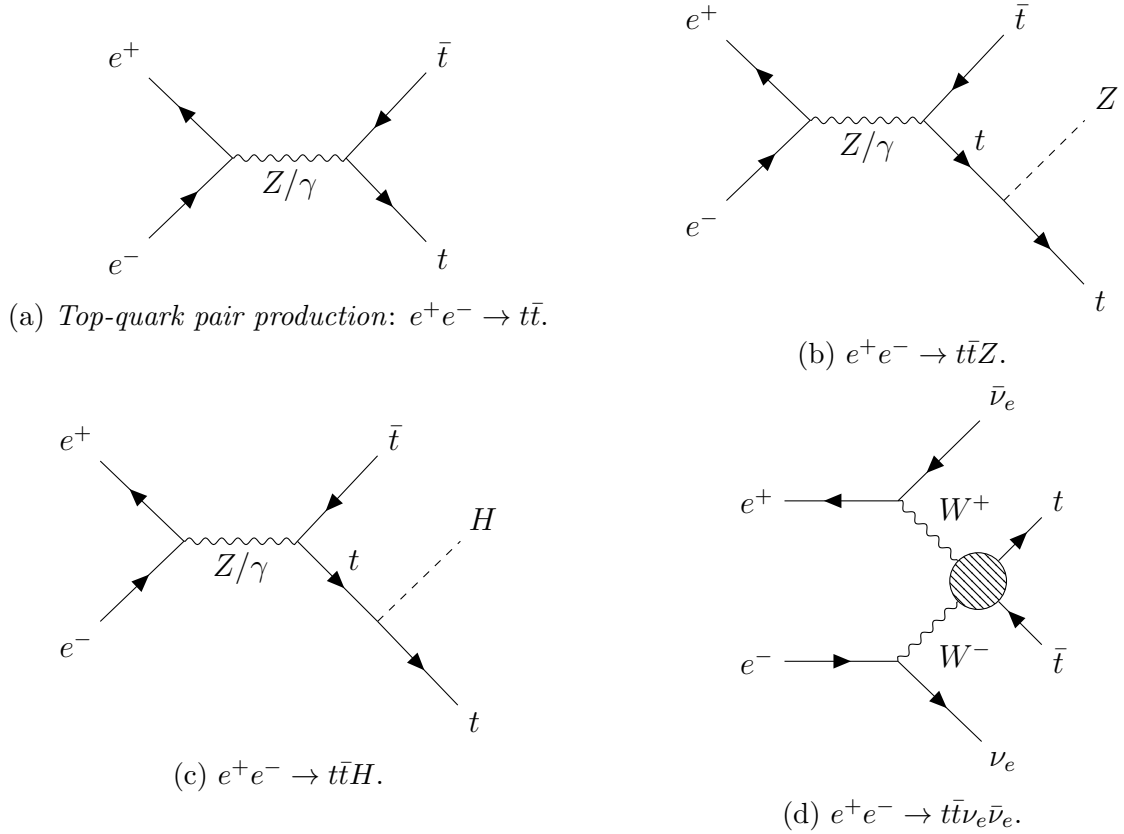


Figure 2.4: Feynman diagrams for top-quark production mechanisms in linear e^+e^- colliders.

2.2 Projects

A schematic diagram of a linear collider beamline is shown in Figure 2.5. Each beam is transported from the particle source to the IP through four sections:

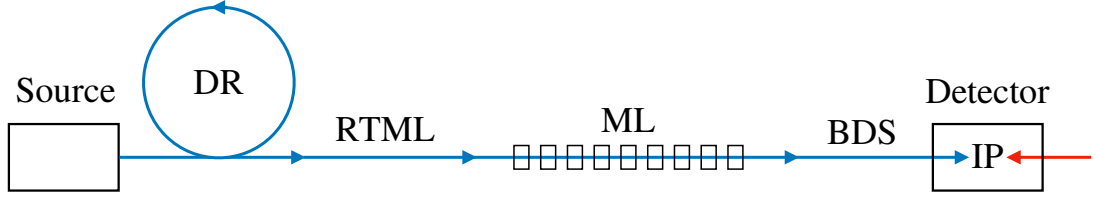


Figure 2.5: Schematic diagram of a linear collider beamline.

- ***Damping Ring (DR)***: This accepts a beam from the particle source with a large emittance. As the beam circulates the DR, it emits SR. This results in momentum being lost in the transverse and longitudinal direction. The energy lost is replenished by RF cavities, which boost momentum in the longitudinal direction only. As a result, transverse motion is damped and the emittance is reduced. The DRs produce ultra-low emittance beams.
- ***Ring to Main Linac (RTML)***: From the DR, the beam is transported through the RTML. The RTML compresses the bunch length so that it is small compared to the RF wavelength in the main accelerating cavities. This ensures the head and tail of a bunch experience similar accelerating gradients. The RTML can also be used to manipulate the polarisation of a beam with a *spin rotator* [22].
- ***Main Linac (ML)***: The beam then enters the ML, which predominantly consists of accelerating cavities. The beam is accelerated to its final energy in this section.
- ***Beam Delivery System (BDS)***: Finally, the BDS prepares the beam for collision. This involves removing particles with large offsets, known as the *beam halo*. Particles with large energy errors are also removed. This process is known as *collimation*. The BDS also focusses the beam to the targeted size for collision at the IP. This is done in the *final focus system* (FFS).

There are two proposed linear e^+e^- colliders: the ILC and CLIC.

2.2.1 The ILC

The ILC consists of two linacs that utilise superconducting RF cavities. The baseline design considers two possible accelerating gradients: either 31.5 MV/m or 35 MV/m [23]. The choice of accelerating gradient depends on the cost of the available technology during construction.

The baseline design is at $E_{\text{CM}} = 250 \text{ GeV}$ with a site length of 20.5 km [24]. Key parameters of the ILC are summarised in Table 2.1.

Parameter	Symbol	Unit	Initial	Upgrades	
Centre-of-mass energy	E_{CM}	GeV	250	500	1000
Particles per bunch	N	10^{10}	2	2	1.74
Train repetition frequency	f_{rep}	Hz	5	5	4
Bunches per train	n_b		1312	1312	2450
Bunch spacing	Δt_b	ns	554	554	366
Accelerating gradient	G	MV/m	31.5 or 35	31.5 or 35	31.5 or 35
Site length		km	20.5	31	40
Horizontal/vertical IP beam size	σ_x^*/σ_y^*	nm	516/7.7	474/5.9	335/2.7
Luminosity	\mathcal{L}	$10^{34} \text{ cm}^{-2} \text{ s}^{-1}$	1.35	1.80	4.9

Table 2.1: Key parameters of the ILC [24].

2.2.2 CLIC

CLIC is a TeV-scale linear e^+e^- collider being developed at CERN. It utilises normal conducting RF cavities for acceleration. The design involves three centre-of-mass energy stages, which are described below.

Energy Staging

The first stage is at $E_{\text{CM}} = 380 \text{ GeV}$, followed by an intermediate stage at $E_{\text{CM}} = 1.5 \text{ TeV}$ and a final stage at $E_{\text{CM}} = 3 \text{ TeV}$. As shown in Figure 2.6 the site is lengthened at each stage. Key parameters of the three stages are shown in Table 2.2.

The first stage at $E_{\text{CM}} = 380 \text{ GeV}$ utilises cavities with an accelerating gradient of

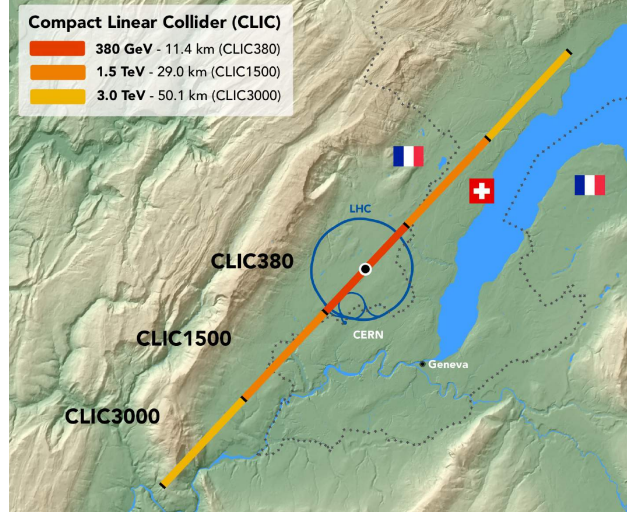


Figure 2.6: Map of the three CLIC stages [25].

Parameter	Symbol	Unit	Stage 1	Stage 2	Stage 3
Centre-of-mass energy	E_{CM}	GeV	380	1500	3000
Particles per bunch	N	10^9	5.2	3.7	3.7
Train repetition frequency	f_{rep}	Hz	50	50	50
Bunches per train	n_b		352	312	312
Bunch spacing	Δt_b	ns	0.5	0.5	0.5
Accelerating gradient	G	MV/m	72	100	100
Site length		km	11.4	29.0	50.1
Horizontal/vertical IP beam size	σ_x^*/σ_y^*	nm	150/3	60/1.5	40/1
Luminosity	\mathcal{L}	$10^{34} \text{ cm}^{-2} \text{ s}^{-1}$	1.5	3.7	5.9

Table 2.2: Key parameters of the three stages of CLIC [25].

72 MV/m, which was chosen from an optimisation of cost [25]. The high-energy stages at $E_{\text{CM}} = 1.5 \text{ TeV}$ and $E_{\text{CM}} = 3 \text{ TeV}$ utilise cavities with 100 MV/m accelerating gradients.

The centre-of-mass energy of 380 GeV for the first stage was chosen to maximise the physics reach in terms of Higgs and top-quark physics [26]. The first stage will also include a run at $E_{\text{CM}} = 350 \text{ GeV}$ to perform a threshold scan for the top quark [26]. The two high-energy stages at $E_{\text{CM}} = 1.5 \text{ TeV}$ and $E_{\text{CM}} = 3 \text{ TeV}$ will focus on direct and indirect searches for BSM physics, as well as rare SM processes [26].

Two-Beam Acceleration

CLIC adopts a novel two-beam acceleration scheme, which is illustrated in Figure 2.7. In this scheme, RF power is extracted from a high-current low-energy beam (*drive beam*) by deceleration using specially designed RF cavities (*Power Extraction and Transfer Structures*). This RF power is transferred to the main accelerating cavities and used to accelerate a low-current beam (*main beam*) to high energies. This acceleration scheme was demonstrated at the CLIC Test Facility 3 [27].

This work primarily focuses on the main beam of CLIC at $E_{\text{CM}} = 380 \text{ GeV}$.

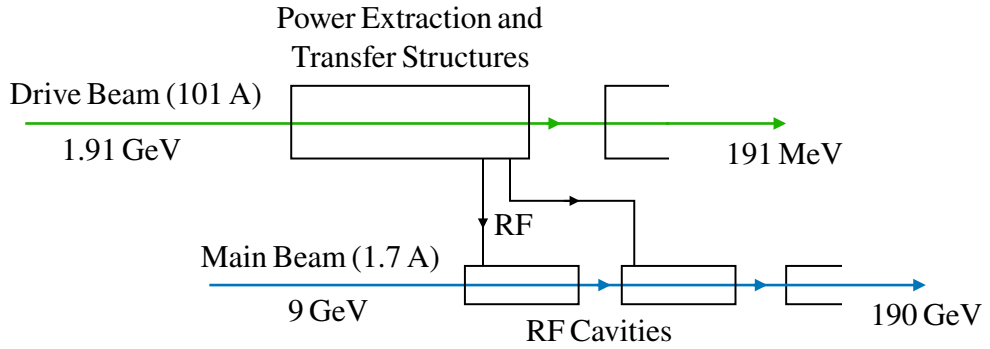


Figure 2.7: Drive-beam concept for CLIC at $E_{\text{CM}} = 380 \text{ GeV}$.

2.3 Beam Dynamics

This section briefly introduces some concepts and terms used to describe particle beams. For a more comprehensive description, the reader should refer to one of the many books [11, 28, 29, 30].

Single Particles

In an accelerator a particle moves under the influence of EM fields. Its motion can be described using Frenet-Serret coordinates [11]

$$\mathbf{x}(s) = (x(s), x'(s), y(s), y'(s), z(s), E(s))^T, \quad (2.1)$$

where x (x') is the horizontal position (angle), y (y') is the vertical position (angle), z is the longitudinal position (or *phase*), E is the energy of the particle and T denotes the transpose. These coordinates are functions of s , which is the distance travelled, and are given with respect to an ‘ideal’ particle. This coordinate system is illustrated in Figure 2.8.

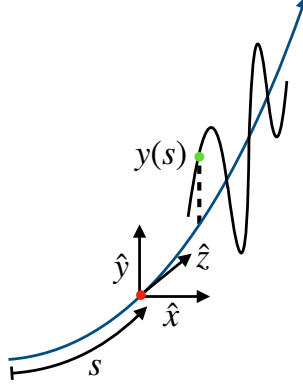


Figure 2.8: The Frenet-Serret coordinate system. \hat{x} , \hat{y} and \hat{z} are orthogonal unit vectors in the horizontal, vertical and longitudinal direction respectively. The origin of the coordinate system moves with the ideal particle (shown in red), which follows the blue path. The vertical motion of a particle (shown in green) is illustrated.

Often the motion in each plane is described separately with the coordinates $(x(s), x'(s))^T$, $(y(s), y'(s))^T$ and $(z(s), E(s))^T$. The space of these coordinates is commonly referred to as *phase space*.

Motion in the transverse plane is governed by Hill’s equation [29]

$$\frac{d^2 u(s)}{ds^2} + K(s)u(s) = F(s), \quad (2.2)$$

where $u(s) = x(s)$ or $y(s)$, $K(s)$ is a restoring force, which depends on the system of magnets used in the accelerator, referred to as the *lattice* (or *optics*), and $F(s)$ is an external force due to other particles or imperfections. Equation (2.2) describes oscillations in position known as *betatron oscillations*, which arise from the influence of magnets. The transverse motion of a particle is often referred to as *betatron motion*.

Similarly, the particle performs oscillations in the longitudinal position and energy, which arise from the acceleration process. These oscillations are known as *synchrotron oscillations*. The longitudinal motion of a particle is often referred to as *synchrotron motion*.

Beams

A beam is an ensemble of particles, which have a distribution over position, angle and energy. Often the distribution of positions and angles is Gaussian, whereas the distribution of energies is not.

Each coordinate has a *mean*

$$\mu_v = \mathbb{E}\{v\}, \quad (2.3)$$

where \mathbb{E} denotes the *ensemble average* (or *expectation value*) and $v = x, y, z, x', y', E$ is one of the coordinates. Each coordinate also has a *standard deviation*

$$\sigma_v = \sqrt{\mathbb{E}\{v^2\} - \mu_v^2}. \quad (2.4)$$

The mean and standard deviation of each coordinate has a term associated to it. These are summarised in Table 2.3.

Term	Symbol
<i>Transverse beam (or bunch) position</i>	μ_u
<i>Longitudinal bunch position (or phase)</i>	μ_z
<i>Beam (or bunch) angle</i>	$\mu_{u'}$
<i>Beam (or bunch) energy</i>	μ_E
<i>Beam size (or spot size)</i>	σ_u
<i>Beam divergence</i>	$\sigma_{u'}$
<i>Bunch length</i>	σ_z
<i>Energy spread</i>	σ_E

Table 2.3: Terms used to describe particle beams.

In each plane, the beam is described by a *mean vector* and *covariance* (or *beam*) *matrix*. For example, in the transverse plane the mean vector is

$$\boldsymbol{\mu}_u = (\mu_u, \mu_{u'})^T \quad (2.5)$$

and the covariance matrix is

$$\begin{aligned}
\Sigma_u &= \mathbb{E}\{\mathbf{x}_u \mathbf{x}_u^T\} - \boldsymbol{\mu}_u \boldsymbol{\mu}_u^T \\
&= \mathbb{E} \left\{ \begin{pmatrix} u \\ u' \end{pmatrix} \begin{pmatrix} u & u' \end{pmatrix} \right\} - \begin{pmatrix} \mu_u \\ \mu_{u'} \end{pmatrix} \begin{pmatrix} \mu_u & \mu_{u'} \end{pmatrix} \\
&= \begin{pmatrix} \sigma_u^2 & \sigma_{uu'} \\ \sigma_{u'u} & \sigma_{u'}^2 \end{pmatrix},
\end{aligned} \tag{2.6}$$

where σ_u^2 is the *variance* and $\sigma_{uu'} = \mathbb{E}\{uu'\} - \mu_u \mu_{u'}$ is the *covariance*.

In the rest of this work, the μ symbol will be dropped. For example, references to the mean transverse beam position μ_u will be denoted by u .

Emittance

The *projected geometric emittance* is defined as

$$\epsilon_{G,u} = \sqrt{|\Sigma_u|} = \sqrt{\sigma_u^2 \sigma_{u'}^2 - \sigma_{uu'}^2}, \tag{2.7}$$

where $|\cdot|$ denotes the determinant. The projected geometric emittance corresponds to the area occupied by the beam when projected onto the uu' plane.

The beam matrix can be written in terms of the projected geometric emittance as

$$\Sigma_u = \begin{pmatrix} \sigma_u^2 & \sigma_{uu'} \\ \sigma_{u'u} & \sigma_{u'}^2 \end{pmatrix} = \epsilon_{G,u} \begin{pmatrix} \beta_u & -\alpha_u \\ -\alpha_u & \gamma_u \end{pmatrix}, \tag{2.8}$$

where $\alpha_u, \beta_u, \gamma_u$ are known as the *Twiss parameters*. β_u is referred to as the *beta function*. The Twiss parameters are a property of the lattice and the injected beam. However, the projected geometric emittance is independent of the lattice.

Particle angles can be written in terms of momentum as $u' = p_u/p$, where p_u is the momentum in the u -direction and $p = \sqrt{p_x^2 + p_y^2 + p_z^2}$. Typically, when a particle is accelerated,

momentum is boosted in the longitudinal direction, but not the transverse. As a result, the beam divergence decreases and the projected geometric emittance shrinks. This process is known as *adiabatic damping*.

The *normalised projected emittance* is defined as

$$\epsilon_u = \beta\gamma\epsilon_{G,u}, \quad (2.9)$$

where β and γ are the conventional relativistic factors. The normalised emittance is preserved during acceleration, but not with dissipative effects, such as SR. In this work, references to ‘the emittance’ are to the normalised projected emittance.

Dispersion and Chromaticity

Dispersion is the effect that particles of differing energy take different paths. A particle whose energy is not the same as the ideal particle is said to be *off-energy*. Considering a vertical dipole field, the difference in the horizontal position of an off-energy particle compared to the ideal particle is given by

$$\Delta x(s) = D_x(s)\delta_E, \quad (2.10)$$

where $D_x(s)$ is the *horizontal dispersion* and $\delta_E = \Delta E/E$ is the fractional energy deviation of the particle. Note that dipole fields are not generated solely from dipole magnets, an offset quadrupole has a dipole field component and can introduce dispersion, this effect is known as *feed down*.

An action that changes the angle of a particle is commonly referred to as a *kick*. The kick applied by a magnet depends on the energy of the particle. This effect is known as *chromaticity* and magnets are said to introduce *chromatic aberrations*. High-energy particles are deflected less than low-energy particles. As a result, high-energy particles perform betatron oscillations with a longer wavelength compared to low-energy particles. This is illustrated in Figure 2.9.

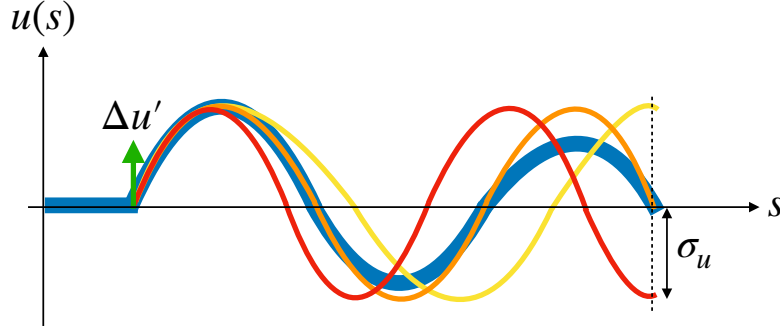


Figure 2.9: Illustration of filamentation. Transverse position $u(s)$ vs longitudinal position s . A kick $\Delta u'$ shown in green leads to a beam size growth $\Delta\sigma_u = \sigma_u - \sigma_{u,0}$, where $\sigma_{u,0}$ is the beam size without the kick. The motion of the beam centroid is shown in blue. The motion of three particles is also shown: an on-energy particle (orange), a high-energy particle (yellow) and a low-energy particle (red).

Filamentation

An energy spread can lead to an increase in emittance. If a beam is kicked, the particles initially perform coherent betatron oscillations. However, due to dispersion and chromatic aberrations, a phase difference between particles of differing energy emerges. Consequently, the motion of individual particles decoheres, the coherent oscillations are damped and the beam size grows. This is illustrated in Figure 2.9. The beam size is related to the geometric emittance by

$$\sigma_u(s) = \sqrt{\epsilon_{G,u}\beta_u(s)}. \quad (2.11)$$

The beta function is a fixed quantity, which is determined by the lattice. Therefore, the beam size growth is due to an emittance growth. This effect is known as *filamentation*.

Offsets and Jitter

The transverse beam position is also known as the *offset*. When bunches or trains have different offsets the beam is said to *jitter*. The standard deviation of offset is known as the *beam jitter*. Bunch phase can also jitter. The standard deviation of phase is known as the *phase jitter*.

2.4 Luminosity

Considering bunches with a Gaussian position distribution in the transverse and longitudinal plane and ignoring any EM interactions, the luminosity of a head-on collision in a linear e^+e^- collider is given by [31]

$$\mathcal{L}_G = \frac{N^2 f_{\text{rep}} n_b}{4\pi \sigma_x^* \sigma_y^*}. \quad (2.12)$$

where N is the number of particles per bunch, f_{rep} is the train repetition frequency, n_b is the number of bunches per train, σ_x^* (σ_y^*) is the horizontal (vertical) beam size at the IP. Equation (2.12) is known as the *geometric luminosity*.

If the beam size of the colliding bunches is not the same, the beam size in Equation (2.12) is replaced with an effective beam size given by

$$\sigma_u^* = \sqrt{\sigma_{u,-}^{*2} + \sigma_{u,+}^{*2}}, \quad (2.13)$$

where ‘ $-$ ’ denotes the electron bunch and ‘ $+$ ’ denotes the positron bunch.

The Hourglass Effect

After the final magnet in an accelerator, the beam size decreases to a minimum at the IP in accordance with [31]

$$\beta_u(s) = \beta_u^* + \frac{s^2}{\beta_u^*}, \quad (2.14)$$

where β_u^* is the beta function at the IP. This is known as the *hourglass effect*. The vertical beta function is illustrated in Figure 2.10. Due to the non-zero bunch length, not all collisions occur at the IP and the luminosity is given by

$$\mathcal{L}_{\text{HG}} = \mathcal{L}_G H = \frac{N^2 f_{\text{rep}} n_b}{4\pi \sigma_x^* \sigma_y^*} H, \quad (2.15)$$

where H is a luminosity reduction factor due to the hourglass effect. The luminosity loss due to the hourglass effect is minimised by colliding short bunches with

$$\sigma_z \leq \beta_y^*. \quad (2.16)$$

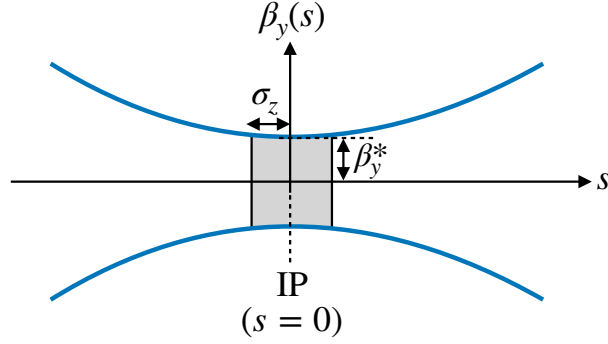


Figure 2.10: Illustration of the hourglass effect. The vertical beta function $\beta_y(s)$ vs longitudinal position s . The vertical beta function is shown in blue and the beam is shown in grey.

Crossing Angle

A *crossing angle* is introduced in the horizontal plane to ensure collisions occur at a single point in a detector and to simplify the extraction of the spent beams. However, with a crossing angle, the bunches do not fully overlap, which reduces the luminosity. If Equation (2.16) is satisfied, the luminosity loss due to a crossing angle ϕ is given by [31]

$$\mathcal{L}_{\text{CA}}(\phi) = \frac{\mathcal{L}_{\text{G}}}{\sqrt{1 + \left(\frac{\sigma_z}{\sigma_x} \tan \phi\right)^2}}. \quad (2.17)$$

Crab cavities are used to minimise luminosity loss from a crossing angle. These are RF cavities that apply opposite kicks to the head and tail of a bunch to rotate them before collision. This is illustrated in Figure 2.11. Using crab cavities, the luminosity loss from a crossing angle can be neglected.

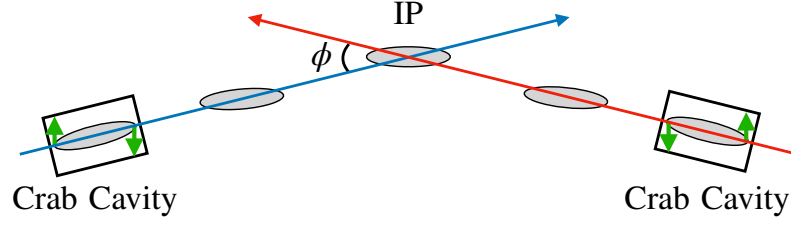


Figure 2.11: Illustration of the use of crab cavities. The colliding beams are shown in blue and red. The bunches are shown in grey. The kicks applied at the crab cavities are shown in green.

Beam-Beam Offset

Assuming Equation (2.16) is satisfied, the luminosity of two beams colliding with a relative offset (*beam-beam offset*) u_{bb} is given by [31]

$$\mathcal{L}_{BBO}(u_{bb}) = \frac{N^2 f_{rep} n_b}{4\pi \sigma_x^* \sigma_y^*} \exp\left(-\frac{u_{bb}^2}{4\sigma_u^{*2}}\right). \quad (2.18)$$

The collision is illustrated in Figure 2.12.

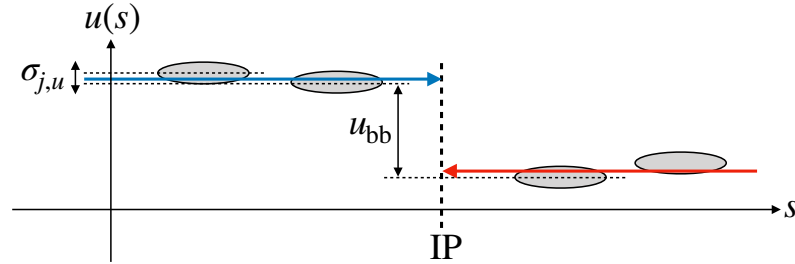


Figure 2.12: Illustration of collisions with a beam-beam offset u_{bb} and beam jitter $\sigma_{j,u}$. Transverse position $u(s)$ vs longitudinal position s . The colliding beams are shown in blue and red. Bunches/trains are shown in grey.

Beam Jitter

If each beam has a position jitter $\sigma_{j,u}$ at the IP, the average luminosity can be calculated as

$$\langle \mathcal{L}_J \rangle (\sigma_{j,u}) = \int_0^\infty \mathcal{L}_{BBO}(u_{bb}) \frac{1}{\sqrt{4\pi\sigma_{j,u}^2}} \exp\left(-\frac{u_{bb}^2}{4\sigma_{j,u}^2}\right) du_{bb}. \quad (2.19)$$

Beam-Beam Effects

The previous expressions neglect the mutual EM interaction of the two beams (*beam-beam effects*). Beam-beam effects are particularly important in linear e^+e^- colliders. The two beams focus each other with a highly non-linear force (*beam-beam force*), which leads to a collision with a smaller effective beam size thereby increasing the luminosity. This is known as the *pinch effect*. The mutual interaction is characterised by the *disruption parameter* [32]

$$\mathcal{D}_u = \frac{2r_e N \sigma_z}{\gamma(\sigma_x^* + \sigma_y^*)\sigma_u^*}, \quad (2.20)$$

where r_e is the classical electron radius. For $\mathcal{D}_u \ll 1$, beam-beam effects are small and can be ignored.

Beam-beam forces result in particles being deflected and therefore the emission of SR, referred to as *beamstrahlung*. Beamstrahlung reduces the energy of the colliding particles so that not all collisions occur at the desired energy. Beamstrahlung photons can have very high energies, enough to produce e^+e^- pairs, which lead to backgrounds in the detector. Beamstrahlung is characterised by the *beamstrahlung parameter* (or *upsilon parameter*) [32]

$$\Upsilon \approx \frac{5r_e \gamma N}{6\alpha_e \sigma_z (\sigma_x^* + \sigma_y^*)}, \quad (2.21)$$

where α_e is the fine structure constant.

Both the disruption and beamstrahlung parameter are proportional to $1/(\sigma_x^* + \sigma_y^*)$. Therefore, to minimise beam-beam effects one wishes to maximise the sum of the horizontal and vertical beam size at the IP. However, one also wishes to maximise the luminosity, which is proportional to $1/(\sigma_x^* \sigma_y^*)$. Both objectives are met by maximising the horizontal beam size and minimising the vertical beam size at the IP.

Analytical models including beam-beam effects are difficult to develop so simulations are often used instead. The luminosity calculated with a full simulation is

$$\mathcal{L} = \mathcal{L}_G H_D = \frac{N^2 f_{\text{rep}} n_b}{4\pi\sigma_x^* \sigma_y^*} H_D, \quad (2.22)$$

where H_D is a luminosity enhancement factor that accounts for beam-beam effects as well as the hourglass effect, crossing angle and beam-beam offset. In this work ‘the luminosity’ refers to this luminosity, calculated with a beam-beam effects simulation including all the above mentioned effects.

Beam-beam effects alter the dependence of luminosity on the beam-beam offset from that described in Equation (2.18). If the disruption is large, small offsets can lead to large luminosity losses. This is due to an instability in the collision known as the *kink stability* [32]. For large offsets, beam-beam effects lead to more luminosity than expected from Equation (2.18) because the beams attract each other.

2.5 Imperfections

Imperfections in a linear collider are unavoidable errors or processes that degrade luminosity. Imperfections are categorised as *static* or *dynamic*. Luminosity degradation can occur via two mechanisms:

- **Emittance growth:** An increase in emittance will increase beam size and reduce luminosity. Imperfections result in kicks to the beam. These kicks lead to an offset and emittance growth via filamentation. Both static and dynamic imperfections lead to emittance growth.
- **Beam-beam offset:** Ignoring beam-beam effects, the luminosity is at a maximum with a head-on collision. Any beam-beam offset at the IP will lead to luminosity loss. However, beam-beam effects and correlations in the beam can lead to the maximum luminosity occurring with a beam-beam offset. The beam-beam offset will be optimised

using correctors to produce the maximum luminosity. Dynamic imperfections can deflect the beam and influence the beam-beam offset.

Collisions can also occur with an angle. However, the luminosity loss due to an angle at the IP is small compared to a beam-beam offset, so usually the angle can be ignored.

Imperfections affect the beam in the horizontal and vertical plane. The vertical beam size is much smaller than the horizontal beam size at the IP. Therefore, imperfections in the vertical plane are of more importance.

2.5.1 Static Imperfections

An important static imperfection is the misalignment of accelerator elements. There are three different types of alignment errors: a transverse *offset* of the centre of an element with respect to the ideal beam; a *roll*, which is a rotation with respect to the longitudinal direction of the beam and a *tilt*, which is a rotation with respect to a direction transverse to the beam. Misalignments are illustrated in Figure 2.13. Accelerator elements can also have static errors in their properties, which are discussed below.

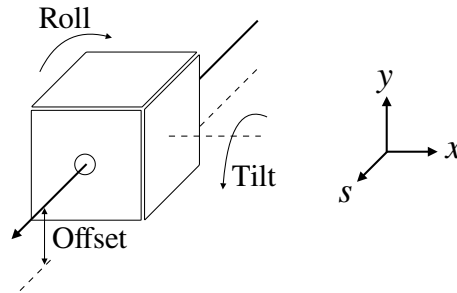


Figure 2.13: Illustration of different types of misalignments.

Beam Position Monitors

One of the most important static imperfections is the misalignment of *beam position monitors* (BPMs). BPMs define the ideal trajectory of the beam, i.e. the beam will be guided through the centre of each BPM. Therefore, if they are offset with respect to a straight-line trajectory,

the beam will not follow a straight path. Additionally, if the BPMs are rolled, a horizontal beam offset can appear partially as a vertical offset and vice versa, which complicates the centring of the beam in each plane.

BPMs do not give a perfect reading of the beam position. Each BPM reading is corrupted by an error, which is assumed to be Gaussian. The standard deviation of this error is known as the *BPM resolution*. Corrections are applied to the beam based on BPM readings. Therefore, a good resolution is desired to minimise the introduction of noise from the BPM readings to the beam.

Magnets

Static imperfections for magnets are strength errors and misalignments with respect to the ideal beam. Offset magnets kick the beam and lead to emittance growth. Additionally, rolls can lead to particles with a horizontal offset receiving a vertical kick and particles with a vertical offset receiving a horizontal kick. I.e. particle motion in the horizontal and vertical plane becomes coupled. This is known as *xy-coupling* and results in emittance growth.

Cavities

If an accelerating cavity is misaligned, the beam does not pass through the centre of the cavity. This results in EM fields being excited in the cavity known as *wakefields*, which are one of the largest sources of emittance growth in a linear accelerator.

There are two types of wakefields: *short-range* wakefields, where particles at the head of a bunch produce a wakefield that affects trailing particles in the same bunch and *long-range* wakefields, where a bunch induces a wakefield that affects trailing bunches. Wakefields from a driving particle (or bunch) are experienced by a witness particle (or bunch). As a result, wakefields are said to be *collective effects* because multiple bodies are required to observe their effect. The wakefield also depends on the amount of charge in the driver, as a result, wakefields are *intensity-dependent effects*.

The short-range wakefield from the head of a bunch results in a decelerating force being felt by the tail of the bunch. As a result, the tail of the bunch has a lower energy compared to the head. Short-range wakefields lead to a correlation between the longitudinal position of a particle in the bunch and energy, which resembles the shape of a banana, giving its name the *banana effect*. Short-range wakefields are usually compensated by the choice of RF phase in accelerating cavities. A phase is chosen to ensure a greater accelerating voltage seen by the tail of the bunch compared to the head.

2.5.2 Dynamic Imperfections

Dynamic imperfections affect the beam on a train-to-train (or bunch-to-bunch) basis. Dynamic imperfections include:

- Beam jitter. A beam is usually extracted from the DRs using a dipole magnet known as a *kicker*. If the kick applied by this magnet is not the same for all trains or bunches, a beam jitter emerges.
- Timing (or phase) errors. A phase error can be introduced by the kicker magnet. Another phase error is the arrival time of the beam with respect to the RF phase in a cavity.
- Time-varying misalignment of accelerator elements. This could be due to GM or a mechanical vibration of accelerator equipment.
- Fluctuations in power, referred to as *ripples*, lead to time-varying errors in magnet strength.
- SFs. These arise from a variety of sources. Any nearby currents will induce SFs.

Dynamic imperfections that vary at the same frequency as the train repetition frequency have the same impact on each train. Such imperfections are effectively static to the beam.

The train-to-train variation of dynamic imperfections makes them difficult to correct. The main tool for mitigating their impact is an active system. This system can measure and

correct the beam (i.e. be *beam-based*) or measure and correct the dynamic imperfection, e.g. an element stabilisation system to mitigate GM.

Beam-Based Feedback and Feedforward Systems

There are two beam-based correction schemes: *feedback systems* [33], which measure the offset of a train (or bunch) and correct the following train (or bunch), or *feedforward systems* [34], which measure and correct the same train (or bunch). Feedforward systems require a turn-around loop or arc so that there is a short cut the correction signal can take in order to arrive before the beam at the corrector.

In a beam-based feedback system, there is a time lag between the measurement of a train offset and the correction applied to the following train. This time lag is referred to as the *latency* of the feedback system. The latency of the system cannot be greater than the period between consecutive trains.

Perturbations with time variation longer than the latency are effectively suppressed with a beam-based feedback system. However, beam-based feedback systems amplify perturbations at some frequencies (discussed in Section 4.2.1). Parameters of the feedback system can be optimised to provide the best suppression of perturbations to the beam. This optimisation depends on the frequency spectrum of the perturbations.

A train-to-train feedback system is typically used across an entire accelerator to correct the beam offset. The train-to-train feedback system minimises emittance growth from filamentation.

IP Feedback System

It is possible to minimise the luminosity loss from a beam-beam offset with a beam-based feedback system located near the IP. This system can either correct the offset of an entire train or bunches within a train. IP feedback systems are discussed further in Section 4.4.

Chapter 3

Integrated Simulations

To perform realistic studies of the impact of imperfections, a simulation starting from the exit of the DRs to the IP was developed. This simulation is referred to as an *integrated simulation*. This chapter uses integrated simulations to benchmark the luminosity performance of CLIC at $E_{\text{CM}} = 380 \text{ GeV}$.

3.1 Simulation Codes

Two codes developed to simulate linear colliders are the particle tracking code PLACET [35, 36] and the beam-beam effects code GUINEA-PIG [37]. These are the codes used in this work.

PLACET

PLACET was developed to simulate CLIC beamlines. It is used to track beams and evaluate the performance of different beam correction schemes in the presence of transverse and longitudinal effects, such as wakefields, SR, element misalignments, etc. PLACET was benchmarked against other particle tracking codes in [38, 39].

Typically, in a particle tracking code *macro-particles* are simulated. These are essen-

tially the same as normal particles, except they take on the charge of many particles. This avoids the need to simulate a large number of particles when intensity-dependent effects are important. This work performs single bunch simulations with 100,000 macro-particles.

The tracking simulations performed in this work include SR, which is a random process. Therefore, the results from each tracking simulation have some random variation. This variation arises from the finite number of macro-particles being simulated. The error of each simulation can be reduced by increasing the number of macro-particles or by averaging the results of several tracking simulations with different initial distributions. A bunch containing 100,000 macro-particles was found to be large enough to produce an error of less than 1% on the beam parameters, such as emittance.

Every macro-particle is described by the coordinates given in Equation (2.1). The coordinates of each macro-particle are propagated through each element in the lattice in turn. The beam matrix is formed from the coordinates of each macro-particle and used to calculate the statistical properties of the beam, such as emittance.

For a description of the usage and the models implemented in PLACET the reader should refer to the documentation [36].

GUINEA-PIG

GUINEA-PIG is used to calculate the luminosity of e^+e^- bunch collisions. It simulates beam-beam interactions in the collision and the production of secondary particles. GUINEA-PIG was benchmarked against other physics generators in [40].

An input to GUINEA-PIG is the beam distribution of the colliding bunches. These two files are generated by a tracking simulation in PLACET. For further details regarding the input files and a description of GUINEA-PIG the reader should refer to [37].

The simulations in PLACET corresponds to the tracking of a single bunch. The electron and positron bunches are tracked independently, i.e. two tracking simulations are performed. The bunches are used in GUINEA-PIG to calculate the luminosity of a single bunch crossing

\mathcal{L}_S , which is used to calculate the total luminosity as

$$\mathcal{L} = \mathcal{L}_S f_{\text{rep}} n_b. \quad (3.1)$$

A random process which occurs in the collision is beamstrahlung. This leads to an error in the luminosity calculation due to the finite number of macro-particles. The error can be reduced by increasing the number of macro-particles or by averaging luminosity calculations with different beam distributions. It was found using 100,000 macro-particles per beam leads to a standard deviation that is approximately 2% of the mean value.

Each luminosity calculation in this work was repeated several times (roughly between 10 and 100) with different beam distributions. Each beam distribution at the IP was generated with its own tracking simulation in PLACET, which averages the errors associated with SR. When the luminosity is given in this work, it is the mean luminosity with its standard error.

3.2 Machine Description

A diagram of CLIC at $E_{\text{CM}} = 380$ GeV is shown in Figure 3.1. The geometry of the electron beamline is shown in Figure 3.2.

Ring to Main Linac

The RTML transports the beam from the DR to the ML. The RTML performs three tasks:

- To compress the bunch length from 1800 μm to 70 μm . This is done with a system of four bending magnets known as a *magnetic chicane* [41]. There is a chicane at BC1 in Figure 3.1, which compresses the bunch length from 1800 μm to 235 μm , and another chicane at BC2, which compresses bunch length from 235 μm to 70 μm .
- To accelerate the beam from 2.86 GeV to 9 GeV. SR is emitted in the bending magnets of each chicane. This SR can either be *coherent* or *incoherent* [41]. Coherent SR

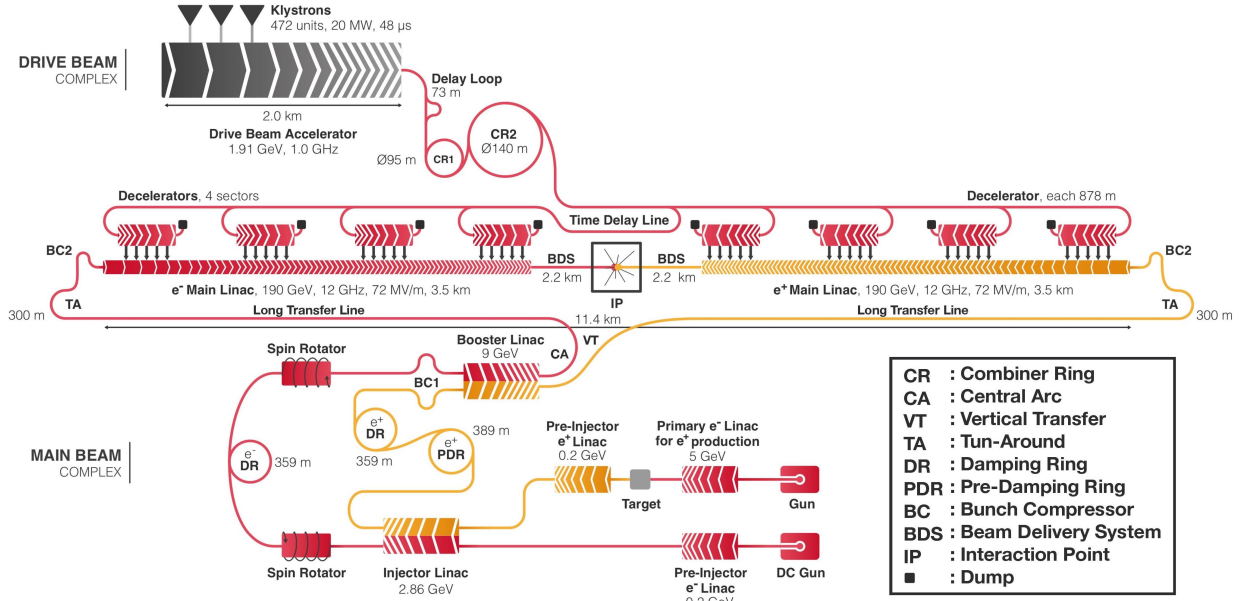


Figure 3.1: Schematic diagram of CLIC at $E_{\text{CM}} = 380 \text{ GeV}$ [25].

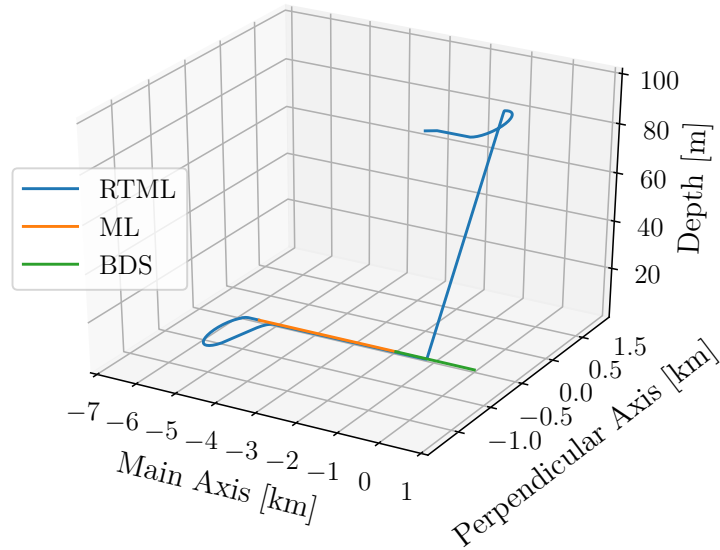


Figure 3.2: Depth vs position along the main axis and perpendicular axis of the CLIC beamline at $E_{\text{CM}} = 380 \text{ GeV}$: RTML (blue); ML (orange) and BDS (green). The IP is at $(0,0,0)$.

can lead to emittance growth, so a small amount of acceleration is performed by the Booster Linac to ensure SR emission in BC2 is incoherent.

- To align the spin of the electrons. This is done with the Spin Rotator. The positron beam is left unpolarised, so the positron RTML does not contain a Spin Rotator.

The electron and positron RTMLs have different sub-systems. Both RTMLs are described in detail in [25, 42]. The positron RTML does not contain a Spin Rotator or *Central Arc* (CA). The CA is used to reverse the direction of the electron beam before injecting it into the subsequent section. Both the electron and positron RTML contain a *Long Transfer Line* (LTL), which as shown in Figure 3.1 runs parallel to the ML. The direction of the beam is reversed in the *Turn-Around Loop* (TAL) before entering the ML. The electron and positron beams share the same Booster Linac.

Half the RTML is housed on the surface and the other half is housed approximated 100 m underground. The *Vertical Transfer* (VT) transports the beam from the surface to the underground tunnel.

Main Linac

The purpose of the ML is to accelerate the beam from 9 GeV to the final energy of 190 GeV. The ML is described in detail in [25, 42]. The design of the ML is essentially the same for the electron and positron beams.

The ML consists mainly of accelerating cavities. The *fill factor*, which is the total length of all cavities over the total length of the ML is approximately 0.718.

Beam Delivery System

The BDS collimates the beam and focuses it to the final beam size of $\sigma_x = 150$ nm and $\sigma_y = 3$ nm. The same BDS design is used for the electron and positron beams.

There are three different BDS designs, which differ in the drift length (L^*) from the final quadrupole to the IP [42]. The baseline design includes a BDS with $L^* = 6$ m. The advantage of this L^* is that the final quadrupole is not housed in the detector cavern [42]. Only the $L^* = 6$ m BDS is studied in this work.

Emittance Growth Budgets

In order to realise the targeted IP beam size, the preservation of emittance is key. Strict emittance growth budgets have been defined for each section of CLIC. The emittance growth budgets for static and dynamic imperfections are presented in Table 3.1.

In the RTML, some emittance growth will occur even in the absence of imperfections due to SR in the bends. This is accounted for in the design budget. The budgets are the same for the electron and positron beams.

Section	ϵ_x [nm]	$\Delta\epsilon_x$ [nm]			ϵ_y [nm]	$\Delta\epsilon_y$ [nm]		
		Design	Static	Dynamic		Design	Static	Dynamic
DR	700	-	-	-	5	-	-	-
RTML	850	100	20	30	10	1	2	2
ML	900	0	25	25	20	0	5	5
BDS	950	0	25	25	30	0	5	5

Table 3.1: Targeted horizontal and vertical emittance at the end of each section and the horizontal and vertical emittance growth budgets ($\Delta\epsilon_x$ and $\Delta\epsilon_y$ respectively): design values and contributions from static and dynamic imperfections.

3.3 Perfect Machine Performance

Typically, elements have imperfections, such as alignment or attribute errors. A perfect machine is one that contains no imperfections. The maximum attainable luminosity can be calculated by simulating a perfect machine. This luminosity is

$$\mathcal{L}_0 = (4.325 \pm 0.004) \times 10^{34} \text{ cm}^{-2}\text{s}^{-1}. \quad (3.2)$$

Although the machine is perfect, there is an error in the luminosity calculation due to random processes in the simulation (see Section 3.1). The beam parameters at the end of each section are shown in Table 3.2.

Sextupoles in the FFS are used to correct chromatic aberrations. In regions where there is horizontal dispersion, the energy of a particle determines its position. Sextupoles are placed

Section	ϵ_x [nm]	ϵ_y [nm]	σ_x [μm]	σ_y [μm]	σ_z [μm]	E [GeV]	σ_E [%]
DR	700	5.00	50.0	2.11	1800	2.86	0.110
RTML	785	5.82	18.9	0.629	70.0	9.00	1.00
ML	791	5.85	8.05	0.291	70.0	190	0.350
BDS	2,220	6.36	0.130	0.00133	70.0	190	0.350

Table 3.2: Simulated beam parameters (given to three significant figures) at the end of each section of a perfect machine.

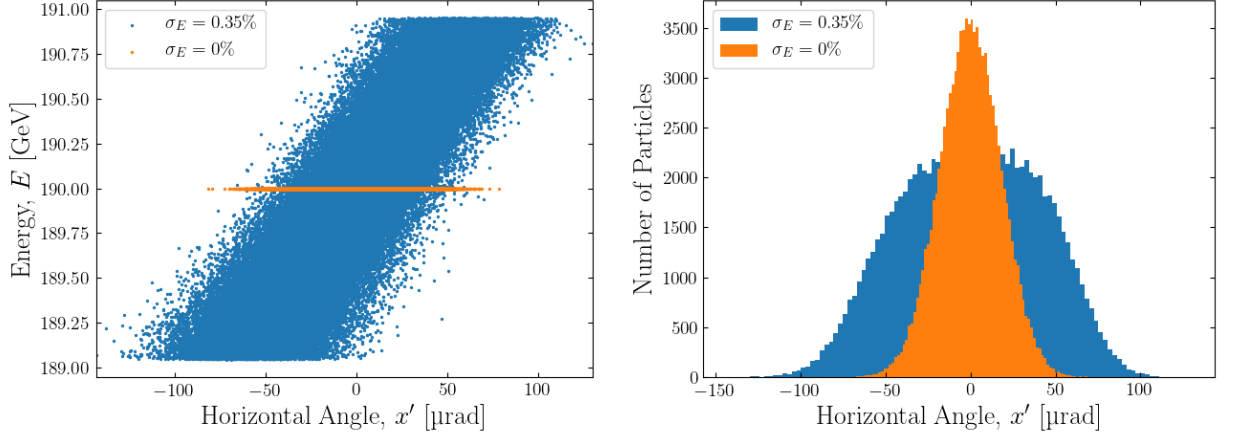


Figure 3.3: Energy vs horizontal angle of the particles in the beam at the IP and the distribution of horizontal angle: using a beam with no energy spread (orange) and using a beam with the nominal energy spread of 0.35% (blue).

in these regions, and as a result, particles of differing energy receive a different kick. Such a scheme results in a correlation between the energy and horizontal angle of the particles in a beam. This is shown in Figure 3.3.

The energy-angle correlation leads to a horizontal emittance growth in the BDS. As this emittance growth is from the angular distribution, it does not significantly impact the IP beam size and luminosity. When examining the BDS, the IP beam size and luminosity are better indicators of performance.

3.4 Nominal Performance

To study the nominal luminosity performance one should implement imperfections in the machine. However, instead of simulating an imperfect machine, it is possible to study the

nominal luminosity performance by simulating a perfect machine and increasing the emittance of the beam from the DRs to account for imperfections.

The full emittance growth budgets for static and dynamic imperfections are assumed. Therefore, the emittance from the DRs is $\epsilon_{x,\text{DR}} = 860 \text{ nm}^1$ and $\epsilon_{y,\text{DR}} = 29 \text{ nm}$. Simulating these DR emittances will be referred to as using *nominal target emittance* (NTE).

The luminosity performance using NTE is

$$\mathcal{L}_0 = (1.5462 \pm 0.0002) \times 10^{34} \text{ cm}^{-2}\text{s}^{-1}. \quad (3.3)$$

The error arises from random processes in the simulation (see Section. 3.1). This simulation shows with all imperfections included CLIC performs marginally above the $1.5 \times 10^{34} \text{ cm}^{-2}\text{s}^{-1}$ luminosity target. The beam parameters at the end of each section are shown in Table 3.3.

Section	ϵ_x [nm]	ϵ_y [nm]	σ_x [μm]	σ_y [μm]	σ_z [μm]	E [GeV]	σ_E [%]
DR	860	29.0	55.4	5.09	1800	2.86	0.110
RTML	945	31.0	20.8	1.45	70.0	9.00	1.00
ML	952	31.0	8.84	0.669	70.0	190	0.350
BDS	2,460	34.0	0.142	0.00305	70.0	190	0.350

Table 3.3: Simulated beam parameters (given to three significant figures) at the end of each section with NTE.

3.5 Static Imperfections

A more realistic simulation involves implementing imperfections in the machine. Simulations of isolated sections: RTML [43, 44], ML [45], BDS [46, 47] show emittance growth due to static imperfections can be kept within budget with beam-based alignment techniques.

Integrated simulations of static imperfections are presented in this section. The imperfections implemented in the RTML, ML and BDS are summarised in Table 3.4.

¹The horizontal emittance from the DR should be $\epsilon_{x,\text{DR}} = 850 \text{ nm}$. However, the horizontal emittance growth in a perfect RTML is only 90 nm instead of 100 nm. Therefore, $\epsilon_{x,\text{DR}} = 860 \text{ nm}$ was chosen instead of $\epsilon_{x,\text{DR}} = 850 \text{ nm}$.

	Imperfection	Value
Ring to Main Linac		
	Magnet and BPM offset	30 μm
	Magnet and BPM roll	100 μrad
	CA and TAL quadrupole strength errors	0.01%
	All other magnet strength errors	0.1%
	BPM resolution	1 μm
Main Linac		
	Magnet and BPM offset	14 μm
	Magnet and BPM roll	100 μrad
	Magnet strength error	0.1%
	BPM resolution	0.1 μm
	Girder end point with respect to reference wire	12 μm
	Girder end point with respect to articulation point	5 μm
	Cavity offset	14 μm
	Cavity tilt	141 μrad
	Wakefield monitor offset	3.5 μm
Beam Delivery System		
	Magnet and BPM offset	10 μm
	Magnet and BPM roll	100 μrad
	Magnet strength errors	0.01%
	BPM resolution	20 nm

Table 3.4: Static imperfections in each section. RMS values are given.

To ensure a sufficient alignment, elements are placed on girders and initially aligned mechanically to an accuracy of 0.1 mm [42]. Each girder is mounted on a mover and equipped with a sensor that measures its position relative to a stretched wire [48]. The movers are then used to align the elements to a *root-mean-square* (RMS) offset of 10 μm [42] over length scales of 200 m across the entire machine. This procedure is known as *pre-alignment*.

Following pre-alignment, beam-based techniques are used. These procedures are referred to as *tuning*. Usually, tuning consists of a few steps:

1. **One-to-one steering:** the beam is steered through the centre of a BPM using correctors.
2. **Dispersion-free steering:** this minimises the difference in the trajectory of two beams of differing energy using correctors.

3. **Specific beam-based techniques:** this usually depends on the section.

In the ML, *RF realignment* is applied. This involves moving the accelerating cavities to minimise the signal measured by a wakefield monitor [49].

In the RTML and BDS, sextupoles are used to correct chromatic aberrations. In the RTML, a simplex algorithm [50] is used to minimise the emittance at the end of the section by moving the sextupoles in the CA and TAL.

In the BDS collimation section, similar to the RTML, a simplex algorithm is used to minimise the emittance at the end of the section (start of the FFS) by moving the sextupoles.

In the FFS, the luminosity is maximised by optimising the sextupole offset. This is done in two stages. First, a random walk is used to take the luminosity from a few percent of the nominal luminosity target to the level of 10%. Following this, *sextupole tuning knobs* [46] are used to take the luminosity to its maximum value.

In dispersion-free steering, the dispersion is conventionally measured using an off-energy beam. The gradient of accelerating cavities must be changed to generate an off-energy beam. Alternatively, tracking an on-energy beam through a lattice with rescaled magnet strength is equivalent to tracking an off-energy beam. Dispersion in the RTML is measured by rescaling the magnet strength. In addition to the imperfections listed in Table 3.4, a magnetic centre shift due to a change in magnet strength is included in the RTML. All magnets are scaled by 5%. This produces a 0.35 μm shift in the magnetic centre for quadrupoles and sextupoles [44].

Tuning was simulated on 100 machines with different initial surveys of static imperfections. The emittance at the end of each section is shown in Figure 3.4. The luminosity of each machine after the full tuning procedure is shown in Figure 3.5. These luminosities were calculated by mirroring the beam at the IP. The average luminosity and its standard error is

$$\mathcal{L}_0 = (3.353 \pm 0.004) \times 10^{34} \text{ cm}^{-2}\text{s}^{-1}. \quad (3.4)$$

A luminosity above $2.7 \times 10^{34} \text{ cm}^{-2}\text{s}^{-1}$ is achieved by 90% of machines.

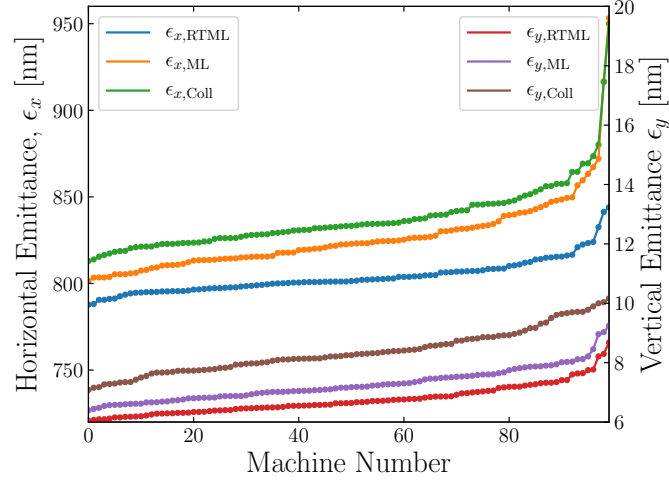


Figure 3.4: Horizontal (LH scale) and vertical emittance (RH scale) after tuning including static imperfections vs machine number: at the end of RTML (blue and red); at the end of the ML (orange and purple) and at the end of BDS collimation section (green and brown). Machines are ordered in ascending emittance.

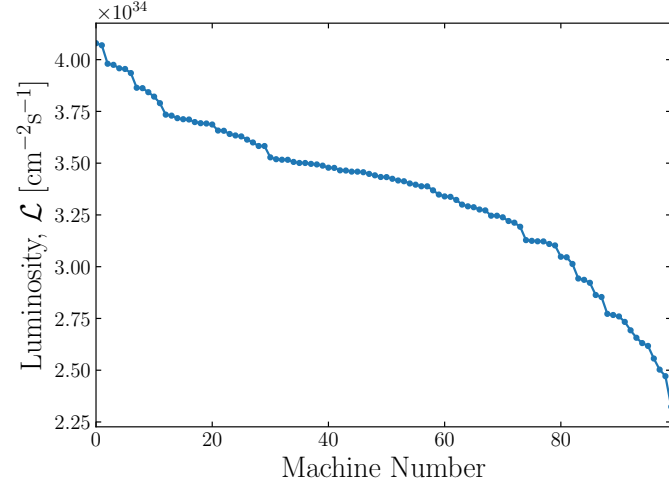


Figure 3.5: Luminosity after tuning, including static imperfections, vs machine number. Machines are ordered in descending luminosity.

Section	ϵ_x [nm]	ϵ_y [nm]	σ_x [μm]	σ_y [μm]	σ_z [μm]	E [GeV]	σ_E [%]
DR	700	5.00	50.0	2.11	1800	2.86	0.110
RTML	803	6.74	18.4	0.710	70.0	9.00	1.00
ML	826	7.25	8.16	0.331	70.0	190	0.350
BDS	2,300	10.4	0.136	0.00207	70.0	190	0.350

Table 3.5: Average simulated beam parameters (given to three significant figures) at the end of each section after tuning of 100 machines including static imperfections.

The average beam parameters at the end of each section of 100 machines after tuning are shown in Table 3.5. The tuning performs comfortably within the budgets specified in Table 3.1, particularly in the ML.

3.6 Dynamic Imperfections

The rest of this work is devoted to the study of dynamic imperfections. A machine including static imperfections should be used for simulations of dynamic imperfections. However, a simplification will be made by assuming an inflated emittance from the DRs to account for static imperfections. The full emittance growth budget for static imperfections is assumed. Therefore, the emittance of the beam from the DRs is $\epsilon_{x,\text{DR}} = 770 \text{ nm}$ and $\epsilon_{y,\text{DR}} = 17 \text{ nm}$. Simulating these emittances will be referred to as using *static target emittance* (STE). The luminosity that can be achieved with STE is

$$\mathcal{L}_0 = (2.263 \pm 0.003) \times 10^{34} \text{ cm}^{-2}\text{s}^{-1}. \quad (3.5)$$

The error arises from random processes in the simulation (see Section. 3.1).

Simulating STE instead of explicitly implementing static imperfections greatly reduces the number of simulations needed. Assuming STE is pessimistic because it was shown in the previous section that the emittance growth due to static imperfections is comfortably within budget and an average luminosity of approximately $3.4 \times 10^{34} \text{ cm}^{-2}\text{s}^{-1}$ can be achieved.

Section	ϵ_x [nm]	ϵ_y [nm]	σ_x [μm]	σ_y [μm]	σ_z [μm]	E [GeV]	σ_E [%]
DR	770	17.0	52.5	3.90	1800	2.86	0.110
RTML	855	18.4	19.8	1.11	70.0	9.00	1.00
ML	862	18.5	8.41	0.515	70.0	190	0.350
BDS	2,330	20.0	0.135	0.00234	70.0	190	0.350

Table 3.6: Simulated beam parameters (given to three significant figures) at the end of each section with STE.

The beam parameters at the end of each section are shown in Table 3.6. The main difference between this scenario and explicitly implementing static imperfections is that the

vertical emittance at the IP is much bigger here. However, looking at the vertical IP beam size in Tables 3.5 and 3.6, they are similar. Despite the similar beam sizes, the luminosity achieved in each simulation is very different.

The objective of tuning is to maximise luminosity, rather than to minimise the IP beam size. In the perfect machine the minimum beam size or *waist* occurs at the IP. However, a larger luminosity can arise from beam-beam effects if the waist is moved before the IP, this is referred to as a *waist shift*. The final tuning procedure involves tuning the position of sextupoles in the FFS to maximise luminosity. This procedure finds the maximum luminosity that occurs with a waist shift, which is why a larger luminosity is achieved when the tuning is explicitly simulated.

3.6.1 Beam-Beam Offset and Jitter

The primary mechanism of luminosity loss from dynamic imperfections is a beam-beam offset. A vertical beam-beam offset (y_{bb}) has the most impact on luminosity. Figure 3.6 shows the luminosity vs beam-beam offset for CLIC and for a rigid (i.e. undisrupted) Gaussian beam. Each curve is normalised by the luminosity with no beam-beam offset, these are the luminosities in Equations (3.2) and (3.3).

CLIC shows some deviation from the luminosity expected from a rigid Gaussian beam. The disruption determines how much the curve differs. When the disruption is large, small beam-beam offsets can lead to large luminosity losses. To study accurately dynamic imperfections, the correct luminosity loss due to a beam-beam offset must be calculated. Figure 3.6 highlights the luminosity loss due to a beam-beam offset can be different depending on the beam size, and therefore emittance, at the IP.

For integrated simulations of dynamic imperfections, STE will be used. Figure 3.7 shows the luminosity loss due to a vertical beam-beam offset in simulations with static imperfections implemented and using STE. The two curves are very similar, which confirms the luminosity loss due to a beam-beam offset will be the same for both scenarios.

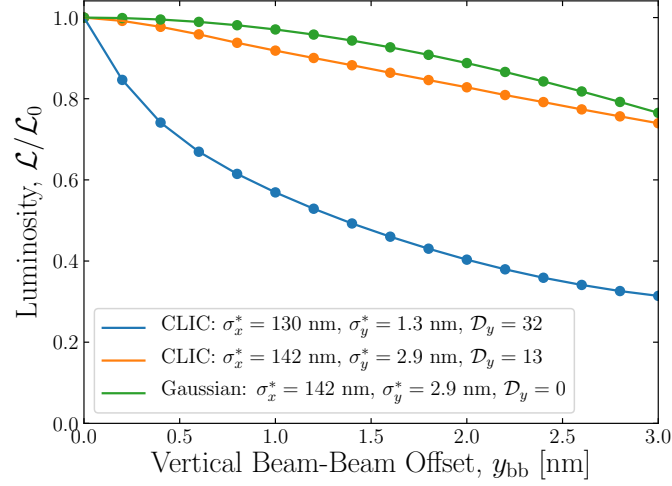


Figure 3.6: Luminosity vs vertical beam-beam offset: calculated with GUINEA-PIG using a realistic CLIC beam (blue and orange) and calculated with Equation (2.18) for a rigid Gaussian beam (green). The blue and orange lines correspond to different beam sizes at the IP, which leads to different disruption parameters. The green line corresponds to the expected luminosity if there were no beam-beam effects.

The vertical disruption is similar in simulations including static imperfections and using STE. Both have $\mathcal{D}_y \approx 17$. This is somewhat greater than the nominal vertical disruption of $\mathcal{D}_y = 13$. Consequently, the luminosity loss due to a beam-beam offset will be increased. Figure 3.7 shows the luminosity loss due to a beam-beam offset is less when NTE is used.

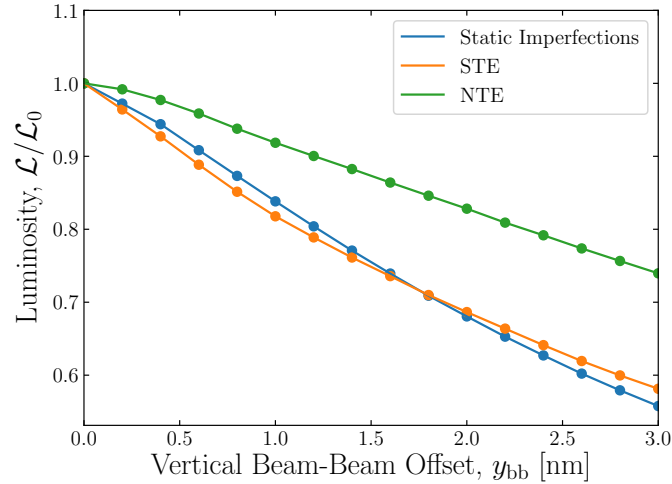


Figure 3.7: Luminosity vs vertical beam-beam offset: with static imperfections implemented (blue); using STE (orange) and using NTE (green).

Equation (2.19) together with the curves in Figure 3.7 can be used to calculate the average luminosity of two colliding beams, which each have a vertical position jitter $\sigma_{j,y}$.

The average luminosity is shown in Figure 3.8. Using NTE, there is a vertical beam position jitter tolerance of $\sigma_{j,y} \leq 0.4$ nm to remain within a 2% luminosity loss budget, whereas it is $\sigma_{j,y} \leq 0.2$ nm using STE.

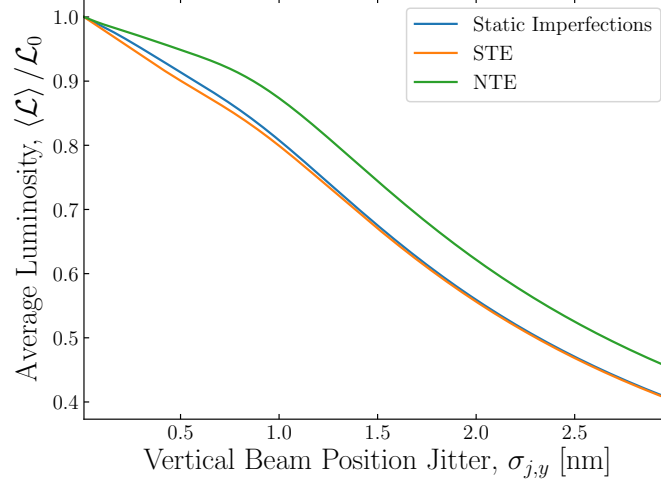


Figure 3.8: Average luminosity vs vertical beam position jitter (of each beam): calculated with static imperfections implemented (blue); using STE (orange) and using NTE (green).

3.6.2 Phase Errors

Phase errors can be thought of as timing errors. This section looks at the impact of coherent phase errors. With a coherent phase error, the arrival time of the beam is shifted by the same amount across the entire machine or a section of the machine.

Beam Delivery System Energy Acceptance

The minimum IP beam size that can be achieved in the BDS depends on the energy spread of a beam because of chromatic aberrations. A larger energy spread leads to a larger beam size, which lowers luminosity. The energy range in which the desired beam size and target luminosity can be reached is known as the *energy acceptance* (or *energy bandwidth*) of the BDS.

Coherent phase errors in the ML cavities can arise from the arrival time of the main beam. Here, the beam arrives before or after the nominal RF phase. Alternatively, there

can be an error in the arrival time of the drive beam, which affects the timing of the RF. These phase errors are equivalent to a change in the effective accelerating gradient. They lead to an energy error, which lowers luminosity because of the limited energy acceptance of the BDS.

The BDS energy acceptance, shown in Figure 3.9, was calculated by varying the effective gradient G_{eff} of the ML cavities directly. The luminosity was calculated using a reference beam, which was tracked through a lattice with the nominal ML cavity gradient. Therefore, tolerances will be calculated with half the total luminosity loss budget. To remain within a 1% luminosity loss, the beam energy error entering the BDS must be within $\Delta E/E \approx \pm 7.5 \times 10^{-4}$. The corresponding effective gradient error that can be tolerated is the same $\Delta G_{\text{eff}}/G_{\text{eff}} \approx \pm 7.5 \times 10^{-4}$. This tolerance can also be expressed as an RF phase error in the ML cavities. A $\pm 0.2^\circ$ RF phase error would lead to 1% luminosity loss.

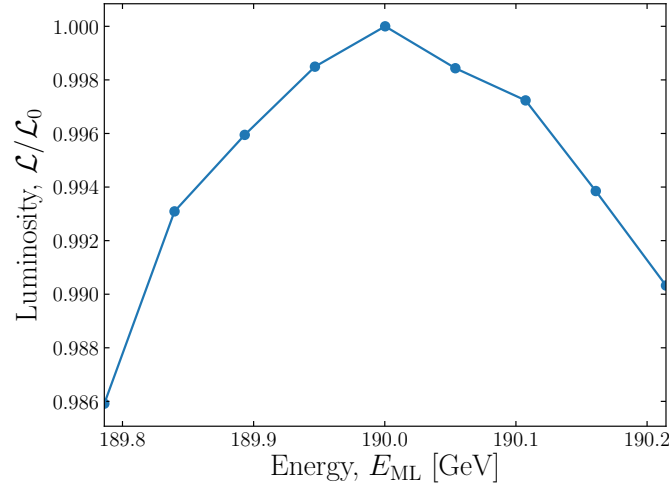


Figure 3.9: Luminosity vs energy at the end of the ML.

Damping Ring Extraction

A phase error from the DRs was also studied. Here, both an error in the effective gradient of the ML cavities and IP arrival time occur, whereas varying the effective gradient of the ML cavities does not affect the arrival time of the colliding bunches.

If there is a relative arrival time error at the IP, the beams will either collide before

or after the nominal collision point, where the beta functions and therefore beam sizes are larger, leading to a luminosity reduction.

Luminosity as a function of the longitudinal bunch position from the DR is shown in Figure 3.10. The luminosity was calculated with a reference beam with no phase error. There is a large tolerance of approximately $\pm 500 \mu\text{m}$ to remain within a 1% luminosity loss due to the bunch compressors in the RTML. The bunch length is compressed by a factor of 26, which leads to a reduction of roughly the same factor in the phase error.

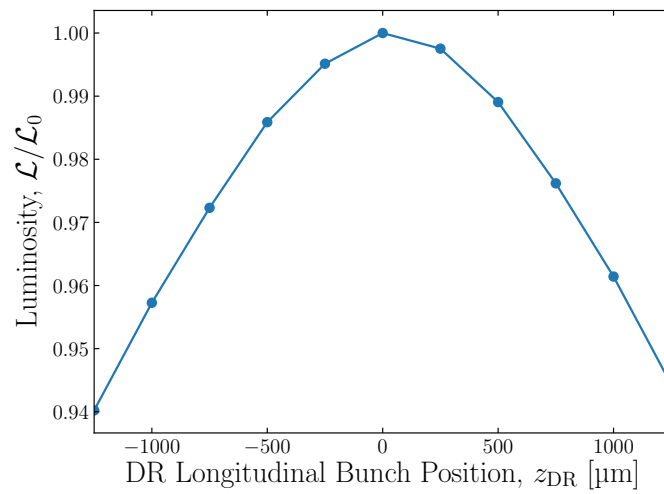


Figure 3.10: Luminosity vs longitudinal bunch position at the end of the DR.

Chapter 4

Ground Motion

Accelerator elements are not perfectly stable. They vibrate because of *ground motion* (GM) or other external forces. The vibration of quadrupole magnets in the vertical plane has the biggest impact on the beam. These vibrations lead to beam jitter, which can either impact luminosity directly or lead to filamentation.

The influence of GM on linear colliders has been studied extensively [51]. The level of GM depends on the accelerator site. Models for different sites are used to generate realistic displacements due to GM for accelerator elements. This chapter evaluates the impact of different GM models on the luminosity of CLIC at $E_{\text{CM}} = 380 \text{ GeV}$.

4.1 Models

The surface layer of the Earth is known as the *crust*, which is formed from a number of *tectonic plates* [52]. This is an elastic medium, which can support the propagation of wavelike motion.

Depending on the timescale, GM can be divided into four categories: [53, 54]

- *Uncorrelated waves*, above 10 Hz: This type of GM is a set of travelling waves with differing frequency and wavelength. The *correlation* (see Appendix A) gives an indication

of whether or not two locations move in phase. Two locations that move independently are said to be *uncorrelated*. At these frequencies, GM becomes uncorrelated over distances of a few metres.

- *Correlated waves*, 0.1-10 Hz: Waves in this frequency range have wavelengths of a few kilometres. Such waves are highly correlated across an accelerator the size of CLIC.
- *Diffusive motion*, 0.01-0.1 Hz: The displacement of an accelerator element with respect to a reference location (*relative displacement*) can be produced from temperature variations, underground water flow, spatial variation of ground properties, etc. The relative displacement D is a *random walk* [55] with variance [56]

$$\sigma_D^2 = A_D T L, \quad (4.1)$$

where A_D is a site-dependent constant, T is the time step and L is the distance to the reference location. Equation (4.1) is known as the *ATL law* [56].

- *Systematic motion*, below 0.01 Hz: This is a slow drift of the ground, e.g. from the motion of tectonic plates or the influence of the moon and tides. Here, the displacement varies linearly with time. Systematic motion S can also be described as a random walk with variance [53]

$$\sigma_S^2 = A_S T^2 L, \quad (4.2)$$

where A_S is a site dependent constant.

The last two types are considered to be slow motion and the first two types are considered to be fast.

Slow GM leads to relative misalignments, which induce a beam offset. This offset is usually cured with a beam-based feedback system. Therefore, the impact on luminosity from slow GM is via emittance growth only.

The impact of fast GM on luminosity is much more critical. The fast temporal variation makes beam offsets difficult to correct. Therefore, there is luminosity loss due to a beam-

beam offset at the IP. This work focuses on the impact of fast GM, which is usually modelled using *power spectral densities* (PSDs), discussed in the following section.

4.1.1 Power Spectral Densities

Fast GM is described as a set of travelling waves with frequency f and wavelength λ . These quantities are related by

$$v_g = f\lambda, \quad (4.3)$$

where v_g is the group velocity of the wave. The power of each wave is described using a *two-dimensional PSD*, denoted by $P(f, \lambda)$ [51]. A one-dimensional PSD $P(f)$ is recovered from the two-dimensional PSD $P(f, \lambda)$: [51]

$$P(f) = \int_0^\infty P(f, \lambda) d\lambda. \quad (4.4)$$

$P(f)$ describes the temporal variation and is commonly referred to as the *noise* of GM.

The two-dimensional PSD depends on the accelerator site. Measurements have been performed at several sites to model $P(f, \lambda)$. Four models based on different sites are described below. The one-dimensional PSD of these models is shown in Figure 4.1.

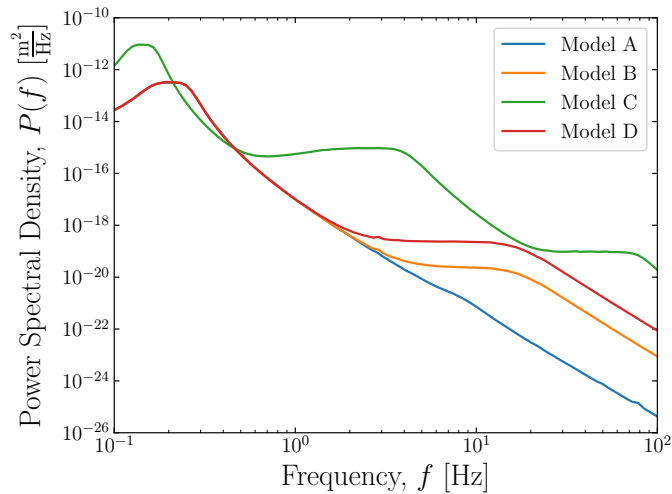


Figure 4.1: PSD vs frequency of different GM models [57, 58, 59, 60, 61].

Model A is based on a measurement in an empty tunnel at CERN [57]. This tunnel is

deep underground, approximately 100 m below the surface. The tunnel previously housed the *Large Electron-Positron* (LEP) collider and is currently occupied by the LHC. Model A is based on a measurement taken at night. It contains a microseismic peak at 0.14 Hz due to a motion of the Earth's crust, which arises from ocean waves [52]. In quiet conditions, the PSD of GM decays rapidly with frequency, approximately as $1/f^4$. Model A represents a low-noise site.

Model B is based on measurements in a shallow tunnel, approximately 9 m underground, at the *Stanford Linear Accelerator Laboratory* (SLAC), USA [58] and a deep mine near the Fermilab site, USA [62]. Model B is based on measurements taken during the day. It contains an additional peak around 20 Hz, which arises from human activity, such motion is referred to as *cultural noise*. Model B represents a site with an intermediate noise.

Model C is based on measurements at the *Hadron-Electron Ring Accelerator* (HERA) in Hamburg, Germany [59]. HERA is in a shallow tunnel, approximately 15-30 m underground. The surface location is highly urbanised. The model is based on a measurement taken during the day when there is a significant amount of cultural noise. Model C represents a very noisy site.

Model D¹ is a modified version of model B. It contains an additional peak based on measurements in Annecy, France [60] and in the *Compact Muon Solenoid* (CMS) detector cavern, which is one of the experiments in the LHC [61]. GM originating from detector vibrations was measured in CMS, which results in the larger amplitude of the peak at 20 Hz. CLIC is designed to withstand the impact of model D. This is a pessimistic approach because model D represents a noise level higher than what is expected for CLIC. For example, the model assumes the noise from the CMS detector is present across the entire machine, which is not the case. The CLIC detector will also be designed not to produce the vibrations measured at CMS.

Models A-D are based on measurements of GM in the vertical plane. Therefore, the two-dimensional PSD represents the amplitude of vertical motion. In simulations, the same

¹Model D is also known as Model B10.

two-dimensional PSD is used to describe horizontal and vertical GM. This is possible because the impact of horizontal imperfections is small in comparison to vertical imperfections.

4.1.2 Generators

The above models form a statistical description of GM. They are used in *generators* to sample GM. The objective of a generator is to calculate the displacement of an element at time t and location s . The implementation of the GM generator in PLACET is described in detail in [63]. A brief description of this generator is given below.

To simulate GM the two-dimensional PSD is discretised into a set of *modes* at discrete frequencies and wavelengths denoted by f_i and λ_j . Each mode is assumed to be independent. The variance of GM is given by

$$\begin{aligned}\sigma^2 &= \int_0^\infty \int_0^\infty P(f, \lambda) df d\lambda \\ &\approx \sum_i \sum_j \left(\int_{f_i}^{f_{i+1}} \int_{\lambda_j}^{\lambda_{j+1}} P(f, \lambda) df d\lambda \right) \\ &\approx \sum_i \sum_j \sigma_{ij}^2, \approx \sum_i \sum_j \frac{a_{ij}^2}{2},\end{aligned}\tag{4.5}$$

where $\sigma_{ij}^2 = a_{ij}^2/2$ is the variance of each mode and a_{ij} is the amplitude.

GM in PLACET is modelled as two travelling waves moving in opposite directions, which form a standing wave. The displacement of an individual mode is given by

$$d_{ij}(t, s) = \frac{a_{ij}}{\sqrt{2}} \left[\sin \left(2\pi f_i t + \frac{2\pi s}{\lambda_j} + \phi_{ij}^{(1)} \right) + \sin \left(2\pi f_i t - \frac{2\pi s}{\lambda_j} + \phi_{ij}^{(2)} \right) \right], \tag{4.6}$$

where $\phi_{ij}^{(1)}$ and $\phi_{ij}^{(2)}$ are uniformly distributed random numbers between 0 and 2π . The displacement at time t and position s is the summation over all modes,

$$d(t, s) = \sum_i \sum_j d_{ij}(t, s). \tag{4.7}$$

A computationally efficient method of calculating Equations (4.6) and (4.7), which is described in [63], is implemented in PLACET.

4.1.3 Impact on Luminosity

The luminosity loss $\Delta\mathcal{L}$ due to GM including the effect of a mitigation system can be estimated as [63]

$$\Delta\mathcal{L} = \int_0^\infty \int_0^\infty P(f, \lambda) |T(f)|^2 G^2(\lambda) \, df \, d\lambda, \quad (4.8)$$

where $T(f)$ is the *transfer function* of the mitigation system and $G(\lambda)$ is a *sensitivity function* for luminosity loss. Equation (4.8) is valid when the luminosity loss is less than 20% [63].

The transfer function $T(f)$ describes the impact of the mitigation system on the amplitude of GM. Therefore, the transfer function squared describes the impact on the two-dimensional PSD $P(f, \lambda)$. The mitigation technique is assumed to work uniformly across the entire accelerator, therefore the transfer function is only a function of frequency. The product $P(f, \lambda)|T(f)|^2$ determines the power (and therefore amplitude) of each GM wave. $G(\lambda)$ accounts for the spatial distribution of the wave and its impact on luminosity loss.

4.2 Mitigation Methods

Two different techniques will be used to mitigate GM: a beam-based feedback system and a mechanical stabilisation for quadrupole magnets.

4.2.1 Beam Trajectory Feedback System

This is a beam-based feedback system that corrects the beam trajectory over the full length of the accelerator. Corrections are applied on a train-to-train basis. A set of BPMs is used to measure the offset of a train and a set of correctors is used to correct the following train. These correctors can either be dipole magnets or displaced quadrupole magnets. The time

duration between trains, referred to as the *train spacing*, is 20 ms.

This section derives the transfer function for the beam trajectory feedback system. The approach treats the feedback system as a *linear, time-invariant* (LTI) system and uses the signal processing techniques described in Appendix A.

An LTI system has an input u and output v . The relationship between input and output is described using a *difference equation*, which has the general form

$$\sum_{p=0}^N a[p]v[n-p] = \sum_{l=0}^M b[l]u[n-l], \quad (4.9)$$

where the coefficients $a[p]$ and $b[l]$ are constants. v represents the corrected beam position and u represents the beam position without the feedback system. The transfer function of the system is calculated using²

$$T(f) = \frac{\sum_{l=0}^M b[l] \exp\left(-\frac{j2\pi fl}{f_{\text{rep}}}\right)}{\sum_{p=0}^N a[p] \exp\left(-\frac{j2\pi fp}{f_{\text{rep}}}\right)}, \quad (4.10)$$

where $j = \sqrt{-1}$.

The feedback system in CLIC uses the full history of outputs to calculate the correction as

$$\begin{aligned} c[n] &= \frac{1}{m}v[n] + \left(1 - \frac{1}{m}\right)c[n-1] \\ &= \sum_{q=0}^n \frac{1}{m} \left(1 - \frac{1}{m}\right)^q v[n-q], \end{aligned} \quad (4.11)$$

where m is the gain. The difference equation for this system is

$$\begin{aligned} v[n] - v[n-1] &= u[n] - u[n-1] - c[n] \\ &= u[n] - u[n-1] - \sum_{q=0}^n \frac{1}{m} \left(1 - \frac{1}{m}\right)^q v[n-q]. \end{aligned} \quad (4.12)$$

²Equation (4.10) is the continuous form of Equation (A.16).

Using Equation (4.10) with the coefficients $a[p]$ and $b[l]$ from Equation (4.12), the transfer function is³

$$T(f) = \frac{1 - \exp\left(-\frac{j2\pi f}{f_{\text{rep}}}\right)}{1 - \exp\left(-\frac{j2\pi f}{f_{\text{rep}}}\right) + \frac{1}{m} \exp\left(-\frac{j2\pi f}{f_{\text{rep}}}\right) \left(\frac{1}{1 - \left(1 - \frac{1}{m}\right) \exp\left(-\frac{j2\pi f}{f_{\text{rep}}}\right)}\right)}. \quad (4.13)$$

The transfer function of the feedback system with different gains is shown in Figure 4.2. The beam trajectory feedback system corrects both the horizontal and vertical beam position with the same transfer function.

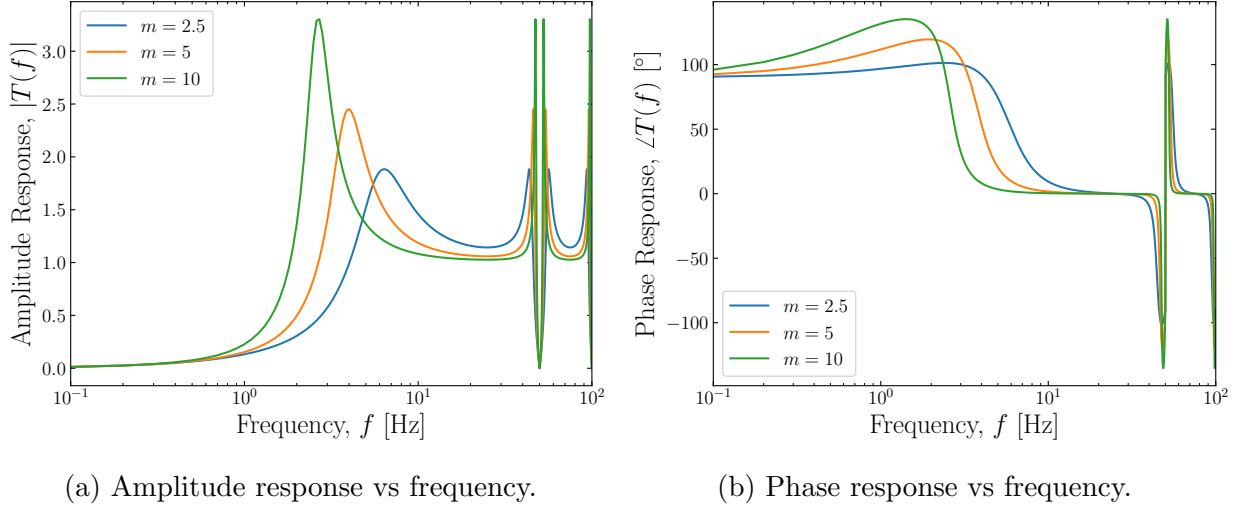


Figure 4.2: Transfer function of a beam trajectory feedback system. Each line corresponds to a different gain m used in Equation (4.13).

The transfer function assumes a perfect correction is applied to the beam, i.e. there is no error term in Equation (4.12). Although the correction may be perfect, the feedback system does not completely cure the imperfection because there is a latency between measurement and correction. This latency can lead to an amplification of the imperfection.

The CLIC feedback system operates with a gain of $m = 2.5$. The feedback system is good at suppressing frequencies below 1 Hz but amplifies the range 4-25 Hz. The transfer function is zero at multiples of the repetition frequency because any imperfection at this frequency appears static to the beam and is completely removed. The transfer function is

³The summation is evaluated using $\sum_{p=0}^{n-1} \alpha^p e^{j\beta p} = \frac{1 - \alpha^n e^{j\beta n}}{1 - \alpha e^{j\beta}}$.

periodic over intervals of 100 Hz.

The transfer function in Equation (4.13) is calculated by examining the impact of the feedback system on beam motion. This means the transfer function should be used to calculate the PSD of corrected beam motion from the PSD of uncorrected beam motion. However, the transfer function will be used on the PSD of GM instead. This is possible because the PSD of beam motion should be directly proportional to the PSD of GM. It is important to note the feedback system does not directly reduce GM, instead its effect is equivalently modelled by reducing the PSD used to generate GM.

4.2.2 Quadrupole Stabilisation System

Although the PSD of GM decays rapidly with frequency, there is significant motion up to 85 Hz that can impact luminosity. An active quadrupole stabilisation system has been designed to address this problem.

The quadrupole stabilisation system is described in [64, 65]. A schematic diagram is shown in Figure 4.3. The quadrupole is exposed to vibrations from GM and external systems, such as pumps and motors. The quadrupole is mounted on a support which affects the propagation of vibrations from the ground. The inertia of the quadrupole also affects its motion.

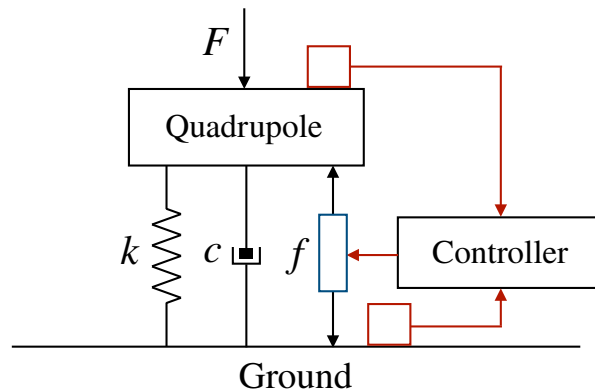
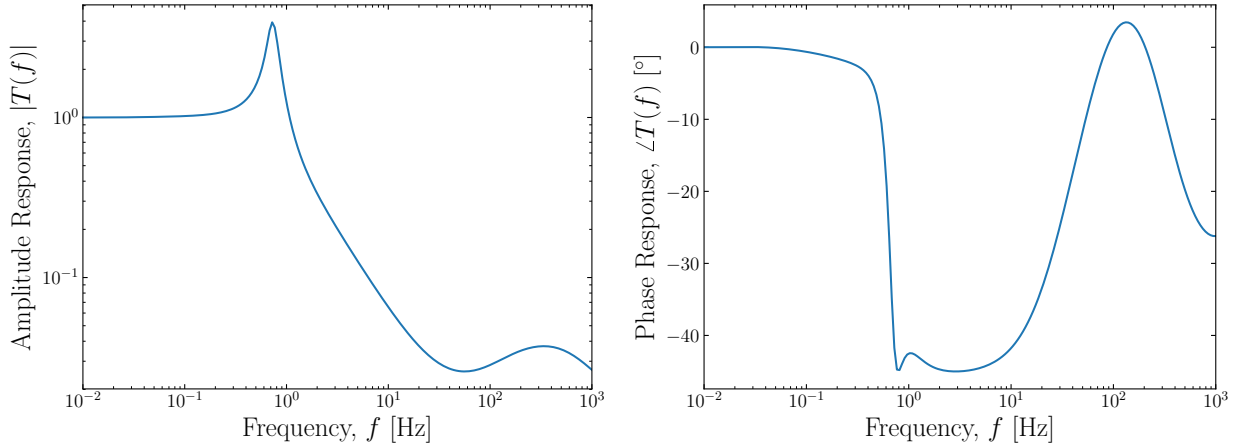


Figure 4.3: Schematic diagram of the quadrupole stabilisation system. k is the *stiffness*, c is the *damping coefficient*, F is the force exerted by external vibrations and f is the force applied by the piezoelectric actuator, which is shown in blue. The motion of the ground and quadrupole are measured using sensors, which are shown in red.

The quadrupole stabilisation system is an active system. It utilises a *piezoelectric actuator* to dynamically apply a force. This is a device which deforms when a voltage is applied to it [64]. Two commercially available motion sensors (*geophones* [64]) are used to measure the motion of the ground and quadrupole. These measurements are used by the controller to calculate a voltage to apply to the piezoelectric actuator with the aim of stabilising the quadrupole.

The stabilisation system directly reduces quadrupole motion with the transfer function shown in Figure 4.4. The system amplifies frequencies around 1 Hz, this is the resonant frequency of the system. The system is effective at damping high-frequency motion but does not affect low frequencies. Low frequency, long wavelength motion is not particularly harmful to the beam as the entire beamline moves coherently, so the system was designed not to break this motion.

The system stabilises horizontal and vertical motion with the same transfer function.



(a) Amplitude response vs frequency.

(b) Phase response vs frequency.

Figure 4.4: Transfer function of the quadrupole stabilisation system [42].

4.3 Integrated Simulations

4.3.1 Specific Sections

The models for GM generate element displacements as a function of time t and position s . The position s is usually the distance from the IP and lies on a straight line. This is correct for the ML and BDS, however, the RTML contains a TAL. In generating GM the RTML was ‘unfolded’ as if the accelerator was a single straight line. This simplification has little effect on the luminosity loss due to GM because virtually all of the luminosity degradation occurs from GM in the BDS.

For illustration, Table 4.1 shows the luminosity loss with GM model D in specific sections of CLIC. STE was simulated with no mitigation. At the interface between sections, the beam position is used as the reference for misalignments, such that the beam is on-axis in sections where GM is not applied.

Section with GM	Luminosity Loss, $\Delta\mathcal{L}/\mathcal{L}_0$ [%]
RTML	0.1
ML	3.4
BDS	46

Table 4.1: Luminosity loss due to GM model D without mitigation in specific sections. Values are expressed as a percentage of Equation (3.5). The error on each value is less than 0.1%.

Table 4.1 shows virtually no luminosity loss occurs from GM in the RTML. This is because beam jitter at the end of the RTML does not reach the IP. Therefore, luminosity loss can only occur via emittance growth. The low beam energy in the RTML means the quadrupole magnets are relatively weak. Consequently, the kick from a displaced quadrupole is small and emittance growth is limited.

GM in the BDS has the biggest impact on luminosity. This leads to a beam jitter at the IP, which directly impacts luminosity. The impact of GM in the ML is much less than in the BDS but is still significant.

4.3.2 Models

The luminosity loss due to the different GM models with a beam trajectory feedback system and quadrupole stabilisation system is shown in Table 4.2. The gain of the feedback system was optimised to minimise luminosity loss. The optimum gain was found to be $m = 2.5$. Simulations were performed using STE and NTE.

Mitigation	Luminosity Loss, $\Delta\mathcal{L}/\mathcal{L}_0$ [%]			
	Model A	Model B	Model C	Model D
Using STE				
No Mitigation	5.1	24	85	46
Beam Trajectory Feedback	0.5	29	90	51
Quadrupole Stabilisation	4.7	14	53	14
Beam Trajectory Feedback + Quadrupole Stabilisation	0.1	0.9	44	4.9
Using NTE				
No Mitigation	2.0	14	81	34
Beam Trajectory Feedback	0.1	18	88	40
Quadrupole Stabilisation	1.8	6.6	40	6.5
Beam Trajectory Feedback + Quadrupole Stabilisation	0.01	0.2	32	1.6

Table 4.2: Luminosity loss due to different GM models. Values are expressed as a percentage of Equation (3.3) for NTE or Equation (3.5) for STE. The error on each value is less than 0.1%.

There is a significant difference in luminosity loss when simulating STE and NTE. The dominant mechanism for luminosity loss is via a vertical beam-beam offset. However, as discussed in Section 3.6, the luminosity loss from a vertical beam-beam offset depends on the disruption parameter \mathcal{D}_y . When NTE is used, the nominal disruption of $\mathcal{D}_y \approx 13$ is simulated, whereas a disruption of $\mathcal{D}_y \approx 17$ is simulated when STE is used. The higher disruption in STE simulations means the luminosity loss from a beam-beam offset is exaggerated. The NTE simulations correspond to the luminosity loss in the limiting case when the nominal IP beam size, and therefore nominal disruption, is realised.

Model A represents the quietest environment that can be expected. CLIC is robust against model A. The luminosity loss is 2% without applying any mitigation. With just the

beam trajectory feedback system, its impact can be almost completely removed.

For model A solely utilising the beam trajectory feedback system reduces luminosity loss. However, for models B, C and D, solely utilising the beam trajectory feedback system results in a larger luminosity loss than not applying any mitigation. This is because the beam trajectory feedback system amplifies cultural noise, which is present in models B, C and D, but not A. High-frequency (above 10 Hz) GM becomes uncorrelated over length scales of a few metres. This means the last two quadrupoles in the BDS for the electron and positron beamlines have uncorrelated motion, which results in a beam-beam offset.

Model B requires the combination of a quadrupole stabilisation system and a beam trajectory feedback system to mitigate GM. The quadrupole stabilisation targets the cultural noise above 10 Hz, which the feedback system cannot correct. The luminosity loss can be kept to within 0.2% with both mitigation systems. Therefore, GM at the level of model B should not pose a danger for CLIC.

Model C represents a much higher level of GM than what is expected for CLIC. Additional mitigation systems would be needed to recover luminosity, such as an IP feedback system, which is discussed in the following section.

Model D represents an upper limit to the level of GM CLIC is expected to experience. Including the effect of the quadrupole stabilisation and beam trajectory feedback, the luminosity loss can be kept to within 1.6%. Therefore, CLIC will be robust against the impact of GM even in the most pessimistic scenario.

4.4 IP Feedback Systems

Beams colliding with a small beam-beam offset receive a large deflection due to beam-beam effects. Figure 4.5 shows the deflection as a function of beam-beam offset. This is exploited by an IP feedback system, which measures the offset with a BPM a few metres downstream of the IP.

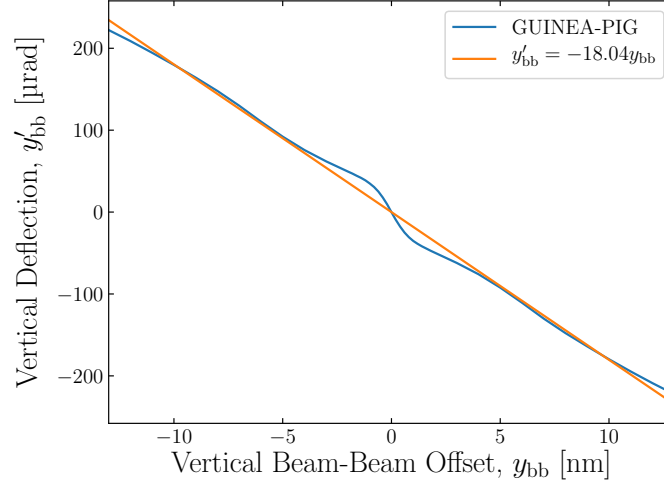


Figure 4.5: Vertical beam-beam deflection vs vertical beam-beam offset: calculated with GUINEA-PIG using a beam with NTE (blue) and a linear fit (orange).

There are two IP feedback systems in CLIC. One that corrects the offset of an entire train, referred to as the *train-to-train IP feedback system*, and another that corrects the offset of individual bunches within a train, referred to as the *intra-train IP feedback system*. Both systems infer the beam-beam offset by measuring the deflection at the IP. They differ in latency.

The transfer function approach to model the impact of the beam trajectory feedback system (described in Section 4.2.1) includes the impact of the train-to-train IP feedback system. This section examines the effectiveness of the intra-train IP feedback system.

An intra-train IP feedback system aims to correct the beam-beam offset of individual bunches. The time duration between bunches in a train, referred to as the *bunch spacing*, is 0.5 ns. A bunch-to-bunch correction with this spacing is very challenging and requires an extremely fast feedback system. An intra-train IP feedback system developed by the *Feedback on Nanosecond Timescales* (FONT) group is a system that could partially provide this [66, 67]. The latency of this system is 37 ns [66], therefore it does not correct bunch-to-bunch variations but does provide some intra-train correction. A schematic diagram of the FONT IP feedback system is shown in Figure 4.6.

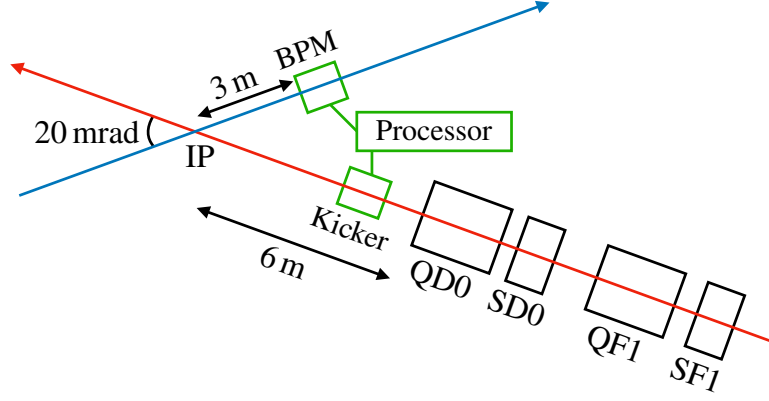


Figure 4.6: Schematic diagram of the FONT IP feedback system [66, 67], which is shown in green. The colliding beams are shown in blue and red. QD0, SD0, QF1 and SF1 are magnets in the FFS.

Control Loop

The beam-beam deflection is inferred from the BPM reading as [66]

$$y'_{bb} = \frac{y_{BPM}}{d_{BPM}}, \quad (4.14)$$

where y_{BPM} is the beam offset measured by the BPM and d_{BPM} is the distance from the IP to BPM. It is assumed that the beam-beam deflection is much greater than any angle the bunch may have at the IP. A linear fit is used to approximate the beam-beam deflection curve in Figure 4.5:

$$y'_{bb} = -18.04 y_{bb}. \quad (4.15)$$

A processor uses Equations (4.14) and (4.15) to infer the beam-beam offset and transmits a signal to a kicker upstream of the IP. A proportional feedback algorithm is implemented in the processor. The resultant change in the beam-beam offset is given by

$$\Delta y_{bb} = g y'_{bb}, \quad (4.16)$$

where g is the *gain*. Ensuring the correction signal is transmitted to the kicker as quickly as possible is essential for an effective feedback system. The kicker is assumed to be perfect.

An accurate BPM measurement is also essential. A Gaussian error with zero mean was added to all recordings. The standard deviation of this error is known as the *BPM resolution* and was assumed to be $1\text{ }\mu\text{m}$, which is achievable with *stripline BPMs* [68]. The current design of the FONT IP feedback system cannot resolve individual bunches with a spacing of 0.5 ns [68]. Therefore, the offset of 10 consecutive bunches was averaged in simulations.

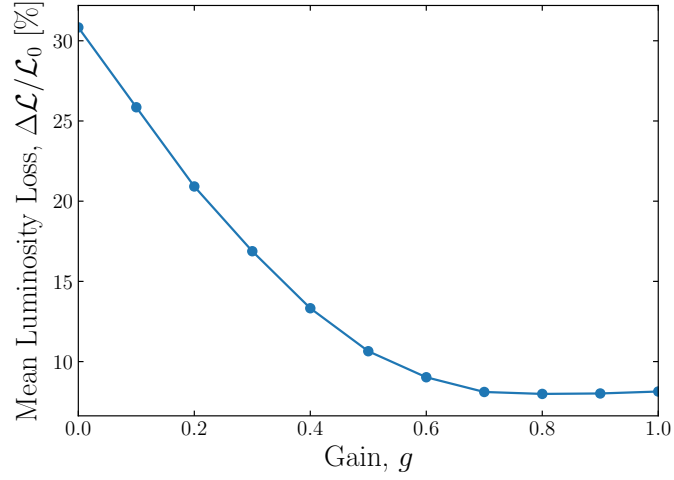


Figure 4.7: Mean luminosity loss vs gain.

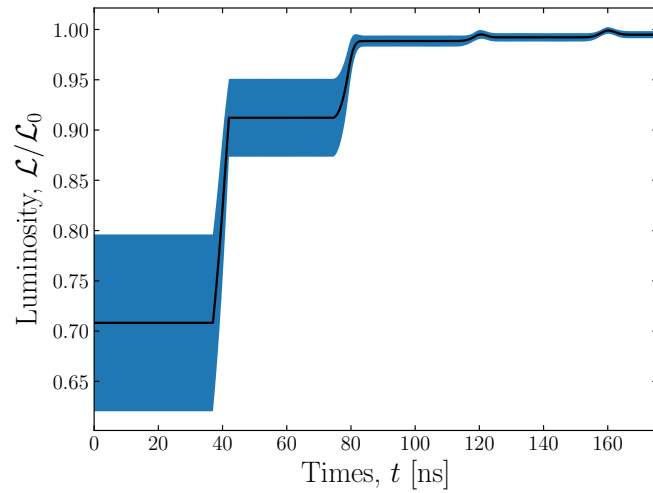


Figure 4.8: Luminosity vs time using the FONT IP feedback system. The blue shaded region is the standard deviation. A gain of $g = 0.8$ was used.

Luminosity Recovery

The beam-beam offset of 500 trains was simulated with GM model C using NTE, including the beam trajectory feedback and quadrupole stabilisation system. All bunches within a train are assumed to have the same offset.

The gain of the intra-train IP feedback can be optimised to provide the best correction. Figure 4.7 shows the luminosity recovery as a function of gain. The optimum gain is approximately 0.8. The luminosity loss can be reduced significantly from 32% to 8% using the intra-train IP feedback system. Figure 4.8 shows the mean luminosity recovery of each train. The latency of the intra-train IP feedback system results in the flat regions in Figure 4.8. The latency is approximately a quarter of the train length. A factor of four reduction in luminosity loss is expected from a system that fully recovers luminosity after a quarter of the train, which is effectively what occurs with the intra-train IP feedback system.

Chapter 5

Stray Magnetic Field Sensitivity and Tolerances

This chapter examines the sensitivity of CLIC at $E_{\text{CM}} = 380 \text{ GeV}$ to *stray magnetic fields* (SFs), and defines tolerances to limit luminosity loss. Studies of CLIC at $E_{\text{CM}} = 3 \text{ TeV}$ are presented in [69, 70].

5.1 Stray Magnetic Fields

Accelerator environments contain SFs from a large number of sources. SFs can be classified in terms of their source as:

- ***Natural***: SFs from non-man-made objects, e.g. the Earth’s magnetic field.
- ***Environmental***: SFs from man-made objects in the vicinity of CLIC, but not elements of CLIC, e.g. power lines or electrified train lines.
- ***Technical***: SFs from elements of CLIC, e.g. power cables, magnets, RF systems, etc.

Each of these classifications is discussed further in Chapters 8-10 along with measurements.

This chapter evaluates the sensitivity of CLIC to SFs by assuming a particular temporal and spatial variation, without assuming anything about the source.

5.1.1 Temporal and Spatial Variation

The impact of static SFs is minimised after tuning (see Section 3.5). Therefore, this work focuses on dynamic SFs. A SF can be written as a standing wave,

$$B(s, t) = B(s) \cos(2\pi ft + \phi), \quad (5.1)$$

where $B(s)$ is the amplitude, s is the position, t is the time, f is the frequency and ϕ is a random phase.

Temporal Variation

A train takes approximately $150 \mu\text{s}$ to travel from the DRs to the IP. The temporal variation of the SF is assumed to be slow enough that it is effectively static to a train. The SF frequency must be $f \ll 6.7 \text{ kHz}$ for this to be true.

To calculate the impact of a SF, its influence over a number of trains should be averaged. The time average (i.e. mean) of the SF is given by

$$\langle B(s, t) \rangle = 0. \quad (5.2)$$

The time average of the SF squared is given by

$$\langle B^2(s, t) \rangle = \frac{1}{2} B^2(s). \quad (5.3)$$

The standard deviation of the SF is given by

$$\sigma_B(s) = \sqrt{\langle B^2(s, t) \rangle - \langle B(s, t) \rangle^2} = \frac{1}{\sqrt{2}} B(s). \quad (5.4)$$

The quantity $\sqrt{\langle B^2(s, t) \rangle}$ is commonly known as the *RMS amplitude*, which in this case is equivalent to the standard deviation because the mean is zero.

Spatial Variation

The spatial variation of the SF is contained in the amplitude $B(s)$. A SF can be particularly detrimental if its kicks are coherent with the betatron motion of the beam. Three different spatial distributions will be considered: *point-like*, *sinusoidal* and *homogeneous* - discussed further in Section 5.2.

5.1.2 Impact on Luminosity

A SF kicks a beam, which can develop into an offset. This offset can either impact luminosity directly via a beam-beam offset at the IP or lead to emittance growth through filamentation.

In a linear collider, the vertical beam size is much smaller than the horizontal beam size. As a result, the beam is more sensitive to imperfections in the vertical plane. A SF oriented in the horizontal plane, which kicks the beam in the vertical direction is considered in the following.

Stray Magnetic Field Kicks

The motion of a relativistic electron in a SF can be described by equating the magnetic force

$$F_B(s) = ecB(s), \quad (5.5)$$

where e is the electric charge of an electron and c is the speed of light, to the centripetal force

$$F_C(s) = \frac{\gamma(s)mc^2}{\rho} = \frac{E(s)}{\rho}, \quad (5.6)$$

where $\gamma(s)$ is the Lorentz factor, m is the electron rest mass, $E(s) = m\gamma(s)$ is the energy of the particle and ρ is the bending radius,

$$F_B(s) = F_C(s) \implies ecB(s) = \frac{E(s)}{\rho}. \quad (5.7)$$

The bending radius can be written in terms of the SF kick as

$$\rho = \frac{ds}{d\theta}, \quad (5.8)$$

where ds is the distance travelled and $d\theta$ is the kick. Substituting Equation (5.8) into Equation (5.7) and rearranging for the kick gives

$$d\theta = \frac{ecB(s)}{E(s)} ds. \quad (5.9)$$

The integrated kick from the SF is

$$\delta = \int_{\theta_1}^{\theta_2} d\theta = \int_{s_1}^{s_2} \frac{ecB(s)}{E(s)} ds. \quad (5.10)$$

Equation (5.10) ignores the betatron motion of the beam. Over length scales comparable to the betatron wavelength, SF kicks can compensate the angle induced by previous kicks. This is the betatron motion can lead to an integrated kick of zero even in the presence of a SF. Equation (5.10) is only valid for calculating the integrated kick over distances that are short compared to the betatron wavelength.

To represent the SF in tracking simulations a grid of zero length dipole elements was inserted into the lattice to kick the beam. The spacing of the dipoles must be short compared to the betatron wavelength and spatial variation of the SF. A dipole spacing of 1 m was chosen. The strength of each dipole was set to apply the integrated kick from the SF over the space between dipoles.

Assuming the SF and energy are constant over the dipole spacing, Equation (5.10) can

be written in practical units as

$$\delta [\mu\text{rad}] = \frac{c [\text{m/s}] \cdot B [\text{nT}] \cdot L [\text{m}]}{E [\text{GeV}]} \times 10^{-12}, \quad (5.11)$$

where L is the dipole spacing.

Linearity and Scaling

Linear sections of CLIC are those which contain linear magnets (dipoles and quadrupoles). Non-linear sections contain higher-order magnets (e.g. sextupoles).

The motion of a single particle can be used to approximate the motion of the centroid of a beam. Considering a particle that is kicked vertically at location s_1 , the offset and angle of the particle at s_2 is given by [71]

$$y(s_2) = \sqrt{\beta_y(s_1)\beta_y(s_2)} \sqrt{\frac{E(s_1)}{E(s_2)}} \sin(\phi_y(s_1) - \phi_y(s_2))\delta, \quad (5.12)$$

and

$$y'(s_2) = \sqrt{\beta_y(s_1)\beta_y(s_2)} \sqrt{\frac{E(s_1)}{E(s_2)}} (\cos(\phi_y(s_2) - \phi_y(s_1)) - \alpha_y(s_2) \sin(\phi_y(s_2) - \phi_y(s_1)))\delta, \quad (5.13)$$

where $\alpha_y(s)$ and $\beta_y(s)$ are Twiss parameters (vertical alpha and beta function respectively), $\phi_y(s)$ is the vertical betatron phase and δ is the kick at s_1 . Equations (5.12) and (5.13) are valid in linear sections.

Combining Equations (5.11) and (5.12), it is clear the resultant beam offset due to a SF kick scales as

$$y \propto \sqrt{\frac{\beta_y}{E}} BL \sin(\Delta\phi_y), \quad (5.14)$$

where β_y and E are the beta function and energy at the kick location and $\Delta\phi_y$ is the betatron phase advance from the kick location to the location of the offset.

Luminosity loss can occur via a beam-beam offset or emittance growth. Ignoring beam-

beam effects, the luminosity of two beams colliding with a beam-beam offset is given by Equation (2.18). The Taylor expansion of Equation (2.18) is

$$\mathcal{L}_{\text{BBO}}(y_{\text{bb}}) \approx \mathcal{L}_{\text{G}} \left[1 - \frac{y_{\text{bb}}^2}{4\sigma_y^{*2}} \right] \approx \mathcal{L}_{\text{G}} - \Delta\mathcal{L}(y_{\text{bb}}), \quad (5.15)$$

where \mathcal{L}_{G} is the geometric luminosity and $\Delta\mathcal{L}(y_{\text{bb}}) = y_{\text{bb}}^2/(4\sigma_y^{*2})$. The luminosity loss is proportional to the beam-beam offset squared and scales as

$$\Delta\mathcal{L}(y_{\text{bb}}) \propto y_{\text{bb}}^2 \propto \frac{\beta_y}{E} B^2 L^2 \sin^2(\Delta\phi_{\text{IP}}), \quad (5.16)$$

where $\Delta\phi_{\text{IP}}$ is the betatron phase advance from the kick location to the IP.

The luminosity of a collision between two beams with vertical emittance $\epsilon_y + \Delta\epsilon_y$ is given by

$$\mathcal{L}_{\text{EG}}(\Delta\epsilon_y) = \frac{N^2 f_{\text{rep}} n_b}{4\pi\sigma_x^* \sqrt{\beta_y^*(\epsilon_y + \Delta\epsilon_y)}} = \frac{N^2 f_{\text{rep}} n_b}{4\pi\sigma_x^* \sigma_y^*} \frac{1}{\sqrt{1 + \frac{\Delta\epsilon_y}{\epsilon_y}}} = \mathcal{L}_{\text{G}} \frac{1}{\sqrt{1 + \frac{\Delta\epsilon_y}{\epsilon_y}}}. \quad (5.17)$$

The Taylor expansion of Equation (5.17) is

$$\mathcal{L}_{\text{EG}}(\Delta\epsilon_y) \approx \mathcal{L}_{\text{G}} \left[1 - \frac{1}{2} \frac{\Delta\epsilon_y}{\epsilon_y} \right] \approx \mathcal{L}_{\text{G}} - \Delta\mathcal{L}_{\text{EG}}(\Delta\epsilon_y), \quad (5.18)$$

where $\Delta\mathcal{L}(\Delta\epsilon_y) = \Delta\epsilon_y/(2\epsilon_y)$. The luminosity loss is therefore proportional to the emittance growth. The emittance growth scales with the beam offset (Equation (5.12)) and angle (Equation (5.13)) squared,

$$\Delta\epsilon_y \propto \frac{\beta_y}{E} B^2 L^2. \quad (5.19)$$

The beam must perform many betatron oscillations for emittance growth via filamentation to occur. Provided enough betatron oscillations occur, the emittance growth does not depend on the betatron phase advance $\Delta\phi_y$ and the luminosity loss due to emittance growth scales as

$$\Delta\mathcal{L}_{\text{EG}}(\Delta\epsilon_y) \propto \Delta\epsilon_y \propto \frac{\beta_y}{E} B^2 L^2. \quad (5.20)$$

Equations (5.16) and (5.20) show the luminosity loss is proportional to the beta function at the kick location, therefore kicks at locations with a large beta function will have a bigger impact. The luminosity loss is inversely proportional to the beam energy, therefore the SF will have a smaller impact if the beam energy is high. The phase difference from the kick location to the IP is also important when the SF leads to a beam-beam offset.

The above scalings are only valid in a linear regime. The RTML and BDS contain non-linear magnets. Despite these magnets, the response of the accelerator as a whole is approximately linear. Simulations show the accelerator behaves linearly for luminosity losses up to 20% [63]. In a linear regime, the luminosity loss from multiple kicks can be summed.

Sensitivity

In a linear regime, the luminosity loss due to a SF is given by

$$\Delta\mathcal{L}(t) = B^2(s, t) G^2, \quad (5.21)$$

where G is the *sensitivity*. The average luminosity loss is given by

$$\langle \Delta\mathcal{L}(t) \rangle = \langle B^2(s, t) \rangle G^2 = \sigma_B^2(s) G^2. \quad (5.22)$$

Using Equation (5.4) this can be written as

$$\langle \Delta\mathcal{L}(t) \rangle = \frac{1}{2} B^2(s) G^2 = \frac{1}{2} \Delta\mathcal{L}_S \quad (5.23)$$

where

$$\Delta\mathcal{L}_S = B^2(s) G^2 \quad (5.24)$$

is the luminosity loss due to a static SF with a spatial variation described by $B(s)$. Equation (5.23) shows that the luminosity loss is halved by averaging the temporal variation.

To calculate the sensitivity a full tracking simulation including a static SF is performed.

This simulation gives the luminosity loss $\Delta\mathcal{L}_S$ for a given amplitude $B(s)$. These quantities are used to calculate the sensitivity as

$$G = \sqrt{\frac{\Delta\mathcal{L}_S}{B^2(s)}}. \quad (5.25)$$

A SF amplitude is chosen to ensure a luminosity loss of 10-15%. This ensures the luminosity loss is above the simulation noise, but still within the region where Equation (5.24) is valid.

Tolerance

A *tolerance* is defined as the standard deviation $\sigma_B(s)$ that corresponds to a particular amount of luminosity loss. A time-averaged luminosity loss budget of 2% is allocated for SFs, this is

$$\langle\Delta\mathcal{L}(t)\rangle_{2\%} = 3 \times 10^{32} \text{ cm}^{-2}\text{s}^{-1}. \quad (5.26)$$

Once the sensitivity G has been found, the tolerance can be calculated as

$$\sigma_{B,\text{tol}}(s) = \sqrt{\frac{\langle\Delta\mathcal{L}(t)\rangle_{2\%}}{G^2}}. \quad (5.27)$$

Magnetic Shielding

Equations (5.16) and (5.20) show the luminosity loss due to a SF kick depends only on the beam parameters (beta function, betatron phase and energy) at the location of the kick. This enables the possibility of identifying sensitive regions, which are susceptible to SF kicks and targeting these sections to mitigate SFs.

Shielding the beam from SFs is a mitigation technique discussed in Chapter 7. Sensitivities and tolerances will be calculated including a perfect shield applied to specific sections. There are no SFs in regions that are perfectly shielded. Such calculations represent a limiting case, which is the maximum impact a magnetic shield could have.

5.2 Spatial Profiles

5.2.1 Point-Like SFs

Here, the SF kick is applied at a single location. The SF amplitude in Equation (5.25) is given by

$$B(s) = \begin{cases} B_0 \delta(s - s_0) & \text{for } s = s_0, \\ 0 & \text{for } s \neq s_0, \end{cases} \quad (5.28)$$

where $\delta(s - s_0)$ is a Dirac delta function, s_0 is the location of the kick and B_0 is the value of the SF at the kick location.

Ring to Main Linac

The sensitivity for a point-like SF and the vertical beta function along the RTML are shown in Figure 5.1. Emittance growth is the dominant mechanism for luminosity loss from a SF in the RTML. This is because a beam offset at the end of the RTML does not reach the IP. This means the betatron phase at the kick location is not important in determining the sensitivity. The beam energy is constant for most of the RTML, which means the sensitivity

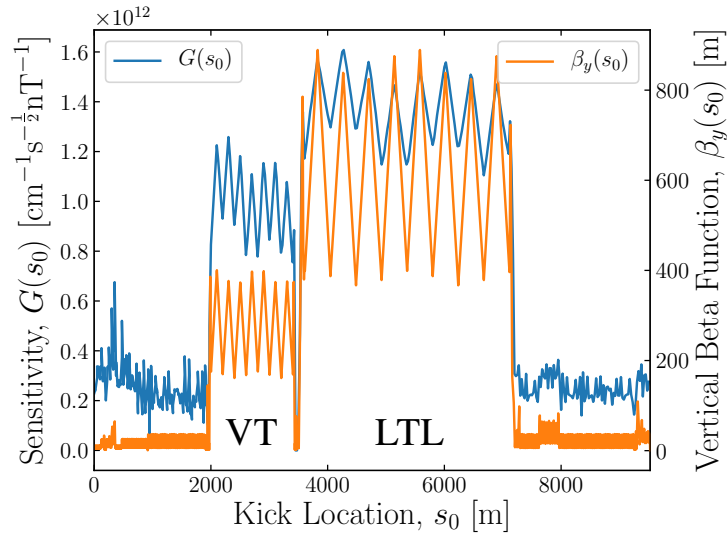


Figure 5.1: Sensitivity for a point-like SF in the RTML (LH scale, blue) and vertical beta function (RH scale, orange) vs kick location.

is predominately determined by the beta function. The most sensitive regions are those with a high beta function. In particular, the *Vertical Transfer* (VT) and *Long Transfer Line* (LTL), which are described in Chapter 3, are sensitive regions.

Main Linac

The sensitivity for a point-like SF in the ML is shown in Figure 5.2. Similar to the RTML, a beam offset at the end of the ML does not reach the IP. Therefore, emittance growth is the dominant mechanism for luminosity loss and the betatron phase is not important in determining the sensitivity. The sensitivity is determined by the beta function and energy. The vertical beta function and energy along the ML are shown in Figure 5.3. The vertical beta function increases with energy. As a result, the sensitivity to a point-like SF is relatively constant across the ML. The fluctuations over short distances are due to the variation of the beta function between focusing and defocusing quadrupoles.

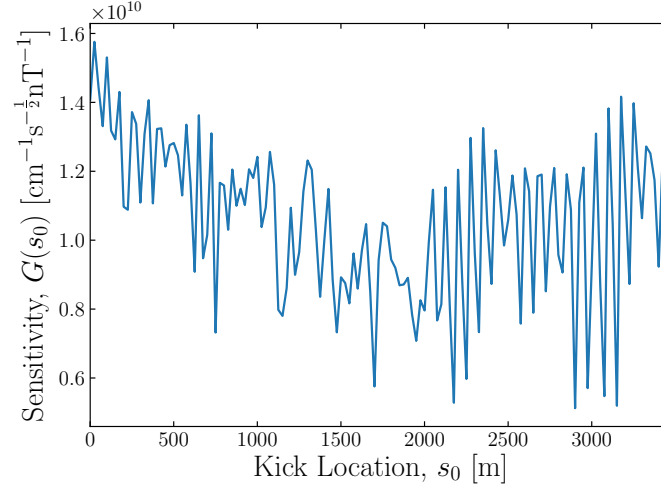


Figure 5.2: Sensitivity for a point-like SF in the ML vs kick location.

Beam Delivery System

The BDS for CLIC is described in [25, 42]. It contains a collimation section and the *Final-Focus System* (FFS). The collimation section can be further divided into an *Energy Collimation Section* (ECS), which removes off-energy particles, and a betatron collimation section,

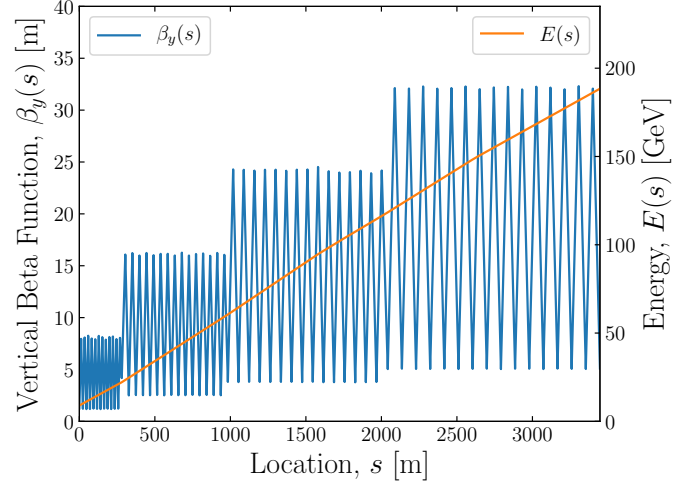


Figure 5.3: Vertical beta function (LH scale, blue) and energy (RH scale, orange) vs position along the ML.

which removes particles with large transverse offsets.

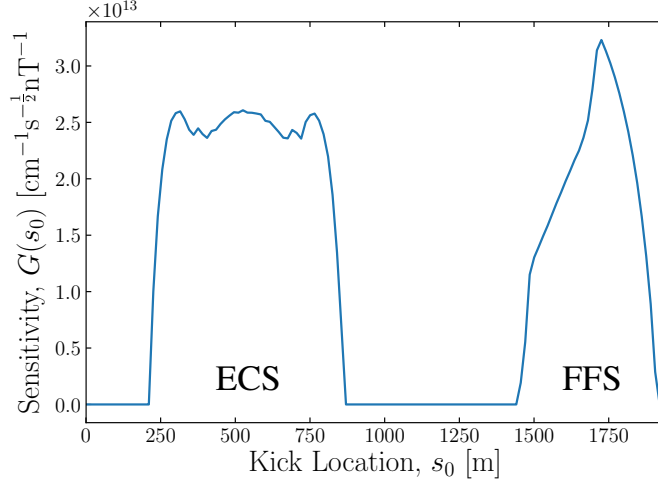


Figure 5.4: Sensitivity for a point-like SF in the BDS vs kick location.

The sensitivity for a point-like SF in the BDS is shown in Figure 5.4. The most sensitive regions of the BDS are the ECS and FFS. The vertical beta function and betatron phase along the BDS are shown in Figure 5.5. The dominant mechanism for producing luminosity loss from a SF in the BDS is a beam-beam offset, which means the phase advance to the IP is important. The energy in the BDS is constant. Therefore, the sensitivity for a point-like SF in the BDS is determined by the beta function and phase advance from the kick location to the IP.

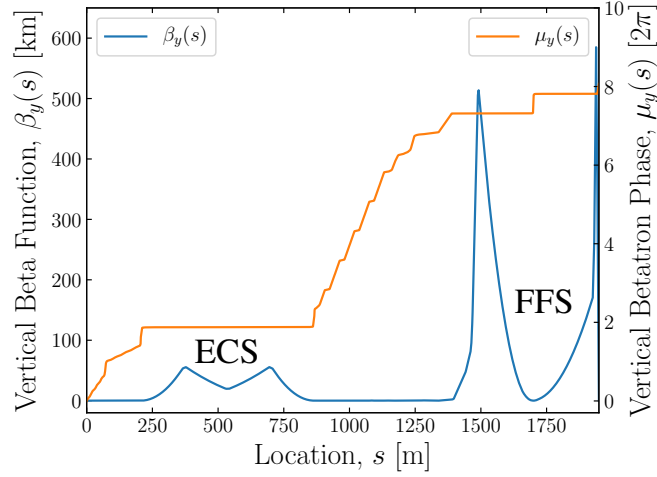


Figure 5.5: Vertical beta function (LH scale, blue) and vertical betatron phase (RH scale, orange) vs position along the BDS.

5.2.2 Sinusoidal SFs

The amplitude of this type of SF has a sinusoidal dependence on position. This model is useful for describing SFs as correlated waves. This was the approach used to develop the wavelike model for fast GM in Chapter 4.

The origin of the spatial wave must be specified to simulate a sinusoidal SF. A natural choice for the origin is the IP. This gives rise to two types of sinusoidal SFs: *sine-like*, which are anti-symmetric about the IP, or *cosine-like*, which are symmetric about the IP. The SF amplitude is calculated as

$$B(s) = \begin{cases} B_0 \sin\left(\frac{2\pi(s-s_{\text{IP}})}{\lambda}\right) & \text{for sine-like SFs,} \\ B_0 \cos\left(\frac{2\pi(s-s_{\text{IP}})}{\lambda}\right) & \text{for cosine-like SFs,} \end{cases} \quad (5.29)$$

where B_0 is the peak amplitude, s_{IP} is the location of the IP and λ is the SF wavelength.

Cosine-like SFs kick the electron and positron beams in the same direction, therefore there is no beam-beam offset at the IP, which generally leads to smaller sensitivities and larger tolerances. Sine-like SFs kick the electron and positron beams in opposite directions and therefore induce a beam-beam offset at the IP, which leads to larger sensitivities and smaller tolerances.

Ring to Main Linac

Figure 5.6 shows the sensitivity for a sinusoidal SF in the RTML. Without any mitigation, there is a large sensitivity for wavelengths of approximately 3 km, which is the wavelength of betatron motion in the LTL. Because the direction of the SF is in resonance with the motion of the beam the kicks add coherently.

There are two mitigation techniques available for the RTML. Sensitive regions, such as the VT and LTL can be surrounded with a magnetic shield to prevent the SF from reaching the beam. Alternatively, a feedforward beam trajectory correction can be applied in the *Turn-Around Loop* (TAL), which corrects the beam offset and angle entering the ML. Figure 5.6 also shows the sensitivity including different mitigation techniques.

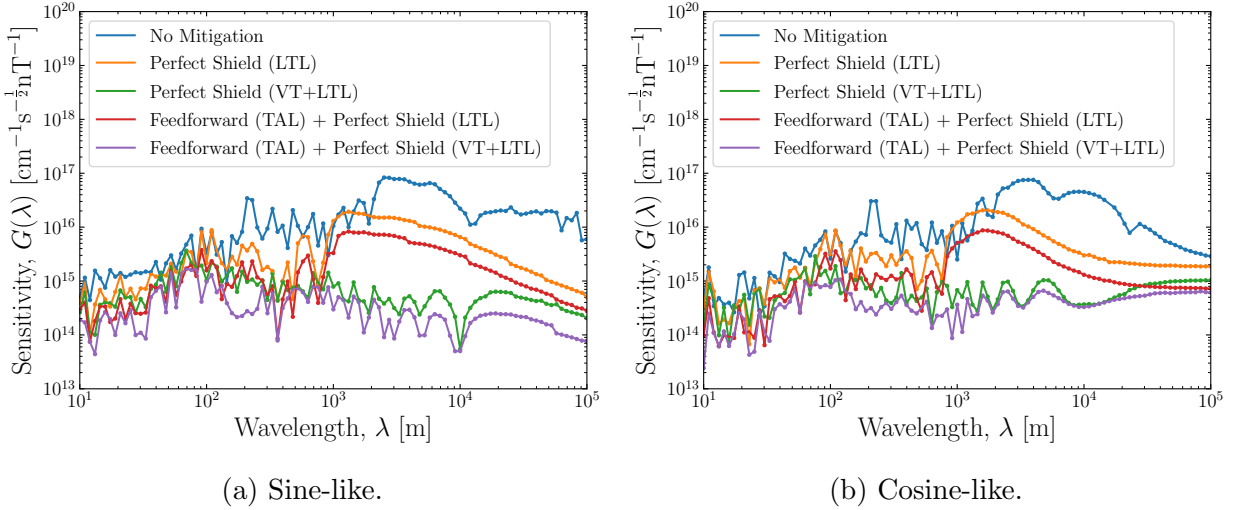


Figure 5.6: Sensitivity for a sinusoidal SF in the RTML vs wavelength with: no mitigation (blue); a perfect magnetic shield in the LTL (orange); a perfect magnetic shield in the VT and LTL (green); a feedforward beam trajectory correction in the TAL and a perfect magnetic shield in the LTL (red); a feedforward beam trajectory correction in the TAL and a perfect magnetic shield in the VT and LTL (purple).

The tolerance for a sinusoidal SF in the RTML is shown in Figure 5.7. Without any mitigation, the tolerance is quite tight, down to 0.2 nT. The tolerance can be increased to approximately 10-100 nT, by shielding the VT and LTL. This is the most effective approach to mitigate SFs. There is also an additional benefit from including a feedforward beam trajectory correction in the TAL.

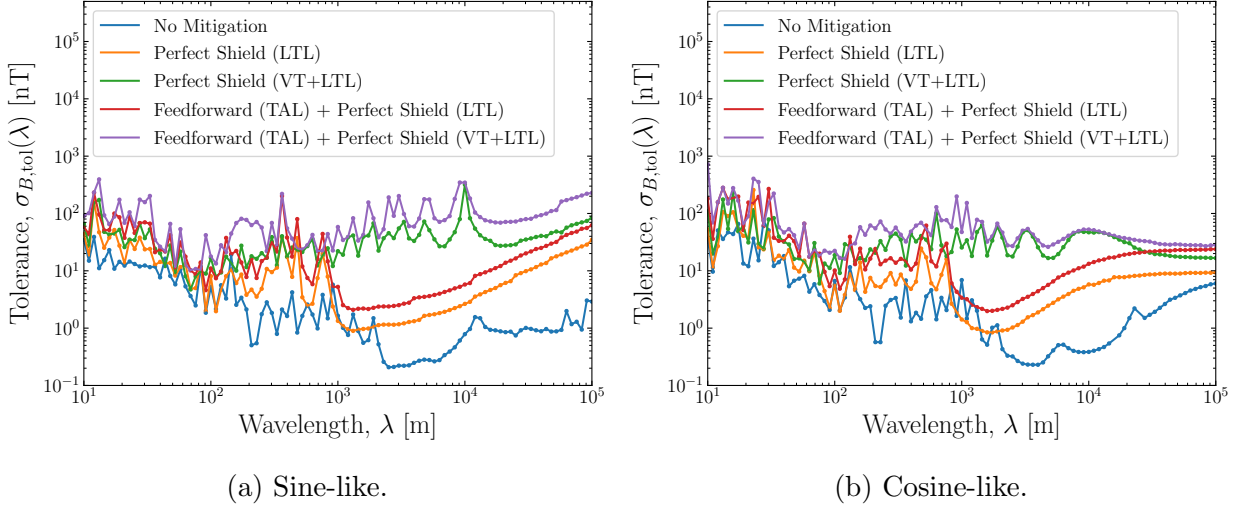


Figure 5.7: Tolerance for a sinusoidal SF in the RTML vs wavelength with: no mitigation (blue); a perfect magnetic shield in the LTL (orange); a perfect magnetic shield in the VT and LTL (green); a feedforward beam trajectory correction in the TAL and a perfect magnetic shield in the LTL (red); a feedforward beam trajectory correction in the TAL and a perfect magnetic shield in the VT and LTL (purple).

Main Linac

The sensitivity for sinusoidal SFs in the ML is shown in Figure 5.8 and the tolerance is shown in Figure 5.9. The sharp peaks in sensitivity at short wavelengths correspond to resonances with the betatron motion in the ML. The tolerances in the ML are approximately 0.1-1 μT . These tolerances are large compared to the RTML and BDS (discussed in the next section).

The ML also benefits from a large number of cavities, which are formed from copper walls of approximately 2 cm thickness that shield the beam from SFs. The ML is therefore the least sensitive section with respect to SFs.

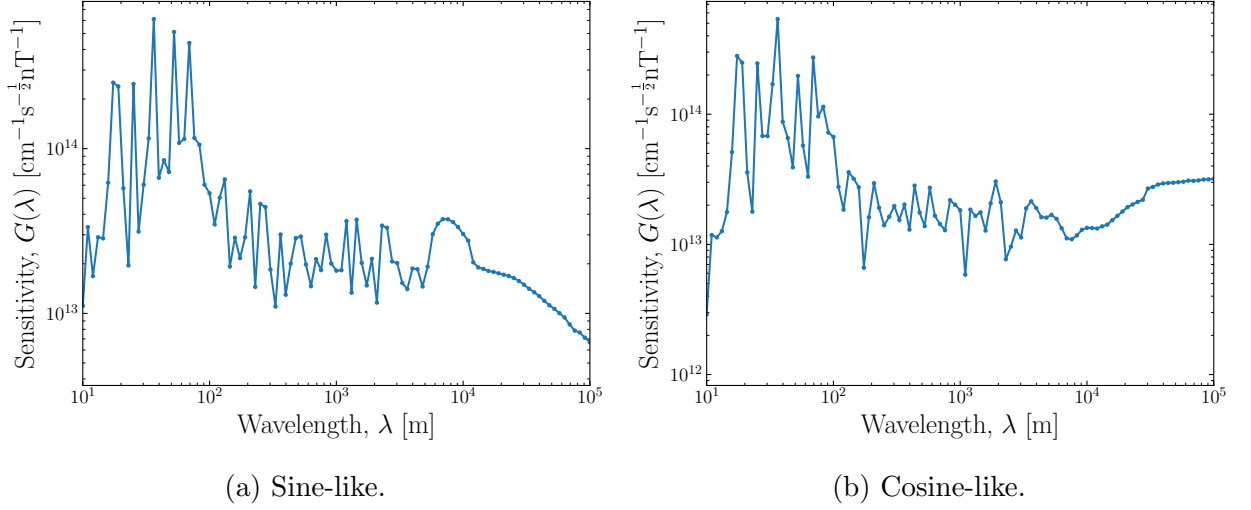


Figure 5.8: Sensitivity for a sinusoidal SF in the ML vs wavelength.

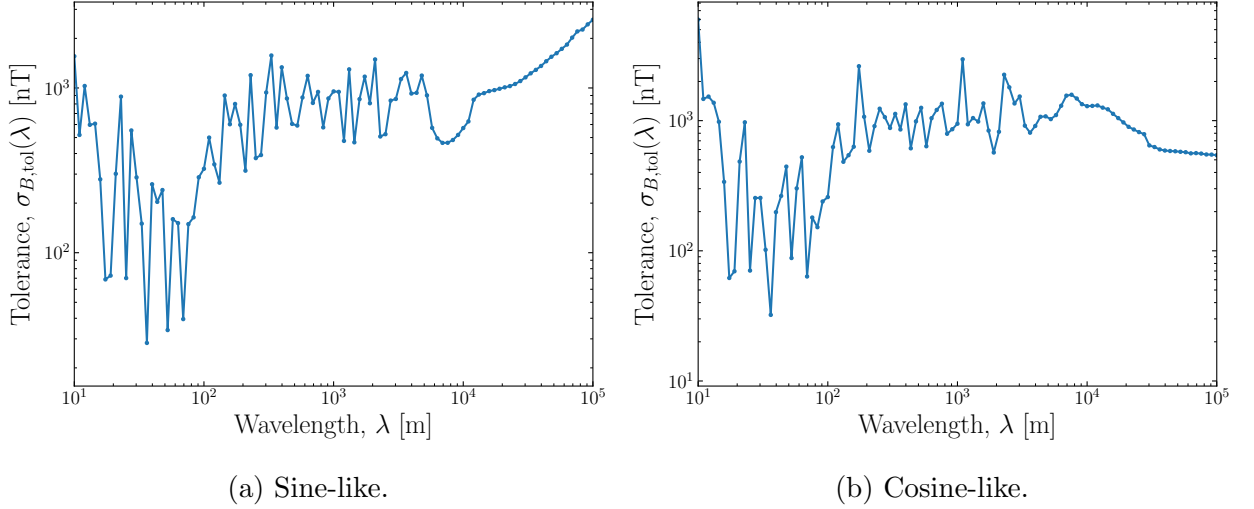


Figure 5.9: Tolerance for a sinusoidal SF in the ML vs wavelength.

Beam Delivery System

The sensitivity with different mitigation techniques for sinusoidal SFs in the BDS is shown in Figure 5.10 and the tolerance with different mitigation techniques is shown in Figure 5.11.

Peaks in the sensitivity arise for wavelengths in which the SF amplitude is at a maximum in the ECS or FFS. The sensitivity at 2 km arises because the SF has a large amplitude in the ECS. The tolerance is approximately 0.2 nT at a SF wavelength of 2 km. The tolerances are tighter for sine-like SFs compared to cosine-like SFs as expected.

Shielding both the ECS and FFS is the most effective mitigation for SFs in the BDS.

The tolerance is increased by roughly two orders of magnitude by shielding both systems.

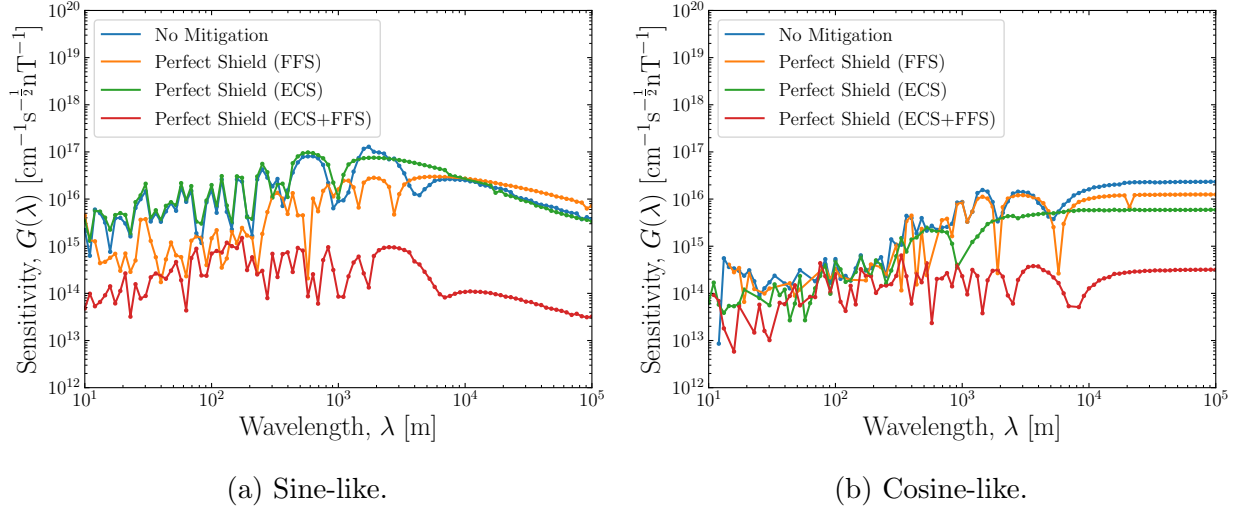


Figure 5.10: Sensitivity for a sinusoidal SF in the BDS vs wavelength with: no mitigation (blue); a perfect magnetic shield in the FFS (orange); a perfect magnetic shield in the ECS (green); a perfect magnetic shield in the ECS and FFS (red).

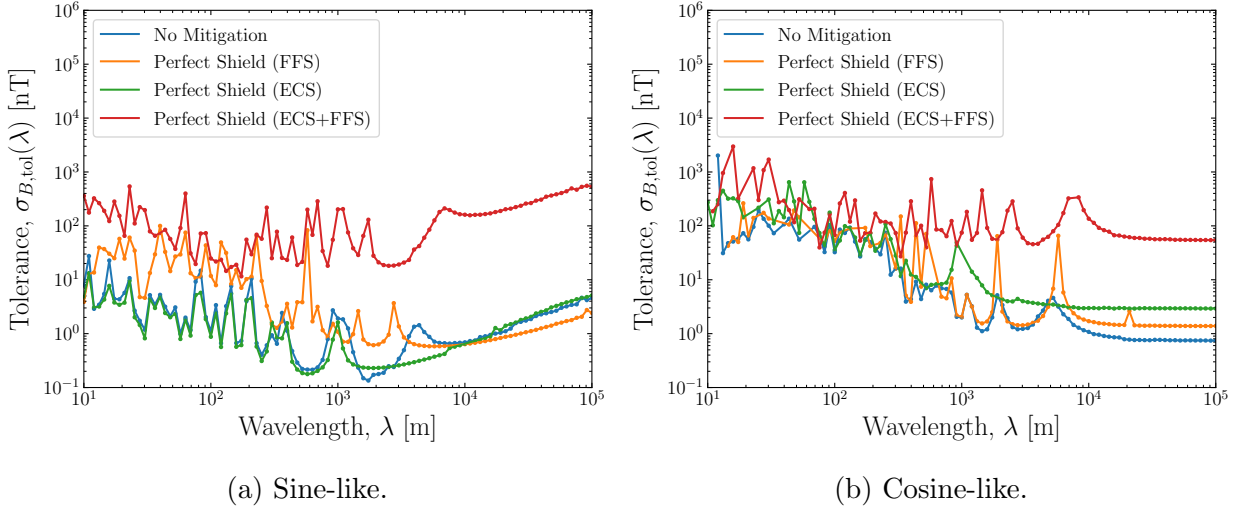


Figure 5.11: Tolerance for a sinusoidal SF in the BDS vs wavelength with: no mitigation (blue); a perfect magnetic shield in the FFS (orange); a perfect magnetic shield in the ECS (green); a perfect magnetic shield in the ECS and FFS (red).

Ring to Main Linac, Main Linac and Beam Delivery System

The sensitivity with different mitigation techniques for sinusoidal SFs in the all three sections (RTML, ML and BDS) is shown in Figure 5.12 and the tolerance with different mitigation techniques is shown in Figure 5.13.

Without any mitigation there are tolerances down to 0.2 nT for specific wavelengths. The minimum tolerance can be increased to approximately 10 nT by shielding sensitive regions in the RTAL and BDS. There is also an additional benefit from including a TAL feedforward beam trajectory correction.

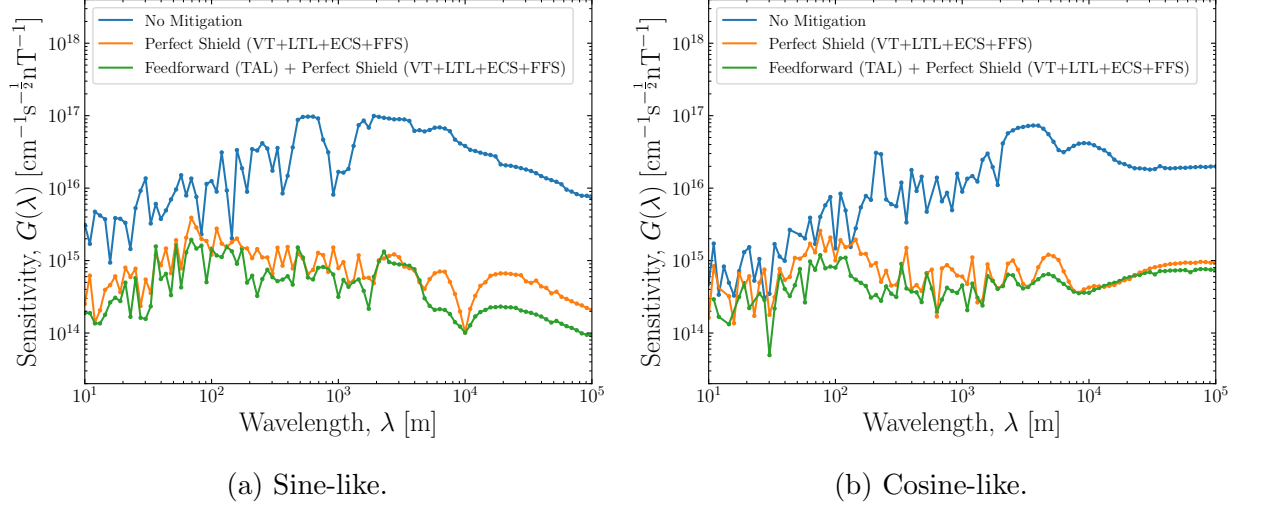


Figure 5.12: Sensitivity for a sinusoidal SF in the RTAL, ML and BDS vs wavelength with: no mitigation (blue); a perfect magnetic shield in the VT, LTL, ECS and FFS (orange); a feedforward beam trajectory correction in the TAL and a perfect magnetic shield in the VT, LTL, ECS and FFS (green).

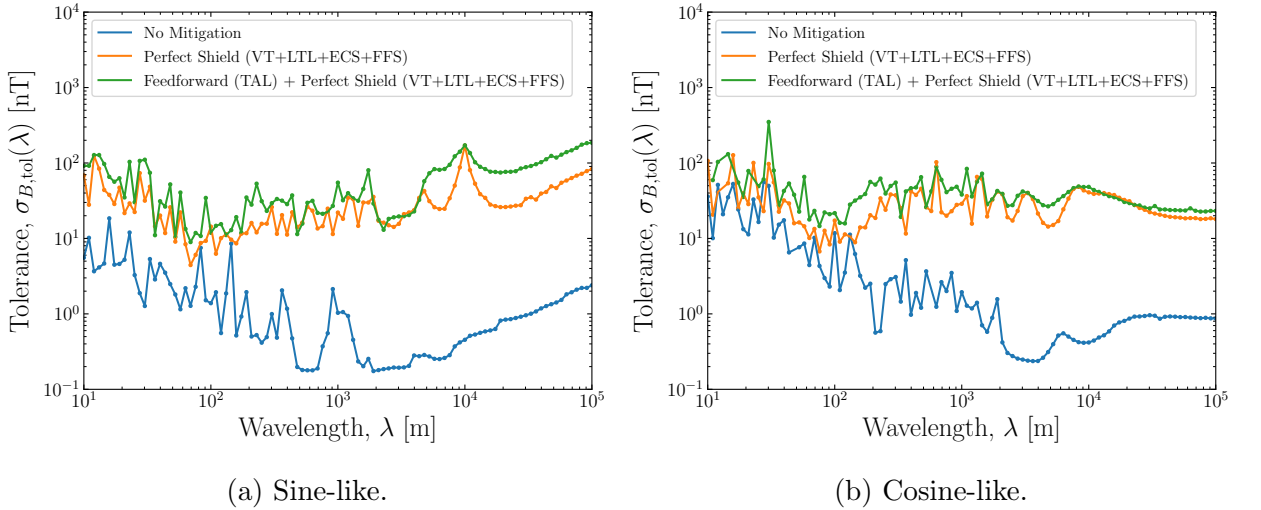


Figure 5.13: Tolerance for a sinusoidal SF in the RTAL, ML and BDS vs wavelength with: no mitigation (blue); a perfect magnetic shield in the VT, LTL, ECS and FFS (orange); a feedforward beam trajectory correction in the TAL and a perfect magnetic shield in the VT, LTL, ECS and FFS (green).

5.2.3 Homogeneous SFs

This type of SF has a constant value across the entire region,

$$B(s) = B_0. \quad (5.30)$$

A homogeneous SF can be thought of as the infinitely long wavelength limit of cosine-like SFs.

The sensitivity and tolerances for a homogeneous SF in different sections and with different mitigation techniques are shown in Table 5.1. They show good agreement with the tolerances for long wavelength cosine-like SFs in Figures 5.7, 5.9, 5.11 and 5.13.

Section with SF	Mitigation	Sensitivity, G [$\text{cm}^{-1}\text{s}^{-\frac{1}{2}}\text{nT}^{-1}$]	Tolerance, $\sigma_{B,\text{tol}}$ [nT]
RTML			
	No mitigation	3.0×10^{15}	5.9
	Perfect shield (LTL)	2.1×10^{15}	8.3
	Perfect shield (VT+LTL)	1.2×10^{15}	15
	Feedforward (TAL)	7.9×10^{14}	22
	+ Perfect shield (LTL)		
	Feedforward (TAL)	7.1×10^{14}	24
	+ Perfect shield (VT+LTL)		
ML			
	No mitigation	3.8×10^{13}	452
BDS			
	No mitigation	2.4×10^{16}	0.7
	Perfect shield (FFS)	1.7×10^{16}	1.0
	Perfect shield (ECS)	6.2×10^{15}	2.8
	Perfect shield (ECS+FFS)	3.9×10^{14}	45
RTML, ML and BDS			
	No mitigation	2.5×10^{16}	0.7
	Perfect shield	1.1×10^{15}	16
	(VT+LTL+ECS+FFS)		
	Feedforward (TAL)		
	+ Perfect shield	8.5×10^{14}	20
	(VT+LTL+ECS+FFS)		

Table 5.1: Sensitivity and tolerances for homogeneous SFs.

The sensitivity for a homogeneous SF can be calculated by integrating the point-like SF sensitivity function. However, in the RTML the beam direction changes several times. As a result, the direction of the kick from the SF changes and kicks orientated in opposite directions cancel. This results in a lower sensitivity than that found by integrating the point-like SF sensitivity function. For the ML and BDS, there is a good agreement between the sensitivity calculated from homogeneous SF simulations and integration of the point-like SF sensitivity function.

The tolerance for a homogeneous SF across the entire accelerator is 0.7 nT without mitigation. The luminosity loss is dominated by the SF in the BDS. Shielding the most sensitive regions of the RTML and BDS, the tolerance is increased to 16 nT and including a feedforward beam trajectory correction in the TAL raises the tolerance to 20 nT.

5.3 Summary

CLIC has an unprecedented sensitivity to SFs. The minimum tolerances for sinusoidal SFs and tolerances for homogeneous SFs across the entire accelerator are summarised in Table 5.2.

Without mitigation, there is a minimum tolerance on the order of 0.1 nT. The tolerance can be improved by two orders of magnitude by shielding sensitive regions.

Mitigation	Sinusoidal		Homogeneous
	$\sigma_{B,\text{tol}}$ [nT]	λ [m]	$\sigma_{B,\text{tol}}$ [nT]
No mitigation	0.2	3,000	0.7
Perfect shield (VT+LTL+ECS+FFS)	5	70	16
Feedforward (TAL) + Perfect shield (VT+LTL+ECS+FFS)	10	70	20

Table 5.2: Summary of SF tolerances.

Chapter 6

Magnetic Field Sensors

Measurements are essential to understand the characteristics of SFs and to develop a model. This chapter describes the magnetic field sensors used in this work.

6.1 Measurements

6.1.1 Magnetometers

A magnetic field sensor is known as a *magnetometer*. The output of a magnetometer is a time series voltage $V(t)$. The conversion to a magnetic field is performed in the frequency domain as

$$B(f) = \frac{V(f)}{S(f)}, \quad (6.1)$$

where $V(f)$ is the Fourier transform of $V(t)$ and $S(f)$ is the *sensitivity* (or *transfer function*) of the magnetometer, which is a complex-valued function.

Sensitivity

The absolute value of the sensitivity is known as the *amplitude response* of a magnetometer. Figure 6.1 shows a typical amplitude response, which resembles a low-pass filter [72]. The

value of the flat part (S_F in Figure 6.1) is known as the *scale factor*. The frequency range in which the amplitude response is above $S_F/\sqrt{2}$ is known as the *frequency bandwidth* and the frequency at which the amplitude response is equal to $S_F/\sqrt{2}$ is known as the *cutoff frequency* (f_c in Figure 6.1).

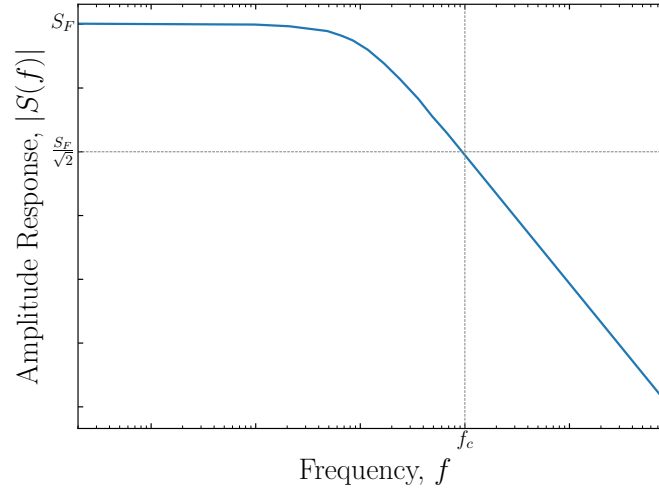


Figure 6.1: Typical amplitude response of a magnetometer.

Noise

A magnetometer would output a voltage even in the absence of a magnetic field. The static part of this voltage (*DC component*) is known as the *offset* of the magnetometer and the dynamic part (*AC component*) is known as the *noise* of the magnetometer. The noise of a magnetometer is often described in the frequency domain and decreases with frequency as $1/f$.

Data Acquisition

A magnetometer outputs an analogue signal, which is digitised with a *data acquisition system* (DAQ). The DAQ also has a noise. The sensitivity of the magnetometer together with the noise of the magnetometer and DAQ determines the smallest magnetic field amplitude that can be measured.

6.1.2 Magnetic Field Calculations

Time Series

Usually, the DC component or low frequency variations of a magnetic field are studied in the time domain. The magnetic field can be approximated as

$$B(t) \approx \frac{V(t)}{S_F}. \quad (6.2)$$

Power Spectral Densities

It is common to describe a magnetic field in the frequency domain with a *power spectral density* (PSD). In this work, the PSD of the output voltage is calculated using Welch's method with a time windowed signal (described in Appendix A). This voltage PSD is converted into a magnetic field PSD using the sensitivity,

$$P_B(f) = \frac{P_V(f)}{|S(f)|^2} \quad (6.3)$$

where $P_V(f)$ is the voltage PSD.

All PSDs in this work were calculated by averaging two seconds of measurement data. This was found to be a good compromise between measurement time and the achieved frequency resolution of the PSD. A two-second measurement corresponds to a frequency bin width of 0.5 Hz. In plots of PSDs in this work, the thickness of the line represents the error in the measurement.

Variance and Standard Deviation

The variance of the magnetic field can be calculated by integrating the PSD,

$$\sigma_B^2 = \int_0^\infty P_B(f) \, df. \quad (6.4)$$

$P_B(f)$ is defined for positive frequencies only and is normalised such that its integral over positive frequencies gives the variance. The standard deviation is given by

$$\sigma_B = \sqrt{\int_0^\infty P_B(f) \, df}. \quad (6.5)$$

In this work, the standard deviation will be plotted as a function of frequency range:

$$\sigma_B(f_0) = \sqrt{\int_{f_0}^\infty P_B(f) \, df}. \quad (6.6)$$

This helps to examine the contribution of particular frequencies to the standard deviation.

6.1.3 Requirements

The magnetometer used to survey SFs for CLIC must satisfy the following requirements:

1. The noise of the magnetometer must be small enough to accurately measure 0.1 nT amplitudes.
2. The frequency bandwidth of the magnetometer must be at least a few kHz.
3. The magnetometer must be able to measure both the direction and magnitude of the magnetic field.

Different types of magnetometers are described in [73]. These differ in the mechanism used to measure the magnetic field. Finding a magnetometer that satisfies the above requirements, particularly the first requirement, is challenging. A magnetometer that meets the above requirements is a *fluxgate* [74] produced by Bartington Instruments, UK [75], called the *Mag-13*. In this work, a collection of four Mag-13 sensors was used. Dedicated measurements to characterise these sensors are described below.

6.2 Mag-13

A diagram of a Mag-13 sensor is shown in Figure 6.2. The details of this sensor are described in the brochure [76] and operation manual [77]. The advertised specifications of this sensor are summarised in Table 6.1. The Mag-13 measures the magnetic field along three orthogonal axes: x , y and z .

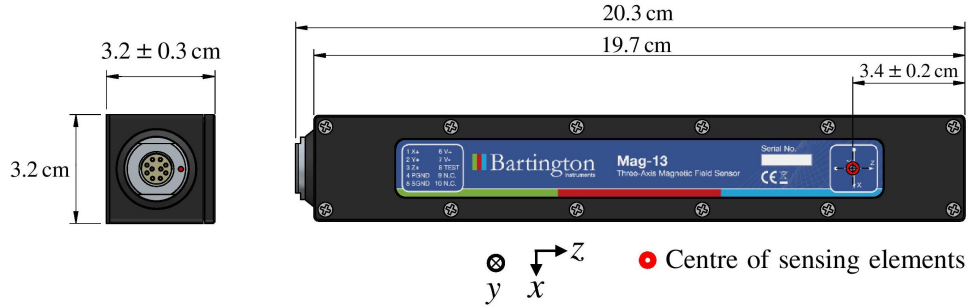


Figure 6.2: Side and front view of a Mag-13 sensor [78].

Parameter	Value
Number of axes	3
Dimensions	$20.3 \times 3.2 \times 3.2$ cm
Weight	227 g
Output voltage range	± 10 V
Magnetic field range	± 100 μ T
Frequency bandwidth	0 – 3 kHz
Flat sensitivity range	0 – 1 kHz
Scale factor	100 mV/ μ T
Noise at 1 Hz	< 7.1 pT/ $\sqrt{\text{Hz}}$
Scale factor error	0.5 mV/ μ T
Orthogonality error	$< \pm 0.1^\circ$
Linearity error	0.0015%
Hysteresis error	< 2 nT
Zero field offset error	± 5 nT
Operable temperature range	-40 – 70 $^\circ$ C

Table 6.1: Advertised Mag-13 specifications [76].

The full measurement setup is illustrated in Figure 6.3. All devices are powered using batteries to ensure currents from the mains do not contaminate the measurement. The setup is highly portable, which is necessary for surveying SFs across the CERN site. Each device in Figure 6.3 is described below.

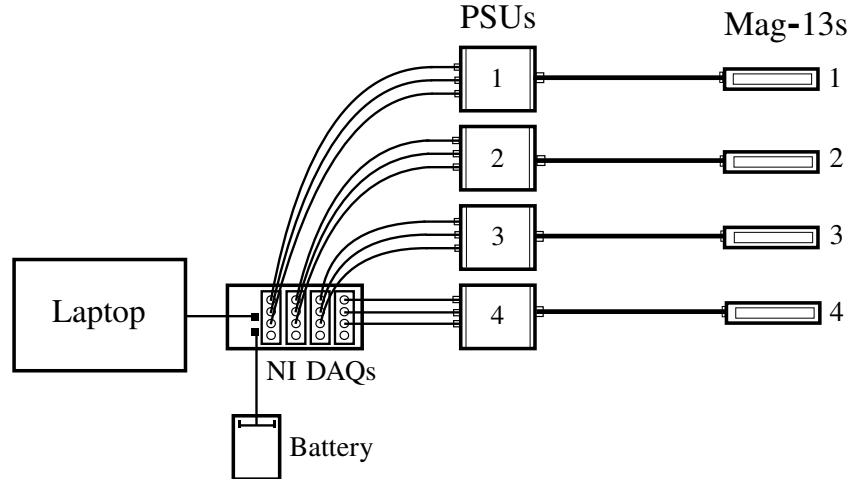


Figure 6.3: Full measurement setup for surveying SFs.

Power Supply Units

A Mag-13 sensor requires a *power supply unit* (PSU), which is also provided by Bartington Instruments, UK¹. Each sensor requires its own PSU. A cable connects the PSU to the Mag-13. This cable must be sufficiently long (over a few metres) to ensure the sensor can be placed far from the PSU and DAQ. This is to prevent the sensor from picking up noise from the auxiliary equipment. The PSU serves two purposes: to power the Mag-13 and to return the output voltage of the sensor. Short cables (less than 20 cm) are used to connect the PSU to the DAQ to prevent noise being picked up by the cables.

The PSU has two modes of operation: *AC mode* and *DC mode*. In AC mode a high-pass filter in the PSU removes frequencies below 0.1 Hz. In DC mode the output voltage of the sensor is unaltered.

Data Acquisition Systems

The DAQs used were produced by *National Instruments* (NI) [80]. Each sensor had its own DAQ module. The modules were placed in a NI chassis (NI cDAQ-9174 [81]), which can hold up to four modules. Data was recorded using a laptop (DELL Latitude 7480 [82]) with a NI LabVIEW VI [83].

¹This item is called power supply unit 1 (PSU1) in the catalogue [79].

The resolution of a DAQ is normally given in terms of a number of *bits* N_{bits} , which together with the output voltage range determines the precision,

$$\Delta V = \frac{V_{\text{max}} - V_{\text{min}}}{2^{N_{\text{bits}}}}, \quad (6.7)$$

where V_{min} and V_{max} is the minimum and maximum output voltage respectively.

The DC component of the sensor's output voltage is often orders of magnitude larger than the AC component. Recording the DC component requires a DAQ that covers the full range of the output voltage. However, in AC mode the DC component is removed and the output voltage only contains the AC component, which is much smaller. This means a DAQ with a smaller voltage range can be used. As a result, a better precision can be achieved with the same number of bits.

In AC mode a 24-bit DAQ with a voltage range of ± 0.5 V (NI 9238 DAQ [84]) was used and in DC mode a 24-bit DAQ with a voltage range of ± 10 V (NI 9239 DAQ [85]) was used.

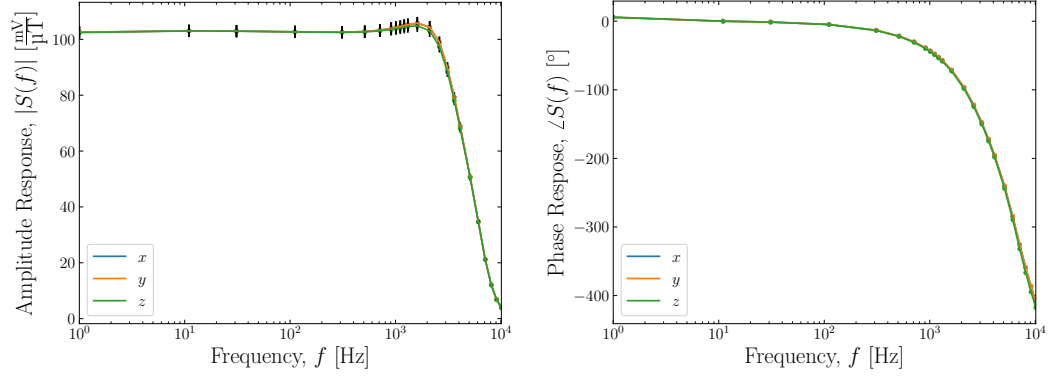
6.2.1 Sensitivity

With a controlled excitation each sensor can be calibrated. A set of Helmholtz coils [73] was used to provide a magnetic field excitation at a precise frequency and amplitude. Figure 6.4 shows the measured sensitivity of each sensor.

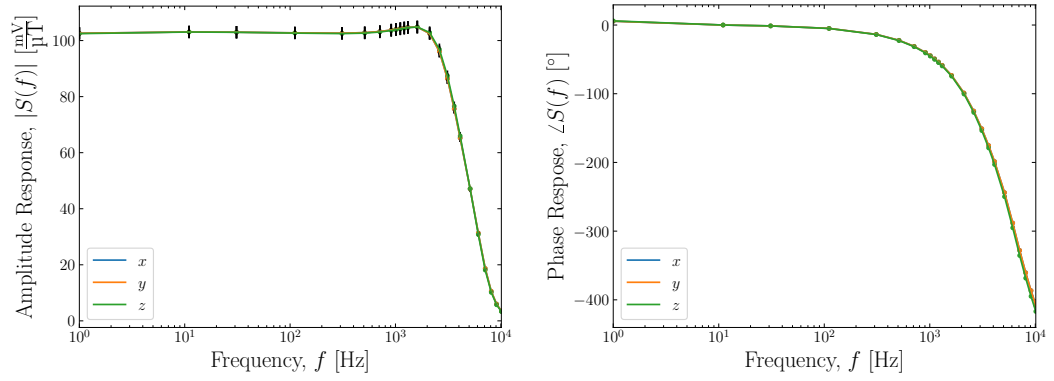
Table 6.2 summarises the measured scale factor and cutoff frequency of each sensor. The measured scale factor is in agreement with the advertised value of (100.0 ± 0.5) mV/ μ T. The advertised cutoff frequency for the sensors is 3 kHz. Most sensors comfortably satisfy this specification apart from the y -axis of sensor 3 and z -axis of sensor 4.

Axis	Scale Factor, S_F [mV/ μ T]	Cutoff Frequency, f_c [Hz]
Sensor 1		
x	102 ± 2	$3,857.4 \pm 0.5$
y	103 ± 2	$3,940.6 \pm 0.5$
z	102 ± 2	$3,894.5 \pm 0.5$
Sensor 2		
x	103 ± 2	$3,873.6 \pm 0.5$
y	103 ± 2	$3,759.7 \pm 0.5$
z	102 ± 2	$3,806.5 \pm 0.5$
Sensor 3		
x	103 ± 2	$3,854.7 \pm 0.5$
y	103 ± 2	$2,934.1 \pm 0.5$
z	103 ± 2	$3,085.8 \pm 0.5$
Sensor 4		
x	103 ± 2	$3,817.4 \pm 0.5$
y	103 ± 2	$3,839.7 \pm 0.5$
z	103 ± 2	$2,787.7 \pm 0.5$

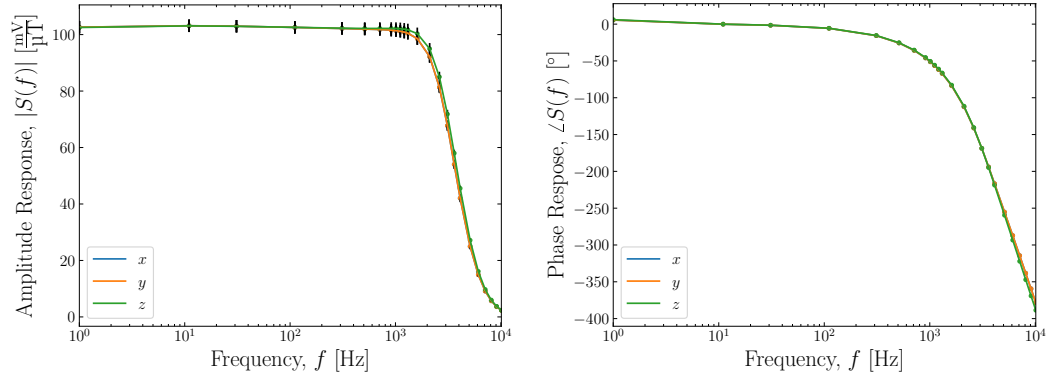
Table 6.2: Measured scales factor and cutoff frequency of each Mag-13 sensor.



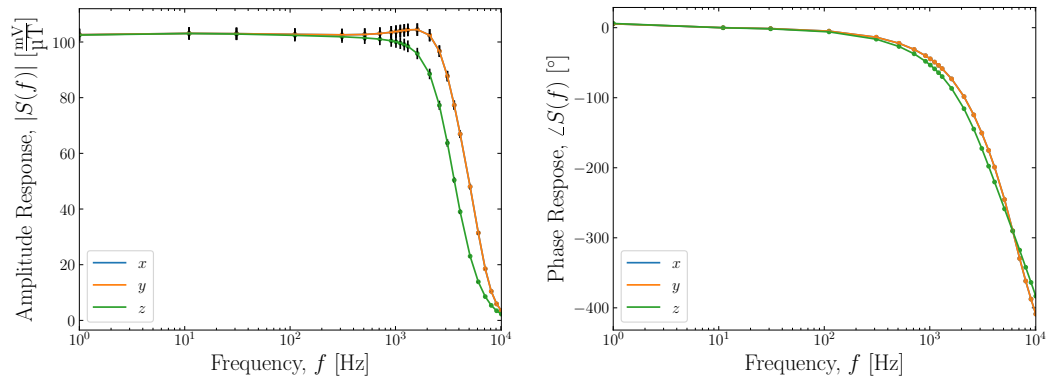
(a) Sensor 1.



(b) Sensor 2.



(c) Sensor 3.



(d) Sensor 4.

Figure 6.4: Amplitude and phase response vs frequency, i.e. sensitivity function, of each Mag-13 sensor.

6.2.2 Linearity

Equation (6.1) describes a linear relationship between the output voltage of a magnetometer and the magnetic field. A precise magnetic field amplitude was excited using the Helmholtz coils and the sensor output voltage was recorded. The amplitude of the excitation was varied to examine the linearity of the sensor. This was done for a few different frequencies.

As an example, Figure 6.5a shows the output voltage of the x -axis of sensor 1 for different excitation amplitudes. At high frequencies, it becomes difficult to drive a current in the Helmholtz coils. This is due to the impedance of the coils. As a result, the maximum excitation amplitude is smaller at high frequencies. The output voltage of the sensor is also smaller at high frequencies. This is due to the reduced sensitivity of the sensor.

A straight line was fitted to each amplitude scan. The difference between the measurement and the straight-line fit (*residual*) is shown in Figure 6.5b.

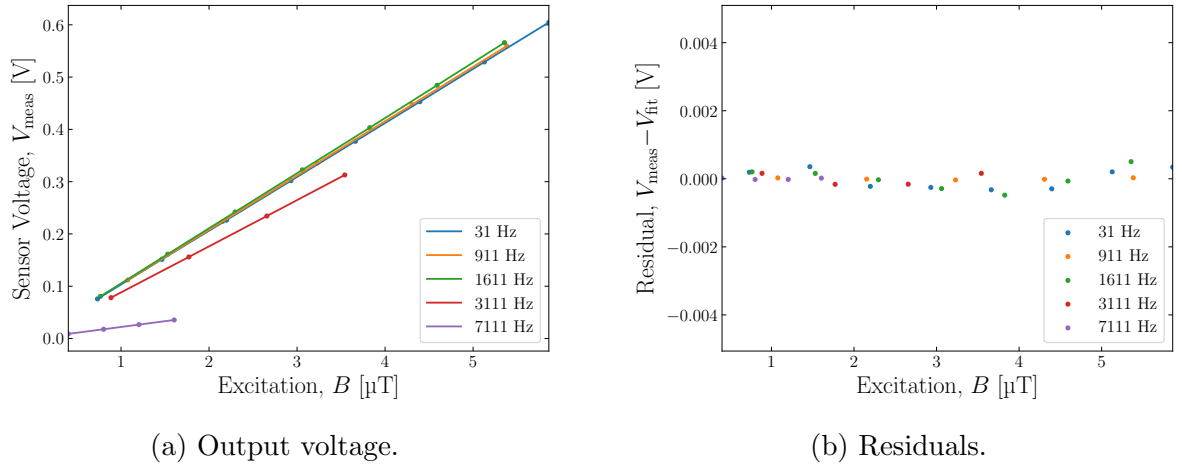


Figure 6.5: Sensor voltage and residual vs excitation of the x -axis for sensor 1 with different excitation frequencies. Error bars too small to be seen.

The *linearity error* is calculated as

$$\text{Linearity Error} = \sqrt{\frac{1}{N-2} \sum_{i=1}^N [V_{\text{meas}}(B_i) - V_{\text{fit}}(B_i)]^2} \quad (6.8)$$

where V_{meas} is the measured sensor output voltage, V_{fit} is the fit, B_i is the magnetic field excitation and N is the number of data points. The linearity error is usually expressed as a percentage of the full output range of the sensor. The intercept of the straight line fit corresponds to the noise of the magnetometer at the excitation frequency.

Table 6.3 summaries the linearity error and intercept of each axis of each sensor measured with a 31 Hz excitation. The linearity error and intercept measured at other frequencies are similar. The advertised linearity error is 0.0015%, which is similar to the measured value.

Axis	Linearity Error [%]	Intercept [mV]
Sensor 1		
x	0.0016	0.0 ± 0.3
y	0.0016	0.0 ± 0.2
z	0.0016	0.0 ± 0.2
Sensor 2		
x	0.0016	0.0 ± 0.3
y	0.0016	0.0 ± 0.3
z	0.0015	0.0 ± 0.2
Sensor 3		
x	0.0016	0.0 ± 0.3
y	0.0016	0.0 ± 0.3
z	0.0016	0.0 ± 0.3
Sensor 4		
x	0.0016	0.0 ± 0.3
y	0.0016	0.0 ± 0.3
z	0.0016	0.0 ± 0.3

Table 6.3: Linearity error and intercept of each Mag-13 sensor.

6.2.3 Noise

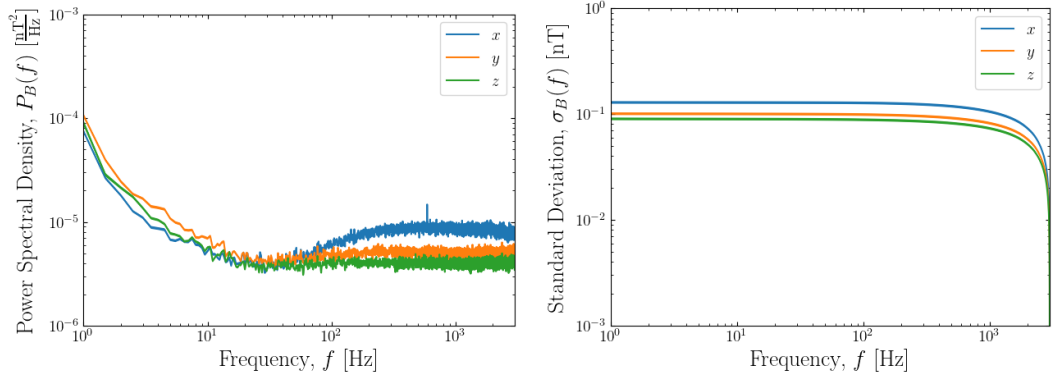
Figure 6.6 shows the noise of each sensor. Measurements were taken at a geomagnetic observatory in Tihany, Hungary. The location was magnetically quiet, far from man-made magnetic field sources. The main background at this observatory is the Earth's magnetic field, which is a DC magnetic field with low-frequency variations.

To remove this background, a set of three nested magnetic shields formed from *mu-metal* was used - this material is discussed further in Chapter 7. Each cylinder had a thickness of 1 mm and diameters of 30.5, 33.5 and 36.5 cm. The height of each cylinder was 1 m. The sensor was placed at the centre of the magnetic shield.

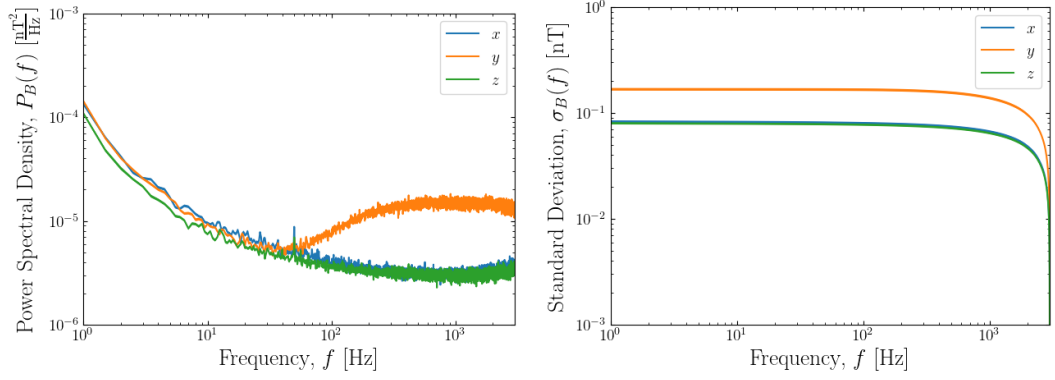
The PSDs in Figure 6.6 decrease with frequency. Above the cutoff frequency, the low sensitivity of the sensors begins to amplify the noise. The noise at 1 Hz for each axis of each sensor is summarised in Table 6.4. The measured noise is similar to the advertised value of $7 \text{ pT}/\sqrt{\text{Hz}}$.

Axis	Noise at 1 Hz [$\text{pT}/\sqrt{\text{Hz}}$]
Sensor 1	
x	8 ± 2
y	10 ± 3
z	9 ± 3
Sensor 2	
x	12 ± 3
y	12 ± 3
z	10 ± 3
Sensor 3	
x	13 ± 3
y	12 ± 3
z	13 ± 6
Sensor 4	
x	13 ± 3
y	12 ± 3
z	13 ± 5

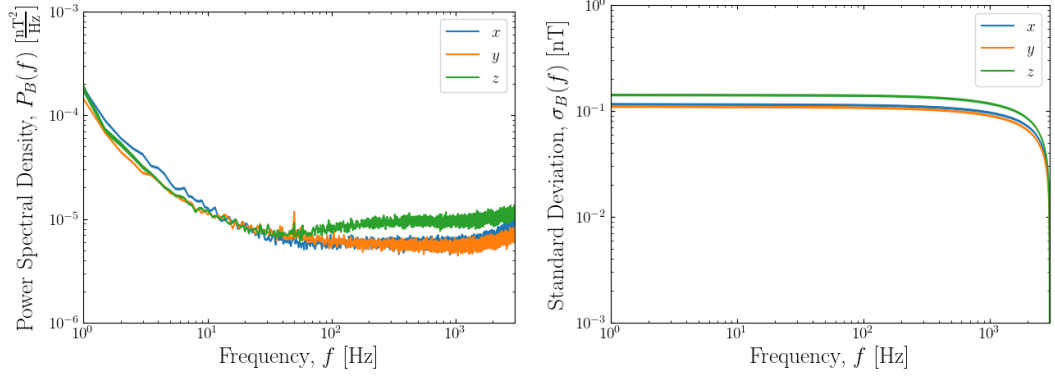
Table 6.4: Noise of each Mag-13 sensor at 1 Hz.



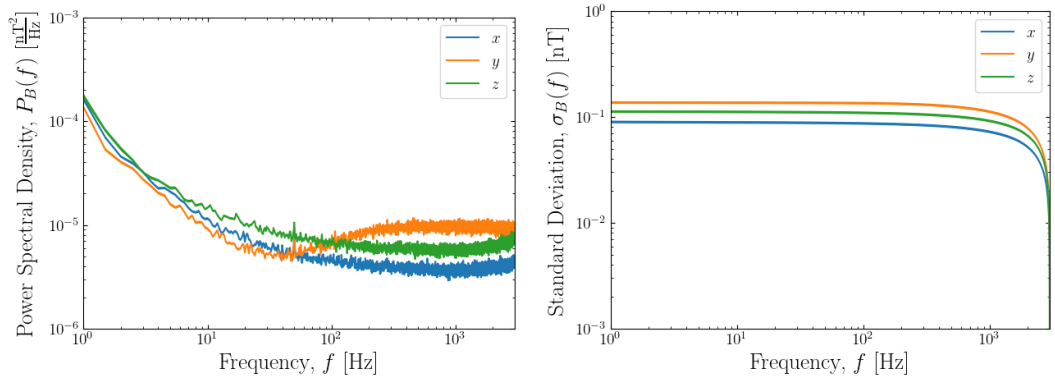
(a) Sensor 1.



(b) Sensor 2.



(c) Sensor 3.



(d) Sensor 4.

Figure 6.6: The PSD and standard deviation of the magnetic field vs frequency measured by each Mag-13 sensor in a magnetically shielded environment. These curves are the noise of each sensor.

Chapter 7

Passive Shielding

The main strategy proposed to mitigate SFs is *passive shielding*. A magnetic shield is used to prevent SFs from reaching the beam. The strategy is said to be ‘passive’ because it is not an active system, which tries to dynamically compensate the magnetic field.

This chapter describes the theory of magnetic shielding and experimentally validates a model. A mitigation strategy using mu-metal for passive shielding is proposed for CLIC.

7.1 Magnetic Shielding Theory

This section describes the factors that affect magnetic shielding and outlines a methodology for calculating the shielding factor.

7.1.1 Magnetic Materials

Absolute and Relative Permeability

The response of a material to a magnetic field is characterised by a *BH curve* expressed as

$$B(H) = \mu H, \tag{7.1}$$

where $B(H)$ is the *magnetic induction* (or *magnetic flux density*) in the material, H is an applied *magnetic field strength* and μ is the *permeability* (or *absolute permeability*) of the material. For free space, the permeability is denoted by $\mu_0 = 4\pi \times 10^{-7}$ H/m. The permeability of a material is often written as

$$\mu = \mu_r \mu_0, \quad (7.2)$$

where μ_r is a dimensionless constant known as the *relative permeability*.

A material can be classified in terms of its BH curve and permeability. A material with a linear BH curve, i.e. constant permeability, is either *paramagnetic* if $\mu_r < 1$ or *diamagnetic* if $\mu_r > 1$. A material with $\mu_r = 1$ is non-magnetic.

Ferromagnetic materials have $\mu_r \gg 1$ and their permeability is a function of applied magnetic field strength. This property is known as *hysteresis*. The BH curve and relative permeability of iron are shown in Figure 7.1.

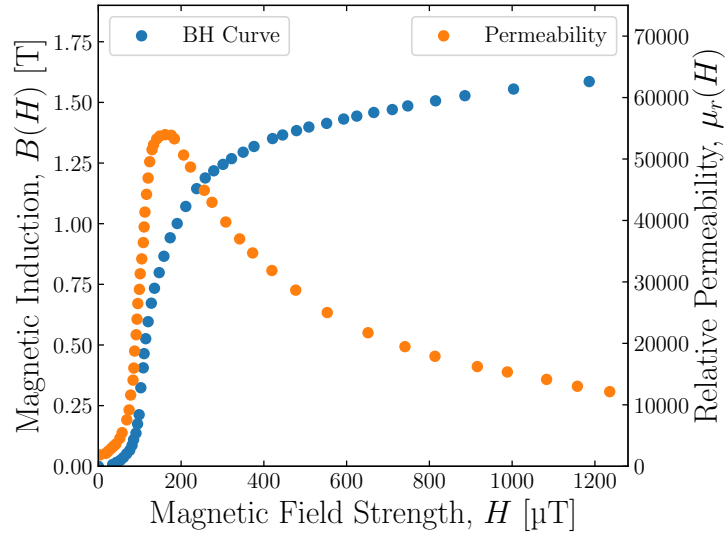


Figure 7.1: Magnetic induction (LH scale, blue) and relative permeability of iron (RH scale, orange) vs magnetic field strength [74]. This BH curve is known as an *initial magnetisation curve* and is measured starting from a demagnetised sample.

Hysteresis Loops

A *hysteresis loop* is the BH curve for a ferromagnetic material found by cycling through a range of magnetic field strengths. Figure 7.2 shows different types of hysteresis loops. To measure a major loop the magnetic field strength is increased until the material becomes *saturated*, which is when the magnetic induction no longer increases with the magnetic field strength. A minor loop occurs when the magnetic field strength performs a small oscillation around a central value.

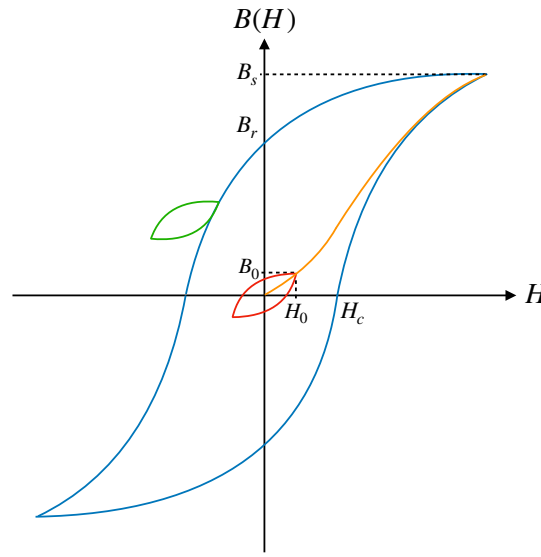


Figure 7.2: Illustration of different hysteresis loops. Magnetic induction (B) vs magnetic field strength (H). The orange curve is the initial magnetisation curve, the blue curve is a major loop and the green curve is a minor loop. The red curve shows the hysteresis loop in the Rayleigh region. H_c is known as the *coercive field* and B_r is known as the *remnant field*. B_s is the magnetic induction at saturation.

The Rayleigh Region

For magnetic field strengths that are much smaller than the coercive field (H_c in Figure 7.2) the material is said to be in the *Rayleigh region*. The shape of the hysteresis loop in this region is shown in Figure 7.2. In the Rayleigh region, the amplitude of the magnetic induction is [74]

$$B_0(H_0) = \mu_i H_0 + \nu H_0^2, \quad (7.3)$$

where μ_i is known as the *initial permeability* and ν is Rayleigh's constant. The hysteresis loop in the Rayleigh region for different magnetic field strengths is illustrated in Figure 7.3.

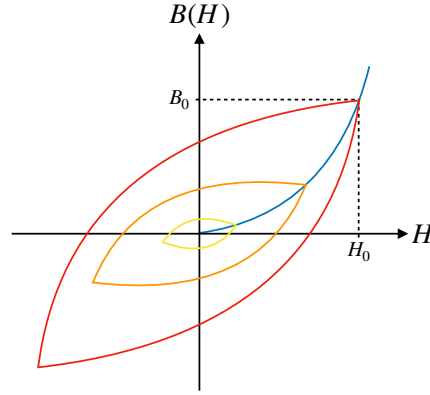


Figure 7.3: Illustration of hysteresis loops in the Rayleigh region with different magnetic field amplitudes. The blue curve is given by Equation (7.3).

The permeability of the material is given by

$$\mu(H_0) = \frac{B_0(H_0)}{H_0} = \mu_i + \nu H_0. \quad (7.4)$$

This is the appropriate permeability to use for a ferromagnetic material when it is exposed to a small-amplitude time-varying magnetic field.

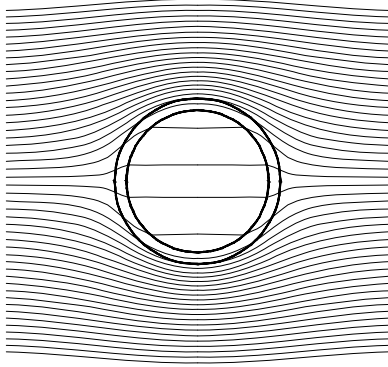
If the magnetic field is oscillating around a static offset, a minor hysteresis loop is mapped out. Provided the material is not close to saturation, the permeability of the material is the same as if it were in the Rayleigh region [86].

7.1.2 Shielding Mechanisms

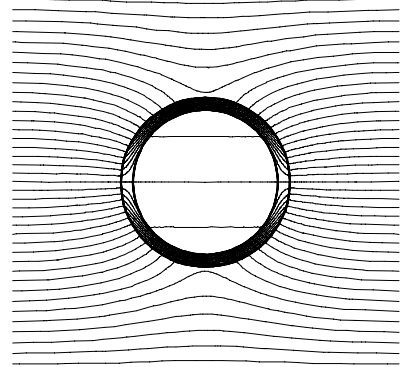
Magnetic shielding is described in [86, 87]. Figure 7.4 shows two different mechanisms for magnetic shielding:

- (a) **Flux shunting**: magnetic flux is diverted through the shield, away from the shielded region.
- (b) **Eddy-current cancellation**: eddy currents are induced by time-varying external

magnetic fields. These eddy currents generate a magnetic field that opposes the external magnetic field, which reduces the net magnetic field in the shielded region.



(a) Flux shunting.



(b) Eddy-current cancellation.

Figure 7.4: Cylindrical shields subject to a uniform magnetic field [87].

Both shielding mechanisms are important. A material can shield magnetic fields with both mechanisms simultaneously, but one mechanism is usually dominant. Static or low-frequency magnetic fields are usually shielded with the flux-shunting mechanism using a material with $\mu_r \gg 1$. Whereas, high-frequency magnetic fields can be shielded with the eddy-current cancellation mechanism using a material with a high electrical conductivity.

7.1.3 Shielding Factor and Transfer Function

Considering a magnetic shield exposed to an external magnetic field $H_e(t) = H_{e,0}e^{j2\pi ft}$, the internal magnetic field is $H_i(t) = H_{i,0}e^{j(2\pi ft+\phi)}$, where ϕ is a phase shift. The *shielding factor* is defined as

$$SHF = \frac{H_{e,0}}{H_{i,0}e^{j\phi}}, \quad (7.5)$$

and the transfer function is given by

$$T = \frac{1}{SHF} = \frac{H_{i,0}e^{j\phi}}{H_{e,0}}. \quad (7.6)$$

The transfer function depends on the frequency, amplitude and polarisation of the external magnetic field. It also depends on the geometry and material properties of the shield.

For simple shield geometries, it is possible to calculate the shielding factor by solving Maxwell's equations directly, analytical calculations can be found in [88, 89, 90, 91]. For more complex geometries numerical methods can be used to solve Maxwell's equations using the finite element method. Several commercial codes are available for this, e.g. COMSOL Multiphysics [92].

Cylindrical Shield in a Transverse Magnetic Field

Of interest to this work are cylindrical magnetic shields formed from multiple layers of different materials. This section outlines the methodology presented in [91] for calculating the shielding factor of multilayered cylindrical shields with transverse time-varying external magnetic fields. This model is valid for shields that are much smaller than the wavelength of the magnetic field. Shields with a diameter of a few centimetres are considered in this work. Therefore, this model is applicable for frequencies up to a few GHz.

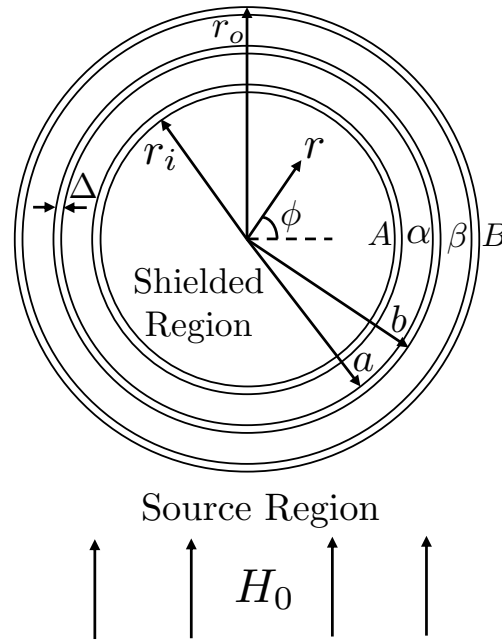


Figure 7.5: Cylindrical multilayer shield geometry.

Figure 7.5 shows the geometry of an infinitely long cylindrical multilayer shield with an imposed uniform time-varying magnetic field $H(t) = H_0 e^{j2\pi ft}$. Any individual layer has thickness Δ , permeability μ , electrical conductivity σ . The outer surface of the outermost

layer of the shield, labelled B , has radius r_o , and the inner surface of the innermost layer of the shield, labelled A , has radius r_i . The inner and outer surfaces of the layers in between are labelled α and β respectively and have inner and outer radii a and b respectively.

The shielding factor is calculated by computing the transmission of two physical quantities, namely the amplitude of the azimuthal component of the magnetic field H_ϕ and the amplitude of the radial component of the magnetic induction B_r , through each layer. This approach is known as the *transmission line method*. The azimuthal component of the magnetic field and radial component of the magnetic induction are defined on each surface, H_ϕ^s and B_r^s denote these quantities on surface s .

Transfer relations are defined to transmit H_ϕ^s and B_r^s through a layer. These are

$$\begin{pmatrix} H_\phi^\alpha \\ B_r^\alpha/\mu_0 \end{pmatrix} = \begin{pmatrix} T_{11} & T_{12} \\ T_{21} & T_{22} \end{pmatrix} \begin{pmatrix} H_\phi^\beta \\ B_r^\beta/\mu_0 \end{pmatrix}, \quad (7.7)$$

where

$$\begin{aligned} T_{11} &= (\gamma a) \{ I_1'(\gamma a) K_1(\gamma b) - I_1(\gamma b) K_1'(\gamma a) \} \\ T_{12} &= \frac{\mu_0}{\mu} (\gamma b)^2 \{ I_1'(\gamma b) K_1'(\gamma a) - I_1'(\gamma a) K_1'(\gamma b) \} \\ T_{21} &= \frac{\mu}{\mu_0} \frac{\gamma b}{\gamma a} \{ I_1(\gamma a) K_1(\gamma b) - I_1(\gamma b) K_1(\gamma a) \} \\ T_{22} &= \frac{(\gamma b)^2}{\gamma a} \{ I_1'(\gamma a) K_1(\gamma a) - I_1(\gamma a) K_1'(\gamma b) \}, \end{aligned} \quad (7.8)$$

$\gamma = \sqrt{\pi f \mu \sigma} (1 + j)$ is the complex wavenumber, I_1 is the first-order modified Bessel function of the first kind, K_1 is the first-order modified Bessel function of the second kind, I_1' is the derivative of I_1 and K_1' is derivative of K_1 .

For each surface a *magnetic impedance* is defined as

$$Z^s = \frac{B_r^s}{\mu_0 H_\phi^s}. \quad (7.9)$$

Z^s is transmitted through a layer with

$$\begin{aligned} Z^\alpha &= \frac{T_{21} + T_{22}Z^\beta}{T_{11} + T_{12}Z^\beta}, \\ Z^\beta &= \frac{T_{11}Z^\alpha - T_{21}}{T_{22} - T_{12}Z^\alpha}. \end{aligned} \quad (7.10)$$

The calculation is performed in a number of steps:

1. The calculation begins at the surface of the shielded region where the magnetic impedance is set as $Z^A = 1$. Equation (7.10) is used to transmit the impedance from the shielded region to the source region. The impedance at the surface of the source region is denoted by Z^B .
2. Z^B is used to calculate the azimuthal component of the magnetic field and radial component of the magnetic induction at the surface of the source region. Both of these quantities are normalised by H_0 . These quantities are given by

$$\frac{H_\phi^B}{H_0} = \frac{2}{1 + Z^B} \quad (7.11)$$

and

$$\frac{B_r^B}{\mu_0 H_0} = Z^B \frac{H_\phi^B}{H_0}. \quad (7.12)$$

3. The inverse relations of Equation (7.7) is used to transmit H_ϕ^B/H_0 and B_r^B/H_0 from the surface of the source region to the surface of the shielded region to give H_ϕ^A/H_0 and B_r^A/H_0 .
4. The transfer function is calculated as

$$T = \frac{H_\phi^A}{H_0} = \frac{B_r^A}{\mu_0 H_0}. \quad (7.13)$$

7.2 Applications in Accelerators

ILC Superconducting Cavities

The performance of a cavity is characterised by the *quality factor* [11]

$$Q_0 = \frac{G}{R_s}, \quad (7.14)$$

where G is a geometric factor and R_s is the surface resistance of the cavity. The quality factor describes how long energy is stored in a cavity.

Cavities in the ILC are manufactured using the superconducting material niobium, which needs to be cooled down to 2 K for superconductivity. If a static magnetic field is present during the cool down, magnetic flux becomes trapped inside the material, which increases the surface resistance and reduces the quality factor.

The required quality factor for the ILC cavities is $Q_0 \geq 10^{10}$ [93]. To achieve this, the ambient magnetic field experienced by the cavities must not exceed 0.5 μT [93]. The Earth's magnetic field has a static component between 20-70 μT [94]. Therefore, a shielding factor of 100 must be achieved with a magnetic shield.

A shielding factor of 100 is an achievable goal with known magnetic shielding materials. However, the concern for this application is the effectiveness of shielding at very low temperatures. Materials for this application are described in [95, 96, 97]. In these papers, the effect of temperature and mechanical stress on shielding is studied.

HL-LHC Crab Cavities

The luminosity of the LHC will be increased in an upgrade known as the *High-Luminosity LHC* (HL-LHC). The HL-LHC utilises RF crab cavities to compensate the luminosity loss from a crossing angle.

The HL-LHC crab cavities operate at the same temperature as the ILC cavities and suffer

the same problem of magnetic flux trapping during cooldown. A material called *cryophy* was developed at CERN to shield the HL-LHC crab cavities from external magnetic fields [98]. The requirement for HL-LHC crab cavities is a static magnetic field of less than 1 μT reaches the crab cavity surface. The maximum expected static external magnetic field was estimated to be 200 μT from measurements at the *Super Proton Synchrotron* (SPS) at CERN [98]. Therefore, the shielding factor must be 200.

CLIC

As described in Chapter 5, CLIC has SF tolerances on the order of 0.1 nT. Measurements of SFs in accelerator environments are presented in Chapter 11. Dynamic magnetic fields with amplitudes up to 100 nT can be expected in an accelerator environment. Therefore, special mitigation will be required to ensure the SF experienced by the CLIC beam is within the tolerance.

Passive shielding is the proposed strategy for mitigation. A shielding factor of approximately 1,000 is required. A variety of materials are available. Any electrically conducting material will provide some shielding of dynamic magnetic fields via eddy-current cancellation. However, this mechanism is only effective at shielding high frequencies. Magnetic materials are a good choice because they can shield low-frequency magnetic fields via flux shunting.

Superconducting materials act as perfect magnetic shields. Magnetic shielding with superconductors is described in [99]. However, these materials need to be cooled down to very low temperatures to be superconducting. CLIC operates at room temperature, which makes the use of superconducting materials unappealing.

7.3 The LHC Beam Screen

The LHC utilises superconducting bending magnets, which need to be cooled to 1.9 K to operate [100]. SR from the LHC beam can heat the magnet and eliminate the superconductivity. The magnetic field generated by the magnet is then lost. This process is known as a *quench* and results in a beam dump. The LHC beam screen (shown in Figure 7.6) is used to intercept SR to prevent a quench.

The LHC beam screen has an inner diameter of 4.4 cm. It consists of 1 mm of steel and an inner copper coating of 50-100 μm . The specification for the beam screen is that its permeability does not exceed 1.005 [100]. Therefore, the beam screen is effectively non-magnetic. The electrical conductivity of the materials in the LHC beam screen is shown in Table 7.1. The LHC beam screen acts as a magnetic shield via eddy-current cancellation.



Figure 7.6: Image of the LHC beam screen.

Material	Electrical Conductivity, σ [S/m]
Steel	1.46×10^6
Copper	5.96×10^7

Table 7.1: Electrical conductivity at room temperature of materials in the LHC beam screen [101].

Transfer Function

Magnetic shielding due to the LHC beam screen was measured using a set of Helmholtz coils to produce a magnetic field excitation at a precise frequency and amplitude.

The transfer function of the LHC beam screen is shown in Figure 7.7. The LHC beam screen is an effective shield for high-frequency magnetic fields. Copper has a much higher electrical conductivity compared to steel. Consequently, virtually all of the shielding originates from the copper layer.

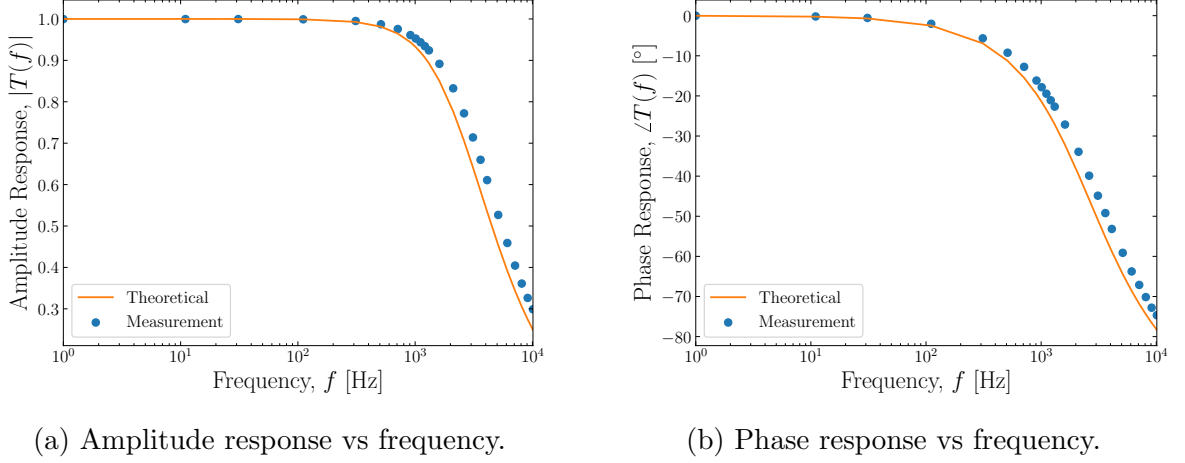


Figure 7.7: Transfer function of the LHC beam screen: measurement (blue) and a theoretical calculation (orange) using Equation (7.16) assuming 50 μm of copper. Errors bars are too small to be seen.

For non-magnetic materials, the transfer relations in Equation (7.8) are simplified to

$$\begin{aligned}
 T_{11} &= 1 \\
 T_{12} &= -j2\pi f \mu_0 \sigma r \Delta \\
 T_{21} &= 0 \\
 T_{22} &= 1,
 \end{aligned} \tag{7.15}$$

and the transfer function for a single layer can be written as

$$T(f) = \frac{1}{1 + j\pi f \mu_0 \sigma a \Delta}. \tag{7.16}$$

The transfer function decreases with frequency and is inversely proportional to the electrical conductivity σ , inner radius a and thickness Δ .

The measurement in Figure 7.7 is compared to a theoretical calculation with Equation (7.16) assuming 50 μm of copper. There is an excellent agreement between the mea-

surement and theoretical calculation.

Impact on the LHC

Protons in the LHC do not emit significant amounts of SR. As a result, the LHC does not have any significant damping mechanisms to reduce emittance. This makes the preservation of transverse emittance important. A feedback system [12] is used to correct the transverse beam position to minimise emittance growth from filamentation. Sources of emittance growth in the LHC must be understood for its operation and to aid the design of future upgrades.

Power supply ripples are one source of emittance growth. These lead to magnetic field ripples in the bending magnets. Perturbations to the beam at harmonics of 50 Hz up to the kHz range have been observed in [102]. These harmonics were attributed to power supply ripples. However, the impact of the LHC beam screen was not included in the study. The LHC beam screen is an effective shield for high-frequency magnetic fields, which should suppress magnetic field ripples in the kHz range. This suggests the high-frequency harmonics may not arise from power supply ripples and further studies are required to understand the impact of power supply ripples on the LHC.

7.4 Soft Magnetic Materials

Soft magnetic materials are often used for magnetic shielding applications. They provide shielding via the flux-shunting mechanism as well as eddy-current cancellation.

Magnetic materials have an advertised value for permeability. These values are rough estimates and vary on a sample-to-sample basis. Additionally, magnetic properties are affected by mechanical stress and deformation. Soft magnetic materials are often heat-treated after being bent into their final shape to remove the effects of mechanical stress. This process is known as *annealing* and heats the material enough to alter its internal crystal structure.

Annealing allows regions of magnetisation, known as *magnetic domains*, to move freely [74]. As a result, the permeability of the material is increased.

Three different materials were tested. Soft iron (99.9% iron) and two different iron-nickel alloys: *supra 36* (64% iron, 36% nickel) and *mu-metal* (approximately 20% iron, 80% nickel).

7.4.1 Soft Iron

A high purity (99.9%) soft iron cylinder produced by AK Steel Corporation, USA [103] was used in measurements. The geometry and advertised specifications of this cylinder are summarised in Table 7.2.

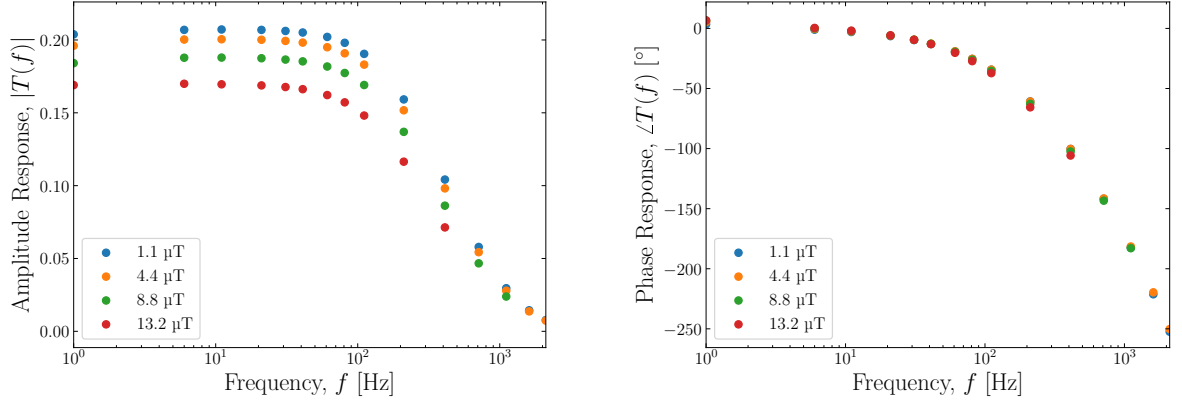
Parameter	Value
Inner diameter	5 cm
Thickness	1 mm
Length	50 cm
Initial permeability	300-500
Maximum relative permeability	3,500-8,000
Coercive field	75-150 μT
Magnetic induction at saturation	2.15 T

Table 7.2: Geometry and specifications of an iron cylinder produced by AK Steel Corporation, USA.

The transfer function of this cylinder measured with different external magnetic field amplitudes is shown in Figure 7.8. There is a clear dependence on the external field amplitude visible at low frequencies, where the shielding improves with external field amplitude. The phase response of the iron cylinder appears to be independent of external field amplitude.

Figure 7.9 shows the measured amplitude response as a function of the external magnetic field amplitude. It is clear the amplitude response tends to a constant as the external magnetic field is decreased.

The model described in Section 7.1.3 can be used to fit a permeability to the measurement of a transfer function. Figure 7.10 shows the relative permeability as a function of external magnetic field amplitude found by fitting the measured transfer function to the model. The



(a) Amplitude response vs frequency.

(b) Phase response vs frequency.

Figure 7.8: Transfer function of the iron cylinder with different external magnetic field amplitudes. Error bars are too small to be seen.

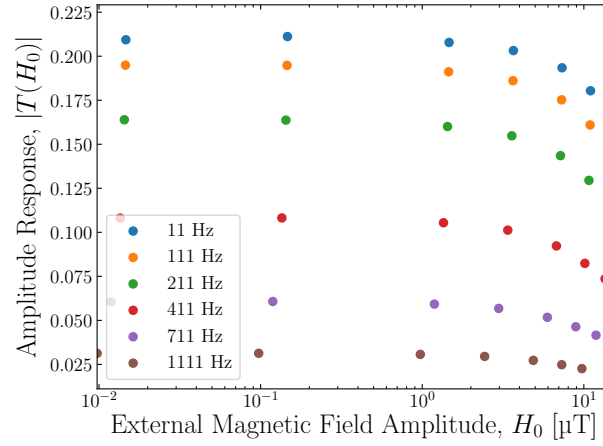


Figure 7.9: Amplitude response at different frequencies of the iron cylinder vs external magnetic field amplitude. Error bars too small to be seen.

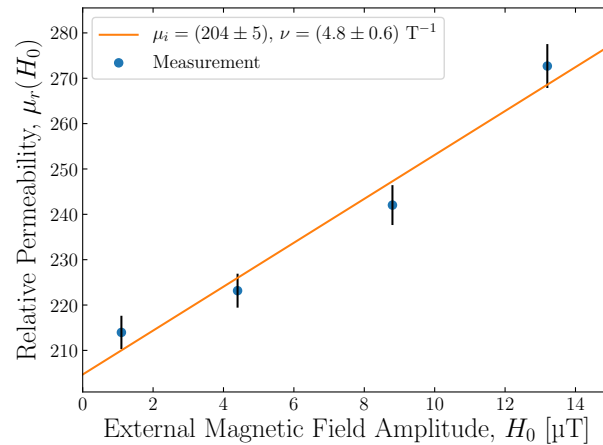


Figure 7.10: Relative permeability of the iron cylinder vs external magnetic field amplitude: measurement (blue) and a straight line fit (orange).

initial permeability is extrapolated by fitting a straight line to the relative permeability.

An initial permeability of $\mu_i = (204 \pm 5)$ was measured for this iron cylinder. This is somewhat below the advertised value of 300-500.

7.4.2 Supra 36

A supra 36 cylinder produced by Aperam, Luxembourg [104] was used in measurements. The geometry and specifications of this cylinder are summarised in Table 7.3. The transfer function of this cylinder measured with different external magnetic field amplitudes is shown in Figure 7.11. The shielding of the cylinder improves with external magnetic field amplitude. The phase response is independent of the external magnetic field amplitude.

Parameter	Value
Inner diameter	5 cm
Thickness	1 mm
Length	50 cm
Initial permeability	7,000
Maximum relative permeability	30,000
Coercive field	7.5 μT
Magnetic induction at saturation	1.3 T

Table 7.3: Geometry and specifications of a supra 36 cylinder produced by Aperam, Luxembourg.

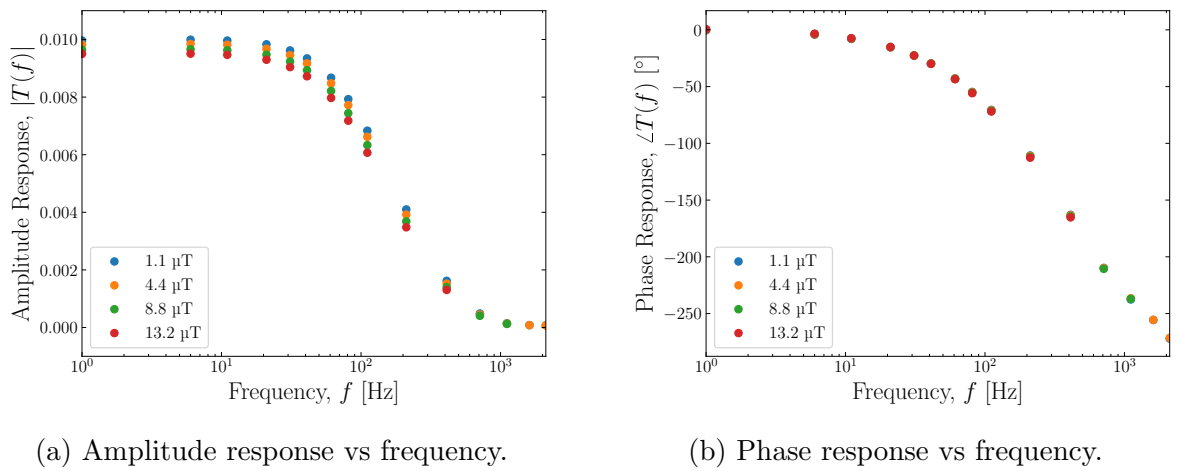


Figure 7.11: Transfer function of the supra 36 cylinder with different external magnetic field amplitudes. Error bars are too small to be seen.

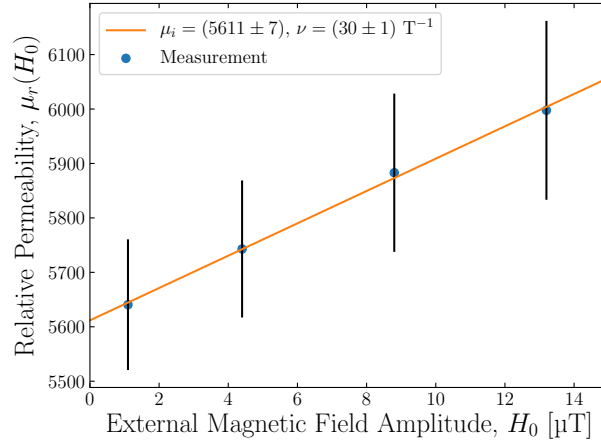


Figure 7.12: Relative permeability of the supra 36 cylinder vs external magnetic field amplitude: measurement (blue) and a straight line fit (orange).

Figure 7.12 shows the permeability fitted to each amplitude response in Figure 7.11. There is a linear relationship between the external magnetic field amplitude and permeability. The initial permeability of the supra 36 cylinder is $\mu_i = (5,611 \pm 7)$.

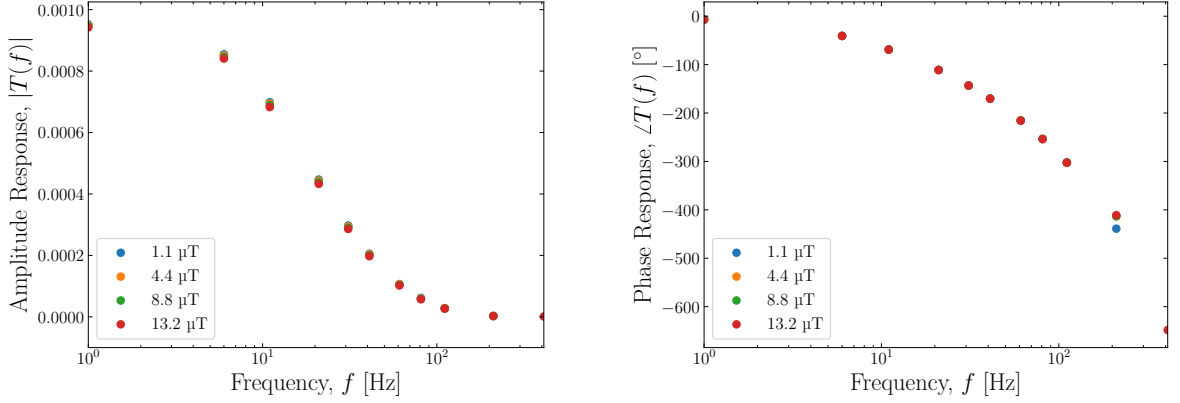
7.4.3 Mu-Metal

A mu-metal cylinder produced by the Magnetic Shield Corporation, USA [105] was used in measurements. The geometry and advertised specifications of this cylinder are summarised in Table 7.4. The transfer function of this cylinder measured with different external magnetic field amplitudes is shown in Figure 7.13. The transfer functions look very similar.

Parameter	Value
Inner diameter	5 cm
Thickness	1 mm
Length	50 cm
Initial permeability	50,000
Maximum relative permeability	250,000
Coercive field	2 μT
Magnetic induction at saturation	0.74 T

Table 7.4: Geometry and specifications of a mu-metal cylinder produced by the Magnetic Shield Corporation, USA.

Figure 7.14 shows the permeability fitted to each amplitude response in Figure 7.13. The



(a) Amplitude response vs frequency.

(b) Phase response vs frequency.

Figure 7.13: Transfer function of the mu-metal cylinder with different external magnetic field amplitudes. Error bars are too small to be seen.

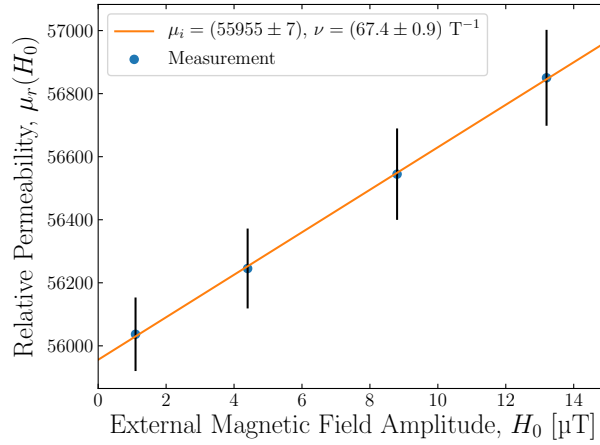


Figure 7.14: Relative permeability of the mu-metal cylinder vs external magnetic field amplitude: measurement (blue) and a straight line fit (orange).

relative change in permeability over the external magnetic field range measured is small compared to the soft iron and supra 36 cylinders. However, there is a linear relationship that is apparent. The initial permeability of the mu-metal cylinder is $\mu_i = (55,955 \pm 7)$, which is above the advertised value of $\mu_i = 50,000$.

The tightest tolerances discussed in Chapter 5 were on the order of 0.1 nT. An objective of this work is to demonstrate a magnetic field amplitude of 0.1 nT inside a shield. Figure 7.15 shows the internal magnetic field amplitude as a function of frequency for an external magnetic field of 1.1 μT . An internal field of less than 0.1 nT can be realised with a mu-metal shield.

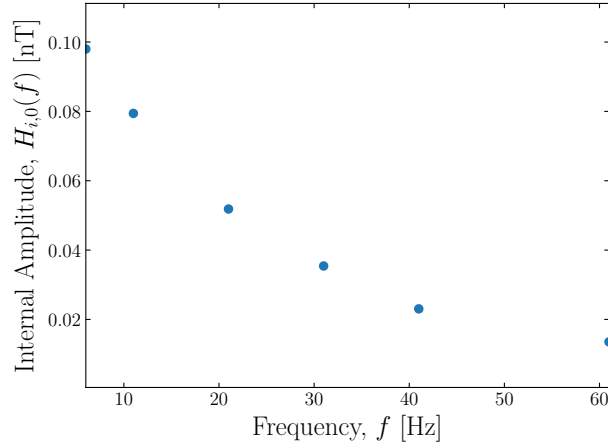


Figure 7.15: Internal magnetic field amplitude vs frequency measured with the mu-metal cylinder. An external magnetic field amplitude of $1.1 \mu\text{T}$ was used. Error bars are too small to be seen.

Mu-Metal Foils

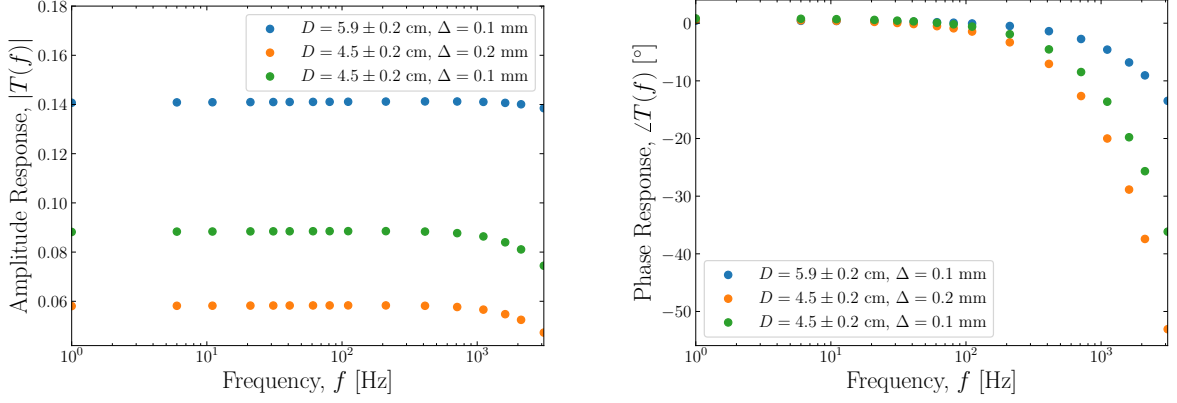
Mu-metal is also available in thin foils, typically of thicknesses between 0.1 and 0.5 mm. These foils are annealed and advertised as retaining their magnetic properties after slight deformation. The advantage of the foil is that it can be simply wrapped around a manufactured beam pipe. That is it would not be necessary to include the mu-metal shield as part of the beam pipe design. Instead, the mu-metal shield can be incorporated into particular sections of CLIC after its construction if required.

A set of three cylindrical shields of varying diameter D and thickness Δ were formed from a mu-metal foil provided by the Magnetic Shield Corporation, USA [105]. This is the same material that is used to create the mu-metal cylinder in the previous section. Figure 7.16 shows the transfer function of shields formed from a mu-metal foil.

Diameter, D [cm]	Thickness, Δ [mm]	Relative Permeability, μ_r
5.9 ± 0.2	0.1	$3,670 \pm 2$
4.5 ± 0.2	0.2	$3,602 \pm 2$
4.5 ± 0.2	0.1	$4,660 \pm 50$

Table 7.5: Measured permeability of three shields formed from a mu-metal foil.

Table 7.5 shows the permeability fitted to each amplitude response. The foils have a relative permeability less than 5,000, which is very poor for mu-metal. The permeability has



(a) Amplitude response vs frequency.

(b) Phase response vs frequency.

Figure 7.16: Transfer function of three shields formed from a mu-metal foil. An external magnetic field amplitude of $1.1 \mu\text{T}$ was used. The 0.2 mm thick shield was formed with two layers of foil. Error bars are too small to be seen.

likely been damaged by deforming the cylinder when rolling the mu-metal foil to produce the shield.

It has been reported in [96] the permeability of mu-metal is extremely sensitive to mechanical stress and deformation. The damage is reversed by re-annealing. This highlights care must be taken with the shields to ensure good performance. Improvements of an order of magnitude have been reported after re-annealing, which would mean the expected value of 50,000 could potentially be reached after re-annealing.

A simple model for the shielding factor of mu-metal is presented in [106]. For a single layer cylinder the amplitude response is given by

$$|T| = \frac{D}{\mu_r \Delta}. \quad (7.17)$$

For small external magnetic field amplitudes, the relative permeability in Equation (7.17) is replaced with the initial permeability. The measured amplitude response for the different mu-metal foils is roughly consistent with Equation (7.17).

7.5 Mitigation of Stray Magnetic Fields

7.5.1 Strategy

Shielding Sources

A possible strategy would be to target SF sources. Either by moving them away from the beam or surrounding them with a magnetic shield. Because the SF amplitude is larger near the source, the shields could be more effective.

Shielding the sources would require identifying them and a dedicated study of whether surround them with a shield is viable. Some sources may have a difficult geometry to shield. Mu-metal shields will also need to be annealed. Some elements cannot be heated, for example, the ML cavities in CLIC cannot be heat treated [42]. A safer approach is to shield the beam.

Shielding the Beam

The SF amplitude experienced by the beam must be within the tolerances described in Chapter 5. There are four sensitive regions: the VT and LTL in the RTML and the ECS and FFS in the BDS. An effective mitigation can be achieved by just targeting these sections.

The proposed strategy is to surround sensitive regions with a 1 mm mu-metal layer. Only the drifts in these sections need to be shielded. Section 10.1 presents requirements for the temporal stability of magnets. The required stability is larger than the typical SF amplitude in accelerator environments (see Chapter 11). A SF will also be drawn in the iron core of the magnet, away from the beam. Therefore, shielding the regions with magnets is not necessary.

Factors Affecting Performance

A relative permeability of 50,000 for mu-metal is assumed. This is a realistic estimate based on the measurements in Section 7.4.3. It was observed in [96] that the shielding factor of a mu-metal shield degrades at very low (superconducting) temperatures. Because CLIC is at room temperature, the degradation of shielding at low temperatures is not a concern.

As discussed in Section 7.4.3, very thin layers of mu-metal suffer from a loss in permeability due to mechanical stress and deformation. The reduction in permeability can be reversed by re-annealing the material. However, this requires the ability to anneal the mu-metal shield in its final form in the tunnel. Mu-metal requires very high annealing temperatures, above 1000 °C [105]. Instead of re-annealing thin layers of mu-metal, a minimum thickness of 1 mm is advised by this work. The measurements in Section 7.4.3 suggest that this thickness is enough to withstand the impact of mechanical stress on permeability.

7.5.2 Transfer Functions

The impact of a mitigation technique can be described using a transfer function $T_M(f)$, which acts on the SF PSD $P_B(f)$ to give a new effective PSD

$$P_{B,M}(f) = |T_M(f)|^2 P_B(f). \quad (7.18)$$

CLIC Beam Pipe

A beam in an accelerator is surrounded by a metallic tube known as a *beam pipe*. The purpose of the beam pipe is to contain the vacuum. The diameter and shape of the beam pipe depend on the beam. Often, it is cylindrical with a diameter of a few centimetres. Typically, beam pipes are composed of multiple layers. The beam pipe must be mechanically rigid and should withstand stress. Steel is often used to provide this. Usually, there is also an inner copper coating to mitigate long-range wakefields.

A beam pipe may attenuate external magnetic fields, preventing them from reaching the beam. Beam pipes run through the aperture of magnets and should not impede the field from the magnet reaching the beam. Studies of eddy-current cancellation in beam pipes are presented in [107] and [108]. Theoretical calculations of the magnetic shielding of the HL-LHC beam screen are presented in [109].

SF measurements in this work have been performed outside of beam pipes. Therefore, to calculate the SF experienced by the beam a transfer function for a beam pipe must be known. A reasonable model for a CLIC beam pipe is a steel cylinder of thickness 1 mm and an inner copper coating of thickness 20 μm .

The transfer function of the CLIC beam pipe, calculated theoretically with the methodology described in Section 7.1.3, is shown in Figure 7.17. The copper and steel have a permeability of μ_0 and the electrical conductivities in Table 7.1. The beam pipe has virtually no effect on frequencies below 1 kHz. However, the beam pipe attenuates SFs above 10 kHz well.

The transfer function in Figure 7.17 will be used for the entire machine. In reality, the beam pipe radius varies along the machine. 1 cm is the minimum beam pipe radius. The shielding factor improves with increasing radius, therefore assuming this transfer function for the entire machine is a pessimistic approach.

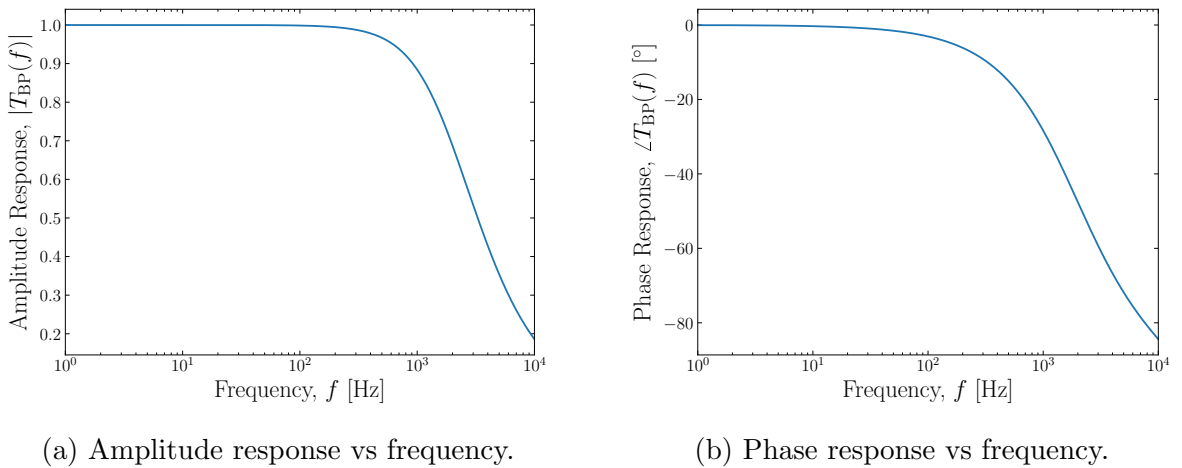


Figure 7.17: Transfer function of the CLIC beam pipe. The beam pipe consists of 1 mm of steel and 20 μm of copper with a inner radius of 1 cm.

Main Linac Cavities

The ML cavities in CLIC are formed from copper walls approximately 2 cm thick, which will have a significant effect on the external magnetic field. The transfer function of the cavity walls, calculated theoretically with the methodology outlined in Section 7.1.3, is shown in Figure 7.18. The cavity walls attenuate SFs above 100 Hz well.

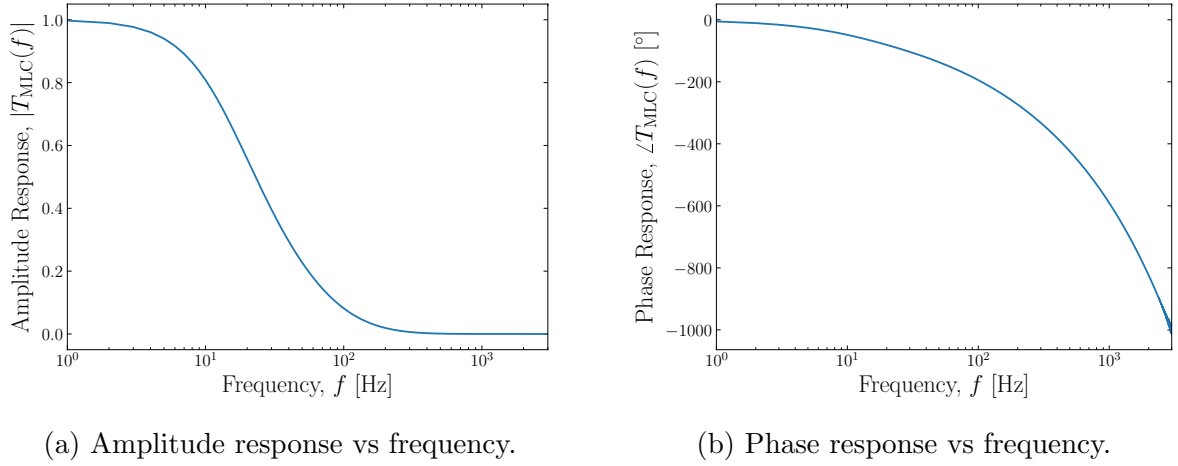


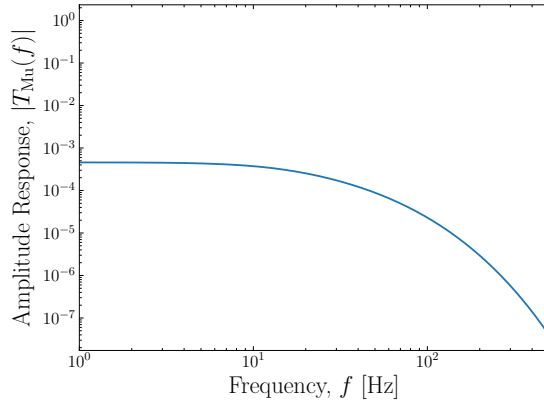
Figure 7.18: Transfer function of the ML cavity walls. The cavity was modelled as a copper cylinder of thickness 2 cm and inner radius 1 cm.

Mu-Metal

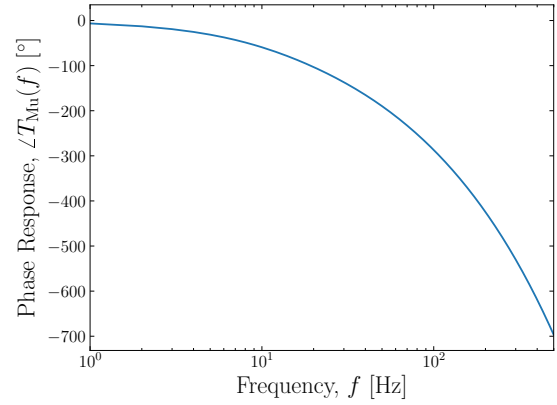
The permeability is a key parameter that determines the transfer function of a magnetic material. The model described in Section 7.1.3 characterises the permeability with a single number. Due to the dependence of the permeability on the amplitude of the magnetic field, it is highly non-uniform across a shield. Accurate shielding calculations require an EM finite element method simulation to include non-uniformity in permeability and hysteresis effects. However, instead of this, a simplified approach will be used to assume the permeability is equal to the initial permeability across the entire shield. This is a pessimistic approach because the initial permeability is the lowest value the permeability can take. This approach greatly simplifies the calculation of the transfer function.

The transfer function of a 1 mm mu-metal layer, calculated using the methodology outlined in Section 7.1.3, is shown in Figure 7.19. A relative permeability of 50,000 and electrical

conductivity of $1.7 \times 10^6 \text{ S/m}$ [105] was used for the mu-metal. The mu-metal layer is a very effective magnetic shield, which can provide a reduction of at least 1,000 in SF amplitude at all frequencies.



(a) Amplitude response vs frequency.



(b) Phase response vs frequency.

Figure 7.19: Transfer function of a mu-metal cylinder with an inner radius of 1 cm and a thickness of 1 mm. A relative permeability of 50,000 was used for the mu-metal.

Chapter 8

Natural Stray Magnetic Fields

Natural SFs are those from non-man-made objects. These were discussed at the Mini-Workshop on the Impact of Stray Fields on Accelerators at CERN in October 2017. An outcome of this workshop was a review of natural sources [110]. The most important natural sources are described below.

8.1 The Geomagnetic Field

The Earth's magnetic field, referred to as the *geomagnetic field*, is the main natural source [94]. The geomagnetic field varies across a wide range of timescales, from milliseconds to millions

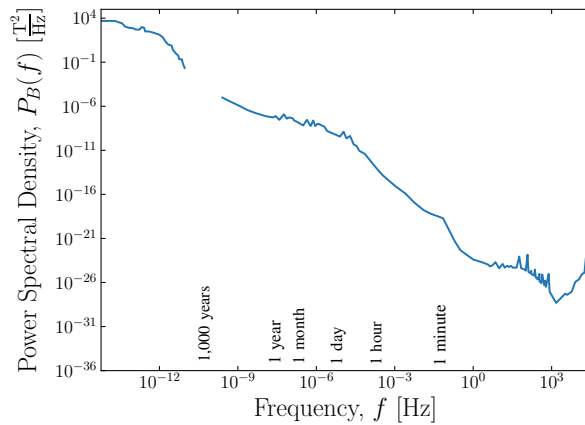


Figure 8.1: PSD vs frequency of natural magnetic field variations [111].

of years. The PSD of natural magnetic field variations is shown in Figure 8.1. The PSD decreases roughly as $1/f^2$.

Penetration into the Earth

The geomagnetic field is usually measured on the Earth's surface. However, the majority of the CLIC main beam is housed 100 m underground. The Earth attenuates EM waves due to the *skin effect* [9]. The magnetic field amplitude underground is given by

$$B(d) = \frac{B_S}{\alpha(d, f)} \quad (8.1)$$

where d is the depth, B_S is the magnetic field amplitude on the surface and $\alpha(d, f)$ is an attenuation factor,

$$\alpha(d, f) = \exp\left(\frac{d}{\delta(f)}\right), \quad (8.2)$$

where $\delta(f)$ is the skin depth (see Equation (1.2)).

The skin depth depends on the magnetic permeability and electrical conductivity of the Earth. These properties are determined by the local geology. For the CERN site, the magnetic permeability is $\mu \approx \mu_0$, where μ_0 is the permeability of free space, i.e. the site is approximately non-magnetic [94]. A reasonable estimate for the electrical conductivity on the CERN site is $\sigma = 10 \text{ mS/m}$ [94].

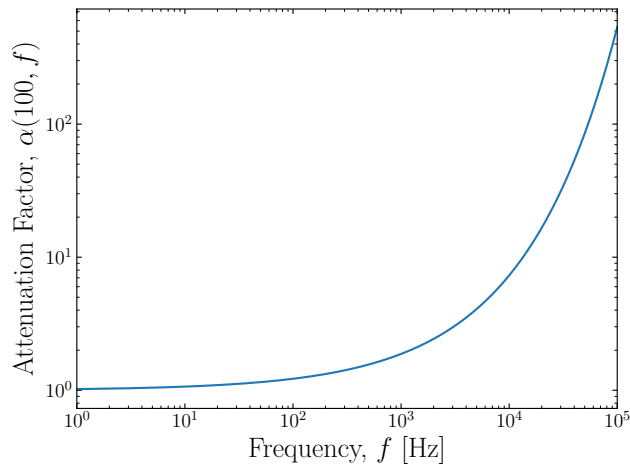


Figure 8.2: Magnetic field attenuation due to the Earth at a depth of 100 m vs frequency.

Figure 8.2 shows the attenuation factor 100 m underground due to the skin effect. Below 1 kHz, the attenuation factor is close to one. Therefore, one can assume a similar magnetic field is observed on the surface and underground.

8.2 Geomagnetic Storms

Short-term variations on timescales of seconds to days arise from an interaction between the sun and geomagnetic field, referred to as *solar-terrestrial interactions*. The amplitude of these variations can range from pT to μ T.

Geomagnetic storms represent solar-terrestrial interactions with the largest amplitude. They typically last from a few hours to days. The occurrence of these storms varies seasonally and with the solar cycle. On average, minor storms occur on a monthly basis and large storms occur less than once a month.

The amplitude of a geomagnetic storm depends strongly on the latitude. At latitudes similar to the CERN site, large storms typically generate geomagnetic field variations of a few hundred nT. However, these variations are over timescales of minutes to days, so they are slow compared to the repetition frequency of the CLIC beam. Such SFs are mitigated with a beam trajectory feedback system (described in Section 4.2).

Power Spectral Density

A representative geomagnetic storm was measured on the 8th June, 2014 at a geomagnetic observatory in Tihany, Hungary, which has a similar latitude and geomagnetic environment to CERN. The sampling frequency for this measurement was 128 Hz. Using this measurement and the orientation of CLIC with respect to the sensor, the SF in the horizontal and vertical direction with respect to the beam was calculated. The PSD of the SF is shown in Figure 8.3.

The PSD in Figure 8.3 describes the amplitude of SFs from a geomagnetic storm on the Earth's surface. The same amplitude is assumed in the tunnel. The PSD of the SF

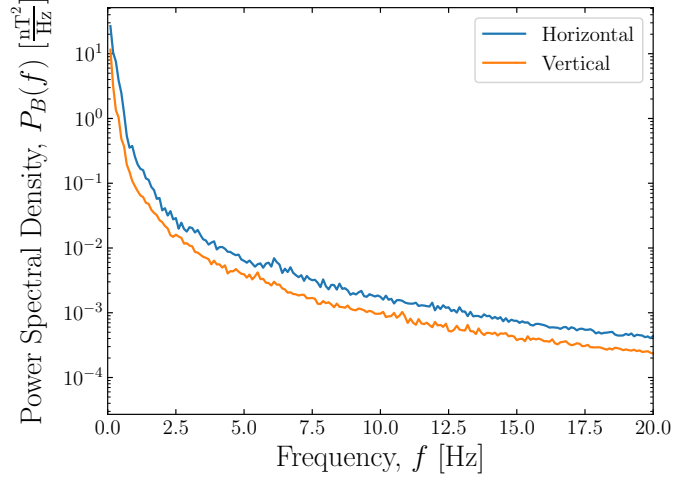


Figure 8.3: PSD vs frequency of a geomagnetic storm.

experienced by the beam is calculated by applying the transfer function of the CLIC beam pipe $T_{BP}(f)$ (shown in Figure 7.17) to the PSD. For the ML cavities, $T_{MLC}(f)$ (shown in Figure 7.18) is used instead.

To include the effect of a beam trajectory feedback system, $T_{FB}(f)$ (shown in Figure 4.2) is applied to the PSD. A gain of $m = 2.5$ was used for the feedback system, which is the same gain used in GM simulations.

Generator

To calculate the SF, the PSD is split into a number of independent modes. The amplitude of each mode is given by

$$a_i = \sqrt{2}\sigma_{B,i} = \sqrt{2 \int_{f_i}^{f_{i+1}} P_{B,M}(f) df} \approx \sqrt{2P_{B,M}(f_i)\Delta f}, \quad (8.3)$$

where $\sigma_{B,i}$ is the standard deviation of mode i , $P_{B,M}(f)$ is the PSD including the impact of a mitigation technique and $\Delta f = f_{i+1} - f_i$. The SF at time t is the summation of each mode,

$$B(t) = \sum_{i=1}^N a_i \cos(2\pi f_i t + \phi_i), \quad (8.4)$$

where N is the number of modes and ϕ_i is a uniformly distributed random number between 0 and 2π . The same $B(t)$ is simulated across the entire accelerator. The SF kick is calculated with Equation (5.11) taking into account the beam direction with respect to the SF.

Luminosity Loss

Table 8.1 shows the luminosity loss with different mitigation techniques. Two scenarios were simulated: using STE, which only includes the emittance growth from static imperfections, and NTE, which simulates nominal beam parameters.

Without mitigation and using NTE there is a significant luminosity loss of 8.1%. The beam trajectory feedback system is extremely effective at mitigating luminosity loss. Using NTE, the luminosity loss is reduced to 0.1%. This is because the feedback system is good at correcting low-frequency SFs. With a feedback system, the impact of a geomagnetic storm is negligible and should not pose a concern for CLIC.

Mitigation	Luminosity Loss, $\Delta\mathcal{L}/\mathcal{L}_0$ [%]
Using STE	
None	21
Feedback System	0.02
Using NTE	
None	8.1
Feedback System	0.01

Table 8.1: Luminosity loss during a representative geomagnetic storm. Values are expressed as a percentage of Equation (3.3) for NTE or Equation (3.5) for STE. The error on each value is less than 0.1%.

8.3 Sources Above 1 Hz

The beam trajectory feedback system is very effective at suppressing the impact of SFs at low frequencies, particularly below 1 Hz. The geomagnetic storm PSD in Figure 8.3 contains one significant peak at a very low frequency close to zero, which is suppressed by the feedback

system.

SFs at frequencies above 1 Hz are not suppressed by the beam trajectory feedback system. In fact, the impact of SFs between 4-25 Hz is amplified by the feedback system. Natural SFs above 1 Hz are described below.

Geomagnetic Pulsations

Geomagnetic pulsations are waves in the geomagnetic field. Geomagnetic pulsations with sinusoidal variations between 0.2-5 Hz are termed *Pc1 pulsations*. Pc1 pulsations last for a few minutes. At the latitude of CERN, they occur infrequently, less than ten times a year, and typically have pT amplitudes.

Because Pc1 pulsations occur infrequently, only for a short duration and are within the tolerances described in Chapter 5, they should not pose a danger for CLIC.

8.3.1 Lightning

The *ionosphere* is an electrically conductive layer of the Earth's upper atmosphere. The Earth's surface is also electrically conductive. This structure forms an EM cavity known as the *Earth-Ionosphere cavity*. Lightning can excite EM waves in the Earth-Ionosphere cavity.

Schumann Resonances

The resonant frequencies of the Earth-Ionosphere cavity are known as *Schumann resonances* and can be excited by lightning [110]. The fundamental resonance is at approximately 7.8 Hz. Higher-order harmonics (15.6 Hz, 23.4 Hz, etc.) are also excited. Schumann resonances occur continuously. The typical amplitude of Schumann resonances is a few pT. As this is within the tolerances in Chapter 5, they should not pose a danger for CLIC.

Sferics

Sferics are EM impulses generated by lightning discharges [110]. The amplitude of the SF depends on the distance to the lightning strike. Within 100 km, the average amplitude is 1-10 nT. Within 100 m of the strike amplitudes of 1 μ T can occur. The typical rise time for discharge near the strike is 1-10 μ s, which is much shorter than the train spacing (20 ms). Potentially dangerous sferics for CLIC are those generated by nearby lightning strikes. These can be predicted based on local weather forecasts. This type of lightning strike occurs approximately once a year.

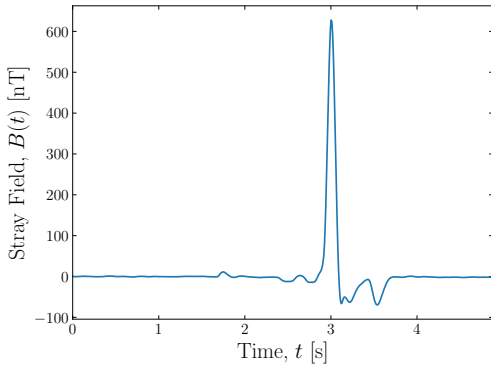
Integrated Simulations

A time-series approach is more appropriate than a PSD model for simulating impulse-like SFs. Figure 8.4a shows a measurement on the 8th June, 2018 of the SFs from a lightning strike in Tihany, Hungary. The magnetic field sensor was within a few hundred metres of the lightning strike. The measurement was performed on the Earth's surface. The same SF is assumed in the tunnel.

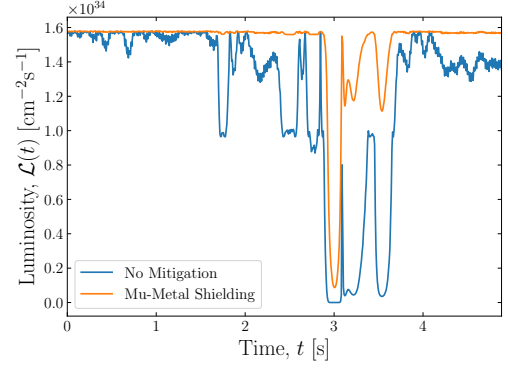
Orienting the SF in the horizontal direction with respect to the beam and assuming a homogeneous spatial profile across the machine, the simulated luminosity loss is shown in Figure 8.4b. Simulations were performed using NTE. Two scenarios were simulated: without mitigation and with a 1 mm mu-metal shield in the VT, LTL, ECS and FFS. The transfer function of the mu-metal shield is shown in Figure 7.19.

Without mitigation, there is a significant impact on luminosity. There are many short pulses of significant luminosity loss. For a short period near $t = 3$ s virtually all of the luminosity is lost. The mu-metal shield mitigates most of the luminosity loss. However, the impulse at $t = 3$ s remains.

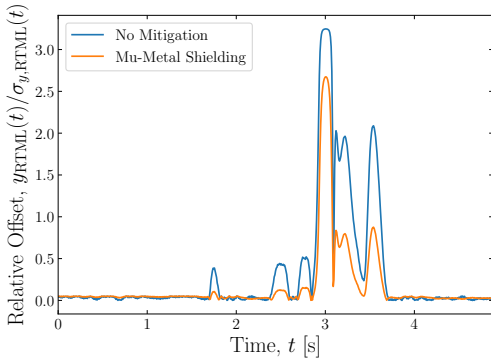
The concern of lightning is from the perspective of machine protection. A SF can deflect the beam enough to hit the machine and cause damage. This is a particular concern for the betatron collimation section in the BDS, which is not designed to withstand the impact of



(a) SF vs time from the lightning strike.



(b) Luminosity vs time during the lightning strike.



(c) Vertical beam offset relative to the beam size at the end of the RTML vs time.

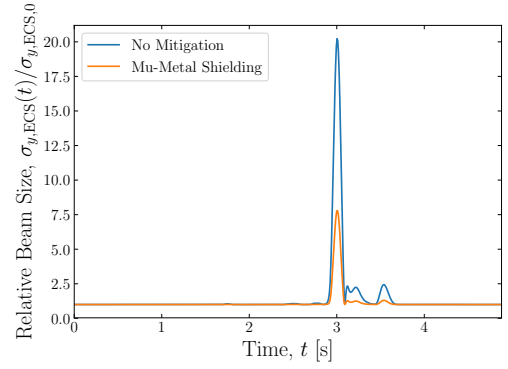
(d) Vertical beam size at the end of the ECS (start of the betatron collimation section) vs time. $\sigma_{y,ECS,0}$ is the beam size at the end of the ECS without the SF.

Figure 8.4: Exemplary SF and impact from a lightning strike with no mitigation (blue) and with a 1 mm mu-metal shield in the VT, LTL, ECS and FFS (orange).

a full train.

The vertical beam offset relative to the beam size at the end of the RTML (start of the ML) is shown in Figure 8.4c. During the strike, there is a peak offset of approximately three times the beam size. The large offset filaments in the ML and leads to a large emittance growth. As shown in Figure 8.4d, the beam size at the start of the ECS in the BDS increases by almost a factor of 20 without mitigation and a factor of 8 with shielding.

The lightning strike leads to a large luminosity loss from emittance growth. There is no large offset at the end of the ECS (start of the betatron collimation section). Therefore, there is no concern regarding machine protection. With shielding, the impact of lightning strikes will be limited to short pulses of luminosity loss.

Chapter 9

Environmental Stray Magnetic Fields

Environmental SFs are from man-made sources, which are not elements of CLIC. Environmental sources are characterised by measuring the ambient magnetic field away from an accelerator. This chapter presents measurements of environmental sources on the CERN site and integrated simulations of their impact on CLIC at $E_{\text{CM}} = 380 \text{ GeV}$.

A useful quantity to calculate from measurements is the PSD. The sensors used in this work measure the magnetic field in three orthogonal directions: x , y and z , as shown in Figure 6.2. A PSD is calculated for each component separately: $P_{B,x}(f)$, $P_{B,y}(f)$ and $P_{B,z}(f)$. The *total PSD* is the sum of all three components,

$$P_B(f) = P_{B,x}(f) + P_{B,y}(f) + P_{B,z}(f). \quad (9.1)$$

9.1 Ambient Magnetic Field at CERN

Measurements were performed on and around the CERN sites in Meyrin, Switzerland and Preveessin, France. A map of the Meyrin site is shown in Figure 9.1 and a map of the Preveessin site is shown in Figure 9.2.

The ambient magnetic field was measured on and around the Meyrin site. The mea-

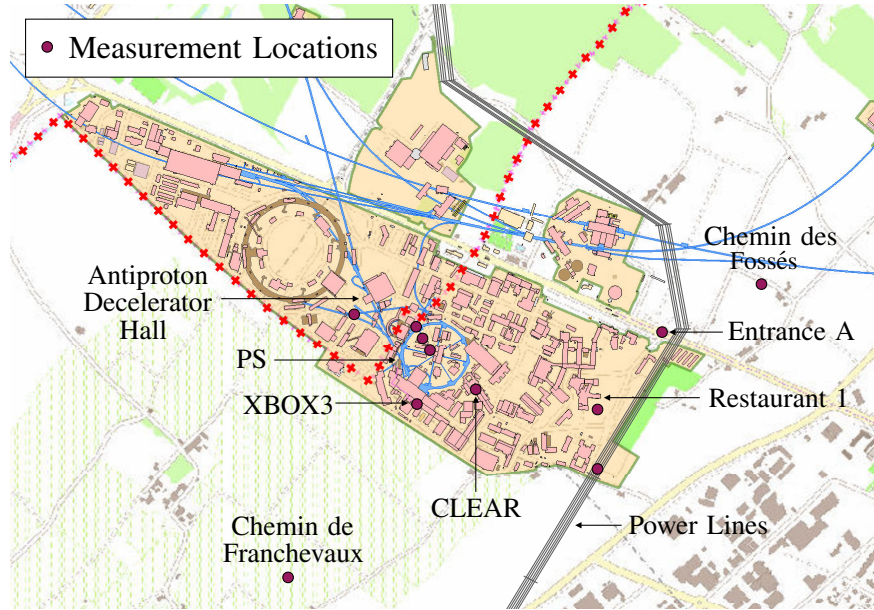


Figure 9.1: Map of the Meyrin, CERN site [112]. The line marked by red crosses outlines the Swiss-French border.

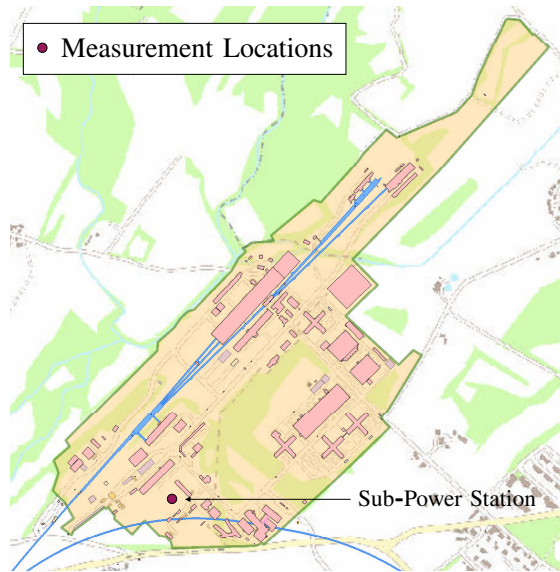


Figure 9.2: Map of the Preessin, CERN site [112].

surement locations are shown in Figure 9.1. These include Chemin de Franchevaux and Chemin des Fossés, which are off-site, and outside Restaurant 1 and outside the Antiproton Decelerator hall, which are on site.

The total PSD and standard deviation of the magnetic field at these locations is shown in Figures 9.3 and 9.4. The standard deviation on the Meyrin site can vary from nT to μ T.

The ambient magnetic field has a large amplitude at harmonics of 50 Hz. Figure 9.5

shows the amplitude of the 50 Hz magnetic field as a function of distance from the power lines shown in Figure 9.1. The amplitude is inversely proportional to the distance. SFs from power lines are discussed further in Section 9.2.1.

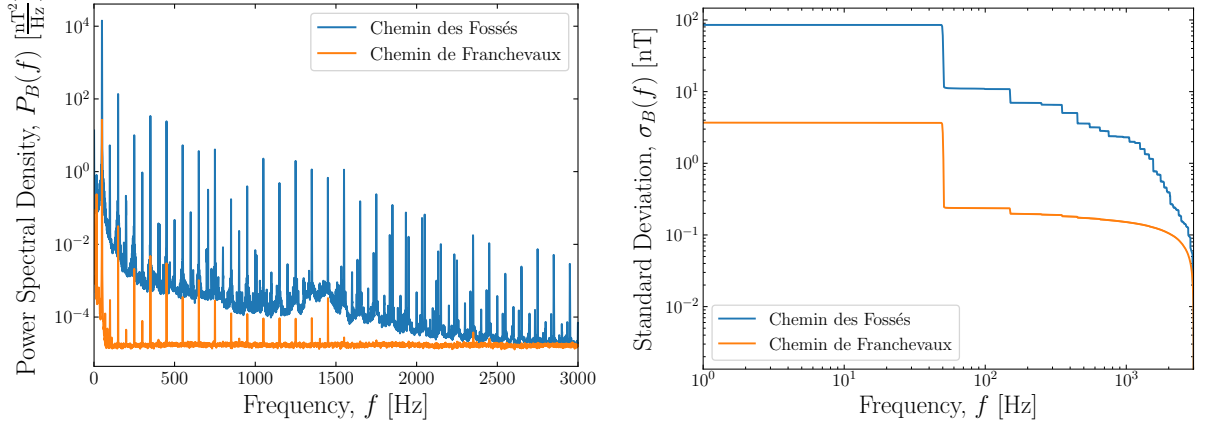


Figure 9.3: Total PSD and standard deviation of the ambient magnetic field vs frequency measured away from the Meyrin, CERN site. The Chemin des Fossés measurement (blue) was taken on the 11th July, 2019 and the Chemin de Franchevaux measurement (orange) was taken on the 12th November, 2019.

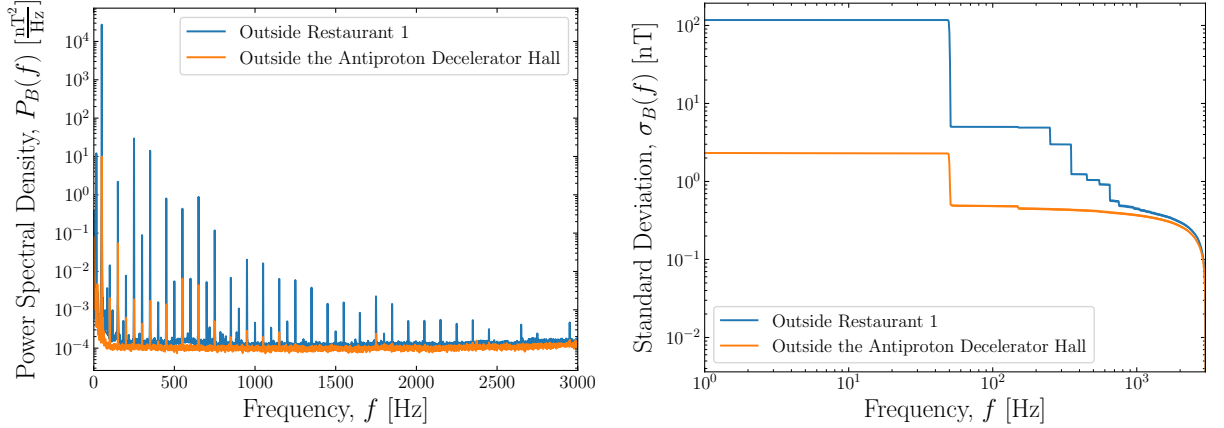


Figure 9.4: Total PSD and standard deviation of the ambient magnetic field vs frequency measured on the Meyrin, CERN site. The measurement outside Restaurant 1 (blue) was taken on the 5th September, 2018 and the measurement outside the Antiproton Decelerator hall (orange) was taken on 12th November, 2019.

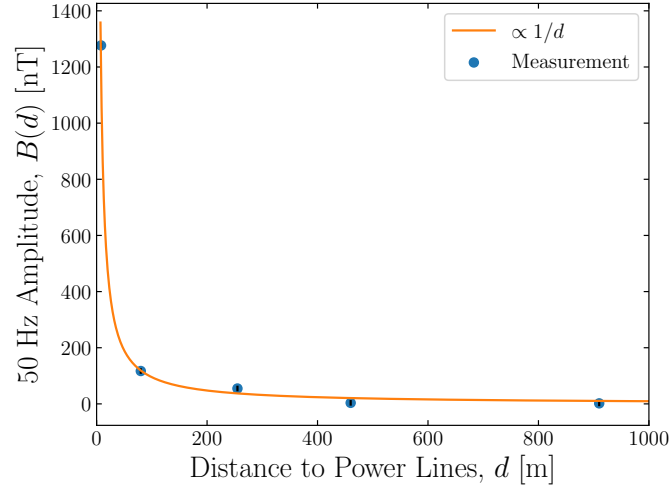


Figure 9.5: Amplitude of the 50 Hz ambient magnetic field on the Meyrin, CERN site vs distance from power lines. A one over distance attenuation (orange) was fitted to the measurement (blue). Measurements for each data point are not simultaneous, but were taken at similar times on separate days.

9.1.1 The PS

The *Proton Synchrotron* (PS) [113] is a circular accelerator on the surface of the Meyrin site. The radius of the PS is 100 m. The PS injects protons into the SPS, which then feeds the LHC. The bending magnets in the PS are only powered for the duration there is beam, they are said to be *pulsed* every 1.2 s.

The location of the PS ring on the Meyrin site is shown on the map in Figure 9.1. It is very central and close to two test facilities related to CLIC: the *CERN Linear Electron Accelerator for Research* (CLEAR) and the *third High-Gradient X-Band Test Facility* (XBOX3).

A regular pattern was observed in the recorded magnetic field at several locations in proximity to the PS. This pattern was found to be correlated to the pulsing of the PS bending magnets. As an example, the magnetic field measured 70 m away from the centre of the PS ring is shown in Figure 9.6.

The magnetic field was measured as a function of distance from the centre of the PS ring. The measurement locations and geometry of the PS are shown in Figure 9.7. The PS was modelled as a ring of 100 equally spaced bending magnets. Each bending magnet

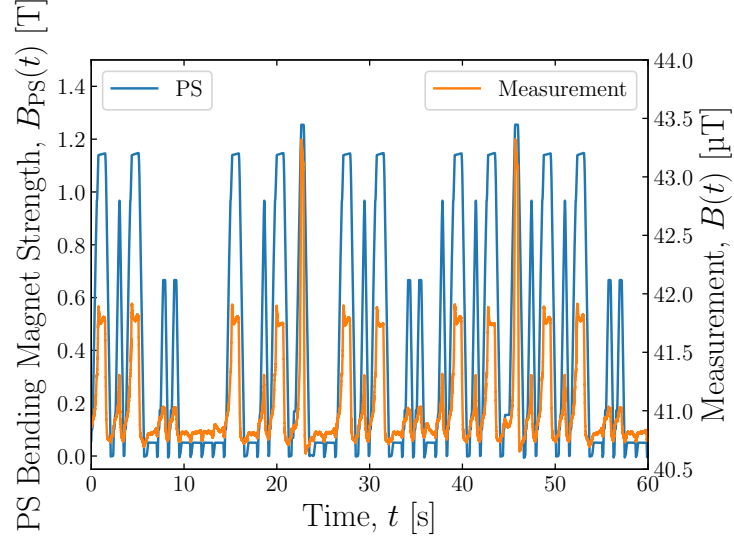


Figure 9.6: Magnetic field vs time measured near the PS on 11th September, 2018 at a distance of 70 m from the centre of the ring. The PS bending magnet strength (LH scale, blue) and measurement (RH scale, orange).

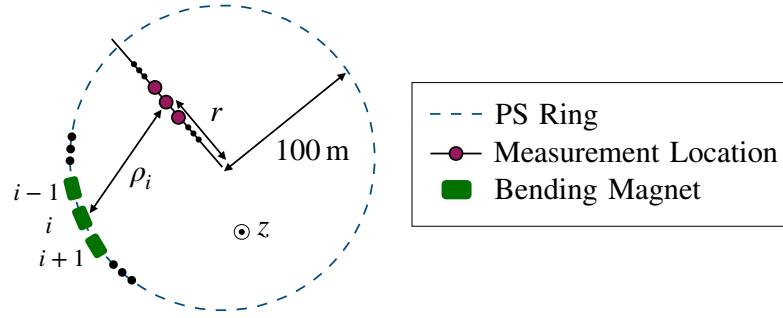


Figure 9.7: Measurement locations with respect to the PS.

contributes a dipole field of the form [114]

$$\mathbf{B}(\rho_i) = \frac{C_1}{(\rho_i + C_2)^3} \left\{ \frac{3}{2} \hat{\rho}_i - \hat{\mathbf{z}} \right\}, \quad (9.2)$$

where $\hat{\mathbf{z}}$ is a unit vector in the vertical direction (radially out of the Earth), $\hat{\rho}_i$ is a unit vector pointing from the i^{th} magnet to the measurement location, ρ_i is the distance from the i^{th} magnet to the measurement location and C_1 and C_2 are constants. The total magnetic field measured at a single location is the summation of the dipole fields from each magnet,

$$B(r) = \left| \sum_{i=1}^{100} \mathbf{B}(\rho_i) \right|, \quad (9.3)$$

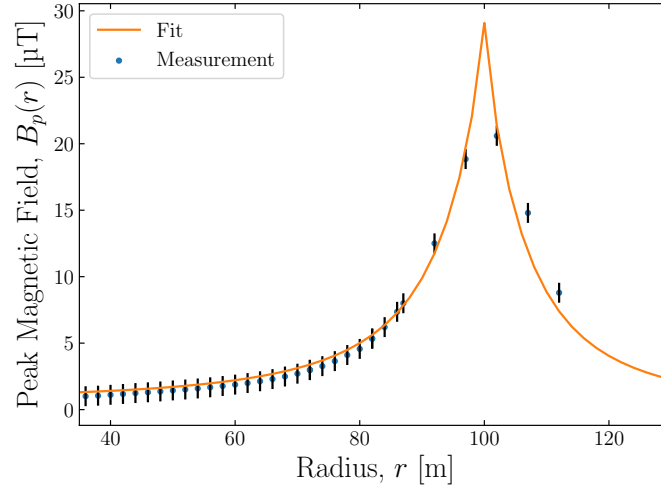


Figure 9.8: Peak magnetic field from the PS bending magnets vs radial distance measured on 11th September, 2018. Measurement (blue) and a fit using the model in Equations (9.2) and (9.3) (orange).

where r is the radial distance from the centre of the PS ring and $|\cdot|$ denotes the magnitude.

The measured magnetic field $B(r)$ is actually also a function of time. It follows the pulsing of the PS bending magnets. The *peak magnetic field* $B_p(r)$ is the maximum value of magnetic field measured over a complete cycle. For example, the peak magnetic field in Figure 9.6 occurs at time $t = 22$ s and again at $t = 46$ s.

Figure 9.8 shows the peak magnetic field from the bending magnets as a function of radial distance from the centre of the ring. From the measurements the fit parameters were calculated to be $C_1 = (6.8 \pm 0.4) \mu\text{Tm}$ and $C_2 = (9.4 \pm 0.4) \text{m}$. In the absence of any shielding material, a distance of approximately 1 km would attenuate the magnetic field to a sub-nT level.

9.2 The Electrical Grid

Typically, the largest contribution to the ambient magnetic field is from the electrical grid. The following sections describe dedicated measurements of SFs from the electrical grid. The measurements were taken in the September and October of 2018. At this time, the LHC and accompanying accelerators were running, this includes the PS and SPS.

9.2.1 Power Lines

The power lines, shown in Figure 9.1, are the dominate magnetic field source on the Meyrin site. The power lines consist of a 400 kV line, a 225 kV line and a 130 kV line, which are all part of the European electrical grid and do not belong to CERN. These power lines transport electricity between sub-power stations.

Power Spectral Density and Standard Deviation

The total PSD of the magnetic field measured directly underneath the power lines is shown in Figure 9.9. The measurement was taken on the 10th September, 2018 at the location shown in Figure 9.1. The power lines are approximately 15 m above the ground and the sensor was elevated approximately 1 m above the ground. The measurement was taken at a time of typical daytime power consumption. The standard deviation of the magnetic field is approximately 1 μ T.

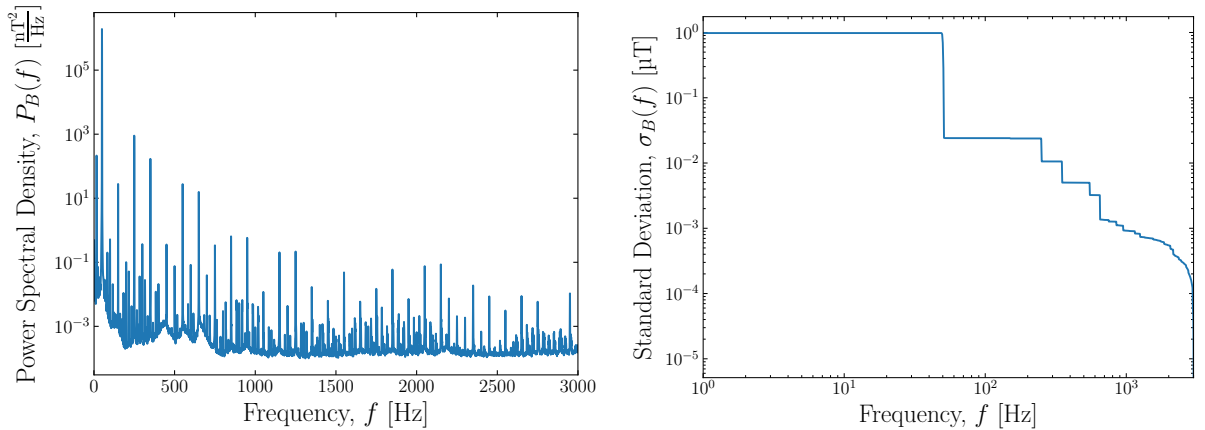


Figure 9.9: Total PSD and standard deviation of the magnetic field vs frequency measured directly underneath power lines on the Meyrin, CERN site.

The power lines carry AC currents, which have a fundamental frequency of 50 Hz. Distortions to the 50 Hz signal result in higher-order harmonics at 100 Hz, 150 Hz, 200 Hz, etc. in the frequency spectrum. The odd harmonics typically have a larger amplitude compared to the even harmonics. The distortions are introduced by non-linear loads on the grid. For example, saturated transformers, rectifiers, switching mode power supplies, etc. [115].

The peaks with the largest amplitude are the harmonics of 50 Hz, which the beam is not sensitive to. However, there are additional peaks with significant amplitudes in between the harmonics of 50 Hz, which can influence the beam. This means power lines are an important SF source.

The amplitude of the current in the lines is determined by the electricity demand on the grid. Usually, the demand on the grid is larger during the day than the night. Therefore, one should expect smaller currents and therefore SFs during the night-time.

Impact of Mitigation

The impact of mitigation can be estimated by applying an appropriate transfer function to the PSD. Figure 9.10 shows the impact of different mitigation techniques on the PSD of SFs from power lines. The standard deviation of the SF with each mitigation technique is summarised in Table 9.1. The mu-metal shield is the most effective mitigation technique.

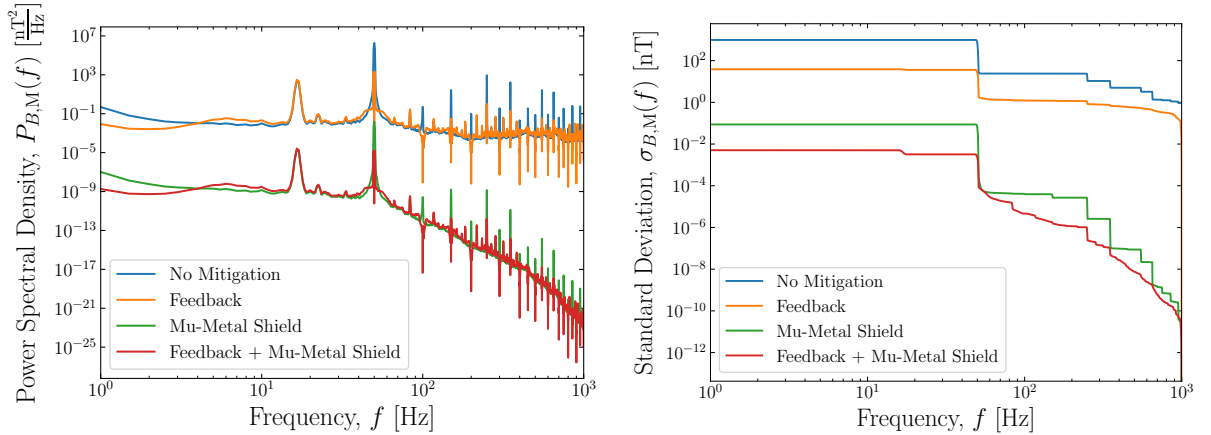


Figure 9.10: Total PSD and standard deviation of the magnetic field vs frequency from power lines: without mitigation (blue); including a beam trajectory feedback system with $m = 2.5$ (orange); including a 1 mm mu-metal shield (green) and with the feedback system and mu-metal shield combined (red).

Mitigation	Standard Deviation, $\sigma_{B,M}$ [nT]
None	980
Feedback System	39
Mu-Metal Shield	0.09
Feedback System + Mu-Metal Shield	0.005

Table 9.1: Standard deviation of the magnetic field from power lines with different mitigation techniques.

Temporal Variation of Power

Figure 9.11 shows the power in the measured magnetic field as a function of time. There is a regular pattern with a period of approximately 20 s present in the measurement.

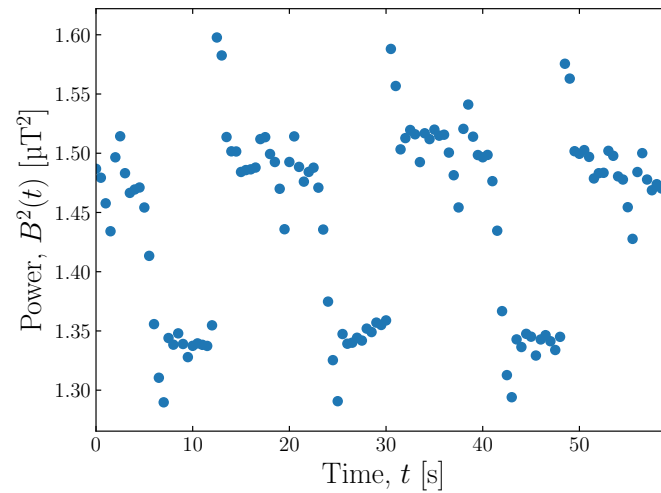


Figure 9.11: Power in the magnetic field vs time measured underneath the power lines on the Meyrin, CERN site.

9.2.2 Sub-Power Stations

The Preveessin site contains a sub-power station, which is used to power the SPS. The location of the sub-power station is shown in Figure 9.2.

Power Spectral Density and Standard Deviation

Figure 9.12 shows the total PSD of the magnetic field measured on the 5th October, 2018 within a few metres of some transformers in the sub-power station on the Preveessin site. The sub-power station is a large SF source. The standard deviation of the magnetic field is a few μT .

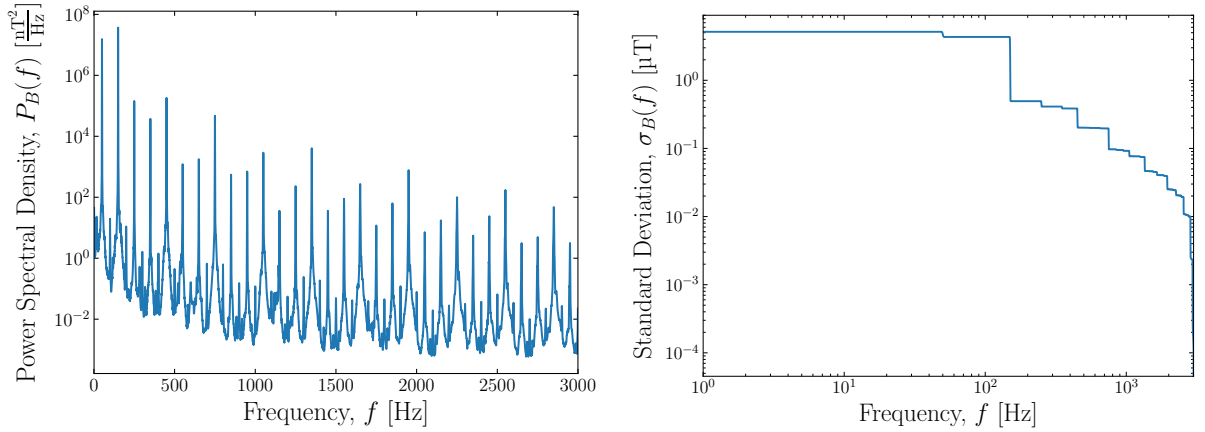
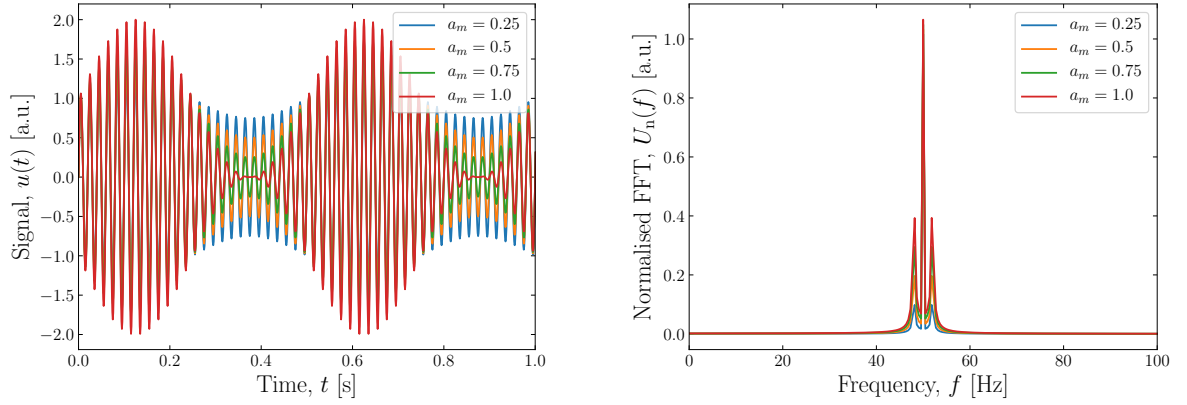


Figure 9.12: Total PSD and standard deviation of the magnetic field vs frequency measured near the sub-power station on the Preveessin, CERN site.

Amplitude Modulation of 50 Hz Harmonics

An *amplitude modulation* is the variation of the amplitude of a signal with time. Examples of amplitude-modulated signals are shown in Figure 9.13a. The normalised *Fast Fourier Transform* (FFT) of these signals is shown in Figure 9.13b. There is a large peak in the normalised FFT at the carrier frequency f_c , which is surrounded by two smaller peaks, known as *sidebands*. This is a characteristic feature of amplitude-modulated signals. The distance between the carrier frequency and sidebands is determined by the modulation frequency f_m and the height of the sidebands is determined by the amplitude sensitivity a_m .

In the PSD shown in Figure 9.12, there are symmetric peaks around the odd harmonics of 50 Hz. Around the 50 Hz peak, the surrounding peaks are at 16.7 Hz and 83.3 Hz. Such a spectrum arises from an amplitude modulation of the 50 Hz at a frequency of $f_m = 33.3$ Hz.



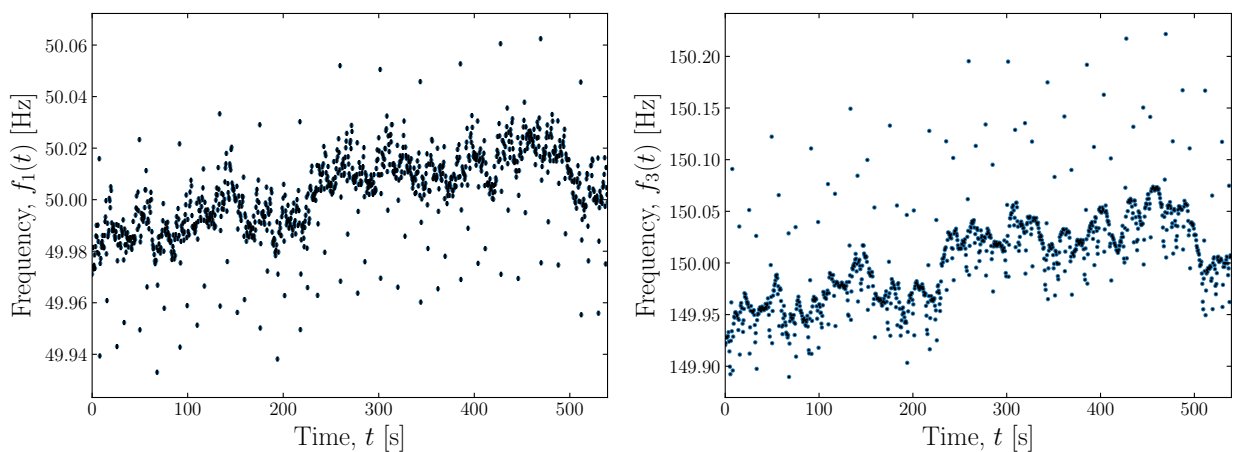
(a) Signals vs time.

(b) Normalised FFT of the signals vs frequency.

Figure 9.13: Examples of sinusoidal amplitude-modulated signals. The signals are calculated as $u(t) = A(t) \sin(2\pi f_c t)$, where f_c is the *carrier frequency*, t is time, $A(t) = 1 + a_m \sin(2\pi f_m t)$ is the amplitude, a_m is the *amplitude sensitivity* and f_m is the *modulation frequency*. A carrier frequency of $f_c = 50$ Hz and modulation frequency of $f_m = 2$ Hz was used.

Stability of 50 Hz Harmonics

Figure 9.14a shows the precise value of the fundamental frequency f_1 (also known as the first harmonic) over the measurement. The first harmonic is not exactly 50 Hz. Small fluctuations of ± 0.02 Hz occur over time scales of seconds and larger variations of ± 0.08 Hz occur on time scales of tens of seconds. The variation of the carrier frequency with time is known as *frequency modulation*.



(a) First harmonic.

(b) Third harmonic.

Figure 9.14: The first harmonic and third harmonic of the magnetic field vs time measured near the sub-power station on the Preveessin, CERN site.

The third harmonic f_3 is shown in Figure 9.14b. The frequency of the third harmonic

follows the same temporal variation as the first harmonic. The variation in frequency contributes to the broadness of peaks in the PSD.

Temporal Variation of Power

Figure 9.15 shows the power in the measured magnetic field as a function of time. There is a very clear pulsing suspected to originate from the variation in power consumption from the SPS. The pulses match the variation in the fundamental frequency.

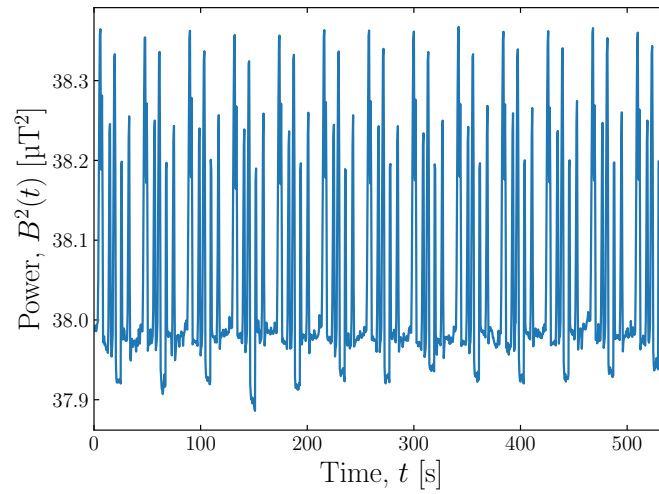


Figure 9.15: Power in the magnetic field vs time measured near the sub-power station on the Preveessin, CERN site.

Breadth of 50 Hz Harmonics

The harmonics of 50 Hz are broader in the PSD measured near the sub-power station compared to underneath the power lines. The breadth can arise from a drift in the frequency of the peak (i.e. frequency modulation), spectral leakage due to the finite signal length (see Appendix A) or distortions in the signal.

The repetition frequency of the CLIC beam will be fixed to the fundamental frequency of the electricity supply. This means the PSD of the SFs experienced by the beam will not include the broadening of peaks due to frequency modulation. A more representative PSD can be calculated using a short segment of the measurement to exclude the effect of

frequency modulation.

Figure 9.16 shows the total PSD calculated with a short segment of the measurement. The PSD calculated using a short segment is noisier because the PSD was calculated by averaging over less data. The peaks at harmonics of 50 Hz are sharper because there is less frequency modulation. The remaining breadth in the peaks at harmonics of 50 Hz can arise from spectral leakage and distortions. The impact of spectral leakage is minimised by windowing, so the breadth is attributed to distortions in the signal.

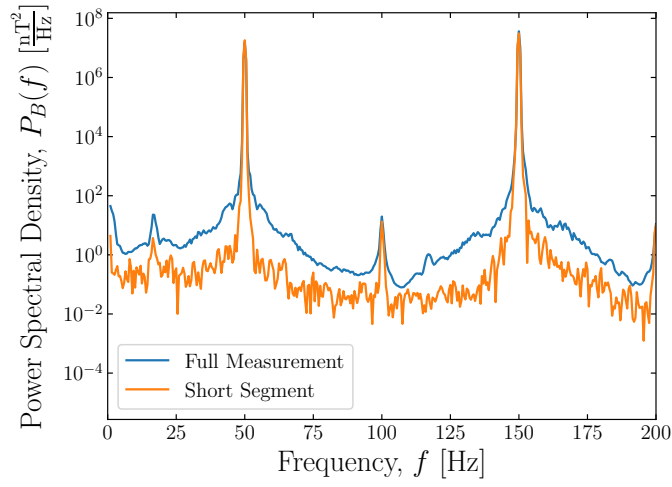


Figure 9.16: Total PSD of the magnetic field vs frequency from a sub-power station calculated with the full measurement and a short segment of the measurement.

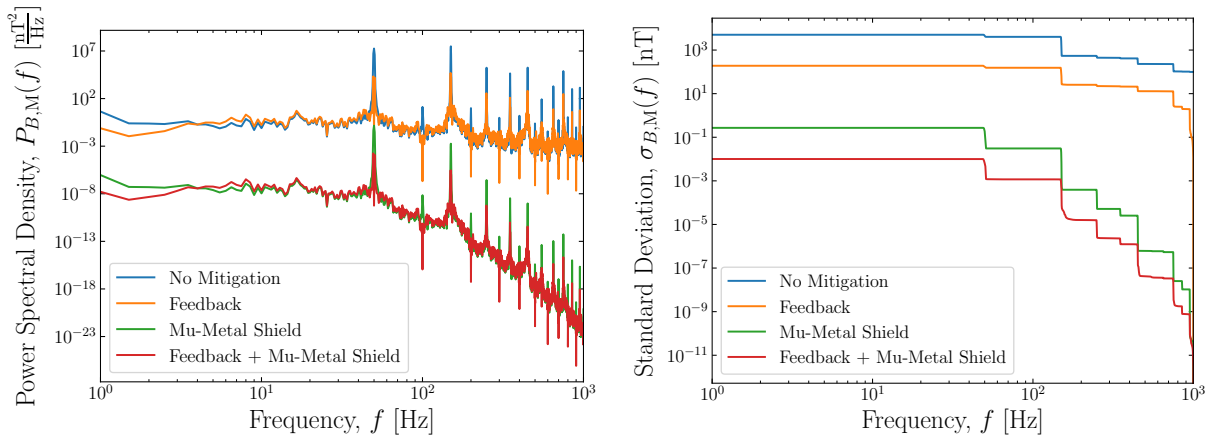


Figure 9.17: Total PSD and standard deviation of the magnetic field vs frequency from sub-power stations: without mitigation (blue); including a beam trajectory feedback system with $m = 2.5$ (orange); including a 1 mm mu-metal shield (green) and with the feedback system and mu-metal shield combined (red).

Impact of Mitigation

Figure 9.17 shows the PSD of SFs from sub-power stations including the impact of different mitigation techniques. The PSD calculated with a short segment of the measurement was used. The standard deviation of the SF with each mitigation technique is summarised in Table 9.2. Both the mu-metal shield and feedback system are needed to reduce the SF to less than 0.1 nT.

Mitigation	Standard Deviation, $\sigma_{B,M}$ [nT]
None	5,100
Feedback System	200
Mu-Metal Shield	0.25
Feedback System + Mu-Metal Shield	0.01

Table 9.2: Standard deviation of the magnetic field from sub-power stations with different mitigation techniques.

9.2.3 Integrated Simulations

CLIC Electrical Network

The electrical network for CLIC is described in [25]. It consists of a *transmission* and *distribution* level:

- The transmission level transports power from the European grid to three surface sites (points 1, 2 and 3) and underground. It operates at high voltages: 400 kV and 135 kV. The transmission network is shown in Figure 9.18.
- The distribution level transports power from the surface sites to the end users at low and medium voltage levels: 400 V to 36 kV. Currents on the order of 100 A will be present in the CLIC tunnel.

The location of the planned sub-power stations and nearby power lines are shown in Figure 9.19. These will be significant SF sources for CLIC. The power lines run approximately

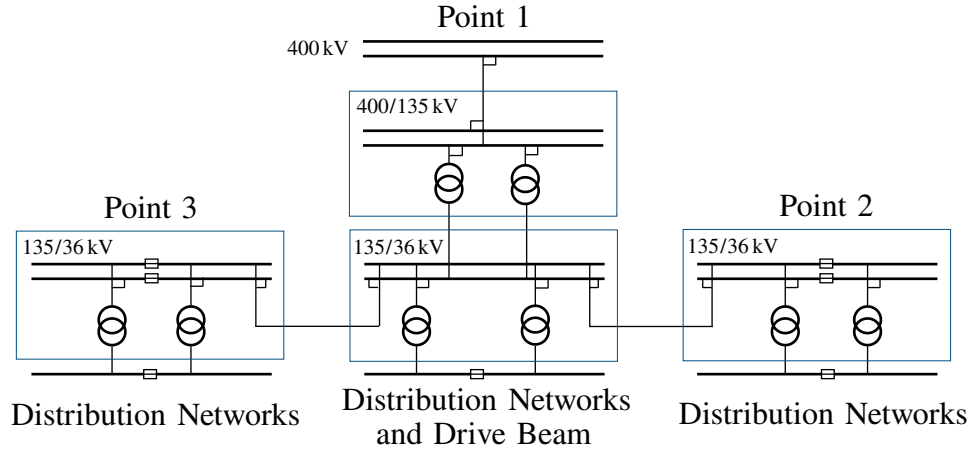


Figure 9.18: Schematic diagram of the electrical network for CLIC at $E_{\text{CM}} = 380 \text{ GeV}$ [25]. The blue boxes represent transformers in sub-power stations.

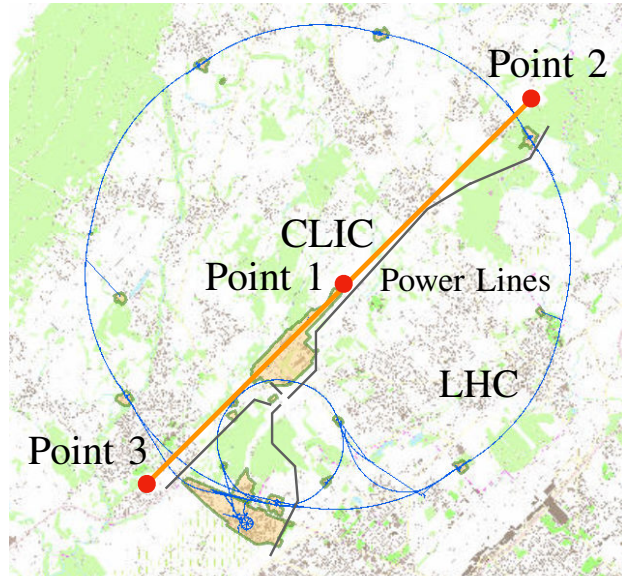


Figure 9.19: Map of the location of CLIC at $E_{\text{CM}} = 380 \text{ GeV}$ with respect to the CERN sites and current accelerator projects [112]. Nearby infrastructure related to the electrical network, such as power lines and sub-power stations (point 1, 2 and 3), are also shown.

parallel to the beamline, which means they will produce SFs in the transverse plane of the beam. They are roughly 200 m away from the beamline.

The CLIC IP is at the same location as the point 1 sub-power station. This is near the Preveessin site, which contains a sub-power station approximately 2 km away from the IP.

Generator

The location of the power lines and sub-power stations can be used to characterise the spatial variation of the SFs. The SF is modelled as a standing wave.

The SF amplitude of a particular frequency mode at the source location is given by

$$a_i = \sqrt{2}\sigma_{B,i} = \sqrt{2 \int_{f_i}^{f_{i+1}} P_{B,M}(f) df} \approx \sqrt{2P_{B,M}(f_i)\Delta f}, \quad (9.4)$$

where $\sigma_{B,i}$ is the standard deviation of mode i , $P_{B,M}(f)$ is the PSD for the power lines or sub-power station including the effect of a mitigation technique and $\Delta f = f_{i+1} - f_i$.

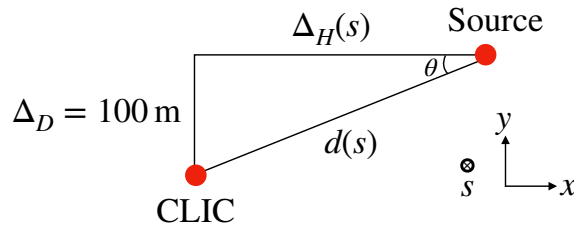


Figure 9.20: Orientation of CLIC with respect to the location of power lines and sub-power stations. s is the longitudinal position along CLIC, which is orientated into the page. x and y are horizontal and vertical directions with respect to the beam.

Figure 9.5 shows the SF amplitude from power lines is attenuated with $1/d$, where d is the distance. This is the expected spatial variation of the magnetic field from a line current. For the sub-power stations a $1/d^2$ attenuation is assumed, which is the attenuation with distance for a current loop. The amplitude at a location along CLIC is calculated as

$$A_i(s) = \begin{cases} a_i/d(s) & \text{for power lines,} \\ a_i/d^2(s) & \text{for sub-power stations,} \end{cases} \quad (9.5)$$

where $d(s)$ is the distance from the source to CLIC as shown in Figure 9.20. The component

of the SF in the horizontal and vertical plane with respect to the beam is calculated as

$$\begin{aligned} A_{i,x}(s) &= A_i(s) \sin \theta = A_i(s) \Delta_D / d(s), \\ A_{i,y}(s) &= A_i(s) \cos \theta = A_i(s) \Delta_H / d(s). \end{aligned} \quad (9.6)$$

The SF is generated as

$$\begin{aligned} B_x(s, t) &= \sum_{i=1}^N A_{i,x}(s) \cos(2\pi f_i t + \phi_{i,x}), \\ B_y(s, t) &= \sum_{i=1}^N A_{i,y}(s) \cos(2\pi f_i t + \phi_{i,y}), \end{aligned} \quad (9.7)$$

where N is the number of modes and $\phi_{i,x}$ and $\phi_{i,y}$ are uniformly distributed random numbers between 0 and 2π . The SF $B_x(s, t)$ and $B_y(s, t)$ are generated separately for each sub-power station and the power lines. The SF experienced by the beam is the summation of the SF from each source. The SF kick is calculated with Equation (5.11) taking into account the beam direction with respect to the SF.

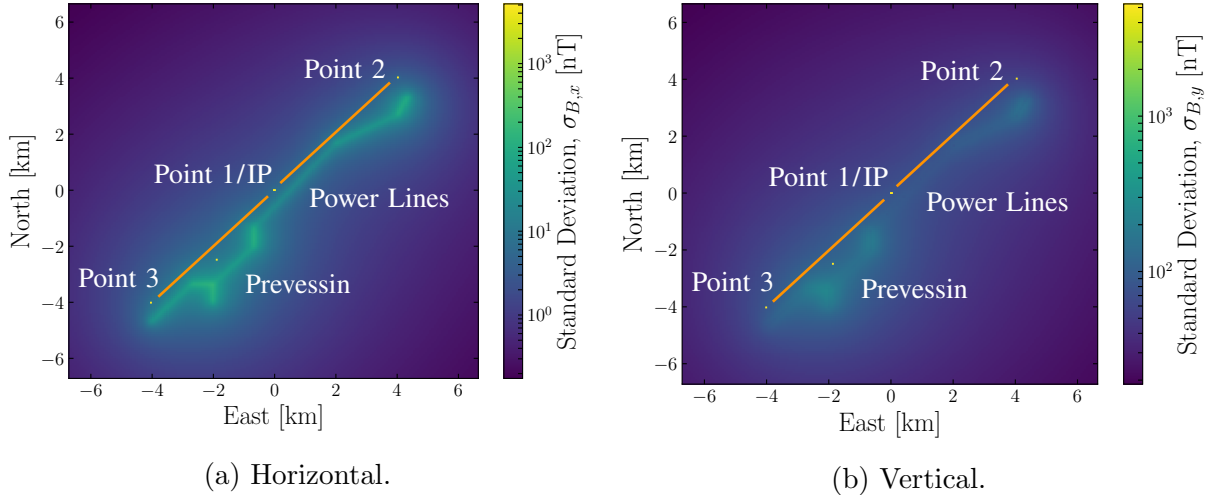


Figure 9.21: Standard deviation (RH scale) vs north coordinate (LH scale) and east coordinate of the magnetic field from power lines and sub-power stations in the horizontal and vertical direction with respect to the beam. CLIC is shown in orange.

Spatial Profile

Figure 9.21 shows the standard deviation of SFs from power lines and sub-power stations across the CLIC site. The power lines are a large SF source. The $1/d^2$ attenuation of SFs from sub-power stations means the amplitude decays quickly.

The standard deviation of the SF along the CLIC beamline is shown in Figure 9.22. Because the SFs from sub-power stations decay rapidly with distance, the standard deviation is predominantly from the power lines. The standard deviation of the SF is similar to the levels measured at accelerator facilities at CERN (see Chapter 11).

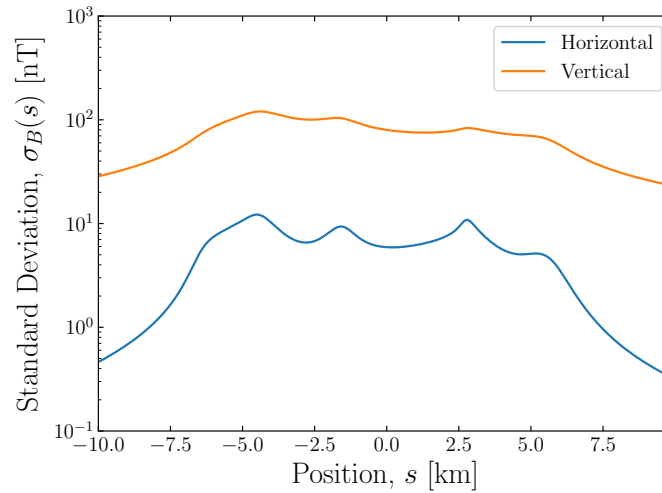


Figure 9.22: Standard deviation of the magnetic field in the horizontal (blue) and vertical plane (orange) with respect to the beam from power lines and sub-power stations vs position along CLIC.

Luminosity Loss

Table 9.3 shows the luminosity loss with different mitigation techniques. Without mitigation, practically all of the luminosity is lost. Neither the beam trajectory feedback system nor mu-metal shield alone is enough to mitigate luminosity loss from SFs. However, the combination of the feedback system and mu-metal shield is extremely effective.

Mitigation	Luminosity Loss, $\Delta\mathcal{L}/\mathcal{L}_0$ [%]
Using STE	
None	94
Feedback System	34
Mu-Metal Shield	39
Feedback System + Mu-Metal Shield	0.20
Using NTE	
None	93
Feedback System	23
Mu-Metal Shield	31
Feedback System + Mu-Metal Shield	0.16

Table 9.3: Luminosity loss due to SFs from power lines and sub-power stations. Values are expressed as a percentage of Equation (3.3) for NTE or Equation (3.5) for STE. The error on each value is less than 0.1%.

9.3 Transport Infrastructure

To examine the impact of SFs from local transport infrastructure, such as trains, trams and cars, the magnetic field near a busy road, which contains a tram line, was measured.

Figure 9.23 shows the location of local transport infrastructure.

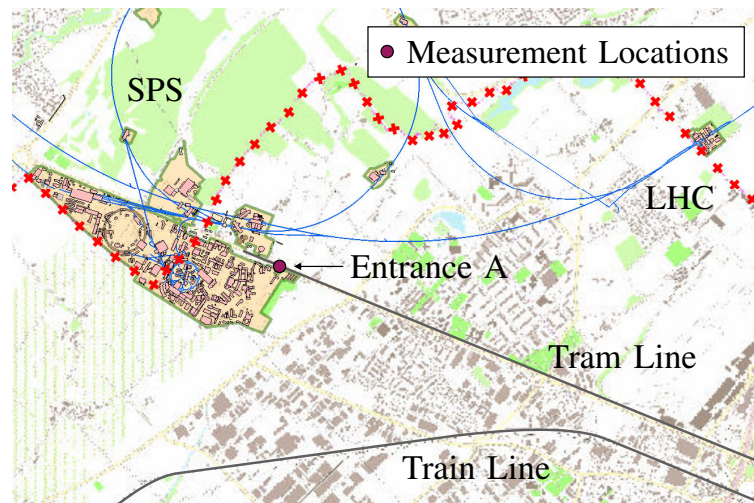
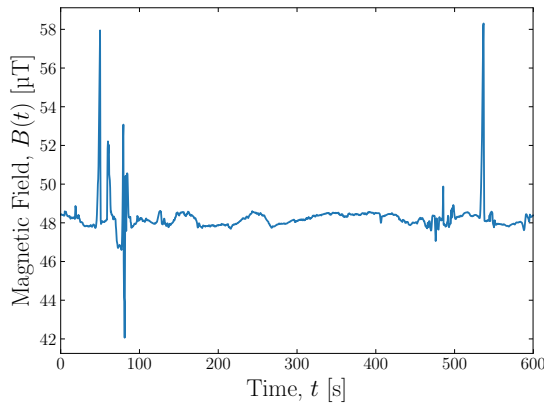


Figure 9.23: Map of the transport infrastructure near the Meyrin site [112]. The line marked by red crosses outlines the Swiss-French border. Accelerators are marked by the blue lines. Nearby transport infrastructure, such as tram and train lines, is also shown.

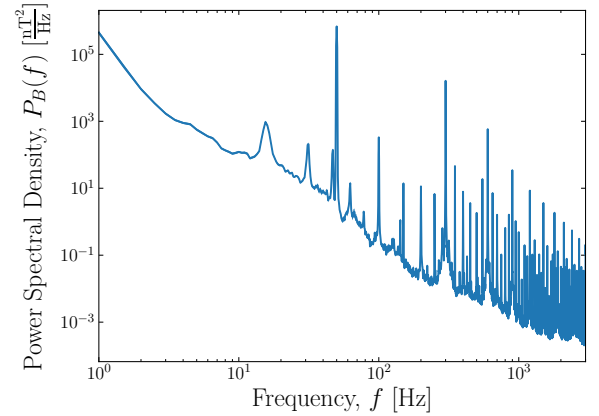
Trams and Vehicles

Figure 9.24a shows the magnetic field measured at Entrance A. The two large spikes in Figure 9.24a at the start and toward the end of the measurement are from passing trams. The sensor was approximately 1 m away from the tram line. The other spikes are from large passing vehicles.

The total PSD of the magnetic field is shown in Figure 9.24b. The broadband peak at low frequencies in the PSD is characteristic of an impulse in the time domain. This feature is not present in any of the ambient magnetic field measurements on the Meyrin site. Therefore, it is safe to assume the SFs from trams and cars do not extend beyond a few hundred metres from the source.



(a) Magnetic field vs time.



(b) Total PSD vs frequency.

Figure 9.24: Magnetic field vs time and total PSD of the magnetic field vs frequency measured near Entrance A on the 12th November, 2019.

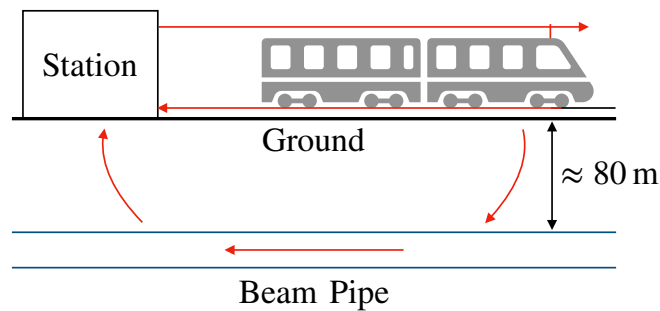


Figure 9.25: Illustration of current leakage from trains. The flow of current is shown in red. The train is shown in grey. The LEP beam pipe is shown in blue.

Trains

A peak at 16.7 Hz is often observed in ambient magnetic field measurements. Figure 9.24b shows a peak at 16.7 Hz and at higher-order harmonics. Electrified railways in Switzerland operate at 16.7 Hz [116]. This could be the source of SFs at this frequency. The nearest railway lines to CERN are shown in Figure 9.23.

Currents can leak from the railway lines and flow underground, e.g. along buried pipes. This can lead to SFs from trains appearing several kilometres away from the railway lines. This phenomenon impacted LEP at CERN. At the time of LEP, the train line in Figure 9.23 used DC power¹. Typically, the current flows along a line above the train and returns along the track as illustrated in Figure 9.25. However, a path of less resistance was provided by LEP, which resulted in DC currents flowing along the beam pipe [117]. To prevent this from happening with CLIC, the beam pipe will be grounded.

¹They now operate with AC power.

Chapter 10

Technical Stray Magnetic Fields

Technical SFs are from elements of CLIC. These pose the greatest danger for CLIC. The characteristic frequency spectrum and amplitude of technical SFs is a priori unknown. Dedicated measurements were performed to characterise technical sources. This section systematically reviews potential technical sources.

10.1 Magnets

Normal conducting accelerator magnets are typically formed by winding a coil around an iron core. Current in the coil generates the magnetic field. The shape of the iron core determines the spatial profile of the magnetic field. Iron exhibits a property known as hysteresis, which was discussed in Chapter 7. This results in a remnant magnetic field even when there is no current flowing through the coil.

Internal Field Stability

The magnetic field inside the core of a magnet, referred to as the *internal field*, is used to guide a particle beam. Ripples in the internal field will be experienced directly by the beam. This section presents measurements of the temporal stability of the magnetic field produced

by a magnet, referred to as the *magnet stability*, which is expressed as σ_B/B , where σ_B is the standard deviation and B is the static component of the magnetic field.

A magnet also has a peripheral field known as the *fringe field*. In magnet design, the term SF often refers specifically to the fringe field. This work generalises SFs to any unwanted magnetic field, either from magnets or external to the accelerator. Fringe fields are therefore one type of SF.

The internal field can also have spatial imperfections, i.e. the desired spatial profile of the internal field cannot always be exactly realised. However, because the spatial imperfections are static this is not a concern.

Integrated simulations were performed to define temporal stability requirements for the quadrupole magnets. These are presented in Table 10.1. For each pulse, a random fluctuation sampled from a Gaussian distribution was applied to each quadrupole.

Section	Requirement, σ_B/B
RTML	10^{-4}
ML	10^{-4}
BDS (Excluding FD)	10^{-5}
FD	10^{-6}

Table 10.1: Quadrupole stability requirements for specific sections. FD is the final doublet.

The relative magnetic strength error that can be tolerated is large. For magnets which have $B \approx 1$ T, ripples on the order of μT can be tolerated. The large ripple tolerances are possible because the magnets are a relatively short fraction of the beamline. The sub-nT tolerances described in Chapter 5 arise from the influence of SFs in long drifts.

CLIC Quadrupole Magnet

The magnet stability of a prototype quadrupole for CLIC was measured on the 12th March, 2019. Two sensors were used in this measurement. The geometry of the magnet and sensors are shown in Figure 10.1. The magnetic field in the y -direction is studied below. This is because both sensors could be accurately placed at the same height relative to the magnet.

It is assumed that the same ripple is present in the internal and fringe field.

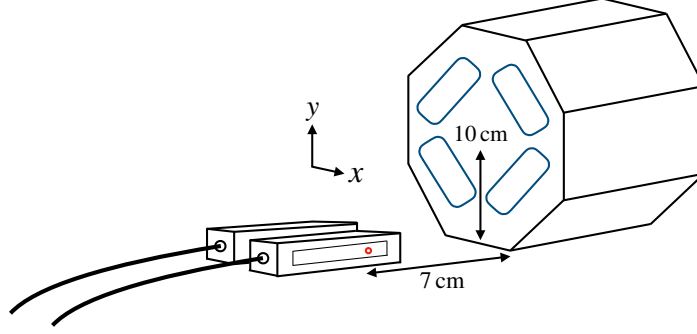


Figure 10.1: Measurement setup to characterise SFs from a CLIC quadrupole magnet.

A DC current was supplied to the magnet to produce a DC magnetic field. The current could be supplied in one of two directions (polarities). Taking the difference of the magnetic field measured with each polarity removes the background. Dividing the difference by two gives the fringe field. Care was taken to ramp down the magnet strength before flipping polarity to ensure hysteresis effects were avoided. A DC fringe field of $B_y = (38 \pm 1) \mu\text{T}$ was measured at a distance of 7 cm from the edge of the magnet when a current of $I = 200 \text{ A}$ was flowing through the coil of the magnet.

The AC magnetic field from the quadrupole can be measured using two sensors by exploiting the symmetry of the magnetic field. The location of the sensors with respect to the magnet is shown in Figure 10.1. Equal and opposite fringe fields should be observed in the y -direction by each sensor. The AC fringe field is found by taking the difference of simultaneous measurements from each sensor and dividing by two. Figure 10.2 shows the PSD of the fringe field of the quadrupole measured 7 cm from the edge of the magnet. The standard deviation of the fringe field is $\sigma_{B,y} = (3.9 \pm 0.5) \text{ nT}$.

Combining these measurements, the magnet stability was measured to be

$$\frac{\sigma_{B,y}}{B_y} = (1.0 \pm 0.1) \times 10^{-4}, \quad (10.1)$$

which is the desired level for the RTML and ML. This measurement is likely to be an overestimation due to the limited alignment accuracy with respect to the magnetic centre of

the quadrupole. It is likely that not all of the background was perfectly cancelled.

The magnet produces a broadband peak at 40 Hz, which is a frequency that will be amplified by a beam trajectory feedback system. However, because the magnet stability is at the level of the requirement (for the RTML and ML) this should not be a danger for CLIC.

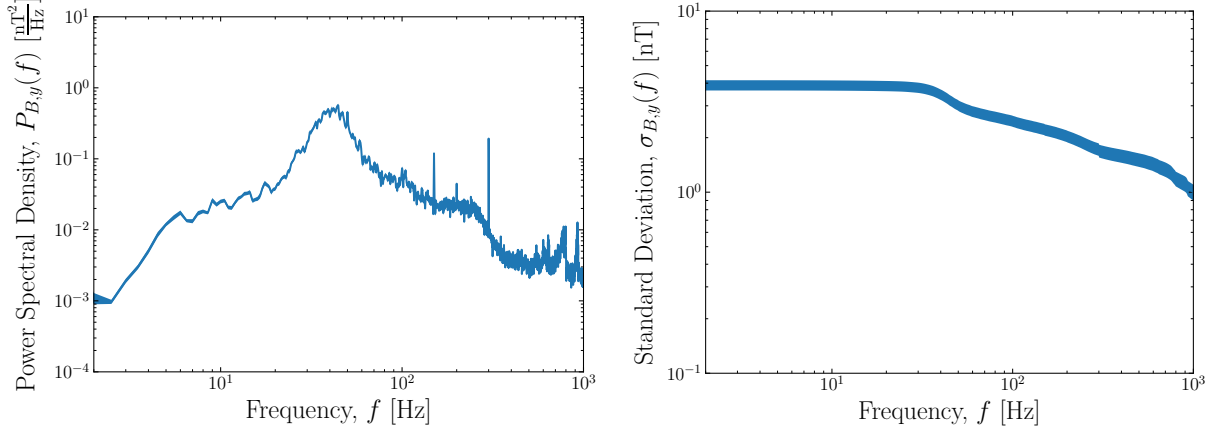


Figure 10.2: PSD and standard deviation of the vertical fringe field vs frequency of a CLIC quadrupole magnet.

CLEAR Quadrupole Magnet

The fringe field of a quadrupole magnet at the CLEAR facility was measured on the 30th August, 2019. Two sensors were used in this measurement. One was placed 5 cm away from the magnet and the other was 25 cm away from the magnet.

The current supplied to the magnet was varied and the magnetic field was recorded. Only the sensor closest to the magnet was able to observe the fringe field of the magnet. There was no change in the PSD of the magnetic field recorded by the far sensor. The total PSD of the magnetic field recorded by the near sensor for different currents supplied to the magnet is shown in Figure 10.3. This measurement contains both the fringe field and the background magnetic field.

Peaks above 100 Hz begin to emerge as the current is increased. A broadband peak around 230 Hz is particularly visible. The amplitude of the SF at 230 Hz varies linearly with

the current in the magnet as expected from Ampère's law [9].

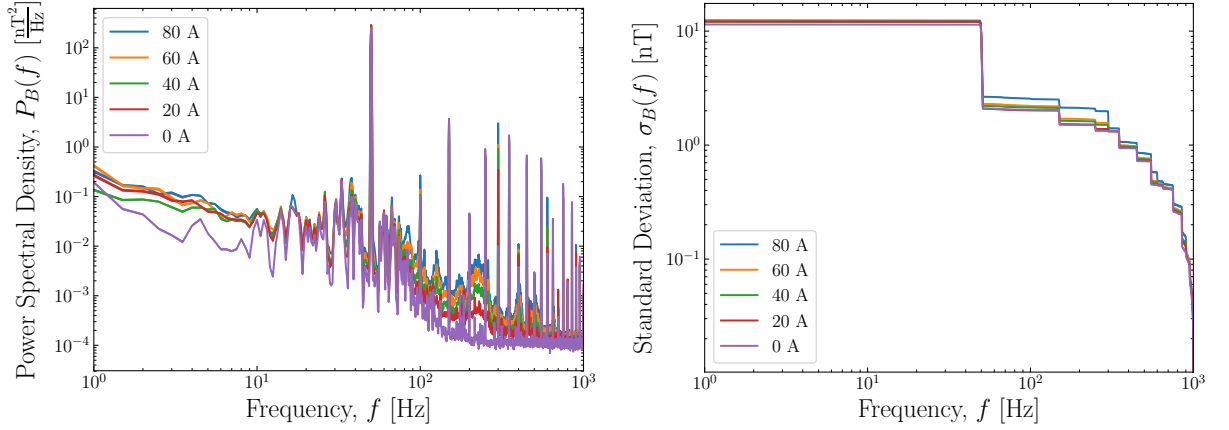


Figure 10.3: Total PSD and standard deviation of the fringe field vs frequency of a CLEAR quadrupole magnet with different currents supplied to the magnet.

10.2 Power Cables

As described in Section 9.2.3 there will be cables carrying significant currents of up to 400 A in the tunnel. Power cables to magnets will carry the most significant currents. These currents are DC.

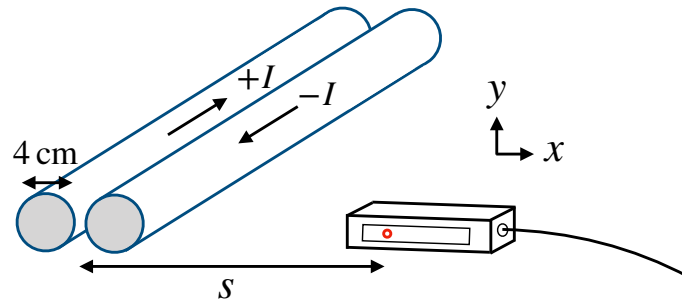


Figure 10.4: Measurement setup to characterise SFs from power cables. I is the current in the cables and s is the distance from the cables.

To minimise the magnetic field from cables they are often arranged in pairs with currents flowing in opposite directions. Alternatively, a pair of cables are twisted. Power cables to magnets are never twisted, instead, they are arranged in parallel pairs. One cable delivers current to the magnet and the other cable carries the return current.

The simple geometry of a power cable means its magnetic field can be calculated using the Biot-Savart law [9]. To verify this, a typical pair of power cables was characterised on the 12th December, 2018. Figure 10.4 shows the arrangement of the cables.

Spatial Profile

The spatial profile of the DC magnetic field was measured as a function of distance from the cables. To isolate the magnetic field of the cables from the background the polarity of the current was flipped at each location. By taking the difference of the magnetic field recorded for each polarity, the background is subtracted and the magnetic field corresponding to twice the current in both cables is measured. A current of 20 A was chosen to ensure the sensor was not saturated.

Figure 10.5 shows the spatial profile of the DC magnetic field. The measurement shows good agreement with the Biot-Savart law, labelled Theoretical in Figure 10.5. The magnetic field appears to drop rapidly with distance from the cables. This configuration of two cables produces a magnetic dipole field, which has a spatial attenuation that decays as $1/s^3$ [114].

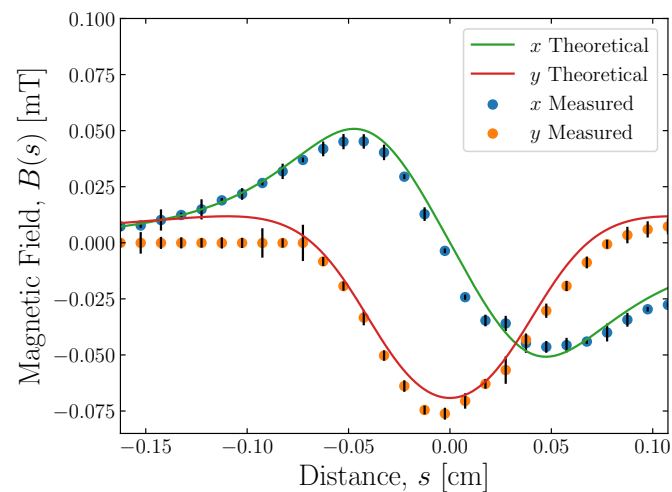


Figure 10.5: DC magnetic field vs distance from the power cables: theoretical calculation in the x and y -direction (green and red) and measurement in the x and y -direction (blue and orange).

Current Ripples

Of more interest in this work is the current ripple in the cables. Using the Biot-Savart law the current can be inferred by measuring the magnetic field. To estimate the current, the AC magnetic field was measured at different s -locations and the current was calculated using the Biot-Savart law. The current inferred at each location was then averaged. Figure 10.6 shows the estimate of the current.

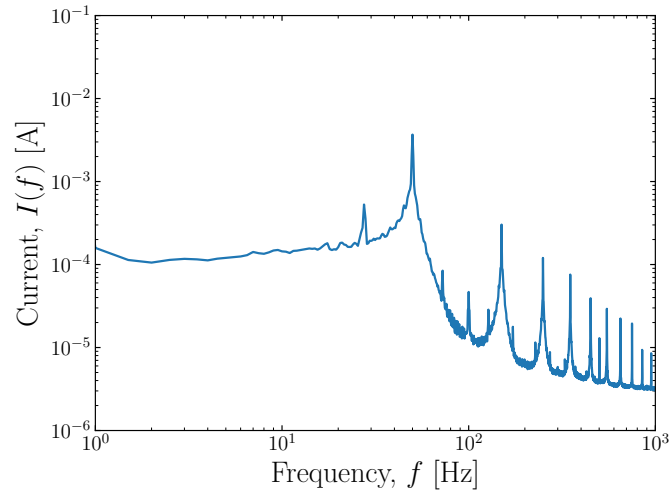


Figure 10.6: Current in the power cables vs frequency.

Figure 10.6 shows there are ripples at harmonics of 50 Hz. This is expected because the current is drawn from the electrical grid, which operates at 50 Hz. There are also ripples at 25 Hz, 75 Hz, etc. Such peaks arise from an amplitude modulation of the 50 Hz, which can be introduced by power converters or can already be present in the electrical grid.

Ripples at harmonics of 50 Hz are not dangerous for the CLIC beam. However, ripples that are introduced by amplitude modulation of the 50 Hz are at frequencies which can affect the CLIC beam.

A ripple of approximately 0.01 A was measured at 50 Hz with a DC current of 40 A. Therefore, one could expect a ripple of 0.1 A at 50 Hz for a DC current of 400 A. The magnetic field this corresponds to depends on distance. Typically, in an accelerator environment power cables run parallel to the beam, approximately 1 m away. At this distance, the current ripple corresponds to a magnetic field of 10 nT, which is a significant amplitude. However, because

this variation is at 50 Hz, it should not pose a danger for CLIC.

10.3 Radio-Frequency Systems

The RF systems in an accelerator use electricity from the grid to accelerate a beam. A typical RF system consists of a:

- *Modulator*: This converts AC power from the grid into high-voltage DC pulses.
- *Klystron*: This converts the DC power from the modulator into RF power.
- *Waveguide*: This transports the RF power from the klystron to an accelerating cavity.
- *Accelerating cavity*: This uses the RF power to accelerate the beam.

CLIC uses the drive beam instead of klystrons and modulators to generate RF power for the ML cavities (see Section 2.2.2). However, RF cavities in the DR and RTML and crab cavities in the BDS will use klystrons and modulators to generate RF power.

XBOX3

The XBOX3 test stand [118] is used for the research and development of CLIC accelerating cavities. It provides 200-300 ns RF pulses of 60 MW peak power at a repetition frequency up to 400 Hz. The test stand consists of four Toshiba 6 MW klystrons, which provide 5 μ s pulses, and four Scandinova modulators. The peak power of 60 MW is produced using a combination scheme, which compresses and combines the pulses from a number of klystrons [118].

Two studies were performed at the XBOX3 test stand on the 15th November, 2019. The first was an on/off study to examine the frequency content of the SFs from RF systems and another that looked at SFs from waveguides. A diagram of the layout of XBOX3 is shown in Figure 10.7.

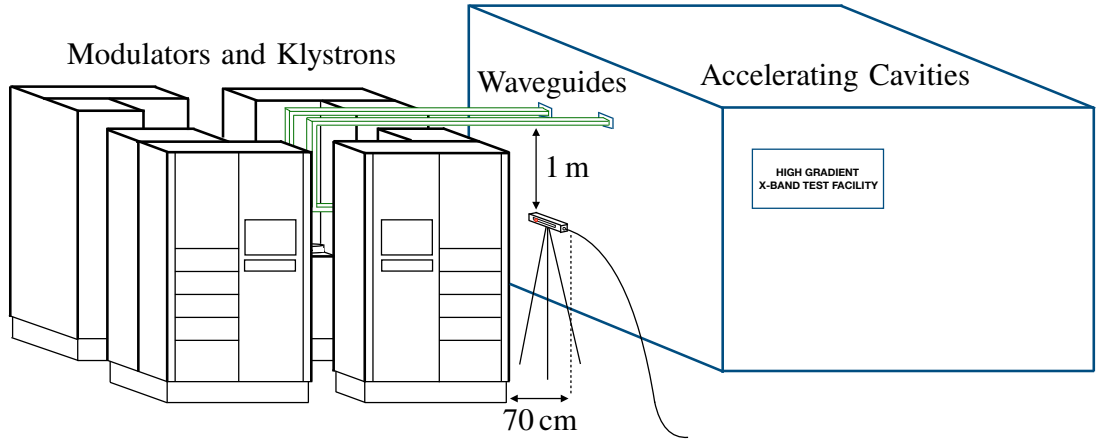


Figure 10.7: Measurement setup to characterise SFs at the XBOX3 test stand. Four CLIC accelerating cavities are housed inside the enclosure shown in blue. The modulators and klystrons are shown in black and the waveguides are shown in green.

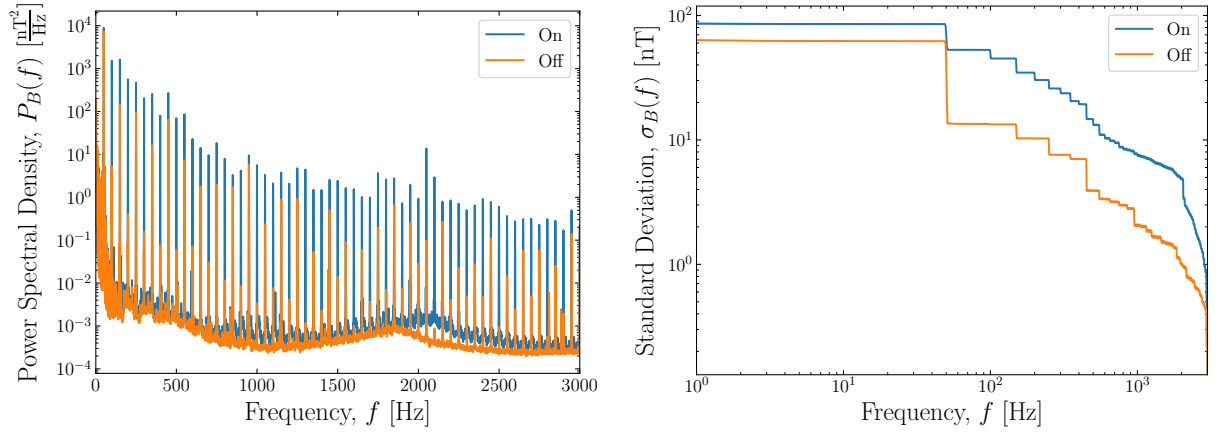


Figure 10.8: Total PSD and standard deviation of the magnetic field vs frequency at the XBOX3 test stand with the RF systems on (blue) and off (orange).

The total PSD of the magnetic field measured in proximity to the RF systems while they were on and off is shown in Figure 10.8. The location of the sensor is shown in Figure 10.7. The PSD with the system on is characteristic of an impulse in the time domain with a repetition frequency of 50 Hz. There is also a slight broadening of peaks at harmonics of 50 Hz when the system is on.

The frequency range of the sensor is up to a few kHz. Therefore, it is unable to measure SFs directly from the RF, which is at a frequency of 12 GHz. Changing the peak power output of the klystrons had no impact on the measured SF. Currents from the discharging of the modulator give rise to the measured SFs. A standard deviation of approximately 20 nT

can be attributed to the modulators.

RF systems operate at the repetition frequency of the beam. Therefore, SFs from RF systems should not pose a danger for CLIC. SFs from RF systems can also be mitigated by placing the klystrons and modulators far from the beamline. Alternatively, they can be surrounded with a magnetic shield.

SFs at XBOX3 were observed even when the modulators were off. These SFs arise from eddy currents induced in the waveguide from the ambient magnetic field. A magnetic field consistent with an AC current of 0.1 A running along the waveguide was measured. To mitigate these SFs the waveguides should be grounded.

CLEAR

An on/off study was performed with the RF systems in the CLEAR beamline on the 4th March, 2019. The on/off measurements were repeated several times. The total PSD of the magnetic field measured approximately 1 m away from the RF cavities in CLEAR is shown in Figure 10.9. The klystrons and modulators are housed in a room above the beamline, approximately 5-10 m away from the sensor.

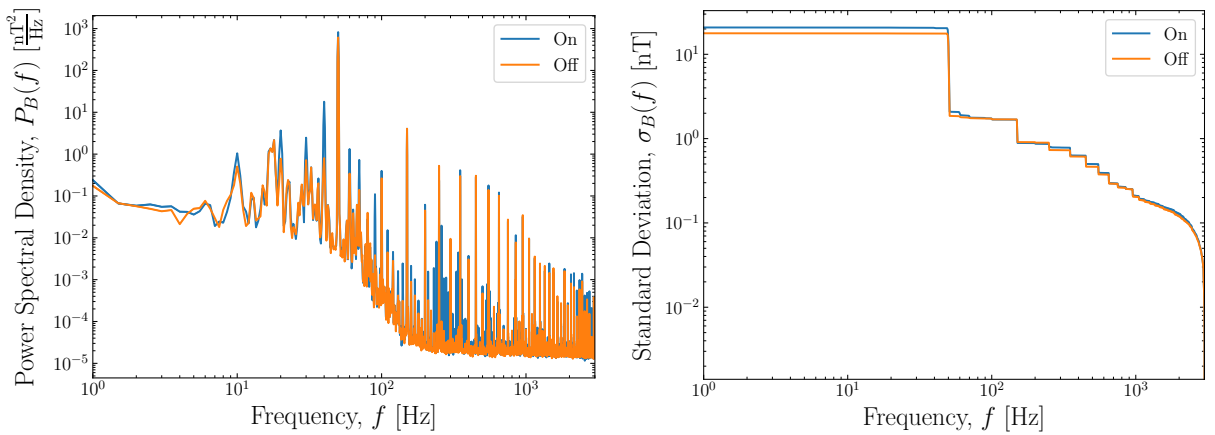


Figure 10.9: Total PSD and standard deviation of the magnetic field vs frequency measured near the RF systems in CLEAR with the systems on (blue) and off (orange).

The RF systems in CLEAR were operating with a repetition frequency of 10 Hz. Figure 10.9 shows the amplitude of the magnetic field at harmonics of 10 Hz has increased. A

standard deviation of a few nT can be attributed to the RF systems.

The RF frequency of the CLEAR cavities is 2 GHz, well beyond the frequency range of the sensor. Therefore, the observed magnetic field is not directly related to the RF inside the cavities. Instead, the SFs are likely to be from the klystrons and modulators.

10.4 Ventilation Systems

Near the CLEAR beamline, there is a room which houses the fans and equipment for the ventilation system - this is the ‘ventilation room’. A one-minute measurement of the magnetic field inside the ventilation room was performed every ten minutes from the 16th March, 2019 to the 26th March, 2019.

A clear pattern emerged in the magnetic field. This pattern was correlated to the temperature of the CLEAR beamline. The standard deviation of the magnetic field and temperature of the CLEAR beamline are shown in Figure 10.10. The variations in the standard deviation are generated by the ventilation system turning on and off, which is triggered by the temperature of the beamline.

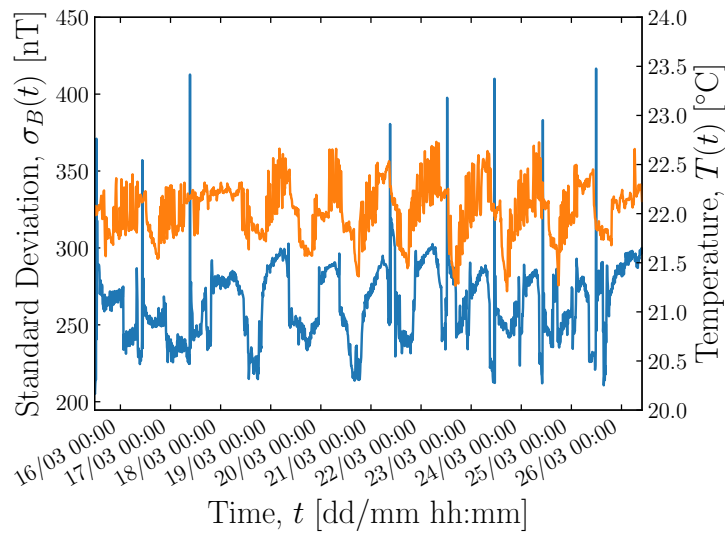


Figure 10.10: Standard deviation of the magnetic field recorded in the CLEAR ventilation room (LH scale, blue) and the temperature of the CLEAR beamline (RH scale, orange) vs time.

Date [dd/mm/yy]	Time, t [hh:mm]	Standard Deviation, σ_B [nT]
15/03/19	12:30	371
16/03/19	10:30	357
17/03/19	9:20	412
21/03/19	9:10	381
22/03/19	12:30	398
23/03/19	11:10	410
24/03/19	10:20	383
25/03/19	11:50	417

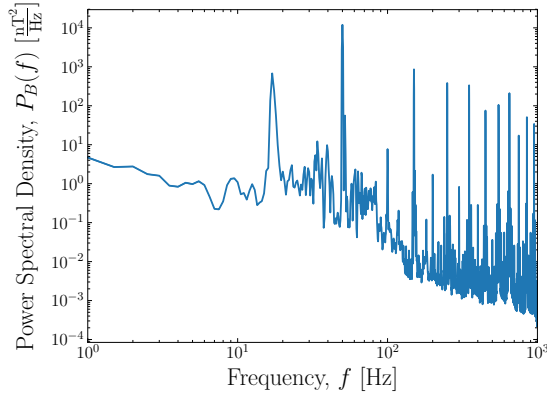
Table 10.2: Date and time of spikes in the standard deviation of the magnetic field measured in the CLEAR ventilation room.

The standard deviation generally remains within 225-300 nT and follows the same oscillations as the temperature in the beamline. However, there are sudden spikes in the magnetic field on most days where the standard deviation almost doubles. There are no two consecutive measurements that both contain the spike, i.e. the large standard deviation disappears within the ten minutes between measurements. The magnitude and time of these spikes are summarised in Table 10.2. The spikes consistently occur during the daytime, usually in the morning. It is possible that spikes in the standard deviation also occurred on the 18th, 19th and 20th March, 2019, but occurred in the ten minutes between measurements.

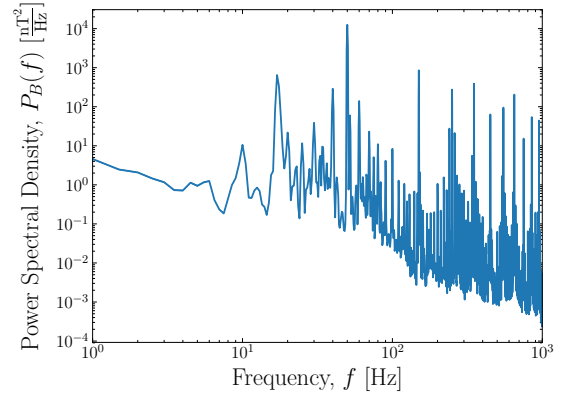
The total PSD with the ventilation system off is shown in Figure 10.11a. When the ventilation system is running there are three different modes which can be distinguished by the frequency content of the magnetic field. These three modes are shown in Figures 10.11b-10.11d. Stage 1 occurs when the ventilation system initially turns on and when it is turning off. The total PSD of the magnetic field then alternates between stages 2 and 3 over cycles of approximately one hour.

The magnetic field measured on the 7th February, 2019 at four locations in the CLEAR beamline is shown in Figure 10.12. The ventilation system was in stage 2 during the time of measurement. There is a clear spatial profile, where the amplitude decreases with distance from the ventilation room. This suggests the source is within the ventilation room.

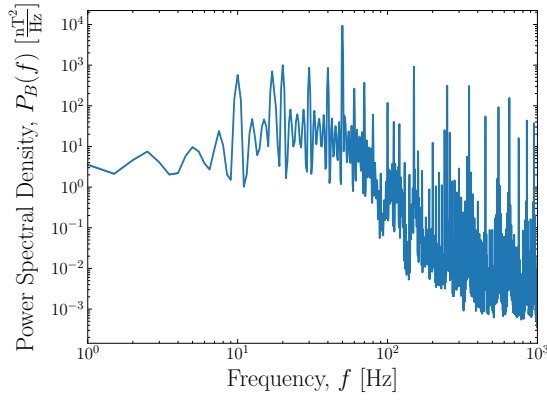
As mitigation, the ventilation system can be housed an appropriate distance from the beamline. Alternatively, in a shielded room to prevent SFs from reaching the beam.



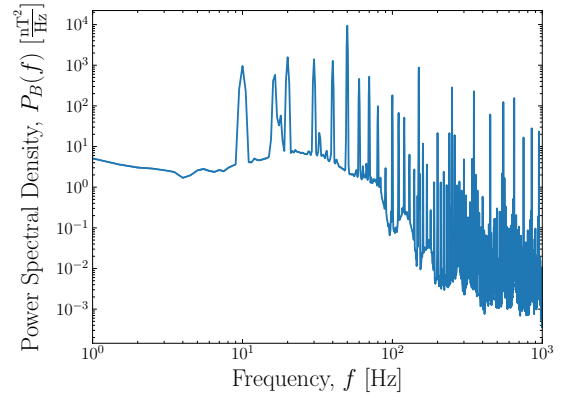
(a) 13:40, 18/03/19 - Ventilation off.



(b) 13:50, 18/03/19 - Ventilation on, stage 1.



(c) 18:20, 18/03/19 - Ventilation on, stage 2.



(d) 18:50, 18/03/19 - Ventilation on, stage 3.

Figure 10.11: Total PSD of the magnetic field vs frequency measured at different times in the CLEAR ventilation room.

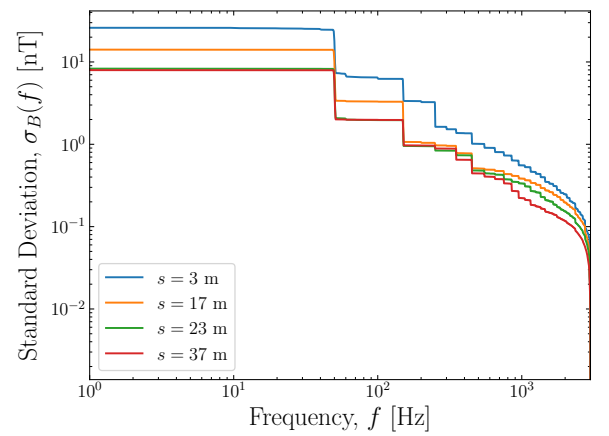
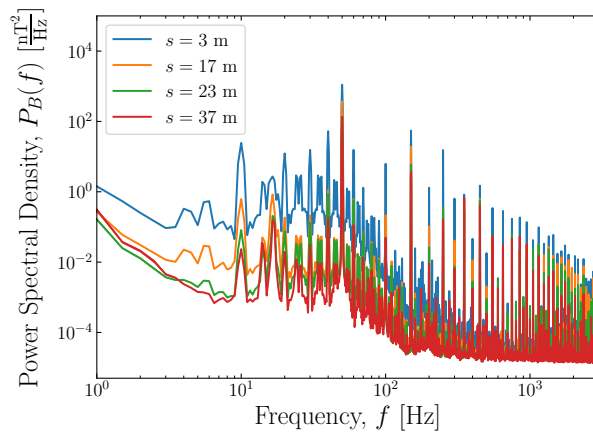


Figure 10.12: Total PSD and standard deviation of the magnetic field vs frequency at different distances s from the CLEAR ventilation room.

10.5 Lights

Measurements were performed to examine SFs from lighting systems in CLEAR. The lighting system includes standard fluorescent light tubes, which are often found in modern buildings. Fluorescent lights contain *rectifiers*, which are devices that convert AC power into DC power [119]. Rectifiers are known to produce strong harmonic distortion [115].

An on/off study was performed on the 30th August, 2019. The measurements were repeated several times with the lights on and off. The total PSD of the magnetic field measured with the lights on and off is shown in Figure 10.13. The ventilation system was off during the measurement.

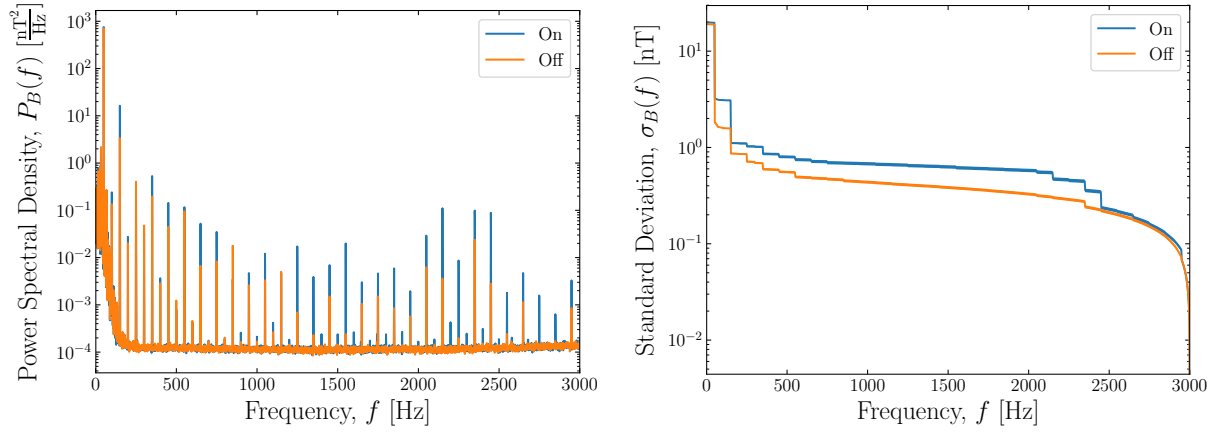


Figure 10.13: Total PSD and standard deviation of the magnetic field vs frequency with the lights on (blue) and off (orange) in CLEAR. The sensor was approximately 1 m away from the lights.

The lights produce SFs at harmonics of 50 Hz. The standard deviation that can be attributed to the lights is small, less than 1 nT. As these SFs are at harmonics of 50 Hz and their amplitude is small, they should not pose a danger for CLIC.

10.6 Other Elements

On/off measurements were performed in CLEAR with vacuum pumps, BPMs and cameras. No significant change in the measured magnetic field could be attributed to these elements. This could be because the sensor was not close enough to the source, the SF is less than the background, or it is not a source. Further measurements are necessary to characterise these elements.

Chapter 11

Stray Magnetic Fields in Accelerator Environments

Chapters 8-10 looked at specific SF sources. This chapter presents measurements of the ambient magnetic field in the vicinity of a live accelerator. Such environments include SFs from all sources (natural, environmental and technical). Two accelerator facilities were surveyed: CLEAR and the LHC.

Measurements at both facilities occurred at a time without beam and did not contain running RF systems. As discussed in Section 10.3, RF systems operate at the repetition frequency of the beam, which means SFs are effectively static to the beam. Therefore, the absence of RF in these measurements is not a serious concern. All other accelerator elements were operational, this includes magnets, vacuum pumps, cooling, ventilation, cryogenics, lighting, etc.

Of interest in this work is the SF seen by the beam. Therefore, measurements should be taken with the sensor inside the beam pipe. However, measuring inside the beam pipe is impractical due to the limited space and access. Accurately positioning and moving the sensor inside the beam pipe is also difficult. The measurements presented in this chapter were taken outside the beam pipe. All known SF sources exist outside the beam pipe, e.g. cables, klystrons, ventilation systems, etc.

11.1 The CLEAR Facility

The ambient magnetic field in the CLEAR facility was surveyed. CLEAR was formerly the CLIC Test Facility 3, and therefore contains elements similar to those that would be used in CLIC. CLEAR is the closest representation of a CLIC-like beamline at CERN.

Measurements

The measurements spanned the full length of the beamline, approximately 41 m. The elements in the beamline are shown in Figure 11.1. There was a wide variety of elements including magnets, BPMs, vacuum pumps, etc. in the beamline. The longitudinal position along the beamline is denoted by s , with $s = 0$ m at the location of the electron gun. The location of the sensors with respect to the beamline is shown in Figure 11.2.

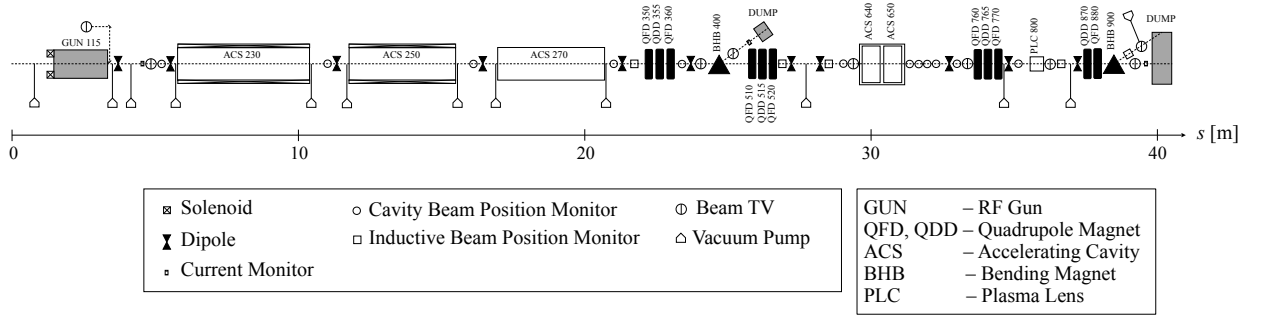


Figure 11.1: Schematic diagram of the elements in the CLEAR beamline. Relative lengths are to scale.

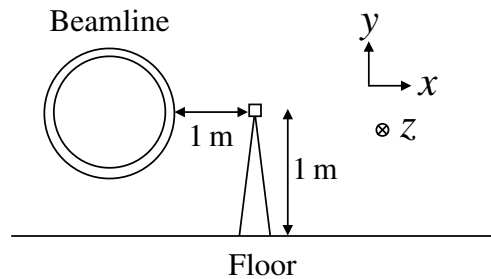


Figure 11.2: Location of sensors with respect to the CLEAR beamline.

The measurements were performed with two sensors and lasted one minute. Each sensor recorded the magnetic field in the three orthogonal directions x , y and z shown in Figure 11.2.

One sensor was kept stationary at $s = 22$ m and the other sensor was moved to a different s -position in between measurements.

The measurements were performed over the course of one hour on the 30th August, 2019. A current of 200 A was supplied to all quadrupoles, which is similar to the currents that would be supplied to CLIC magnets. The ventilation system was turned off to isolate SFs from the beamline.

Power Spectral Density and Standard Deviation

The PSD of the magnetic field in the x , y and z -direction and total PSD is shown in Figure 11.3. Frequencies below 100 Hz have larger amplitudes compared to above 100 Hz. The most prominent peak is at 50 Hz, which arises from the electrical grid.

The sensor was saturated in the region $s = 13$ m to 19 m in the x and z -direction. This saturation is due to the static magnetic field being beyond the detectable range of the sensor. The saturation is suspected to arise from iron in the ground, which has a large remnant magnetic field (see Figure 7.2). The sensor consists of three independent coils. Therefore, the unsaturated y -component is still accurate. The magnetic field variations in this region are likely to be similar to the rest of the beamline, but cannot be measured because of the saturation.

The standard deviation of the magnetic field as a function of position is shown in Figure 11.4. The standard deviation appears to be relatively low for most of the beamline, approximately at the level of 10 nT. There is a large magnetic field source near the electron gun, where the standard deviation is almost 60 nT. Apart from the electron gun, there is no clear correlation between standard deviation and accelerator elements.

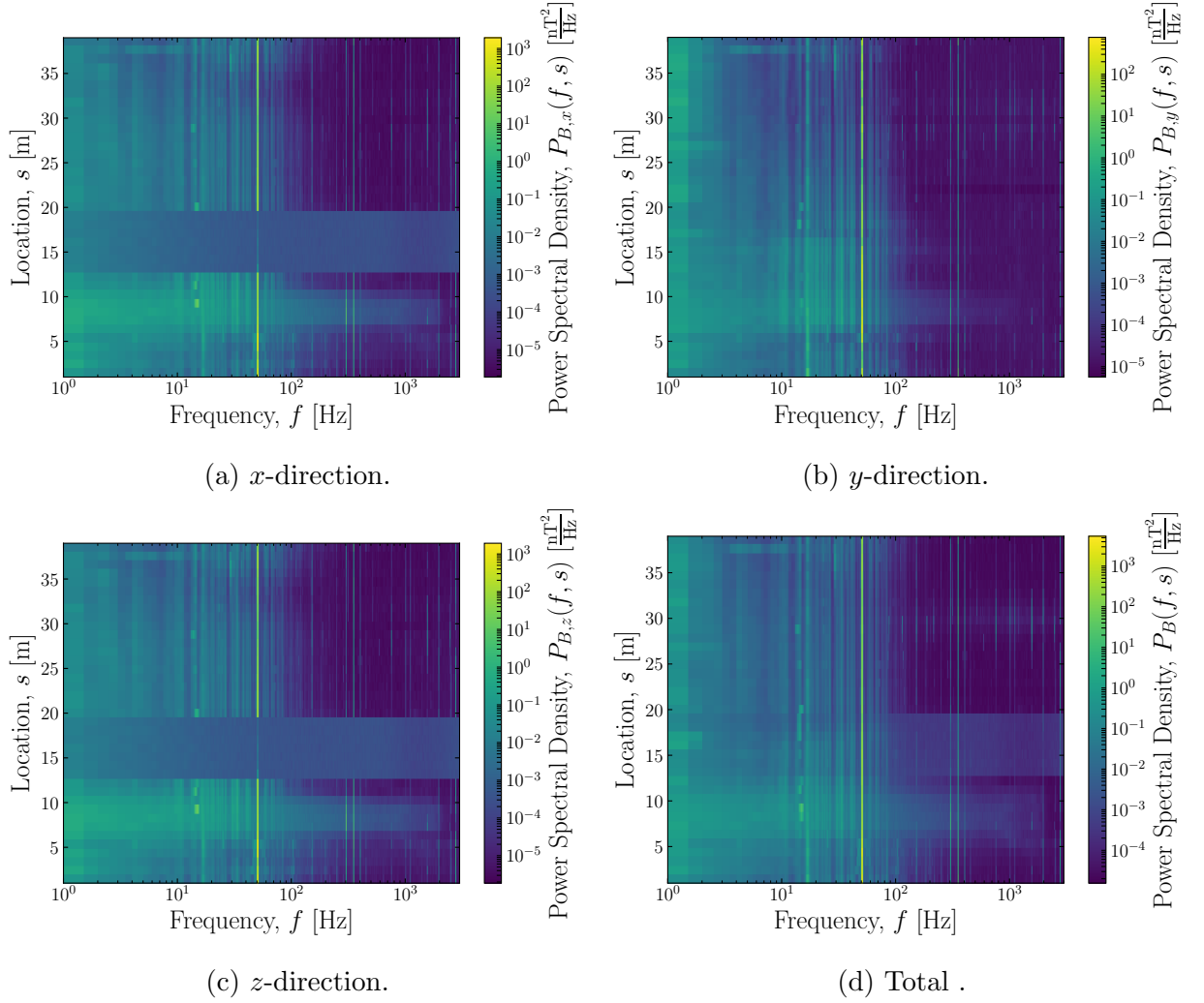


Figure 11.3: PSD of the magnetic field measured in CLEAR (RH scale) vs location (LH scale) and frequency.

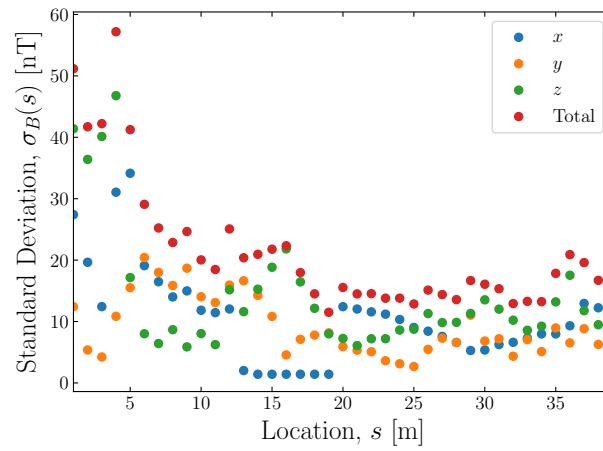


Figure 11.4: Standard deviation of the magnetic field in the x -direction (blue), y -direction (orange), z -direction (green) and total (red) vs position along CLEAR.

Impact of Mitigation

The total PSD averaged over all locations is

$$\overline{P}_B(f) = \frac{1}{M} \sum_{i=1}^M P_B(f, s_i), \quad (11.1)$$

where M is the number of measurement locations. This can be used to represent the PSD of SFs in CLEAR. Locations where the x and z -component were saturated were not included in the average.

The impact of a mitigation technique can be estimated by applying the appropriate transfer function to the PSD of SFs. Figure 11.5 shows the impact of different mitigation techniques on the average total PSD of SFs in CLEAR. Table 11.1 summarises the standard deviation with each mitigation technique.

Without mitigation, the standard deviation is 23 nT. Including the beam trajectory feedback system, the standard deviation is 2.1 nT, which is above the required level of 0.1 nT. The mu-metal shield is the most effective mitigation technique, which reduces the standard deviation to 2 pT. Including the beam trajectory feedback system and mu-metal shield, the standard deviation is 0.5 pT.

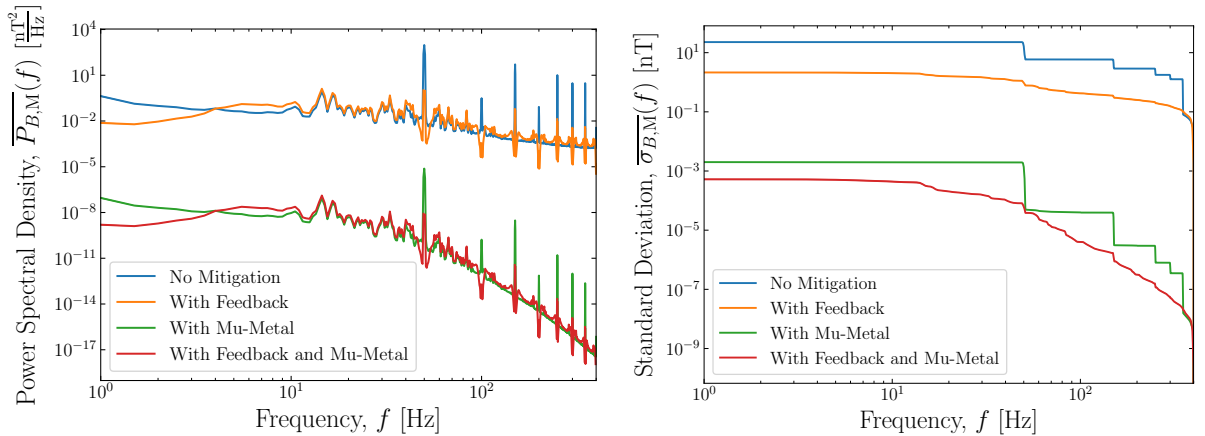


Figure 11.5: Average total PSD and standard deviation of the magnetic field vs frequency measured in CLEAR: without mitigation (blue); including a beam trajectory feedback system with a gain of $m = 2.5$ (orange); including a 1 mm mu-metal shield (green) and with the feedback system and mu-metal shield combined (red).

Mitigation	Standard Deviation, $\overline{\sigma_{B,M}}$ [nT]
None	23
Feedback System	2.1
Mu-Metal Shield	2.0×10^{-3}
Feedback System + Mu-Metal Shield	0.5×10^{-3}

Table 11.1: Standard deviation of the magnetic field in CLEAR with different mitigation techniques.

11.2 The LHC

The LHC represents a realistic magnetic environment for an accelerator. Although the LHC and CLIC utilise different technologies: the LHC contains superconducting magnets, whereas CLIC is a normal conducting machine, they are both located at CERN and are at the same depth underground.

Measurements

The ambient magnetic field was measured near the CMS detector, this is point 5 of the LHC. Specifically, the measurements were taken in LSS5, which is the long straight section preceding the CMS detector. The measurements were performed on the 29th April, 2019 during long shutdown 2.

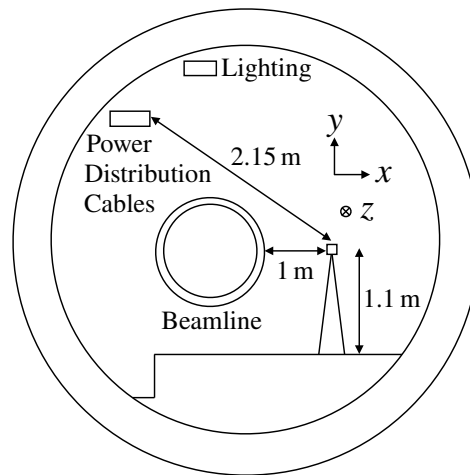


Figure 11.6: Location of the sensors in the LHC tunnel with respect to the beamline.

The measurement procedure involved placing the four sensors on a parallel line alongside the beamline at different longitudinal positions, denoted by s . A diagram of the placement of the sensors is shown in Figure 11.6. They were approximately 1 m away from the beamline. The magnetic field in three orthogonal directions: x , y and z in Figure 11.6, was measured. Each measurement lasted one minute. The sensors were then moved to a new location in between measurements. A 40 m section of the beamline was mapped with a spacing of 1 m between sensors. One sensor was kept stationary as a reference at $s = 30$ m.

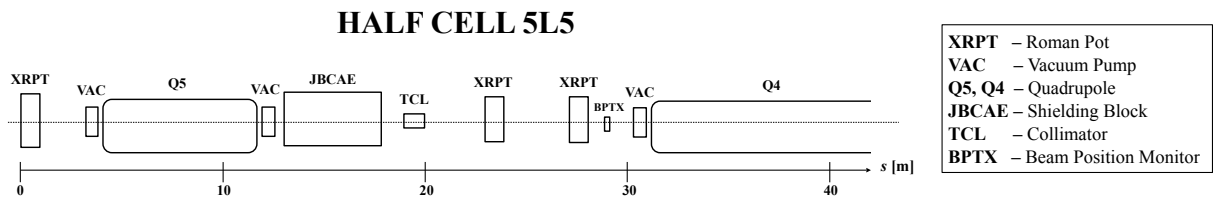


Figure 11.7: Schematic diagram of the elements in the beamline near point 5 of the LHC. Relative lengths are to scale.

Beamline Description

A schematic diagram of the elements in the beamline is shown in Figure 11.7. The beamline includes:

- Two roman pots (XRPT), which are particle detectors used for machine protection [120].
- Three vacuum pumps (VAC), which are used to maintain the vacuum inside the beam pipe.
- Two quadrupoles (Q5, Q4). These are the fifth and fourth closest quadrupoles to the IP at CMS.
- One concrete shielding block (JBCAE).
- One collimator (TCL), which is used to collimate the beam before collision.
- One BPM (BPTX).

Power Spectral Density and Standard Deviation

The PSD of the magnetic field in the x , y and z -direction and total PSD is shown in Figure 11.8. The x and y -components are relatively homogeneous over the length of the beamline. The z -component has the smallest amplitude. The most prominent peaks are at harmonics of 50 Hz, which are from the electrical grid. Frequencies close to 1 Hz also have large amplitudes.

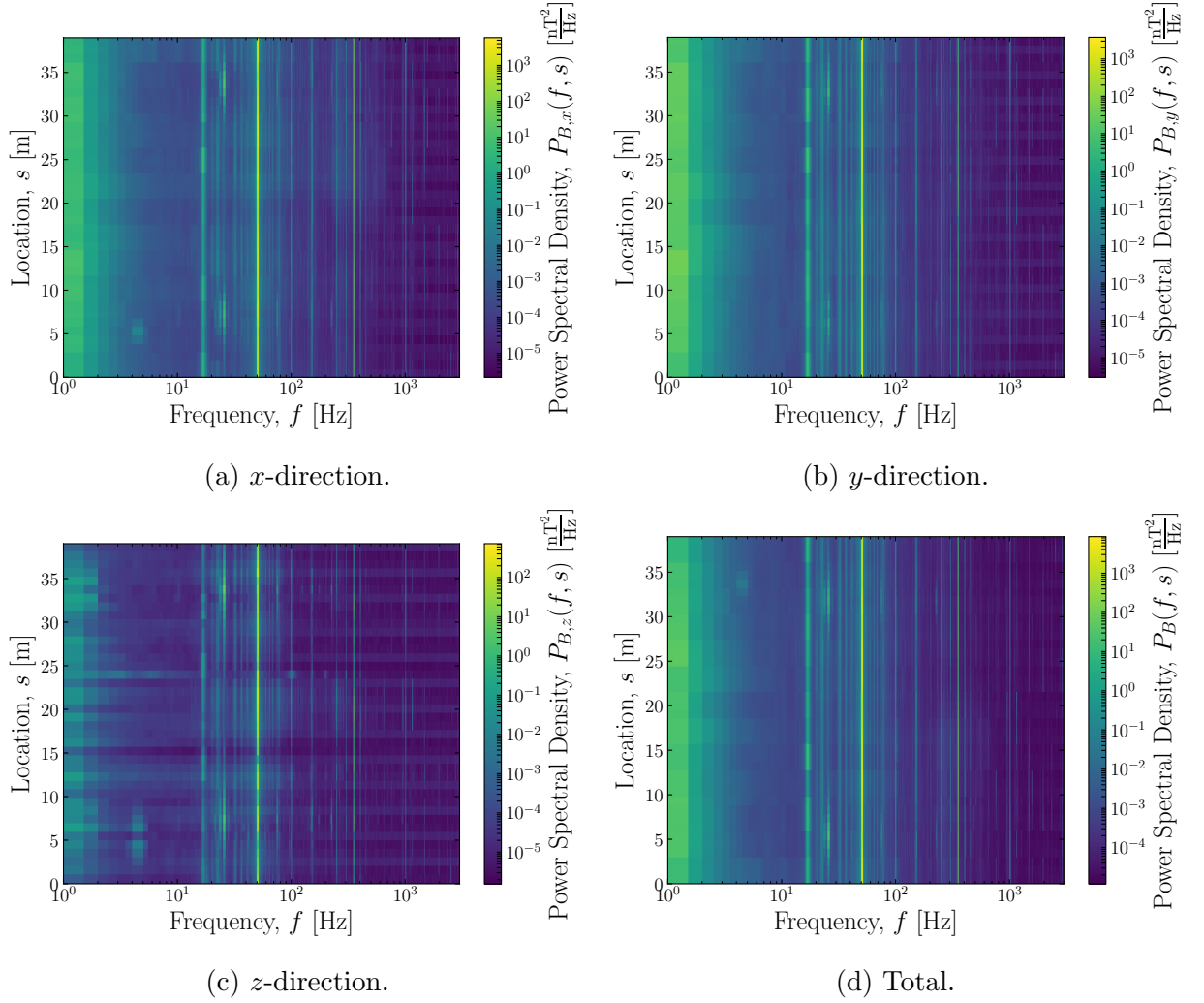


Figure 11.8: PSD of the magnetic field measured in the LHC tunnel (RH scale) vs location (LH scale) and frequency.

The smallest, largest and average total PSD is shown in Figure 11.9. The average total PSD was calculated with Equation (11.1). The largest magnetic field was measured at $s = 13$ m, which is near the concrete block (JBCAE), and the smallest magnetic field was measured at $s = 5$ m, which is just before a quadrupole (Q5).

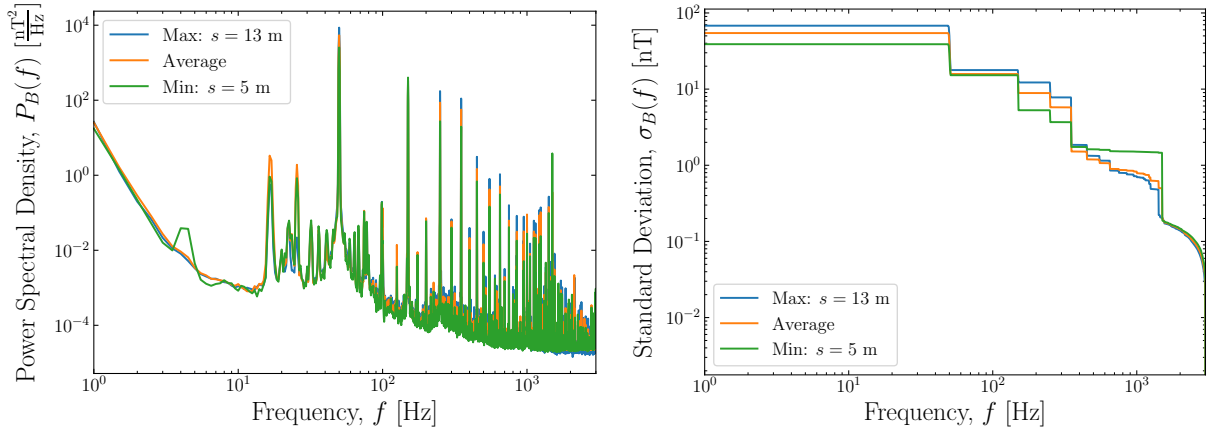


Figure 11.9: Largest (blue), average (orange) and smallest (green) total PSD and standard deviation of the magnetic field vs frequency measured in the LHC tunnel.

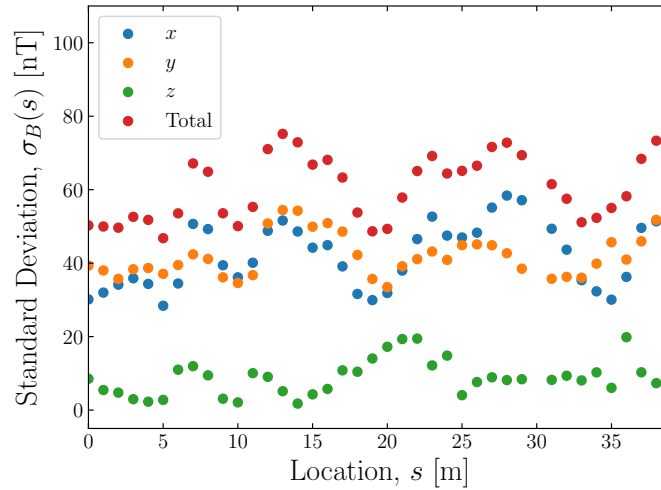


Figure 11.10: Standard deviation of the magnetic field in the x -direction (blue), y -direction (orange), z -direction (green) and total (red) vs position along the LHC beamline.

The standard deviation of the magnetic field as a function of position is shown in Figure 11.10. There is no clear correlation between the standard deviation and the location of elements.

The amplitude of the magnetic field in the x and y -direction is similar and the smallest component is in the z -direction. This is consistent with a line current running in the z -direction. Assuming the line current is at the location of the power distribution cables in Figure 11.6, the measurements are consistent with a net current of approximately 0.5 A running along the cables. This is a relatively modest current, which suggests there must be a cancellation effect from currents flowing in opposite directions in different cables.

Specific Peaks

Most significant peaks in the PSD are in the frequency range 0-200 Hz. Above 200 Hz, the only significant peaks are the harmonics of 50 Hz. Figure 11.11 identifies *specific peaks* in the range 0-200 Hz. The PSD in Figure 11.11 is the average total PSD measured by the reference sensor,

$$\overline{P_{B,\text{ref}}}(f) = \frac{1}{M} \sum_{i=1}^M P_{B,i}(f, s_{\text{ref}}), \quad (11.2)$$

where $P_{B,i}(f, s_{\text{ref}})$ is PSD of the i^{th} measurement made by the reference sensor and M is the number of measurements.

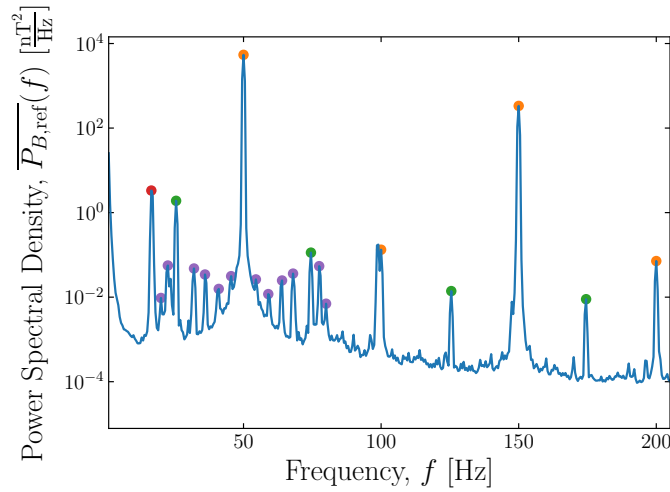


Figure 11.11: Average total PSD of the magnetic field vs frequency measured by the reference sensor in the LHC tunnel (blue) with significant peaks highlighted: harmonics of 50 Hz (orange); 16.7 Hz peak (red); peak from modulation (green and purple).

The peaks can be divided into four groups related to their suspected origin. The orange peaks at harmonics of 50 Hz are characteristically from the electrical grid. The red peak at 16.7 Hz is also suspected to originate from the electrical grid. The peaks that are symmetric around the 50 Hz and 100 Hz, i.e. the purple and green peaks, arise from the amplitude modulation of the carrier frequency, which are suspected to originate from the power converters. The precise frequency of the specific peaks is summarised in Table 11.2.

Colour	Frequency, f [Hz]
Orange	49.989, 98.776, 149.961, 199.954
Red	16.697
Green	25.514, 125.497
Purple	74.540, 174.424
Purple	20.039, 22.339, 31.945, 36.157, 40.801, 45.443
Purple	79.979, 77.642, 68.037, 63.816, 59.197, 54.521

Table 11.2: Precise frequency of the peaks in Figure 11.11. The error on each frequency is ± 0.004 Hz.

Dynamic Power Spectral Density

Each measurement was over a one-minute period. In this period, SF sources may be switched on or off, which could lead to peaks appearing or disappearing over the course of the measurement. The PSDs in the previous section would not observe this because they display an average over the one-minute measurement. A *dynamic PSD* can be used to examine the temporal behaviour. A dynamic PSD calculates a PSD with a short segment of the signal as a function of time.

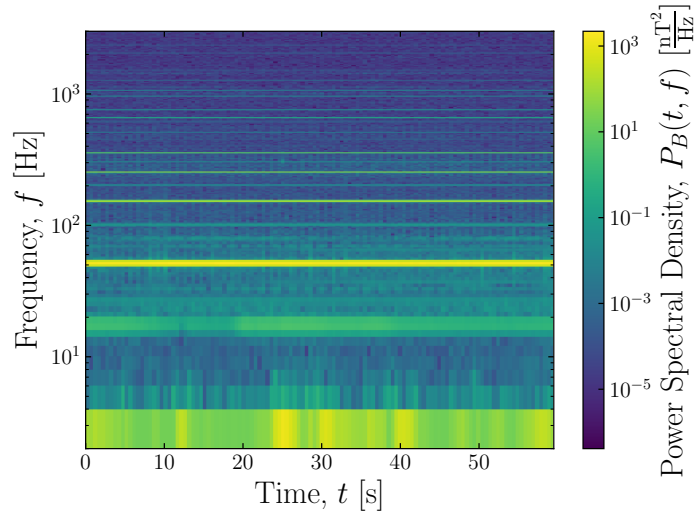


Figure 11.12: Total PSD of the magnetic field measured in the LHC tunnel (RH scale) vs frequency (LH scale) and time.

The dynamic total PSD of the magnetic field recorded by the reference sensor in one of the measurements is shown in Figure 11.12. A period of 0.5 s was used to calculate the PSD at each instance in time. It is clear the frequency of the peaks are stable for the duration of

one minute. Very low frequencies, close to 1 Hz, show some power variation over one minute. The variation does not seem to be periodic.

Reference Sensor Standard Deviation

The reference sensor at $s = 30$ m can be used to examine the temporal variation over the course of the measurements. The standard deviation of the magnetic field measured by the reference sensor is shown in Figure 11.13. The variation in the standard deviation is fairly random. The range is a few nT.

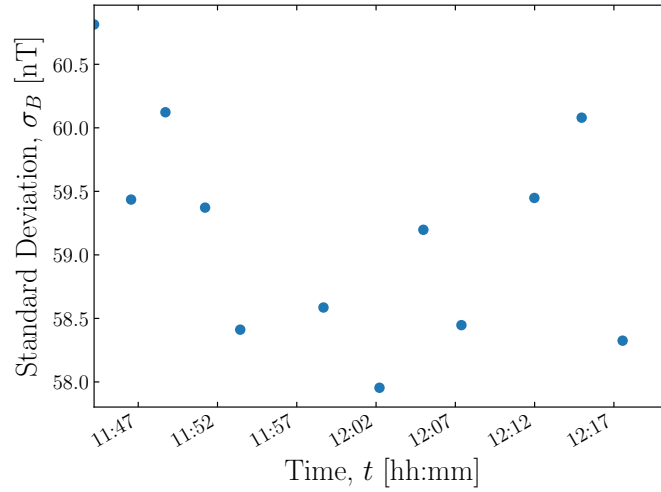


Figure 11.13: Standard deviation of the magnetic field vs time measured by the reference sensor at $s = 30$ m in the LHC tunnel.

Normalised Power Spectral Density

Magnetic field maps were measured with a limited number of sensors (four). Therefore, not all measurements at the 40 locations are simultaneous. This can lead to a temporal variation of the amplitude appearing as a spatial variation. The temporal variation can be removed by normalising the PSD by the PSD measured at the reference location,

$$P_{B,n}(f, s) = \frac{P_B(f, s)}{P_B(f, s_{\text{ref}})}, \quad (11.3)$$

where $P_B(f, s)$ is the PSD measured at location s . Performing such a normalisation relies on the temporal variation being common for the measurement and reference location. A value of one corresponds to the same amplitude being recorded at the measurement and reference location.

Figure 11.14 shows the normalised total PSD across the section. Most of the section has the same amplitude as the reference. There are two hot spots at the location of Q4 and Q5 where the normalised total PSD is much greater than one. These hot spots are at the frequencies 25, 75, 125 and 175 Hz. Q4 and Q5 are suspected to emit these SFs. Previous measurements of SFs from power cables for magnets (Section 10.2) show SFs at these frequencies.

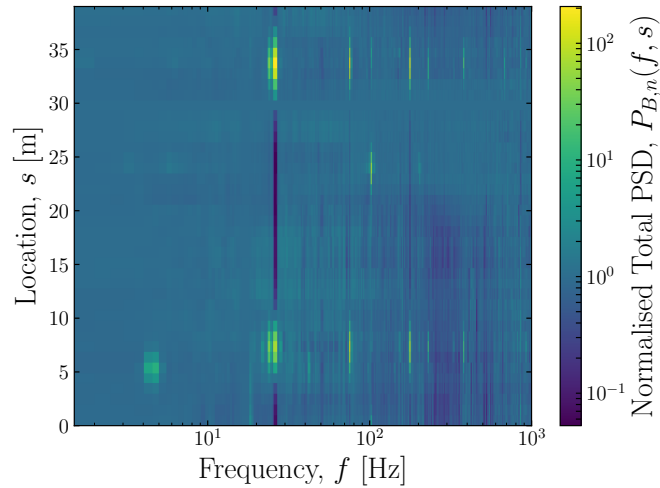


Figure 11.14: Normalised total PSD of the magnetic field measured in the LHC tunnel (RH scale) vs location (LH scale) and frequency.

The normalised total PSD describes the SF amplitude with respect to the reference sensor. A SF is described as a standing wave with a sinusoidal temporal variation. A normalised total PSD of one does not mean the value of the SF is the same at each location, rather the amplitude is the same. The SF value can be different due to a phase difference.

Correlation

The correlation describes the phase difference between two signals (see Appendix A). It takes a value between -1 and +1. A value of +1 occurs when there is a phase difference of zero

and -1 occurs when there is a phase difference of 180° . The correlation is only meaningful if the signals are coherent (i.e. the phase difference remains constant). The correlation has a value of zero if there is a phase difference of 90° or if the signals are incoherent.

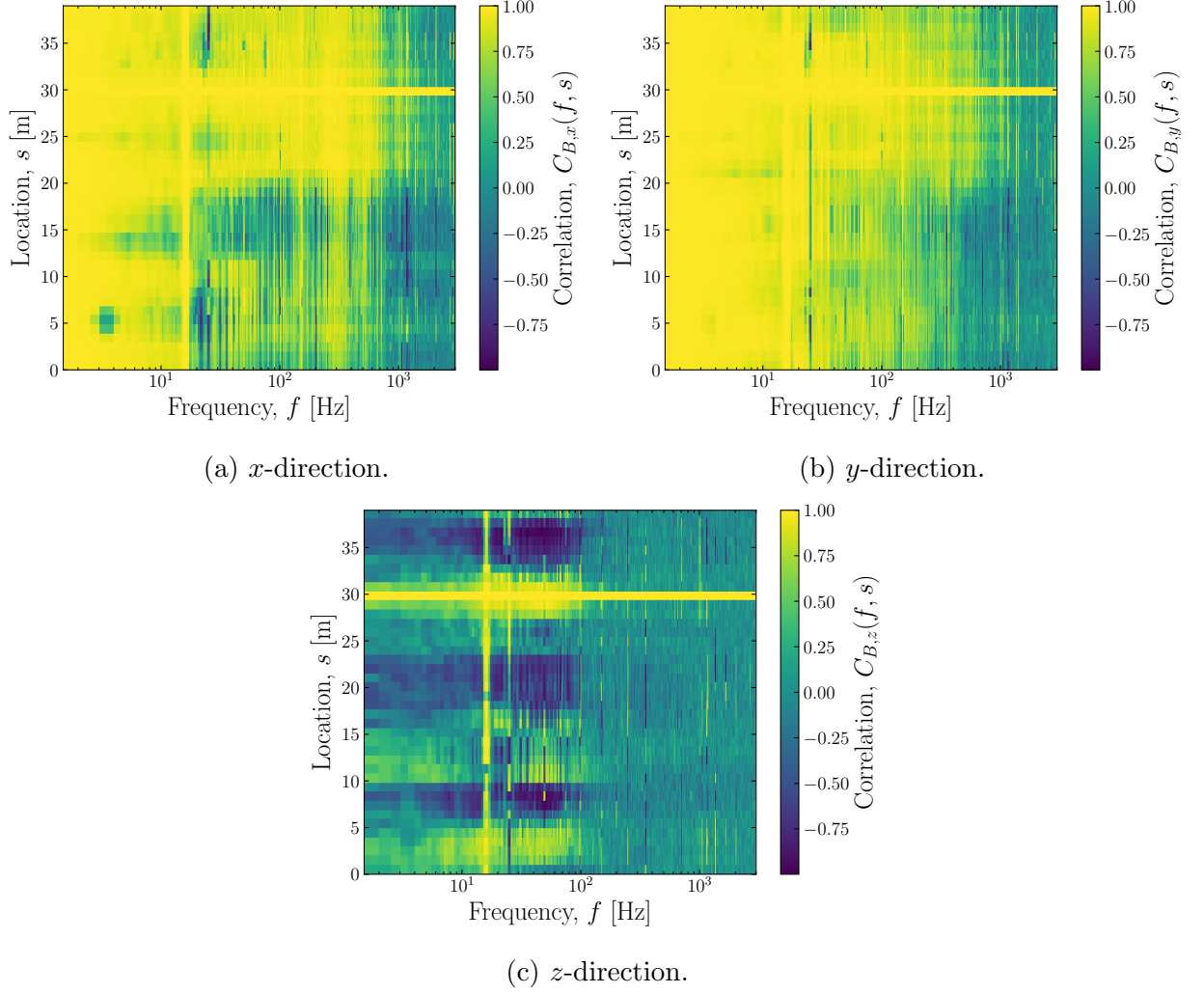


Figure 11.15: Correlation of the magnetic field with respect to a reference sensor at $s = 30$ m measured in the LHC tunnel (RH scale) vs location (LH scale) and frequency.

The correlation of the magnetic field in the x , y and z -direction with respect to the reference sensor at $s = 30$ m is shown in Figure 11.15. The magnetic field is highly correlated for low frequencies (below 10 Hz) in the x and y -direction. In the z -direction the magnetic field flips direction several times. This is consistent with elements in the beamline with a high iron content attracting the magnetic field. The locations of anti-correlated motion coincide with the minima of standard deviation shown in Figure 11.10.

Coherence

A coherence spectrum can be used to examine whether different frequencies have a constant phase difference (see Appendix A). A signal is said to be *incoherent* if the coherence is close to zero and *coherent* if the coherence is close to one. The coherence gives no information regarding the value of the phase difference.

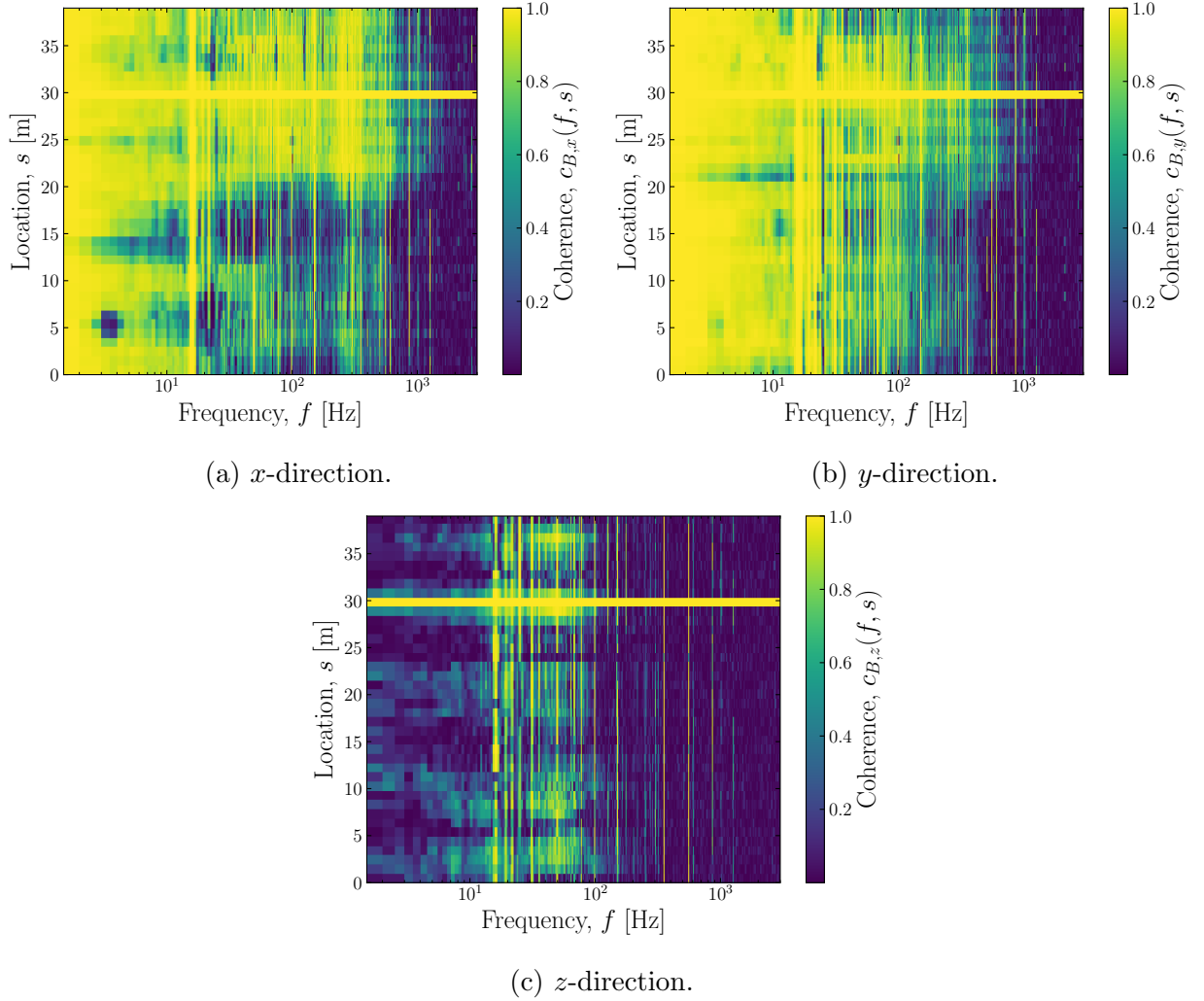


Figure 11.16: Coherence of the magnetic field with respect to a reference sensor at $s = 30$ m measured in the LHC tunnel (RH scale) vs location (LH scale) and frequency.

The coherence of the magnetic field in the x , y and z -direction with respect to the reference sensor at $s = 30$ m is shown in Figure 11.15. In the x and y -direction, the magnetic field is coherent for low frequencies (below 10 Hz) and incoherent for high frequencies (above 1 kHz). In between the magnetic field is coherent for length scales of 10 m. In the z -direction, there is generally low coherence. In the frequency range 10-100 Hz, there are small hot spots

of coherence scattered along the beamline. Outside of the range 10-100 Hz the magnetic field is completely incoherent.

Impact of Mitigation

Figure 11.17 shows the effect of different mitigation techniques on the average total PSD of the magnetic field in the LHC tunnel. The average total PSD was calculated with Equation (11.1). Table 11.3 summarises the standard deviation of the magnetic field with each mitigation technique.

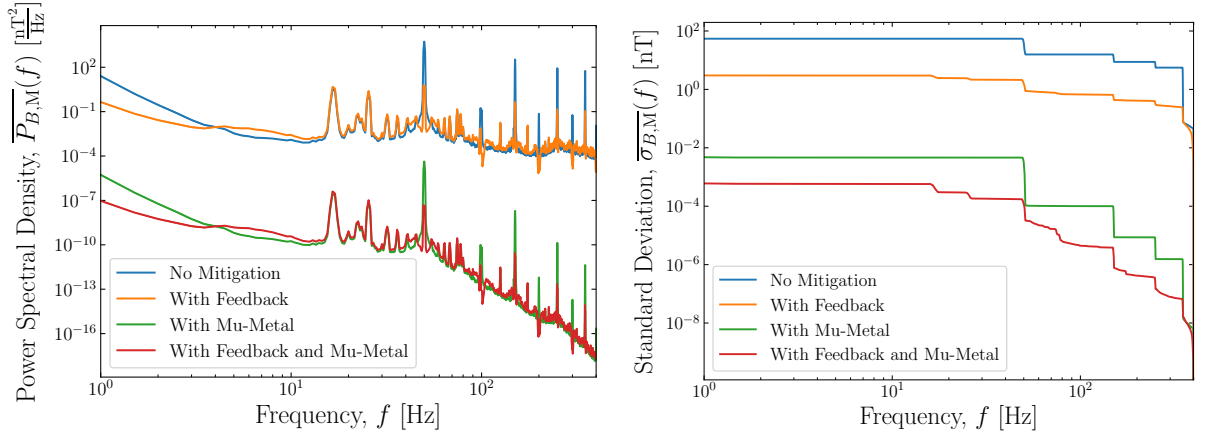


Figure 11.17: Average total PSD and standard deviation of the magnetic field vs frequency measured in the LHC tunnel: without mitigation (blue); including a beam trajectory feedback system with a gain of $m = 2.5$ (orange); including a 1 mm mu-metal shield (green) and with the feedback system and mu-metal shield combined (red).

Mitigation	Standard Deviation, $\overline{\sigma_{B,M}}$ [nT]
None	54
Feedback System	3.0
Mu-Metal Shield	4.6×10^{-3}
Feedback System + Mu-Metal Shield	0.6×10^{-3}

Table 11.3: Standard deviation of the magnetic field in the LHC tunnel with different mitigation techniques.

Without mitigation there is a standard deviation of 54 nT. The beam trajectory feedback system reduces the SF to a standard deviation of 3 nT. The feedback system alone is not enough to mitigate the SF. The mu-metal shield is an extremely effective mitigation tech-

nique. The standard deviation of the SF including the mu-metal shield is 4.6 pT. For the beam trajectory feedback system and mu-metal shield combined, the standard deviation is 0.6 pT.

11.3 Modelling

Developing a realistic model for SFs in CLIC is challenging. Ultimately, a model must be developed from dedicated measurements after construction.

SF measurements at CLEAR and in the LHC tunnel were described in Sections 11.1 and 11.2. Both facilities have similar amplitudes. Unfortunately, a section of the CLEAR beamline could not be mapped due to the static component of the magnetic field saturating the sensor. Therefore, the CLEAR measurements are only over a limited distance. This makes developing a model from the CLEAR measurements difficult.

This section develops a two-dimensional PSD model for SFs based on the LHC measurements. There are two characteristics of SFs that must be accurately captured in the model: the amplitude and the spatial correlation.

Amplitude

The amplitude of the magnetic field measured in the LHC tunnel was similar in the two transverse directions to the beam (x and y in Figure 11.6). The y -component measurements will be used to develop a model. The average PSD of the magnetic field in the y -direction measured by the reference sensor is shown in Figure 11.18.

Figure 11.8 shows the amplitude is relatively constant over the measured section. Therefore, a PSD measured at one location can be representative of the amplitude across the entire section. The PSD shown in Figure 11.18 will be used to characterise the PSD of SFs. The standard deviation of the SF is approximately 30 nT.

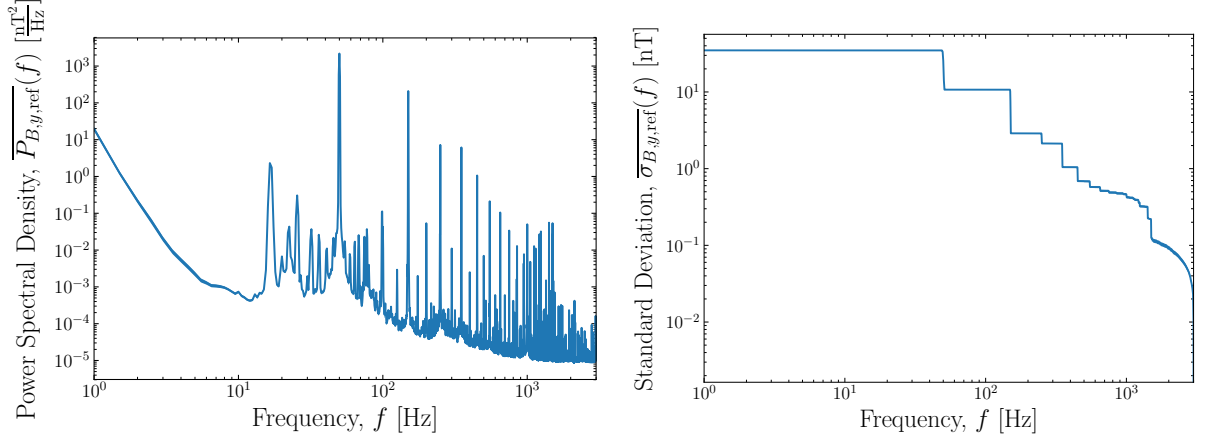


Figure 11.18: SF PSD and standard deviation in an accelerator environment vs frequency.

Correlation

The SF model should reproduce the correlation shown in Figure 11.15b. There are three different regions in Figure 11.15b:

- Frequencies below 10 Hz, which are highly correlated over the section.
- Frequencies between 10 Hz and 400 Hz, which are correlated over length scales of 10 m.
- Frequencies above 400 Hz, which are uncorrelated.

Two-Dimensional Power Spectral Density

The SF is described as a set of modes, each with a particular frequency f_i and wavelength λ_j (or equivalently wavenumber $k_j = 2\pi/\lambda_j$). The two-dimensional PSD determines the amplitude of each mode as

$$a_{ij} = \sqrt{2}\sigma_{B,ij} = \sqrt{2 \int_{k_j}^{k_{j+1}} \int_{f_i}^{f_{i+1}} P_B(f, k) df dk} \approx \sqrt{2P_B(f_i, k_j)\Delta f \Delta k}, \quad (11.4)$$

where $\sigma_{B,ij}$ is the standard deviation of each mode, $\Delta f = f_{i+1} - f_i$ and $\Delta k = k_{j+1} - k_j$.

Wavenumber Distribution

The PSD in Figure 11.18 characterises the power distribution over different frequencies. To calculate a two-dimensional PSD, the power in each frequency must be distributed over different wavenumbers. The distribution over wavenumbers determines the spatial correlation of the SF. If there are many modes of differing wavenumber, their superposition leads to an uncorrelated SF. Whereas if the modes have similar wavenumbers, the SF is highly correlated.

Simultaneous measurements at many locations are required to determine the wavenumber spectrum. However, only a maximum of four sensors was available for measurements. This is not enough to parameterise a wavenumber spectrum from measurements.

A particular functional form for the wavenumber spectrum must be assumed. One can intuitively choose a wavenumber spectrum by considering different spatial profiles one wishes to produce. For example, a completely random spatial variation at each location corresponds to a uniform wavenumber spectrum. The integral of the wavenumber spectrum must be finite, otherwise it corresponds to a process with infinite power, which is not physical.

A Gaussian function was used to distribute power over different wavenumbers. The power density of a mode with frequency f_i and wavenumber k_j is given by

$$P_B(f_i, k_j) = P_B(f_i) \sqrt{\frac{2}{\pi\alpha^2}} \exp\left(-\frac{k_j^2}{2\alpha^2}\right), \quad (11.5)$$

where $P_B(f_i)$ is the power density of frequency mode i and α is half the width of the distribution. The factor $\sqrt{2/(\pi\alpha^2)}$ was introduced to ensure the two-dimensional PSD correctly recovers the one-dimensional PSD $P_B(f)$ after integrating over all wavenumbers,

$$P_B(f) = \int_0^\infty P_B(f, k) dk. \quad (11.6)$$

The half width α is parameterised from measurements to produce a desired spatial correlation. A small value for α produces a SF which is correlated over large distances, whereas a

large value for α produces a SF which is only correlated over short distances. The following widths were found to reproduce the correlation measured in the LHC tunnel,

$$\alpha = \begin{cases} 0.002\pi & \text{for } f \leq 10 \text{ Hz}, \\ 0.04\pi & \text{for } 10 \text{ Hz} < f \leq 400 \text{ Hz}, \\ 0.5\pi & \text{for } f > 400 \text{ Hz}. \end{cases} \quad (11.7)$$

Generator

The SF is represented as a grid of zero length dipoles. The purpose of the generator is to calculate the kick applied by each dipole. With a dipole spacing of 1 m, only wavelengths of $\lambda_{\min} > 2 \text{ m}$ can be represented. This corresponds to a maximum wavenumber of $k_{\max} = 2\pi/\lambda_{\min} = \pi$.

The SF is modelled as a standing wave. The SF at location s and time t is given by

$$B(s, t) = \sum_i \sum_j a_{ij} \cos(k_j s + \theta_j) \cos(2\pi f_i t + \phi_{ij}), \quad (11.8)$$

where θ_j and ϕ_{ij} are uniformly distributed random numbers between 0 and 2π . The computational efficiency of calculating Equation (11.8) can be improved by calculating a time-dependent amplitude,

$$A_{ij}(t) = a_{ij} \cos(2\pi f_i t + \phi_{ij}), \quad (11.9)$$

and calculating the SF as

$$B(s, t) = \sum_i \sum_j A_{ij}(t) \cos(k_j s + \theta_j). \quad (11.10)$$

This significantly reduces the computation time because $A_{ij}(t)$ only needs to be calculated once per time step.

The SF in the horizontal and vertical direction is calculated independently with different random phases θ_j and ϕ_{ij} . The SF kick applied by each dipole is calculated using

Equation (5.11) taking into account the beam direction with respect to the SF.

The generator was used to sample the SF in a 40 m section of the beamline. Figure 11.19 shows the PSD and correlation of the SF from the generator. The generator is able to accurately reproduce the features measured in the LHC tunnel.

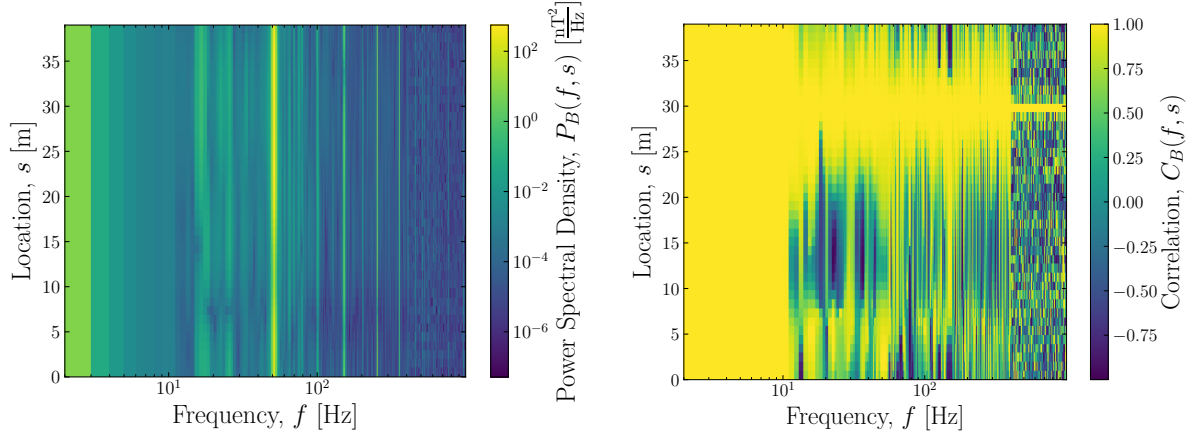


Figure 11.19: A sample from the generator. Left: SF PSD (RH scale) vs location (LH scale) and frequency. Right: correlation with respect to the SF at $s = 30$ m (RH scale) vs location (LH scale) and frequency.

Comparison to Ground Motion Models

The PSD of different GM models are shown in Figure 4.1. The PSD of GM and SFs are very different. The noise floor of the GM PSD decays very rapidly, approximately as $1/f^4$, whereas the noise floor of the SF PSD looks flat. The SF PSD also has a high number of narrowband peaks, whereas the GM PSD has a one or two broadband peaks.

The modelling of SFs is based on a different physical picture to the models for GM. In GM, the frequency and wavelength of the waves are related by Equation (4.3). Such a description means the temporal and spatial variation of GM are related. I.e. waves with long wavelengths must also be waves with low frequencies. This is not the case for SFs. The frequency does not determine the wavelength. In the modelling of SFs, for any given frequency there are waves with all possible wavelengths. The amplitude of each wave is chosen to produce the desired characteristics.

11.4 Integrated Simulations

The two-dimensional PSD model described above was used in integrated simulations of CLIC at $E_{\text{CM}} = 380 \text{ GeV}$. Table 11.4 shows the luminosity loss including a beam trajectory feedback system with a gain of $m = 2.5$ and a 1 mm mu-metal shield in sensitive regions (VT, LTL, ECS and FFS).

Using NTE, there is a significant luminosity loss of 43% without mitigation, 15% if only the beam trajectory feedback system is used or 2% if only a mu-metal shield is used. The combined use of a beam trajectory feedback system and mu-metal shield is very effective, which using NTE reduces the luminosity loss to 0.4%.

Mitigation	Luminosity Loss, $\Delta\mathcal{L}/\mathcal{L}_0$ [%]
Using STE	
None	57
Feedback System	31
Mu-Metal Shield	3.4
Feedback System + Mu-Metal Shield	1.0
Using NTE	
None	43
Feedback System	15
Mu-Metal Shield	2.0
Feedback System + Mu-Metal Shield	0.4

Table 11.4: Luminosity loss due an accelerator environment SF. Values are expressed as a percentage of Equation (3.3) for NTE or Equation (3.5) for STE. The error on each value is less than 0.1%.

Chapter 12

Design Choices

This chapter describes the design choices in CLIC relating to dynamic imperfections. The proposed mitigation strategy is summarised along with alternative options. The feasibility of an alternative high-luminosity design is discussed. The key changes from the first stage to the final high-energy stage are described along with the impact of dynamic imperfections.

12.1 Mitigation Options

The effectiveness of various mitigation systems for dynamic imperfections was described in the previous chapters. This section proposes a consistent and effective strategy for mitigating the combined effects of GM and SFs in CLIC. The advantages and disadvantages of alternative options are also discussed.

Beam Trajectory Feedback System

The beam trajectory feedback system will be an essential part of CLIC to cure beam jitter and limit emittance growth in the machine. This feedback system will amplify perturbations to the beam at some frequencies while suppressing others. Generally, the feedback system is good at suppressing perturbations that are slow compared to the repetition frequency. The

gain of the feedback system can be optimised to maximise its impact. The gain must be chosen carefully to ensure the collective impact of dynamic imperfections is mitigated.

The optimum gain in the real machine depends on the level of GM and SFs in the CLIC tunnel. Measurements after construction will be used to develop the exact model for GM and SFs in CLIC. However, an optimum gain can be estimated from simulations using current models for GM and SFs.

A gain of $m = 2.5$ was used in this work, which was optimised to minimise the luminosity loss from GM model D. This model represents the highest level of GM CLIC can expect to experience. The transfer function of the beam trajectory feedback system is shown in Figure 4.2. With a gain of $m = 2.5$, the feedback system is effective at mitigating frequencies below 1 Hz but amplifies frequencies in the range 4-25 Hz. As shown in Figure 11.18, there are significant peaks at these frequencies in the PSD of SFs. This highlights that the optimum gain for mitigating one dynamic imperfection may not necessarily be the optimum for another.

Despite the amplification of SFs in the range 4-25 Hz, integrated simulations (in Section 11.4) show this gain can be used to mitigate SFs. This is because the largest contribution to the SF is at harmonics of 50 Hz, which appear static to the beam, and intermediate frequencies between the harmonics are effectively mitigated with the mu-metal shield.

The proposed strategy to mitigate the impact of dynamic imperfections in CLIC includes a beam trajectory feedback system with a gain of $m = 2.5$.

Quadrupole Stabilisation System

If the noise level for GM in the CLIC tunnel happens to be low, similar to model A, GM may be mitigated with just the beam trajectory feedback system. Model A is based on measurements performed on the CERN site. Therefore, this could be a realistic model for CLIC. However, to ensure CLIC is robust against the highest level of GM that can be expected, similar to model D, a quadrupole stabilisation system is also necessary.

A quadrupole stabilisation system is included in the proposed mitigation. Combined with the beam trajectory feedback, these are the only systems needed to mitigate GM in CLIC at $E_{\text{CM}} = 380 \text{ GeV}$.

Mu-Metal Shield

This work advises a 1 mm mu-metal layer for the VT and LTL in the RTML and the ECS and FFS in the BDS. This was suggested because the material samples used in this work retained their magnetic properties at this thickness.

From measurements in CLEAR and the LHC tunnel (see Chapter 11) a reasonable estimate for the level of SFs in accelerator environments is $\sigma_B \approx 50 \text{ nT}$. A mu-metal cylinder with a diameter of a few centimetres and a relative permeability of 50,000 would need a thickness of approximately 0.1 mm to shield the SF to a level of $\sigma_B \approx 0.1 \text{ nT}$. Therefore, there is a significant reduction in the amount of mu-metal needed if its material properties can be guaranteed for very thin layers.

The beam pipe is the closest component to the beam. Surrounding the beam pipe with a mu-metal shield is the safest option to mitigate SFs because it shields the beam from all external sources outside of the beam pipe. It is also a straightforward and robust solution to implement. Alternatively, SF sources can be shielded. This would require a large effort to identify sources and assess whether surrounding them with a shield is feasible. Therefore, surrounding the beam pipe with the mu-metal shield is the preferred option.

TAL Feedforward Correction

The RTML has relatively weak quadrupoles, which means the betatron phase advance is small and betatron oscillations are preserved. This means SFs in the RTML predominantly leads to a beam offset at the end of the section. This offset leads to emittance growth in the ML, which leads to luminosity loss. The beam offset at the start of the ML can be mitigated with either a mu-metal shield in the VT and LTL or with a feedforward system in the TAL,

which corrects the beam trajectory before the ML.

The SF model described in Section 11.3 was used in integrated simulations including alternative mitigation systems. The luminosity loss with each system is given in Table 12.1. A perfect feedforward correction, which completely corrects the beam offset and angle entering the ML, was simulated in the TAL.

Mitigation	Luminosity Loss, $\Delta\mathcal{L}/\mathcal{L}_0$ [%]
Using STE	
Feedforward System (TAL) + Mu-Metal Shield (ECS, FFS)	1.7
Intra-Train IP Feedback + Mu-Metal Shield (VT, LTL)	7.4
Using NTE	
Feedforward System (TAL) + Mu-Metal Shield (ECS, FFS)	0.7
Intra-Train IP Feedback + Mu-Metal Shield (VT, LTL)	3.8

Table 12.1: Luminosity loss due an accelerator environment SF with alternative mitigation techniques. All simulations include a beam trajectory feedback system with a gain of $m = 2.5$. Values are expressed as a percentage of Equation (3.3) for NTE or Equation (3.5) for STE. The error on each value is less than 0.1%.

Tables 11.4 and 12.1 show the luminosity loss using NTE is within the 2% budget when a mu-metal shield for the VT and LTL or a feedforward system in the TAL is used. The mu-metal shield has the advantage that it is a passive system, which will not introduce noise into the system. This provides some level of robustness. Whereas, because the feedforward system is an active correction, there is a possibility of introducing noise. Integrated simulations show both systems can work. The choice between the mu-metal shield and feedforward correction can be made at a later date after evaluating the cost of each system. Alternatively, both systems can be included to provide a margin of safety.

Intra-Train IP Feedback System

For SFs in the BDS, the dominant mechanism for luminosity loss is a beam-beam offset at the IP. An alternative approach to mitigated SFs in the BDS could be to cure the beam-beam offset with an intra-train IP feedback system. Table 12.1 shows the luminosity loss using NTE is 3.8% with an intra-train IP feedback system instead of a mu-metal shield in the BDS. Whereas with the mu-metal shield, the luminosity loss is 0.4% (see Table 11.4).

The intra-train IP feedback system is not as effective as the mu-metal shield for two reasons: firstly, because the intra-train feedback system only cures the beam-beam offset of 3/4 of a train due to its latency, and secondly, because it does not cure emittance growth due to the SF. An offset beam is susceptible to emittance growth in the BDS because it is a non-linear system with a large betatron phase advance.

The mu-metal shield is essential in the BDS to mitigate SFs. The intra-train IP feedback system can be included in addition to the mu-metal shield to provide a margin of safety.

Lattice Design and Technical Sources

The sensitivity to a SF depends on its wavelength. The RTML LTL is particularly sensitive to SFs that have a wavelength equal to the betatron wavelength.

Beamline components, i.e. technical sources, have a natural periodicity. The distribution of technical sources and lattice design should be considered carefully to minimise the impact of SFs. For example, the number of decelerators and the betatron phase advance along the LTL was chosen to minimise the impact of SFs. A system of kicker magnets is used to deflect the drive beam into each decelerator. Each kicker can apply a SF kick to the main beam in the LTL. The betatron phase advance between kicks was designed to be 90° to provide a compensation effect. This is illustrated in Figure 12.1. The two green kicks and the two pink kicks compensate each other.

Although the compensation corrects the beam trajectory, the beam travels some distance

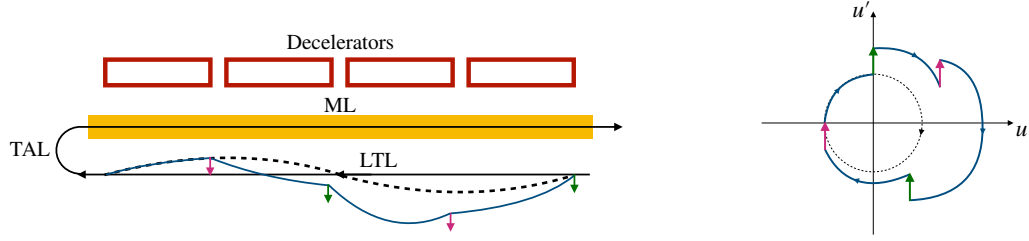


Figure 12.1: Illustration of compensation of SF kicks from the decelerators in the LTL. Left: schematic diagram of the LTL, TAL, ML and decelerators. Right: beam trajectory in phase space, angle (u') vs position (u). The SF kicks are shown in green and pink. The beam trajectory without the SF kicks is shown by the black dashed line and the beam trajectory with the SF kicks is shown by the blue solid line.

before the compensating kick is applied. In this distance, emittance growth from filamentation can occur, which is not cured by the compensating kick. In the LTL, the betatron phase advance is small, which limits filamentation. This means the emittance growth should be small.

Further studies are needed to characterise technical sources and to optimise their layout. The mu-metal shielding is effective enough that irrespective of the periodicity of the SF the amplitude will be reduced to within the tolerance. However, as a precaution, arranging technical equipment to avoid resonances with the betatron motion of the beam, particularly in the LTL, would be beneficial.

12.2 High-Luminosity CLIC

A number of reports, which describe the CLIC accelerator complex and performance, were submitted as input to the 2018-2020 European Strategy for Particle Physics Update. Here, a committee decides the future direction of particle physics research in Europe. In the spring of 2019, questions from the committee were raised regarding the possibility of doubling the baseline luminosity of the first stage by doubling the repetition frequency.

The choice of $f_{\text{rep}} = 50 \text{ Hz}$ in the baseline design is directly related to SFs. This frequency was chosen because significant SFs from the electrical grid at harmonics of 50 Hz are expected in the CLIC tunnel. Choosing $f_{\text{rep}} = 50 \text{ Hz}$ minimises the impact of these SFs.

Technologically it is possible to operate CLIC at $f_{\text{rep}} = 100$ Hz with a modest increase in power consumption and running cost [121]. All systems are able to be operated at 100 Hz. The only consideration preventing operation at $f_{\text{rep}} = 100$ Hz is the impact of SFs.

With $f_{\text{rep}} = 100$ Hz, the beam is able to resolve perturbations at 50 Hz. The concern is that the beam trajectory feedback system amplifies perturbations at this frequency. The transfer function of a beam trajectory feedback system operating at 100 Hz is shown in Figure 12.2. With a gain of $m = 2.5$, the feedback system amplifies perturbations at 50 Hz by approximately a factor of 1.25.

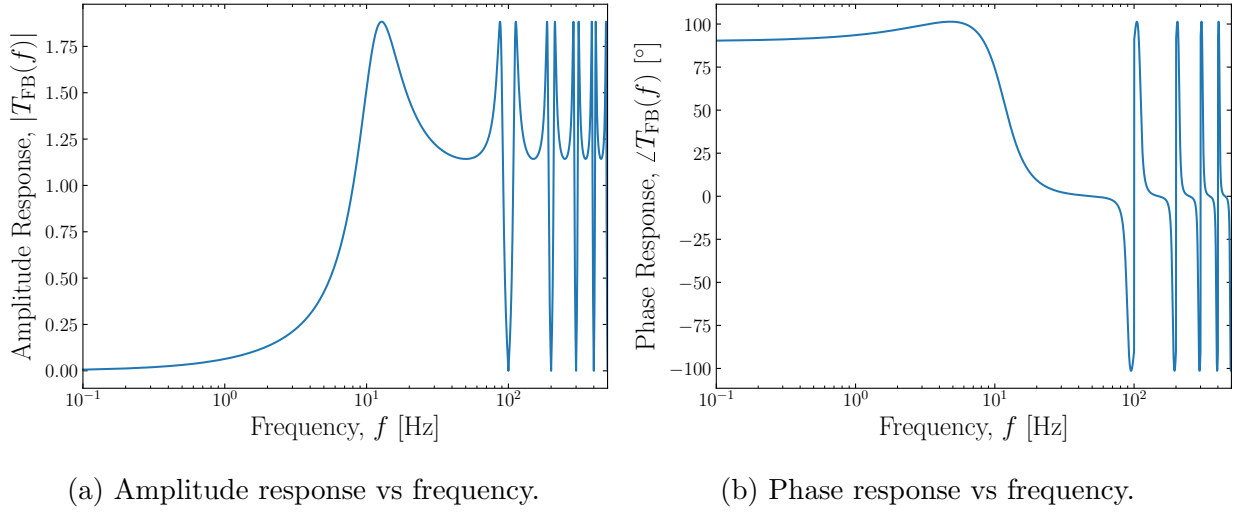


Figure 12.2: Transfer function of a beam trajectory feedback system operating at 100 Hz. The gain of this feedback system is $m = 2.5$.

Mitigation	Standard Deviation, $\overline{\sigma_{B,M}}$ [nT]
None	54
Feedback System	62
Mu-Metal Shield	4.8×10^{-3}
Feedback System + Mu-Metal Shield	5.3×10^{-3}

Table 12.2: Standard deviation of the magnetic field in the LHC tunnel: with no mitigation; a beam trajectory feedback system operating at 100 Hz with a gain of $m = 2.5$; a 1 mm mu-metal shield and the feedback system and mu-metal shield combined.

Figure 12.3 shows the average total PSD measured in the LHC tunnel (see Chapter 11) with different mitigation techniques. The standard deviation of the SF with each mitigation technique is summarised in Table 12.2. Without mitigation, the standard deviation is 54 nT.

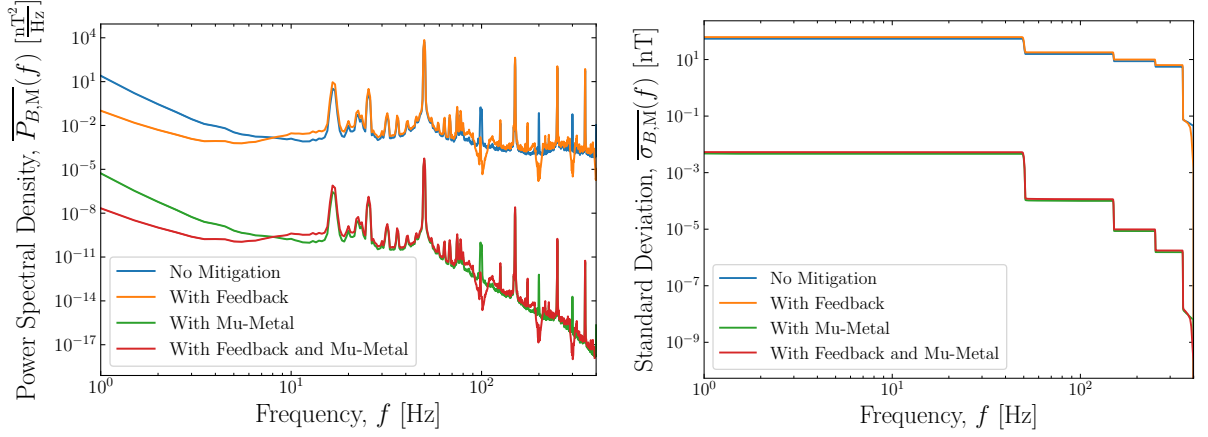


Figure 12.3: Average total PSD and standard deviation of the magnetic field vs frequency measured in the LHC tunnel: without mitigation (blue); including a beam trajectory feedback system operating at 100 Hz with a gain of $m = 2.5$; including a 1 mm mu-metal shield (green) and with the feedback system and mu-metal shield combined (red).

With the beam trajectory feedback system, the standard deviation is effectively amplified to 62 nT. The required level for SFs is 0.1 nT. Including a 1 mm mu-metal shield with the feedback system, the standard deviation is reduced to 5.3 pT, which is within the tolerance.

The effective amplification due to the beam trajectory feedback system can be avoided by implementing two independent feedback loops for alternating trains. In such a system, the position of a train is used to correct the train that is two periods behind it. This requires the correctors to alternate between the corrections for odd and even-numbered trains.

The high-luminosity upgrade is feasible if a mu-metal shield is included. Implementing two feedback loops is not necessary, but can be held in reserve.

12.3 Final Stage

The design of the final high-energy stage is described in the CLIC conceptual design report [42]. The only update in the design is that the $L^* = 6$ m BDS is now used instead of the $L^* = 3.5$ m BDS described in the report. With the new BDS, the final quadrupole is moved outside of the detector into the tunnel.

Key Changes

The ML is lengthened to provide a higher beam energy (illustrated in Figure 2.6). The length of the ML is increased from 3.5 km to 21 km, a factor 6 increase. New accelerating cavities with an accelerating gradient of 100 MV/m are added. The beam parameters are changed to accommodate the new accelerating cavities. The key changes are:

- The beam energy is increased from 190 GeV to 1.5 TeV.
- The horizontal IP beam size is reduced from 150 nm to 40 nm and the vertical IP beam size is reduced from 3 nm to 1 nm.
- The number of particles per bunch is reduced from 5.2×10^9 to 3.7×10^9 .
- The number of bunches per train is reduced from 352 to 312.
- The bunch length is reduced from 70 μm to 44 μm .
- The luminosity is increased from $1.5 \times 10^{34} \text{ cm}^{-2}\text{s}^{-1}$ to $5.9 \times 10^{34} \text{ cm}^{-2}\text{s}^{-1}$.

The RTML LTL is lengthened to match the extended ML and the bunch compressors (BC1 and BC2) are retuned to provide the reduced bunch length.

The BDS length is increased from 1.95 km to 3.1 km. The BDS contains several bending magnets. SR in these magnets can lead to emittance growth [122]. To minimise this emittance growth, less aggressive bends are used, which lengthens the beamline.

Dynamic Imperfections

The first and final stage of CLIC represent the two extremes in terms of machine length and beam energy. If there is an effective mitigation strategy for dynamic imperfections in the first and final stage, there must also be an effective mitigation strategy for the intermediate stage. Therefore, this section focuses on the final stage.

The impact of dynamic imperfections in the final stage is described in the conceptual design report [42]. The most important dynamic imperfections are GM and SFs.

Ground Motion

GM in the RTML has a negligible impact on luminosity (see Section 4.3.1). This is because of the relatively weak magnets, which do not exert significant kicks on the beam. GM in the RTML in later stages is not expected to pose a danger.

The smaller IP beam size in the final stage leads to a stricter tolerance for beam jitter at the IP. An additional mitigation system is envisaged for the final doublet in the BDS to reduce the IP beam jitter. The final doublet will be placed on a large mass known as the *preisolator* [42], which damps high-frequency GM. The baseline design for the first stage omits this system.

The ML is significantly longer in the final stage compared to the first stage. This means GM can have a much bigger impact. Integrated simulations of the ML and BDS in the final stage with GM are presented in [42]. The luminosity loss can be kept to within 3% using a beam trajectory feedback system, quadrupole stabilisation system and a preisolator [42]. Therefore, GM is not a significant concern in the final stage.

Stray Magnetic Fields

Sensitivity studies and tolerances for SFs in the final stage are presented in [69]. The minimum tolerance for SFs in the ML and BDS is $\sigma_{B,\text{tol}} \approx 1 \text{ nT}$ for sinusoidal SFs with the worst wavelength ($\lambda \approx 5 \text{ km}$). This is approximately an order of magnitude larger than the minimum tolerance for sinusoidal SFs in the first stage.

The BDS in the final stage is less sensitive to SFs because of the higher beam energy. Therefore, the proposed mitigation for the BDS in the first stage should also be effective for mitigating SFs in the final stage. The extended ML still benefits from the shielding provided by the copper cavities and should not need any additional mitigation for SFs.

The beam energy in the RTML LTL is the same in the first and final stage. However, the LTL is 6 times longer. The beam is particularly sensitive to sinusoidal SFs at the betatron wavelength in the LTL. In accordance with Equation (5.19), the emittance growth from a sinusoidal SF at a particular wavelength scales with length squared. Therefore, 36 times more emittance growth can be expected from SFs at the betatron wavelength. This can significantly impact luminosity. Luminosity loss can be mitigated by preventing the SF from reaching the beam with a mu-metal shield.

With the beam trajectory feedback system and a mu-metal shield, SFs should not be a concern for later stages of CLIC.

Chapter 13

Conclusions

CLIC

CLIC is a proposed future e^+e^- collider for the CERN site. The first stage is at $E_{\text{CM}} = 380 \text{ GeV}$, which is optimised for Higgs and top-quark physics, and the final stage is at $E_{\text{CM}} = 3 \text{ TeV}$.

Nominal Luminosity

The nominal luminosity target of the first stage is $1.5 \times 10^{34} \text{ cm}^{-2}\text{s}^{-1}$. Integrated simulations show with nominal emittance at the IP a luminosity of $1.55 \times 10^{34} \text{ cm}^{-2}\text{s}^{-1}$ is achieved. This means in the worst case where imperfections generate their full emittance growth budgets, a luminosity marginally above the nominal luminosity target will be achieved.

Perfect Machine Luminosity

In the idealised case without imperfections, integrated simulations show a luminosity of $4.3 \times 10^{34} \text{ cm}^{-2}\text{s}^{-1}$ can be achieved. This is almost three times the nominal luminosity target.

Luminosity with Static Imperfections

Explicitly implementing static imperfections and simulating beam-based tuning, integrated simulations of 100 machines show an average luminosity of $3.4 \times 10^{34} \text{ cm}^{-2} \text{ s}^{-1}$ is achieved, which is more than twice the nominal luminosity target. 90% of machines achieve a luminosity above $2.7 \times 10^{34} \text{ cm}^{-2} \text{ s}^{-1}$. Expressed as a percentage of the nominal luminosity target this is 180%.

The tuning procedure described in Section 3.5 is extremely effective and surpasses the required level of performance. This means CLIC is robust against the impact of static imperfections and if dynamic imperfections are mitigated, a luminosity significantly above the nominal luminosity target could be reached.

Dynamic Imperfections

Beam Jitter and Phase Errors

Integrated simulations show the IP position jitter of each beam must be within 0.4 nm to stay within a 2% luminosity loss budget. There is a tolerance of 0.2° for coherent RF phase errors in ML cavities to remain within a 1% luminosity loss budget.

Ground Motion

Model A represents a low-noise environment. A luminosity loss of 0.1% occurs when including the beam trajectory feedback system. Only the beam trajectory feedback is required to mitigate GM model A.

Model D represents a higher than expected noise level. The combined use of a quadrupole stabilisation system and beam trajectory feedback system is effective at mitigating luminosity loss from GM model D. With these systems the luminosity loss is 1.6%, which is within the luminosity loss budget for GM. Therefore, CLIC is robust against the impact of GM.

Stray Magnetic Fields

CLIC has an unprecedented sensitivity to SFs with tolerances down to the level of 0.1 nT for the worst spatial wavelengths.

The regions most susceptible to the effect of SFs are those with large beta functions. These are the VT and LTL in the RTML and the ECS and FFS in the BDS. The ML is the most robust section with respect to SFs. The ML benefits from a large number of accelerating cavities, which are formed from copper and shield the beam from SFs.

SFs are divided into three classifications. **Natural:** SFs from non-man-made objects. These have a slow temporal variation compared to the repetition frequency of the beam, which means they can be mitigated with beam trajectory feedback systems. This was illustrated in Section 8.2 with an integrated simulation of a geomagnetic storm. Natural SFs above 1 Hz are within the tolerances described in Chapter 5 or occur infrequently. Therefore, natural SFs are not a concern for CLIC.

Environmental: SFs from man-made objects, which are not elements of CLIC. The largest source is the electrical grid, which has a limited impact because the SFs are predominately at harmonics of 50 Hz and therefore appear static to the beam. Amplitude modulation of the 50 Hz SFs results in peaks at more problematic frequencies, e.g. 16.7 Hz, 25 Hz, etc. The beam trajectory feedback system is not effective at mitigating SFs at these frequencies. Instead, these frequencies are mitigated with the mu-metal shield.

Technical: SFs from elements of CLIC. These are challenging to characterise. Dedicated measurements of CLIC elements during and after construction will be required to fully understand technical sources. However, the following can be concluded from SF measurements of specific elements:

- Magnets: magnet ripples are not a concern because their stability tolerance is larger the typical level of SFs in accelerator environments.
- Power cables: can be a significant SF source, but their impact can be minimised by

arranging them to provide a cancellation of current.

- RF systems: the impact of SFs from RF systems is limited because they typically operate at the same repetition frequency as the beam and can be placed far from the beam.
- Ventilation systems: can be a significant SF source, but can be avoided by designing a ventilation system that does not produce SFs at harmful frequencies. Alternatively, the system can be placed far away from the beam or shielded.

Passive Shielding with Mu-Metal

The shielding performance of mu-metal has been experimentally verified and a model has been validated. A relative permeability of 50,000 has been measured, which corresponds to a shielding factor greater than 10^3 with a cylindrical shield of 1 mm thickness. These measurements demonstrate mu-metal can be used in an accelerator to shield to the beam from SFs. Measurements have also shown extremely small internal magnetic field amplitudes of less than 0.1 nT can be realised with a mu-metal shield.

A large variation in the permeability of different mu-metal samples was found. The measured permeability of a mu-metal foil was found to be significantly less than the typical advertised value. The discrepancy is assumed to be due to mechanical stress damaging the material. The damage can be reversed by re-annealing the material. Alternatively, damage can be avoided by using thicker shields, which are less fragile. This work recommends a minimum thickness of 1 mm.

Passive shielding with mu-metal is equally applicable to other accelerators that wish to shield the beam from SFs. Mu-metal is also effective for shielding static SFs provided it is not saturated.

Luminosity Loss from Stray Magnetic Fields

A two-dimensional PSD model for SFs in an accelerator environment was proposed in Section 11.3. Integrated simulations show a luminosity loss of 0.4% with a beam trajectory feedback system and a mu-metal shield in the VT, LTL, ECS and FFS. The mu-metal shielding is essential to mitigate the impact of SFs. With the shielding, CLIC is robust against luminosity loss from SFs.

Luminosity with Dynamic Imperfections

GM and SFs are the two most important dynamic imperfections for CLIC. This work describes a consistent strategy to mitigate both of these imperfections. With the mitigation, the luminosity loss from each of these imperfections is on the percent level.

The luminosity achieved by 90% of machines including static imperfections is above 180% of the nominal luminosity target. Therefore, there could be a margin of up to 80% for dynamic imperfections. The maximum luminosity loss from GM and SFs is up to 4%. This is a small fraction of the 80% surplus. Therefore, the impact of dynamic imperfections should not pose a concern for the operation of CLIC and a luminosity significantly above the nominal luminosity target can be expected.

Later Stages and Alternative Designs

GM and SFs should not seriously impact the luminosity of later stages provided the proposed mitigation is used. With the mu-metal shielding, doubling the repetition frequency to achieve a higher luminosity is feasible.

Appendix A

Signal Processing

A brief introduction to the signal processing techniques used in this work is given here. For a more complete description, the reader should refer to [72].

A.1 Discrete-Time Signals

A measurement procedure samples a process $u(t)$ at discrete times given by

$$t = nT_s = \frac{n}{f_s}, \quad (\text{A.1})$$

where n is an integer, T_s is the *sampling period* and $f_s = 1/T_s$ is the *sampling frequency* (or *sampling rate*). As a result, a measurement produces a sequence of numbers $u[n]$, referred to as a *discrete-time signal*. The sampling of a process is illustrated in Figure A.1a.

The choice of sampling frequency depends on the maximum frequency one wishes to observe. The maximum observable frequency for a given sampling frequency is $f_s/2$, this is known as the *Nyquist frequency*. Any signal above this frequency will be undersampled and appear as a lower frequency. This effect is known as *aliasing*. Usually, this is avoided by removing frequencies above the Nyquist frequency before sampling.

A discrete-time signal can be represented in the frequency domain using the *Discrete*

Fourier Transform (DFT),

$$U[k] = \sum_{n=0}^{N-1} u[n] e^{-j \frac{2\pi k}{N} n}, \quad (\text{A.2})$$

where N is the number of data points in the signal. The DFT represents a signal over the frequency range $[-f_s/2, f_s/2]$. The *resolution* (or *frequency bin width*) of a DFT is given by

$$\Delta f = \frac{f_s}{N}. \quad (\text{A.3})$$

The DFT $U[k]$ is a sequence of N complex numbers, whereas the discrete-time signal $u[n]$ is a sequence of N real numbers. An example of a DFT is shown in Figure A.1b

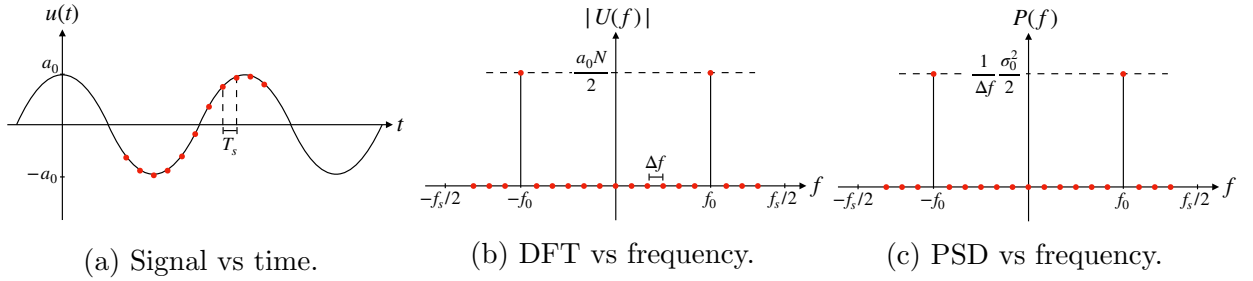


Figure A.1: Illustration of the sampling of a process and its DFT and PSD. The red dots highlight data points. a_0 is the amplitude of the signal and $\sigma_0^2 = a_0^2/2$ is the variance of the signal.

A.2 Spectral Estimation

Power Spectral Density

A convenient way to characterise a process is via its *power spectral density* (PSD), which represents the power distribution over frequencies.

A PSD can be estimated as [123]

$$P_{uu}[k] = \frac{1}{\Delta f} \frac{U[k] \cdot U^*[k]}{N^2}, \quad (\text{A.4})$$

where $*$ denotes the complex conjugate. This estimate is known as the *periodogram*. However, this is a poor method of calculating a PSD because its estimation does not improve with

increasing signal length [123].

A better estimate of a PSD can be calculated with *Bartlett's method* [124]. This involves splitting the signal $u[n]$ into M equal parts, to form the ensemble $\{u_m[n]; m = 0, \dots, M-1\}$. The periodogram $P_{uu}^{(m)}[k]$ of each $u_m[n]$ segment is calculated and averaged to give

$$P_{uu}[k] = \frac{1}{M} \sum_{m=0}^{M-1} P_{uu}^{(m)}[k]. \quad (\text{A.5})$$

A further improvement can be made by dividing the signal into $(2M-1)$ overlapping segments instead of M consecutive segments. Each segment contains 50% of the data in the two neighbouring segments. Averaging the periodogram of each segment gives the estimate of a PSD. This is known as *Welch's method* [125]. Bartlett's method can be thought of as Welch's method with 0% overlap. An example of a PSD is shown in Figure A.1c.

Variance and Standard Deviation

The integral of a PSD over all frequencies gives the *variance* [55]

$$\sigma^2 = \sum_{k=0}^{N-1} P_{uu}[k] \cdot \Delta f. \quad (\text{A.6})$$

The square root of Equation (A.6) is the *standard deviation*.

Cross Spectral Density

The *cross power spectral density*, or *cross spectral density* (CSD) in short, can be estimated by calculating the *cross periodogram* (or *correlogram*)

$$P_{uv}[k] = \frac{1}{\Delta f} \frac{U[k] \cdot V^*[k]}{N^2}, \quad (\text{A.7})$$

where $V[k]$ is the DFT of the signal $v[n]$. The CSD is a complex-valued function, as opposed to the PSD which is real-valued. The CSD therefore gives relative phase information of the

two input signals.

Coherence and Correlation

The *magnitude-squared coherence*, or simply *coherence*, is calculated as

$$c_{uv} = \frac{|P_{uv}[k]|^2}{P_{uu}[k]P_{vv}[k]}. \quad (\text{A.8})$$

The coherence is a real-valued function. The two signals $u[n]$ and $v[n]$ are said to be *coherent* if c_{uv} is close to one, which occurs if $u[n]$ and $v[n]$ have a constant phase difference. The coherence does not give any information regarding the value of the phase difference.

The *correlation coefficient*, or simply *correlation*, is

$$C_{uv} = \frac{\text{Re}\{P_{uv}[k]\}}{\sqrt{P_{uu}[k]P_{vv}[k]}}, \quad (\text{A.9})$$

which describes whether the signals $u[n]$ and $v[n]$ are moving in phase or anti-phase. The correlation is a real-valued function. Signals with a phase difference close to 0° ($C_{uv} = 1$) are said to be *highly correlated*, signals with a phase difference close to 90° ($C_{uv} = 0$) or signals that vary independently are said to be *uncorrelated* and signals with a phase difference close to 180° ($C_{uv} = -1$) are said to be highly *anti-correlated*.

A.3 Linear Time-Invariant Filters

A *filter* is a process which removes unwanted features from a signal [72]. The type of filter that is of interest to this work is *linear* and *time-invariant* (LTI). A *non-recursive* LTI filter produces the output signal

$$v[n] = \sum_{l=-\infty}^{\infty} h[l]u[n-l], \quad (\text{A.10})$$

where $u[n-l]$ is the input signal and $h[l]$ is the *impulse function*. Equation (A.10) is known as a *convolution sum*. Here, the value of the output $v[n]$ depends only on the input values

$u[n - l]$.

The convolution theorem states that Equation (A.10) can be written in the frequency domain as [72]

$$V[k] = H[k]U[k], \quad (\text{A.11})$$

where $V[k]$, $H[k]$ and $U[k]$ are the DFTs of $v[n]$, $h[n]$ and $u[n]$ respectively. $H[k]$ is known as the *frequency response* of the filter. This is a complex-valued function. The frequency response is commonly referred to as the *transfer function*.

The magnitude of the frequency response is a real-valued function known as the *amplitude response*,

$$|H[k]| = \sqrt{\text{Re}\{H[k]\}^2 + \text{Im}\{H[k]\}^2}. \quad (\text{A.12})$$

The phase (or angle) of the frequency response is known as the *phase response*,

$$\angle H[k] = \arctan\left(\frac{\text{Im}\{H[k]\}}{\text{Re}\{H[k]\}}\right). \quad (\text{A.13})$$

A *recursive* LTI filter has the following relationship between input and output

$$\sum_{m=0}^N a[m]v[n - m] = \sum_{l=0}^M b[l]u[n - l], \quad (\text{A.14})$$

where $a[m]$ and $b[l]$ are constants. Here, the output value $v[n]$ depends on the the input value $u[n]$, previous input values $u[n - l]$ and previous output values $v[n - m]$. Equation (A.14) is known as a *difference equation*. The DFT of Equation (A.14) is¹

$$\sum_{k=0}^N a[m] V[k] e^{-j\frac{2\pi k}{N}m} = \sum_{l=0}^M b[l] U[k] e^{-j\frac{2\pi k}{N}l}. \quad (\text{A.15})$$

¹The time-shifting property of DFTs, $\mathcal{DFT}\{u[n - l]\} = U[k]e^{-j\frac{2\pi n}{N}l}$, has been used.

This can be used to calculate the frequency response of the filter as

$$H[k] = \frac{V[k]}{U[k]} = \frac{\sum_{l=0}^M b[l] e^{-j \frac{2\pi k}{N} l}}{\sum_{m=0}^N a[m] e^{-j \frac{2\pi k}{N} m}}. \quad (\text{A.16})$$

For the processes of interest to this work,² it can be shown that the PSD of an output signal of a LTI filter is related to the PSD of the input signal by [55]

$$P_{vv}[k] = |H[k]|^2 P_{uu}[k]. \quad (\text{A.17})$$

This is a powerful result that is used frequently in this work. The product of a PSD with the frequency response gives a CSD [55]

$$P_{uv}[k] = H[k] P_{uu}[k]. \quad (\text{A.18})$$

This is another important result, which can be used to estimate the frequency response of a LTI filter as

$$H[k] = \frac{P_{uv}[k]}{P_{uu}[k]}. \quad (\text{A.19})$$

A.4 Measurement Errors

There are several well-known error sources in processing signals from measurements. This section summarises techniques used in this work to minimise the effect of these errors.

Fast Fourier Transform

To calculate a DFT, which will be referred to as the *frequency spectrum*, a *Fast Fourier Transform* (FFT) algorithm is often used [126].

²Equations (A.17) and (A.18) are true for *wide-sense stationary stochastic processes* [55].

A FFT is conjugate symmetric, i.e. it satisfies

$$U[k] = U^*[N - k]. \quad (\text{A.20})$$

This means half of the array is redundant. As a result, it is common only to consider the FFT over the positive frequency range $[0, f_s/2]$ opposed to the full range $[-f_s/2, f_s/2]$.

FFTs are either normalised by dividing by N if the full frequency range is kept or normalised as

$$U_n[k] = \frac{2U[k]}{N} \quad (\text{A.21})$$

if only positive frequencies are kept.

Spectral Leakage

Measurements can only record a finite segment of a process. A FFT assumes the recorded segment is repeated infinitely many times. Usually, this leads to discontinuities at the borders between segments. The discontinuities lead to an effect known as *spectral leakage*, where the power in a particular frequency bin is smeared out into neighbouring bins. For signals whose periodicity fits the length of the segment exactly, spectral leakage does not occur.

A technique known as *windowing* is used to reduce spectral leakage. The recorded signal is multiplied in the time domain by a window whose effect is to amplify the signal in the middle and suppress the signal at the ends,

$$u_w[n] = w[n]u[n], \quad (\text{A.22})$$

where $w[n]$ is the window. Different windows are summarised in Table A.1. Typically, the Hann window is used for general purpose and the flat-top window is used when accurate amplitude measurements are important. The effect on the frequency spectrum of different windows is shown in Figure A.2.

Window	$w[n]$
Hann	$0.5 - 0.5 \cos\left(\frac{2\pi n}{N}\right)$
Hamming	$0.54 - 0.46 \cos\left(\frac{2\pi n}{N}\right)$
Flattop	$a_0 + a_1 \cos\left(\frac{2\pi n}{N}\right) + a_2 \cos\left(\frac{4\pi n}{N}\right) + a_3 \cos\left(\frac{6\pi n}{N}\right) + a_4 \cos\left(\frac{8\pi n}{N}\right)$
Blackman	$0.42 - 0.5 \cos\left(\frac{2\pi n}{N}\right) + 0.08 \cos\left(\frac{4\pi n}{N}\right)$

Table A.1: Summary of different windows used in signal processing [127]. The coefficients for the flattop window are $a_0 = 0.21557895$, $a_1 = 0.41663158$, $a_2 = 0.277263158$, $a_3 = 0.083578947$, $a_4 = 0.006947368$.

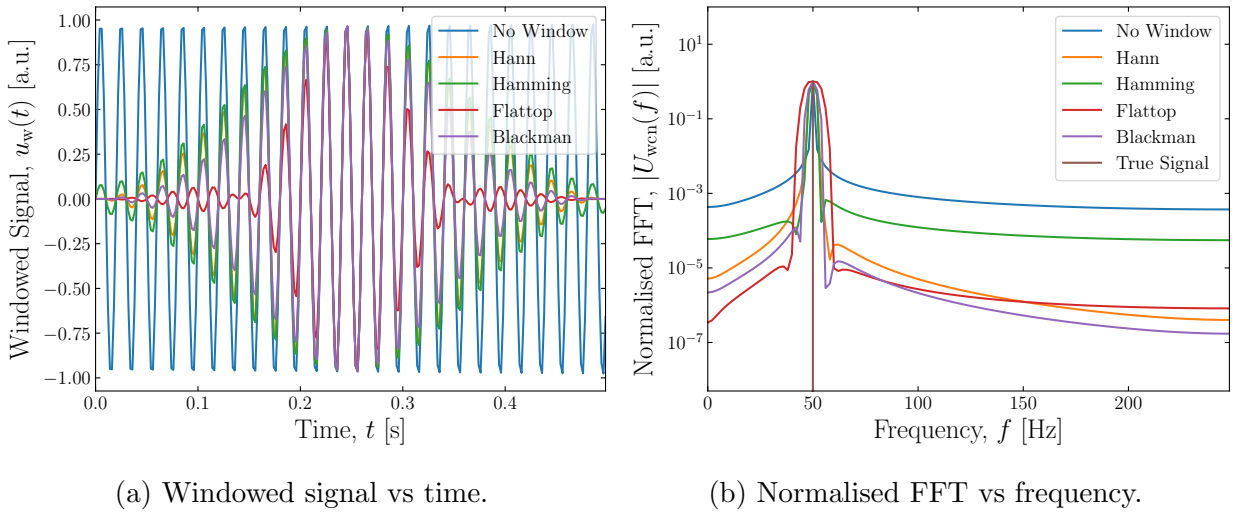


Figure A.2: Windowed signals and their normalised FFTs. The signal $u(t) = \sin(2\pi ft)$ with a frequency of $f = 49.97$ Hz was simulated for 0.5 s and sampled at $f_s = 500$ Hz. Different windows were applied to the signal: no window (blue); a Hann window (orange); a Hamming window (green); a flattop window (red) and a Blackman window (purple). The appropriate compensation for coherent power gain was applied to each normalised FFT.

Coherent Power Gain

The application of a window is also a source of error. By suppressing the signal near the ends, the window leads to a reduction in the amplitude of all frequencies in the FFT. This reduction is known as *coherent power gain*. Every window has a fixed, characteristic coherent power gain. To compensate for this, the FFT is divided by

$$C = \frac{1}{N} \sum_{n=0}^N w[n], \quad (\text{A.23})$$

so that the frequency spectrum is given by

$$U_{\text{wcn}}[k] = \frac{1}{C} \frac{2U_{\text{w}}[k]}{N}, \quad (\text{A.24})$$

where $U_{\text{w}}[k]$ is the FFT of the windowed signal $u_{\text{w}}[n]$.

Scalloping Loss

Each frequency bin of a FFT corresponds to a discrete frequency. The frequency of a signal can fall between two frequency bins. If this is the case, the power in the signal is spread over both bins. This is called *scallop loss*. The severity of scalloping loss depends on the applied window.

Unfortunately, scalloping loss cannot be described by a fixed value for each window, so it is difficult to compensate for it. However, certain windows exhibit less scalloping loss than others. In particular, a flattop window has very little scalloping loss. Scalloping loss can also be avoided by selecting a sampling frequency that is a multiple of the signal frequency, which also avoids spectral leakage.

Narrowband Signals

Narrowband signals, such as sinusoidal signals, show up as peaks in a frequency spectrum. Accurate measurements of the frequency and amplitude of these peaks are of interest.

Measuring the frequency of a peak is straightforward if the desired accuracy is equal to or greater than the frequency bin width. Interpolation methods are also available to increase the frequency resolution without increasing the number of data points, e.g. the method outlined in [128] is used in this work.

The true amplitude of a narrowband signal can be calculated with Equation (A.24) if the signal can be captured in a single frequency bin by selecting a good measurement time and sampling frequency. If the signal frequency cannot be centred on a single frequency bin, a

flattop window can be used to suppress scalloping loss.

Spectral Calculations

In this work, a Hann window is applied to all measurements, FFTs are normalised with Equation (A.21) and the appropriate compensation is applied for coherent power gain. Only positive frequencies are considered. Periodograms are estimated as

$$P_{uu}[k] = \frac{1}{\Delta f} \frac{U_{\text{wcn}}[k] \cdot U_{\text{wcn}}^*[k]}{2}. \quad (\text{A.25})$$

All PSDs in this work are calculated using Welch's method with periodograms given by Equation (A.25). The calculation is illustrated in Figure A.3. Similarly, CSDs are calculated using Welch's method with cross periodograms that have the same normalisation as periodograms.

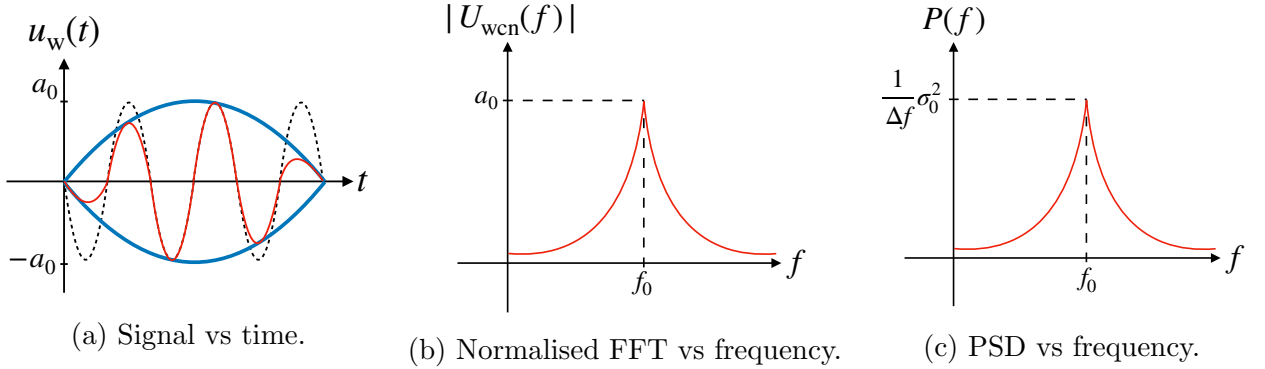


Figure A.3: Illustration of the calculation of a PSD. The windowed signal is shown in red. The signal before applying the window is shown by the dashed black line in (a) and the window is shown in blue. a_0 is the amplitude of the signal and $\sigma_0^2 = a_0^2/2$ is the variance of the signal.

Bibliography

- [1] W.N. Cottingham and D.A. Greenwood, *An Introduction to the Standard Model of Particle Physics* (Cambridge University Press, 1998).
- [2] M. Tanabashi, et al., Particle Data Group, *Physical Review D* **98**, 030001 (2018).
- [3] P.W. Higgs, Broken Symmetries and the Masses of Gauge Bosons, *Physical Review Letters* **13(16)**, 508-509 (1964).
- [4] G. Aad, et al., Observation of a new particle in the search for the Standard Model Higgs boson with the ATLAS detector at the LHC, *Physical Review Letters* **B 716(1)**, 1-29 (2012).
- [5] S. Chatrchyan, et al., Observation of a new boson at a mass of 125 GeV with the CMS experiment at the LHC, *Physical Review Letters* **B 716(1)**, 30-61 (2012).
- [6] C. Rovelli, *Quantum Gravity* (Cambridge University Press, 2007).
- [7] G. Bertone, D. Hooper and J. Silk, Particle dark matter: Evidence, candidates and constraints, *Physics Reports* **405(5-6)**, 279-390 (2005).
- [8] S.M. Bilenky, C. Giunti and W. Grimus, Phenomenology of neutrino oscillations, *Progress in Particle and Nuclear Physics* **43**, 1-86 (1999).
- [9] J. Jackson, *Classical Electrodynamics 3rd Edition* (John Wiley & Sons, 2007).
- [10] H. Padamsee, The science and technology of superconducting cavities for accelerators, *Superconductor Science and Technology* **14(4)**, 28-51 (2001).
- [11] E. Wilson, *An Introduction to Particle Accelerators* (Oxford University Press, 2001).
- [12] O. Brüning, et al., LHC Design Report, Technical Report CERN-2004-003-V-1 (2004).
- [13] L. Rossi and E. Todesco, Conceptual design of 20 T dipoles for high-energy LHC, Technical Report CERN-2011-003 (2011).
- [14] W. Wuensch, High-Gradient RF Development and Applications, *Proceedings of the 28th Linear Accelerator Conference (LINAC'16)*, East Lansing, MI, USA, Sept. 2016, TU2A04, pp. 368-373.

- [15] M. Benedikt, et al., FCC-ee: The Lepton Collider, *European Physical Journal Special Topics* **228(2)**, 261-623 (2019).
- [16] M. Benedikt, et al., FCC-hh: The Hadron Collider, *European Physical Journal Special Topics* **228(4)**, 755-1107 (2019).
- [17] The CEPC Study Group, CEPC Conceptual Design Report - Volume 1: Accelerator, Technical Report IHEP-CEPC-DR-2018-01 (2018).
- [18] J. de Blas, et al., The CLIC Potential for New Physics, Technical Report CERN-2018-009-M (2018).
- [19] T. Barklow, et al., The International Linear Collider Technical Design Report - Volume 2: Physics, Technical Report ILC-REPORT-2013-040 (2013).
- [20] H. Abramowicz, et al., Higgs physics at the CLIC electron-positron linear collider, *European Physical Journal C* **77(7)**, 475 (2017).
- [21] H. Abramowicz, et al., Top-Quark Physics at the CLIC Electron-Positron Linear Collider, *Journal of High Energy Physics* **2019(11)**, 3 (2019).
- [22] P. Emma, A Spin Rotator for the NLC, Technical Report SLAC-NLC-Note-07 (1994).
- [23] L. Evans, S. Michizono, The International Linear Collider Machine Staging Report, Technical Report KEK-2017-3 (2017).
- [24] H. Aihara, et al., The International Linear Collider. A Global Project, Technical Report DESY-2019-037 (2019).
- [25] M. Aicheler, et al., The Compact Linear Collider (CLIC) - Project Implementation Plan, Technical Report CERN-2018-010-M (2018).
- [26] CLIC and CLICdp collaborations, Updated baseline for a staged Compact Linear Collider, Technical Report CERN-2016-004 (2016).
- [27] G. Geschonke and A. Ghigo, CTF3 Design Report, Technical Report CERN-PS-2002-008-RF (2002).
- [28] A. Chao and M. Tigner, *Handbook of Accelerator Physics and Engineering* (World Scientific, 1999).
- [29] S. Lee, *Accelerator Physics* (World Scientific, 2004).
- [30] H. Wiedemann, *Particle Accelerator Physics* (Springer, 2007).
- [31] W. Herr and B. Muratori, Concept of luminosity, *Proceedings of the CERN Accelerator School: Intermediate Accelerator Physics*, Zeuthen, Germany (2003).
- [32] K. Yokoya and P. Chen, Beam-beam phenomena in linear colliders, *Frontiers of Particle Beams: Intensity Limitations*, 415-445 (1992).

- [33] L. Hendrickson, et al., Feedback systems for linear colliders, *Proceedings of the 1999 Particle Accelerator Conference (PAC'99)*, New York, New York, USA, Mar.-Apr. 1999, SLAC-PUB-8055, pp. 338-342.
- [34] J. Pfingstner, et al., Mitigation of ground motion effects in linear accelerators via feed-forward control, *Physical Review Special Topics - Accelerators and Beams* **17(12)**, 122801 (2014).
- [35] A. Latina, et al., Recent Improvements in the Tracking Code PLACET, *Proceedings of the 11th European Particle Accelerator Conference, (EPAC'08)*, Genoa, Italy, June 2008, TUPP094, pp. 1750-1752.
- [36] PLACET documentation. URL: <https://gitlab.cern.ch/clic-software/placet/blob/master/doc/placet.pdf>.
- [37] D. Schulte, *Study of electromagnetic and hadronic background in the interaction region of the tesla collider*, PhD thesis, University of Hamburg (1997).
- [38] D. Schulte, et al., Tests of 3 linear collider beam dynamics simulation programs, Technical Report CERN-OPEN-2002-059 (2002).
- [39] J. C. Smith, et al., Benchmarking/Crosschecking DFS in the ILC Main Linac, Technical Report FERMILAB-TM-2373-CD (2007).
- [40] P. Bambade, et al., Results of the EUROTeV Beam-Beam Simulation (BBSIM) Task, Technical Report EUROTeV-2008-065 (2008).
- [41] A. Wolski, A Short Introduction to Bunch Compressors for Linear Colliders, *Notes for USPAS Course on Linear Colliders*, Santa Barbara, California, USA (2003).
- [42] M. Aicheler, et al., A Multi-TeV Linear Collider Based on CLIC Technology: CLIC Conceptual Design Report, Technical Report CERN-2012-007 (2012).
- [43] Y. Han, et al., Static beam-based alignment for the Ring-To-Main-Linac of the Compact Linear Collider, *Journal of Instrumentation* **12(6)**, 06010 (2017).
- [44] Y. Han, et al., Beam-Based Alignment for the Rebaselining of CLIC RTML, *Proceedings of the 8th International Particle Accelerator Conference (IPAC'17)*, Copenhagen, Denmark, May 2017, TUPIK099, pp. 1939-1942.
- [45] N. Blaskovic Kraljevic and D. Schulte, Beam-based beamline element alignment for the main linac of the 380 GeV stage of CLIC, *Proceedings of the 10th International Particle Accelerator Conference (IPAC'19)*, Melbourne, Australia, May 2009, MOPMP018, pp. 465-467.
- [46] J. A. Ögren, et al., Tuning of the CLIC 380 GeV Final-Focus System with Static Imperfections, Technical Report CERN-ACC-2018-0055 (2018).

- [47] E. Marin, et al., Tuning of CLIC-Final Focus System 3 TeV Baseline Design Under Static and Dynamic Imperfections, *Proceedings of the 9th International Particle Accelerator Conference (IPAC'18)*, Vancouver, Canada, Apr.-May 2018, MOPMF043, pp. 196-199.
- [48] W. Coosemans and H. Mainaud, Pre-alignment of CLIC using the double-wire method, *Proceedings of the 5th International Workshop Accelerator Alignment (IWAA'97)*, Argonne, USA, Oct. 1997, IWAA-1997-027, pp. 27-30.
- [49] F. Peauger, et al., Wakefield monitor development for CLIC accelerating structure, *Proceedings of the 25th International Linear Accelerator Conference (LINAC'10)*, Tsukuba, Japan, Sept. 2010, TUP098, pp. 461-463.
- [50] W.H. Press, et al., *Numerical recipes 3rd edition: The art of scientific computing* (Cambridge University Press, 2007).
- [51] A. Seryi and O. Napoly, Influence of ground motion on the time evolution of beams in linear colliders, *Physical Review* **E 53**, 5323-5337 (1996).
- [52] G.E. Fischer, Ground Motion and Its Effects in Accelerator Design, *Proceedings of the SLAC Summer School: Physics of High-Energy Particle Accelerators*, Stanford, California (1985).
- [53] A. Seryi, Ground motion models for future linear colliders, *Proceedings of the 7th European Particle Accelerator Conference (EPAC'00)*, Vienna, Austria, June 2000, THP6A13, pp. 501-503.
- [54] A. Seryi and T. Raubenheimer, Ground motion model of the SLAC site, Technical Report SLAC-PUB-8595 (2000).
- [55] A. Papoulis and S.U. Pillai, *Probability, random variables, and stochastic processes* (Tata McGraw-Hill Education, 2002).
- [56] V. Shiltsev, Space-time ground diffusion: The ATL law for accelerators, *Proceedings of the 4th International Workshop on Accelerator Alignment (IWAA'95)*, Tsukuba, Japan, Nov. 1995, IWAA-1995-036, pp. 352-381.
- [57] V.M. Juravlev, et al., Investigations of power and spatial correlation characteristics of seismic vibrations in the CERN LEP tunnel for linear collider studies, Technical Report CERN-SL-93-53 (1993).
- [58] Zeroth-Order Design Report for the Next Linear Collider, Technical Report SLAC-R-474 (1996).
- [59] V. Shiltsev, et al., Technical Report DESY-HERA-95-06 (1995, unpublished).
- [60] B. Bolzon, *Etude des vibrations et de la stabilisation à l'échelle sous-nanométrique des doublets finaux d'un collisionneur linéaire*, PhD thesis, Université de Savoie (2007).

- [61] A. Kuzmin, Ground vibration measurements and experiment parts motion measurement at CMS, Technical Report EDMS:1027459 (2009).
- [62] B. Balkakov, et al., Ground vibration measurements for Fermilab future collider projects, *Physical Review Special Topics - Accelerators and Beams* **1(3)**, 031001 (1998).
- [63] J. Pfingstner, *Mitigation of ground motion effects via feedback systems in the Compact Linear Collider*, PhD thesis, Vienna University of Technology (2013).
- [64] S. Janssens, *Stabilisation and precision pointing quadrupole magnets in the Compact Linear Collider (CLIC)*, PhD thesis, University of Amsterdam (2015).
- [65] C. Collette, et al., Active quadrupole stabilization for future linear particle colliders, *Nuclear Instruments and Methods in Physics Research A* **621(1-3)**, 71-78 (2010).
- [66] J. Resta-López, P.N. Burrows and G. Christian, Luminosity performance studies of the compact linear collider with intra-train feedback system at the interaction point, *Journal of Instrumentation* **5(9)** 09007 (2010).
- [67] R. Bodenstein, et al., Intra-beam IP Feedback Studies for the 380 GeV CLIC Beam Delivery System, *Proceedings of the 7th International Particle Accelerator Conference (IPAC'16)*, Busan, Korea, May 2016, WEPOR009, pp. 2683-2686.
- [68] R. J. Apsimon, et al., Design and performance of a high resolution, low latency stripline beam position monitor system, *Physical Review Special Topics - Accelerators and Beams* **18**, 032803 (2015).
- [69] J. Snuverink, et al., Impact of Dynamic Magnetic Fields on the CLIC Main Beam, *Proceedings of the 1st International Particle Accelerator Conference (IPAC'10)*, Kyoto, Japan, May 2010, WEPE023, pp. 3398-3400.
- [70] E. Marin, et al., Impact of Dynamical Stray Fields on CLIC, *Proceedings of the 8th International Particle Accelerator Conference (IPAC'17)*, Copenhagen, Denmark, May 2017, MOPIK077, pp. 708-711.
- [71] O. Brüning, Linear imperfections, *Proceedings of the CERN Accelerator School: Intermediate Accelerator Physics*, Zeuthen, Germany (2003).
- [72] S. Smith, *Digital signal processing: a practical guide for engineers and scientists* (Elsevier, 2013).
- [73] P. Ripka, *Magnetic sensors and magnetometers* (Artech House, 2001).
- [74] D. Jiles, *Introduction to magnetism and magnetic materials* (CRC Press, 1991).
- [75] Bartington Instruments Ltd, UK. URL: <https://www.bartington.com>.
- [76] Bartington Instruments Ltd, UK, Mag-13 brochure. URL: https://www.bartington.com/wp-content/uploads/pdfs/datasheets/Mag-13_DS3143.pdf.

- [77] Bartington Instruments Ltd, UK, Mag-13 operation manual. URL: https://www.bartington.com/wp-content/uploads/pdfs/operation_manuals/Mag-13_OM3143.pdf.
- [78] Bartington Instruments Ltd, UK, Mag-13 technical drawings. URL: https://www.bartington.com/wp-content/uploads/pdfs/drawings/Mag-13MS_DR3359.pdf.
- [79] Bartington Instruments Ltd, UK, PSU1 brochure. URL: https://www.bartington.com/wp-content/uploads/pdfs/datasheets/Magnetometer_Power_Supplies_DS2520.pdf.
- [80] National Instruments. URL: <https://www.ni.com>.
- [81] National Instruments, NI 9174 datasheet. URL: <https://www.ni.com/pdf/manuals/374045a.pdf>.
- [82] DELL.
URL: <https://www.dell.com/en-us/work/shop/dell-laptops-and-notebooks/latitude-7480-business-laptop/spd/latitude-14-7480-laptop>.
- [83] National Instruments, LabVIEW. URL: <https://www.ni.com/en-us/shop/labview.html>.
- [84] National Instruments, NI 9238 datasheet. URL: http://www.ni.com/pdf/manuals/376138a_02.pdf.
- [85] National Instruments, NI 9239 datasheet. URL: http://www.ni.com/pdf/manuals/375939b_02.pdf.
- [86] T. J Sumner, J. M. Pendlebury and K. Smith, Convectional magnetic shielding, *Journal of Physics D: Applied Physics* **20(9)**, 1095 (1987).
- [87] S. Celozzi, R. Araneo and G. Lovat, *Electromagnetic shielding* (John Wiley & Sons, 2008).
- [88] L. V. King, Electromagnetic shielding at radio frequencies, *Philosophical Magazine and Journal of Science* **15(97)**, 201-223 (1933).
- [89] J. R. Wait and D. A. Hill, Electromagnetic shielding of sources within a metal-cased bore hole, *IEEE Transactions on Geoscience Electronics* **15(2)**, 108-112 (1977).
- [90] J. F. Hoburg, Principles of quasistatic magnetic shielding with cylindrical and spherical shields, *IEEE Transactions on Electromagnetic Compatibility* **37(4)**, 574-579 (1995).
- [91] J. F. Hoburg, A Computational Methodology and Results for Quasistatic Multilayered Magnetic Shielding, *IEEE Transactions on Electromagnetic Compatibility* **38(1)**, 93-103 (1996).
- [92] COMSOL Multiphysics. URL: <https://www.comsol.com>.

- [93] T. Behnke, et al., The International Linear Collider Technical Design Report - Volume 1: Executive Summary, Technical Report ILC-REPORT-2013-040 (2013).
- [94] R. T. Merrill, M. McElhinny and P. McFadden, *The Magnetic Field of the Earth: Paleomagnetism, the Core, and the Deep Mantle* (Academic Press, 1998).
- [95] K. Tsuchiya, et al., Cryomodule development for superconducting RF test facility (STF) at KEK, *Proceedings of the 10th European Particle Accelerator Conference (EPAC'06)*, Edinburgh, Scotland, June 2006, MOPCH190, pp. 505-507.
- [96] M. Masuzawa, et al., Magnetic shielding: Our experience with various shielding materials, *Proceedings of the 16th International RF Superconductivity Conference (SRF'13)*, Paris, France, Sep. 2013, WEIOD02, pp. 808-811.
- [97] M. Masuzawa, K. Tsuchiya and A. Terashima, Study of Magnetic Shielding Materials and Fabrication of Magnetic Shield for Superconducting Cavities, *IEEE transactions on applied superconductivity* **24(3)**, 1-4 (2014).
- [98] P. Arpaia, et al., Effects of temperature and mechanical strain on Ni-Fe alloy CRYOPHY for magnetic shields, *Journal of Magnetism and Magnetic Materials* **475**, 514-523 (2019).
- [99] W. O. Hamilton, Superconducting shielding, *Revue de physique appliquée* **5(1)**, 41-48 (1970).
- [100] B. Angerth, et al., The LHC beam screen: Specification and design, *Proceedings of the 4th European Particle Accelerator Conference (EPAC'94)*, London, England, June 1994, CERN-MT-94-04, pp. 208-210.
- [101] N. Mounet, *The LHC transverse coupled-bunch instability*, PhD thesis, École Polytechnique Fédérale de Lausanne (2012).
- [102] S. Kostoglou, et al., MD4147: 50 Hz harmonics perturbation, Technical Report CERN-ACC-NOTE-2019-0055 (2019).
- [103] AK Steel Corporation, USA. URL: <https://www.aksteel.com>.
- [104] Aperam, Luxembourg. URL: <https://www.aperam.com/homepage>.
- [105] Magnetic Shielding Corporation, USA. URL: <http://www.magnetic-shield.com/index.html>.
- [106] D. Dubbers, Simple formula for multiple mu-metal shields, *Nuclear Instruments and Methods in Physics Research A* **243**, 511-517 (1986).
- [107] B. Podobedov, et al., Eddy Current Shielding by Electrically Thick Vacuum Chambers, *Proceedings of the 23rd Particle Accelerator Conference (PAC'09)*, Vancouver, Canada, May 2009, TH5PFP083, pp. 3398-3400.

- [108] N. Wang, et al., Shielding of Beam Pipe on Rapidly Varying Magnetic Field, *Proceedings of the 8th International Particle Accelerator Conference (IPAC'17)*, Copenhagen, Denmark, May 2017, WEPIK077, pp. 3107-3109.
- [109] M. Morrone, et al., Magnetic frequency response of high-luminosity large hadron collider beam screens, *Physical Review Special Topics - Accelerators and Beams* **22**, 013501 (2019).
- [110] B. Heilig, C. Beggan and J. Lichtenberger, Natural sources of geomagnetic field variations, Technical Report CERN-ACC-2018-0033 (2018).
- [111] C. Constable, Earth's Electromagnetic Environment, *Surveys in Geophysics* **37(1)**, 27-45 (2016).
- [112] CERN maps. URL: <https://maps.web.cern.ch>.
- [113] J.-P. Burnet, et al., Fifty years of the CERN Proton Synchrotron - Volume 1, Technical Report CERN-2011-004 (2011).
- [114] K. Seleznyova, M. Strugatsky and J. Kliava, Modelling the magnetic dipole, *European Journal of Physics* **37(2)**, 025203 (2016).
- [115] I. Ahmed, M. Z. Shames and M. M. Alam, An overview of harmonic sources in power system, *IOSR Journal of Electrical and Electronics Engineering* **7(3)**, 01-03 (2013).
- [116] V. Profillidis, *Railway management and engineering* (Routledge, 2016).
- [117] E. Bravin, et al., The influence of train leakage currents on the LEP dipole field, *Nuclear Instruments and Methods in Physics Research A* **417**, 9-15 (1997).
- [118] N. Catalán Lasheras, et al., Commissioning of XBOX-3: A very high capacity X-band test stand, *Proceedings of the 28th International Linear Accelerator Conference (LINAC'16)*, East Lansing, Michigan, USA, Sept. 2016, TUPLR047, pp. 568-571.
- [119] R. W. Erickson and D. Maksimovic, *Fundamentals of power electronics* (Springer Science & Business Media, 2007).
- [120] M. Oriunno, et al., The Roman Pot for LHC, *Proceedings of the 10th European Particle Accelerator Conference (EPAC'06)*, Edinburgh, UK, Jun. 2006, MOPLS013, pp. 562-564.
- [121] A. Latina, D. Schulte and S. Stapnes, CLIC study update August 2019, Technical Report CERN- ACC-2019-0051 (2019).
- [122] M. Sands, Emittance Growth from Radiation Fluctuations, Technical Report SLAC-AP-047 (1985).
- [123] P. Stoica and R. Moses, *Spectral Analysis of Signals* (Pearson Prentice Hall, 2005).
- [124] M. S. Bartlett, Periodogram analysis and continuous spectra, *Biometrika* **37(1-2)**, 1-16 (1950).

- [125] P. Welch, The use of fast Fourier transform for the estimation of power spectra: a method based on time averaging over short, modified periodograms, *IEEE Transactions on Audio and Electroacoustics* **15**(2), 70-73 (1967).
- [126] P. Duhamel and M. Vetterli, Fast Fourier transforms: A tutorial review and a state of the art, *Signal Processing* **19**, 259-299 (1990).
- [127] K. Prabhu, *Window functions and their applications in signal processing* (CRC Press, 2013).
- [128] M. Gasior and J. L. Gonzalez, Improving FFT frequency measurement resolution by parabolic and Gaussian spectrum interpolation, *AIP Conference Proceedings* **732**(1), 276-285 (2004).